THE CONTRIBUTION OF MOLECULAR LINE EMISSION TO BROADBAND FLUX MEASUREMENTS AT MILLIMETER AND SUBMILLIMETER WAVELENGTHS

Thesis by

Todd D. Groesbeck

in Partial Fulfillment of the Requirements

for the Degree of

Doctor of Philosophy

California Institute of Technology
Pasadena, California
1995
(Defended September 9, 1994)

Acknowledgements

First, more thanks than I can express go to Lisa for her love, patience, and support during these many years. She and Matthew and Michael bring joy into my life, remind me of the things that are important, and help make life fun. I am grateful that we can share our lives together as a family.

My parents have always been supportive, helpful, and interested in what I have been doing. It has been especially gratifying to be able to return in some small way during the past few years the love, friendship, and support which they have for so long given unhesitatingly to me. My brothers have always believed in me and have been examples as well as friends to me throughout my life. While it is a great pleasure to finally join them as a fellow doctor, I am more grateful for the wonderful association with them and my parents which I have enjoyed since my birth.

While my association with Lisa's family extends back for a shorter time, they have been no less loving and supportive, and I am truly glad to have become a part of their family and to call them my friends.

There have also been many other friends who have become important parts of my life outside of my Caltech experience. I owe them all a great debt for their friendship and the things which I have learned from them.

My fellow graduate students deserve special thanks for their friendship and also for their help in many ways. Dave Carico and Rob Schoelkopf were particularly helpful and pleasant to work with as we shared offices, and a million thanks are owed to Taco for the many many questions answered and computer and/or observatory problems solved, all with exemplary grace. Thomas Büttgenbach was another

with whom I shared many of the experiences of a grad student and who made those experiences better. I also enjoyed and appreciated the shared experiences with the many other students in our group who have preceded or followed me, including Mike Wengler, Erich Grossman, Jeff Stern, Todd Hunter, Dominic Benford, and John Ward.

Others who added in many ways to my learning and who made it enjoyable to be at Caltech were Chris and Connie Walker, Darek Lis, George Ugras, Brian Ellison (who also made this work possible by building the wonderful 345 GHz receiver used for the line surveys), Gene Serabyn, and Jocelyn Keene. Peter Schilke merits special mention for his work on the analysis of the Orion-KL survey for which I am in his debt.

Observing at the Caltech Submillimeter Observatory was always made a more pleasant and successful experience by the consistently helpful work of the observatory staff. Antony Schinckel deserves special praise and thanks for the apparently endless and tireless nights and days spent by him in support of CSO work, as well as the friendship which I have enjoyed both in Hawaii and at Caltech.

Tom Phillips has given me excellent access to the CSO in order to complete this project and has provided support and suggestions for my thesis work and throughout my stay at Caltech. Geoff Blake was my observing partner during nearly all of the time at the CSO; in addition to teaching me the techniques of observing (from scientific to stylistic concerns) he has also been extremely helpful in answering questions, explaining concepts, and in helping me learn about astronomy and science in general. Ewine van Dishoeck was a willing teacher and source of information and suggestions while here at Caltech and has continued to assist me from her current position in Leiden.

I wish to acknowledge the generous financial support which I received from the ARCS foundation, and while less directly given to me, the stipend and tuition which have been paid by unknowing taxpayers courtesy of the U.S. Government and the NSF. I have greatly appreciated the willing help I have received from the staff at Caltech, and their interest in the success of graduate students here. Donna Driscoll of the Physics Graduate Office deserves particular mention for her cheerful kindness and hard work.

Finally, I wish to again thank my wife Lisa, who deserves a huge amount of credit for any of my success. I shall be forever grateful to her.

Abstract

We present measurements of the ratio of flux carried by molecular emission lines to the total flux observed from six astronomical sources in the 330–360 GHz frequency range, demonstrating that the integrated line emission can represent a significant fraction, and in some cases even the majority, of the total flux observed. Given the narrow widths of these emission lines for most sources in the interstellar medium, it has generally been assumed that the contribution of the integrated lines would be negligible when compared to the continuum flux measured by a very broadband instrument. We extend the previous work by Sutton *et al.* (1984), which demonstrated that line emission was responsible for a large part of the total flux observed from Orion-KL, by presenting observations at higher frequencies of Orion-KL and several additional sources. These observations provide the most comprehensive determination of the ratio of line flux to continuum flux yet made at submillimeter wavelengths.

We have performed spectral line surveys of the star-forming regions Orion-KL, Orion-S, and IRAS 16293–2422, and the evolved stars IRC +10216, VY Canis Majoris, and OH 231.8+4.2. Observations for Orion-KL and IRC +10216 give continuous frequency coverage over approximately the 330–360 GHz band; for the other sources the coverage ranges between 30 and 60% of the same frequency band. Comparisons of the line survey data with total flux measurements demonstrates that the contribution of the integrated line emission to the total flux at these frequencies ranges from as low as ~10% for Orion-S and IRAS 16293–2422 to at least ~60% for Orion-KL and IRC +10216. We also estimate the amount of flux carried in weak lines below our sensitivity limits based on the observed distributions of line intensities.

An improved deconvolution method has been used to obtain a single sideband spectrum from the

double sideband observations. We have also developed computer versions of line catalogs which allow immediate line identification and analysis, assuming conditions of local thermodynamic equilibrium (LTE) prevail. The same catalog programs also permit simulation of emission line spectra for arbitrary molecular abundances and excitation temperatures, again assuming LTE. For each of the observed sources, we present simulations of the spectrum from 0 to 1000 GHz, using molecular parameters derived from our data and additional published observations. In all cases, the simulations indicate that the relative importance of the line emission decreases at higher frequencies ($\gtrsim$ 700 GHz). We discuss the significance of these findings regarding the determination of dust parameters from broadband flux measurements, concluding that such measurements must be corrected for possible line flux contributions before they can be reliably used.

Table of Contents

Appendix C

List of Figures

List of Tables

Chapter 1

Introduction

1.1. Introduction and Background

Submillimeter astronomy is a relative newcomer among the different branches of observational astronomy, with the first submillimeter spectral line observed fewer than 20 years ago (Phillips *et al.* 1977). The millimeter and submillimeter bands (dealing with radiation having wavelengths on the order of a millimeter, or roughly the frequency region between 100 GHz and 3000 GHz) are among the last regions of the electromagnetic spectrum to become available to astronomers in their study of the universe.* Situated between the infrared (IR) band and the radio region at longer wavelengths, the radiation from astronomical objects at these frequencies contains a wealth of information with important consequences for such topics as star formation, cosmochemistry, and the dust and gas in the interstellar medium (ISM).

Molecular clouds in the ISM are particularly well suited for study at these wavelengths, where the photon energy when expressed in temperature units ($T = h\nu/k_B$) ranges from about 5 to 100 K, matching the physical conditions of typical clouds. Hence the thermal energy will essentially be radiated at submillimeter wavelengths. This is important not only from an observational standpoint, enabling us to

* While there are some minor differences between the millimeter and submillimeter bands, the similarities in emission mechanisms, etc., are of greater importance for our purposes. For simplicity, we will generally refer only to the submillimeter band but the discussion will apply in most cases to both millimeter and submillimeter radiation.

detect these objects more efficiently, but also for the physical and chemical processes taking place in these clouds. The collapse of a cloud leading to star formation, for example, would be halted by the increasing pressure resulting from heating if thermal energy were not carried away by radiation. In addition to the correspondence between the thermal energy of clouds and the photon energy in the submillimeter band, the thermal energy is also comparable to the excitation energies of the rotational levels of many molecules. These molecules therefore are effective emitters and absorbers of submillimeter radiation. Transitions between different rotational levels may be seen in either absorption or emission, and in conjunction with laboratory spectroscopy the specific molecules and energy levels involved may be identified. The particular molecules present in a cloud may affect the efficiency with which energy is radiated through their transitions making the chemistry important for the physical evolution of clouds. The interplay between radiation, chemistry, and physical processes in these clouds is now being recognized and studied, with submillimeter observations playing a key role (van Dishoeck *et al.* 1993).

Figure 1.1 shows the emission expected from a "typical" molecular cloud, including both dust emission and atomic and molecular transitions. The thermal emission is modeled for dust at a temperature of 30 K, with curves representing the emission from a 30 K blackbody and from a much cooler blackbody at 2.7 K (corresponding to the cosmic microwave background emission) shown for comparison. In addition, vertical ticks representing the transitions of many of the simpler species known to exist in the ISM are shown, with the multitude of lines at frequencies below 500 GHz resulting from "heavy" molecules indicated by the hatched region. At mid-infrared and shorter wavelengths the dust emission from clouds is typically optically thick, preventing observations of the cloud interiors and accurate determination of cloud masses and composition. At submillimeter wavelengths, where the optical depth is lower, observations can sample the radiation from the entire cloud, allowing observations of both the dust and the transitions of the various species present. At even longer wavelengths, however, the optical depth may become so low that the dust emission cannot be detected.

A number of other types of sources may also be studied with submillimeter observations, including circumstellar shells, galaxies outside our own Milky Way, as well as the cosmic microwave background and cosmologically distant sources whose radiation at higher frequencies may be Doppler shifted into the

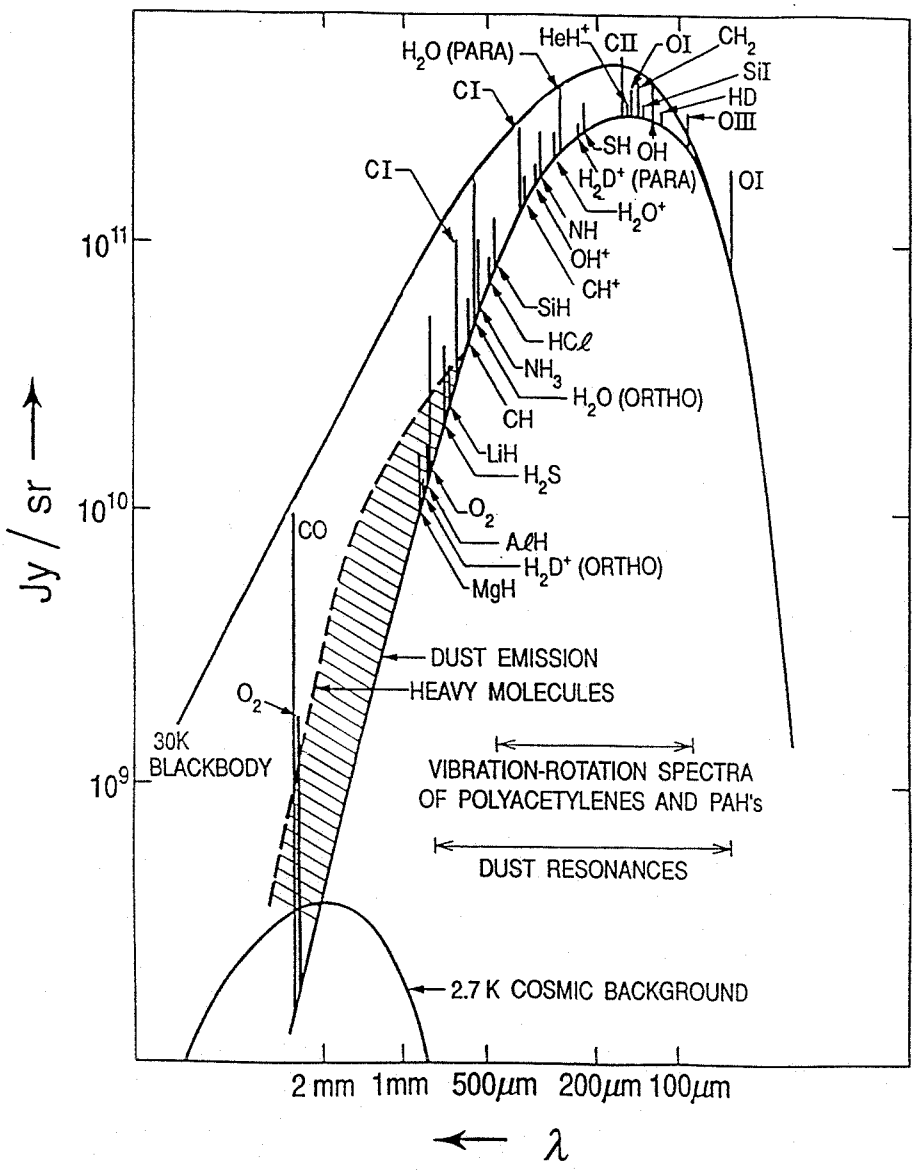

Figure 1.1 A schematic presentation of the emission spectrum from a typical molecular cloud with a physical temperature of 30 K (from Phillips & Keene 1992). Atomic and molecular transitions are shown together with the underlying dust continuum emission. Blackbody emission curves for 30 K and 2.7 K are shown for reference. Note $1\,\mathrm{Jy} = 10^{-26}\,\mathrm{W\,m^{-2}\,Hz^{-1}}$.

submillimeter band. The sources considered in this thesis are discrete galactic sources exhibiting molecular emission, namely molecular clouds and circumstellar shells of evolved stars. The specific sources observed are discussed in Chapter 5 in connection with our results and in the appendices where the observed spectra are presented.

It is only fairly recently that astronomers have been able to take observational advantage of the

submillimeter band, largely because of the severe challenges posed by atmospheric absorption and technical requirements at these wavelengths. Depending upon the actual frequency considered, the atmosphere is at best only partially transparent and is often completely opaque. The correspondence between the energies involved that makes the submillimeter band useful for studying molecular transitions also holds in the Earth's atmosphere, where the most prevalent molecules, particularly water vapor, oxygen, and ozone, can become effective absorbers of incident radiation. Efforts have therefore been made to perform observations above as much of the atmosphere as possible, by using rocket-borne sensors, satellite space missions, or the Kuiper Airborne Observatory, an infrared and submillimeter 0.9 m telescope mounted on an airplane and flown at altitudes of up to ~45000 feet. However, these methods have thus far only involved the use of relatively small telescopes ($\lesssim$1 m diameter), providing only limited resolution and sensitivity to small-diameter sources. Future space missions with larger apertures are planned, but will not be operational until the late 1990's at the earliest. To obtain the desired sensitivity and resolution, large telescopes ($\gtrsim$ 10 m diameter) with high surface accuracies ($\lesssim \lambda/20$ or $\lesssim 20\,\mu$m) are required and must be situated at high altitude sites. The Caltech Submillimeter Observatory (CSO), the first telescope designed specifically for submillimeter observations and satisfying these requirements, went into operation in 1987 on Mauna Kea, Hawaii at an altitude of 4200 m. Shortly thereafter, the James Clerk Maxwell Telescope (JCMT), located at the same site, also went into operation. There are now several submillimeter telescopes operational or under construction at sites around the world, including an interferometric array of telescopes slated for Mauna Kea.

In Figure 1.2 a model of the atmospheric transmission is shown for typical observing conditions at the CSO. Nearly all of the strong absorption lines seen in the figure result from only a few species, most notably H_2O, O_2 and O_3 (see above). For $\nu \geq 400$ GHz, even for the fairly good conditions and the high altitude site used for the plot, the transmission never goes above 0.5. While not shown in the figure, the transmission is nearly zero over the entire range from 1000 to 3000 GHz at the high frequency end of the submillimeter band so that these frequencies are simply not accessible in a practical sense from ground-based telescopes.

The detector technology required for submillimeter receivers also presents challenges to astronomers.

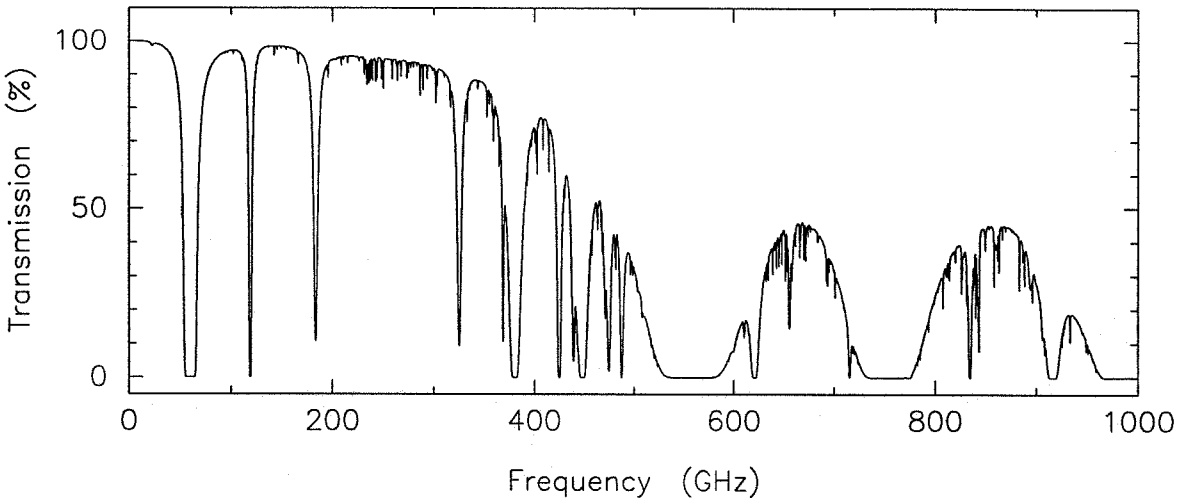

Figure 1.2 Atmospheric transmission as a function of frequency at the CSO. The trace shows a model (Grossman 1989) of the transmission calculated for 1 mm precipitable water vapor and an altitude of 4200 m.

Submillimeter astronomy, falling as it does between the radio and infrared portions of the spectrum, borrows observing techniques which have been developed and used at these neighboring wavelengths. In particular, the actual detectors used are generally either bolometers for direct detection (borrowed from infrared astronomy) or heterodyne mixers (borrowed from radio astronomy). The heterodyne mixers are used for high-resolution spectroscopy and allow observations to be made of the individual molecular or atomic transitions within a fairly narrow instantaneous bandwidth (typically on the order of 1 GHz). These can be tuned to select particular lines of interest, or as is done in this thesis, spectral line surveys can be performed which provide detailed information over a much larger bandwidth but which require correspondingly large amounts of telescope time and data processing to complete. Bolometric measurements, by contrast, usually give much broader spectral coverage, but have a resolution equal to the entire bandwidth (typically on the order of 30–100 GHz) and are generally used for studies of the continuum flux from sources. The method of choice for a particular observation depends upon the desired resolution and the detector performance; a detailed discussion of the relative merits of the two techniques is given by Phillips (1988).

Both of these types of detectors require adaptations to be useful at submillimeter wavelengths. Relative to infrared wavelengths, the submillimeter photons are less energetic requiring differences in the bolometric receivers. The heterodyne receivers must operate at much higher frequencies than for radio

TABLE 1.1

HISTORY OF FACILITY HETERODYNE RECEIVERS
INSTALLED AT THE CALTECH SUBMILLIMETER OBSERVATORY

Year Installed	Nominal Frequency [a] (GHz)	Receiver Noise Temperature [b] (K)	Reference
1987	230	170	1
1988	345	160	2
1991	230	50	3
1991	490	180	4
1993	345	65	5
1993	660	210	6
1994	230	35 [c]	5
1994	850	— [d]	7

[a] Nominal design frequency of the receivers, which may typically be used over a 25–40% bandwidth.
[b] A representative receiver temperature (DSB) obtained with the receiver installed at the observatory.
[c] Laboratory measurement of receiver temperature; not yet installed at the observatory.
[d] Receiver currently being built, completion anticipated in late 1994.

REFERENCES:

1. Ellison & Miller 1987; 2. Ellison *et al.* 1989; 3. Kooi *et al.* 1992; 4. Walker *et al.* 1992; 5. Kooi *et al.* 1994a; 6. Kooi *et al.* 1994b; 7. Kooi, private communication.

astronomy while maintaining very low noise temperatures. Note that reducing the system noise temperature by a factor f reduces the integration time required to achieve a given sensitivity by f^2, making the receiver noise temperature an extremely important measure of performance. The history of the facility heterodyne receivers installed at the CSO is summarized in Table 1.1 and demonstrates both the progress being made and the challenge which remains to develop receivers with low noise temperatures at higher frequencies.

Like submillimeter astronomy, the study of interstellar chemistry and molecules is relatively young. The first evidence for the existence of interstellar molecules was observed in 1936 in the form of narrow absorption lines at visible wavelengths (Dunham & Adams 1937), which were later identified with CH and CH^+ (Swings & Rosenfield 1937, Douglas & Herzberg 1941). Confirmation of these identifications and the additional identification of the CN molecule (McKellar 1941) added to the evidence for molecules in space. However, these were generally considered to be of little significance for the ISM, as most theories predicted that harsh interstellar conditions would rapidly destroy the few molecules which might form. Following World War II, with newly available microwave techniques and equipment, astronomical searches were made for radio frequency lines of simple molecules based on newly obtained laboratory

spectroscopic data (*e.g.*, Townes 1954). However, it was not until two decades after the identification of the first interstellar molecules that OH, the next molecule identified and the first observed using radio techniques, was detected (Weinreb *et al.* 1963). Another five years later, the additional molecules H_2O, NH_3, and H_2CO were identified through radio detections (Cheung *et al.* 1968, Cheung *et al.* 1969, Snyder *et al.* 1969). Since then, ever more complex molecules have been identified in the ISM, with a total of nearly 100 molecules detected thus far, many of which have also been detected with isotopic substitutions (*cf.* van Dishoeck *et al.* 1993). Perhaps even more significant has been the recognition of the existence of molecular clouds and their role in star formation and as reservoirs of neutral material in the ISM. The OVRO and CSO spectral line surveys of Orion-KL are shown in Figure 1.3 as an example of the rich spectrum which can result from molecular transitions. The many insights into the chemistry and physics of molecular clouds which may be obtained from such spectra have only recently become available to astronomers.

While dust has been recognized as an important component of the ISM for a longer period of time, many questions regarding its formation and composition remain unanswered. Thorough discussions of interstellar dust, including observational issues and theoretical models, have been given in recent review papers (Mathis 1993, Mathis 1990, Cox & Mezger 1989, Tielens 1989, Tielens & Allamandola 1987). Through its interaction with radiation, dust plays a significant role in determining the opacities, the heating and cooling and the infrared and submillimeter spectra of interstellar sources. It is also clear that dust is crucial to the formation of H_2, which is formed on grain surfaces and then released into the gas phase. At millimeter and submillimeter wavelengths the dust is generally optically thin, so that observations sample dust emission from all depths in a source and may be used to determine the mass of the dust present (Hildebrand 1983). The dust emission is largely featureless at these wavelengths, in contrast to the infrared where several spectral features are observed. However, observations at different wavelengths may be used to determine the variation of the dust emissivity with frequency. This frequency dependence will reflect the composition of the dust and can be an important constraint on dust models. Millimeter and submillimeter flux measurements are particularly helpful because the dust is more likely to be optically thin and the Rayleigh-Jeans approximation ($h\nu/kT \ll 1$) is more likely to be valid relative to infrared wavelengths,

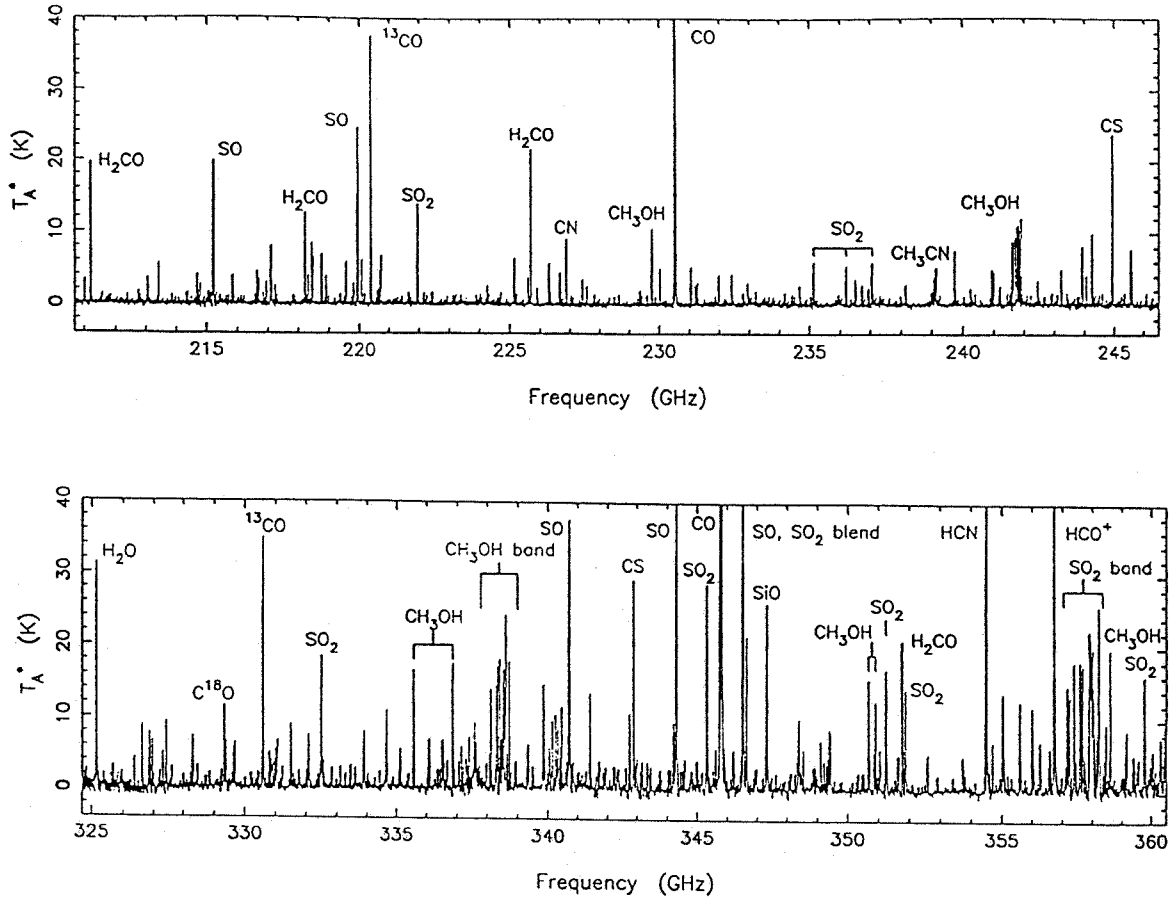

Figure 1.3 Compressed views of spectral line surveys of Orion-KL performed at OVRO (Sutton *et al.* 1985, Blake *et al.* 1986) and at the CSO (this work).

thereby allowing the frequency dependence of the emissivity to be more directly determined from the spectral index of the radiation.

Given the continuum nature of the thermal dust emission and the increase in sensitivity gained by using a larger bandwidth, most observations of dust emission have been performed using broadband detectors. Because of their lack of frequency resolution, however, such measurements give no information about any possible contributions of molecular emission lines. The first published evidence that the flux contributed by emission lines could be substantial came during the analysis of a spectral line survey of Orion-KL between 215 and 270 GHz performed at the Caltech Owens Valley Radio Observatory (OVRO) (Sutton *et al.* 1984, hereafter SBMP). The high spectral resolution of the survey allowed the individual emission lines to be seen and their integrated flux compared to the total flux observed in the course of the survey. The integrated line flux was found to represent ~40% of the total flux, with some suggestion that

weaker, undetected lines might raise that contribution even higher. Prior to this it was generally assumed that when averaged over the large bandwidths of most continuum observations, the contribution of emission lines would be negligible. Since Orion-KL possesses an unusually rich and bright emission line spectrum, it might be supposed that it is also unusual in having a large fraction of its millimeter-wavelength flux radiated in the form of emission lines. We therefore undertook to determine how the contribution of the lines to the total flux might vary with frequency, and also to determine the line flux contribution in a variety of other sources. If the lines contribute a significant fraction of the flux measured in broadband observations, corrections must be made to such observations in order to derive the correct flux from thermal dust emission. This will in turn have an impact on derived quantities such as mass, or if the contribution varies with frequency, the emissivity index of the dust.

1.2. Thesis Outline

This thesis presents the observational and analytical work performed to carry out the project outlined above, and as will be demonstrated, presents evidence that in some additional cases, the line flux can represent a significant fraction of the total flux observed. In addition, we present specific new computational methods for data processing and line analysis and simulation that were developed and implemented in the course of this work. These methods may be used both for spectral line surveys and observations of individual lines and are available as part of the standard software at the CSO.

The primary research described herein is concerned with the integrated line flux derived from the spectral line surveys performed at the CSO covering the 330 - 360 GHz atmospheric window. Surveys with continuous coverage of essentially the entire range were obtained for Orion-KL and IRC +10216. We have also performed partial surveys with coverage of between 30% and 70% of the window in discrete sections for Orion-S, IRAS 16293–2422, OH 231.8+4.2, and VY Canis Majoris. The integrated line flux results of these surveys are compared with published values for the flux as measured with broadband detectors. In some cases, data is available at lower frequencies, permitting some discussion of the possible variation of the line flux contribution with wavelength. We also model the frequency dependence of both the thermal dust emission and the line emission and compare their variation at frequencies up to 1000 GHz. These

models rely on the particular source parameters (*i.e.*, temperature, molecular column densities, line profiles) and are specific to the sources observed. However, the modeling methods may be applied to additional sources without requiring a spectral line survey of each source. As an example of this possibility, we perform simulations of the emission line spectra which result as the source temperature is varied while the chemical composition is held fixed.

The presentation of the thesis is given as follows: Chapter 2 describes the formation of spectra, both for thermal dust emission and molecular transitions. We also discuss the effects of different physical parameters and the interpretation of spectra in deriving various source parameters. In Chapter 3 we discuss our observing and calibration methods. These become particularly important when comparing data from different telescopes as we do, especially since line and continuum data are generally given in different units. Chapter 4 presents the computational methods developed for the surveys. These consist of an improved algorithm and implementation for the deconvolution of double sideband data and the development of an online catalog of molecular transitions. This catalog may be used for line identification and analysis, and also has the capability of simulating emission line spectra based upon physical and chemical source parameters. Chapter 5 contains the discussion of the integrated line fluxes and comparisons with broadband data for the different sources. The modeling of the source spectra and the variation of the flux with frequency are also presented. Chapter 6 gives a summary of our results and presents some speculations on possible directions for future work. The actual line surveys of the different sources are presented in appendices following the main body of the thesis.

Chapter 2

Radiation Processes and Astronomical Spectra

Through the interpretation of the spectra observed towards different sources, astronomers attempt to discover the physical conditions and processes present in these sources. Different types of radiation have different spectral signatures, appearing as sharp spectral features or broad continuum emission with a particular frequency dependence. The presence of these signatures in a spectrum alerts us to the presence of the corresponding physical process in the source. In the case of molecular lines, their detection and identification gives us information about the chemistry of the source, and may enable us to extract information about the mass, density, and temperature as well, while dust emission may also give information regarding cloud composition, mass, and temperature. In this chapter, we discuss the spectral signatures of dust emission and molecular transitions and the relations between the physical parameters of the source and the emitted radiation.

2.1. Radiative Transfer

We first consider the general problem of radiation passing through a medium in which both absorption and emission occur, as is the case for the molecular clouds and other sources described in this thesis. The well-known equation of radiative transfer which describes the intensity of the spectrum along a path through such a medium is

$$\frac{dI_\nu}{ds} = j_\nu - \kappa_\nu I_\nu \tag{2.1}$$

where I_ν is the specific intensity at frequency ν, ds is a differential element of length along the path, j_ν is the emission coefficient, and κ_ν is the absorption coefficient of the medium.

A change of variable from s to τ, the optical depth, can be made using $d\tau_\nu \equiv \kappa_\nu \, ds$ which allows the transfer equation to be written,

$$\frac{dI_\nu}{d\tau_\nu} = S_\nu - I_\nu \tag{2.2}$$

where $S_\nu \equiv j_\nu / \kappa_\nu$ is called the source function. After integration, the solution to this equation is

$$I_\nu \left(\tau_\nu\right) = I_\nu \left(0\right) \, e^{-\tau_\nu} + \int_0^{\tau_\nu} S_\nu \left(\tau'_\nu\right) e^{-\left(\tau_\nu - \tau'_\nu\right)} \, d\tau'_\nu \, . \tag{2.3}$$

This solution is easily interpreted as the sum of two components: the incident intensity diminished by absorption as it passes through the entire medium and the integrated intensity arising within the medium (the integrated source function) diminished by absorption through the remainder of the medium.

It is instructive to consider the case of a source function which is constant throughout the intervening medium. Performing the integration of (2.3) for $S_\nu \left(\tau_\nu\right) = S_\nu \equiv \textit{constant}$ yields

$$I_\nu \left(\tau_\nu\right) = I_\nu \left(0\right) \, e^{-\tau_\nu} + S_\nu \left(1 - e^{-\tau_\nu}\right) \tag{2.4}$$

where the two terms described above are again seen. We can now readily distinguish between the optically thin and thick limiting cases and understand the effects of increasing optical depth. For the optically thin case, where $\tau_\nu \ll 1$, we can write

$$I_\nu \left(\tau_\nu\right) = I_\nu \left(0\right) \, \left(1 - \tau_\nu\right) \, + \, S_\nu \tau_\nu . \tag{2.5}$$

In this regime, an increase in the optical depth produces a linear attenuation of the incident intensity and a linear increase in the integrated intensity from the medium itself. In the optically thick limit, where $\tau_\nu \gg 1$, (2.4) becomes simply

$$I_\nu \left(\tau_\nu\right) = S_\nu . \tag{2.6}$$

Between these two extremes, the value of $I_\nu \left(\tau_\nu\right)$ changes smoothly and monotonically from $I_\nu \left(0\right)$ to S_ν.

For the purposes of this thesis, we consider the typical astronomical case shown in Figure 2.1. For a molecular cloud, the incident radiation is usually the 2.7 K cosmic microwave background radiation, while

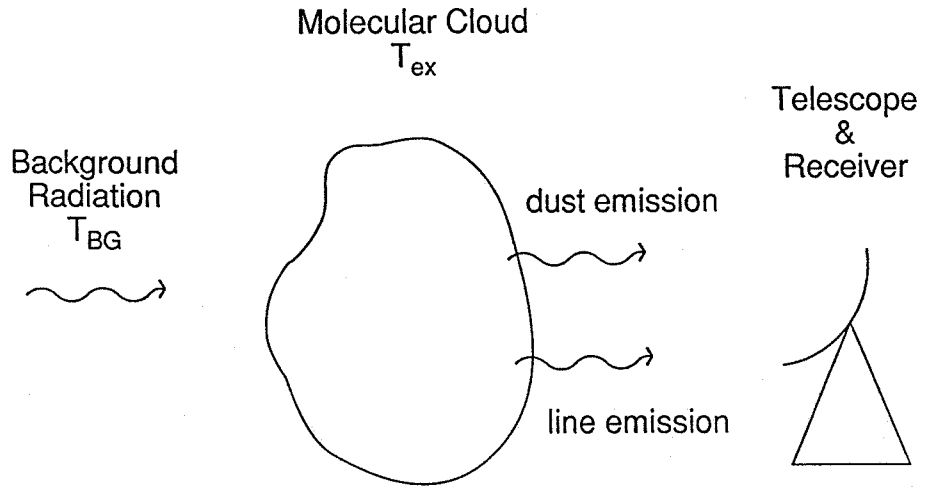

Figure 2.1 Schematic depiction of the typical radiative transfer geometry in observations of a molecular cloud.

the dust and gas in the cloud generally exhibit emission at higher temperatures (typically 10 – 100 K). We first discuss the general characteristics of radiation emitted by dust and gas in the ISM.

2.2. Thermal Continuum Radiation from Dust

While our main focus is concerned with molecular line emission, we wish to compare this emission with the underlying continuum radiation, which at submillimeter wavelengths generally results from the thermal emission from dust. A complete analysis of interstellar dust properties and dust emission would extend beyond the scope of this thesis and is not warranted here. A number of excellent reviews concerning interstellar dust have recently appeared to which the reader is referred for a more complete treatment of the subject (Mathis 1993, Mathis 1990, Cox & Mezger 1989, Tielens 1989, Tielens & Allamandola 1987). We summarize here some characteristics of dust emission spectra at submillimeter wavelengths, particularly those related to the composition and structure of the dust.

When radiation is in thermodynamic equilibrium with its surroundings, the spectral distribution of the radiation is given by the familiar Planck law

$$B_\nu(T) = \frac{2h\nu^3}{c^2} \frac{1}{e^{h\nu/kT} - 1}. \tag{2.7}$$

This blackbody radiation is dependent only upon the temperature T. Full thermodynamic equilibrium is generally not realized in the astronomical sources considered here. However, local thermodynamic

equilibrium (LTE), where a single temperature T governs the matter's physical state, is more often used to describe conditions in the ISM. In this case the radiation emitted satisfies Kirchhoff's law relating j_ν, κ_ν and T, namely

$$j_\nu = \kappa_\nu B_\nu (T) . \tag{2.8}$$

The source function is then the Planck spectrum, but only in the optically thick case does the observed brightness I_ν also become the Planck spectrum. We note here that independent of the physical conditions, the intensity I_ν may be specified as though it were blackbody radiation of a given temperature. That is, at a frequency ν and for an intensity I_ν, we may uniquely determine the value of T_{equiv} for which $B_\nu (T_{equiv}) = I_\nu$. In turn, a given T_{equiv} uniquely specifies the value of I_ν. It is often convenient to specify the intensity in terms of an equivalent temperature, whether or not the emission is thermal in nature.

In Figure 2.2, we show again a model of the dust emission which might be expected from a cloud with a temperature of 30 K. At short wavelengths, the dust is optically thick and its emission follows the blackbody curve. At longer wavelengths, the dust becomes optically thin and the thermal emission drops below the blackbody curve. In this figure we have constrained the dust to have an optical depth of unity at 150 μm and have assumed the emissivity of the dust varies as ν^β, with the resulting emission shown for $\beta = 1$ and $\beta = 2$, representing the range of expected and observed values for β. This variation of the emissivity with frequency reflects the physical and chemical composition of the dust and is therefore of great interest for studying dust in the ISM. At long wavelengths, the frequency dependence of the emissivity is apparent as a steeper slope than would be observed for blackbody radiation.

A variety of mechanisms have been suggested for producing the observed emissivity variation with frequency. The reader is again referred to the reviews for detailed discussions of the models and comparisons with observations. Proposed models of the dust must account for the observed infrared spectral features, the visible interstellar extinction, and be consistent with our understanding of the chemistry and processes present in the ISM. Detailed models have been constructed which specify the size distribution and composition of the dust, generally invoking a combination of different dust components including silicates, amorphous carbon, graphite, PAH's, and others.

At submillimeter wavelengths, the chief spectral signature of the dust is the frequency dependence

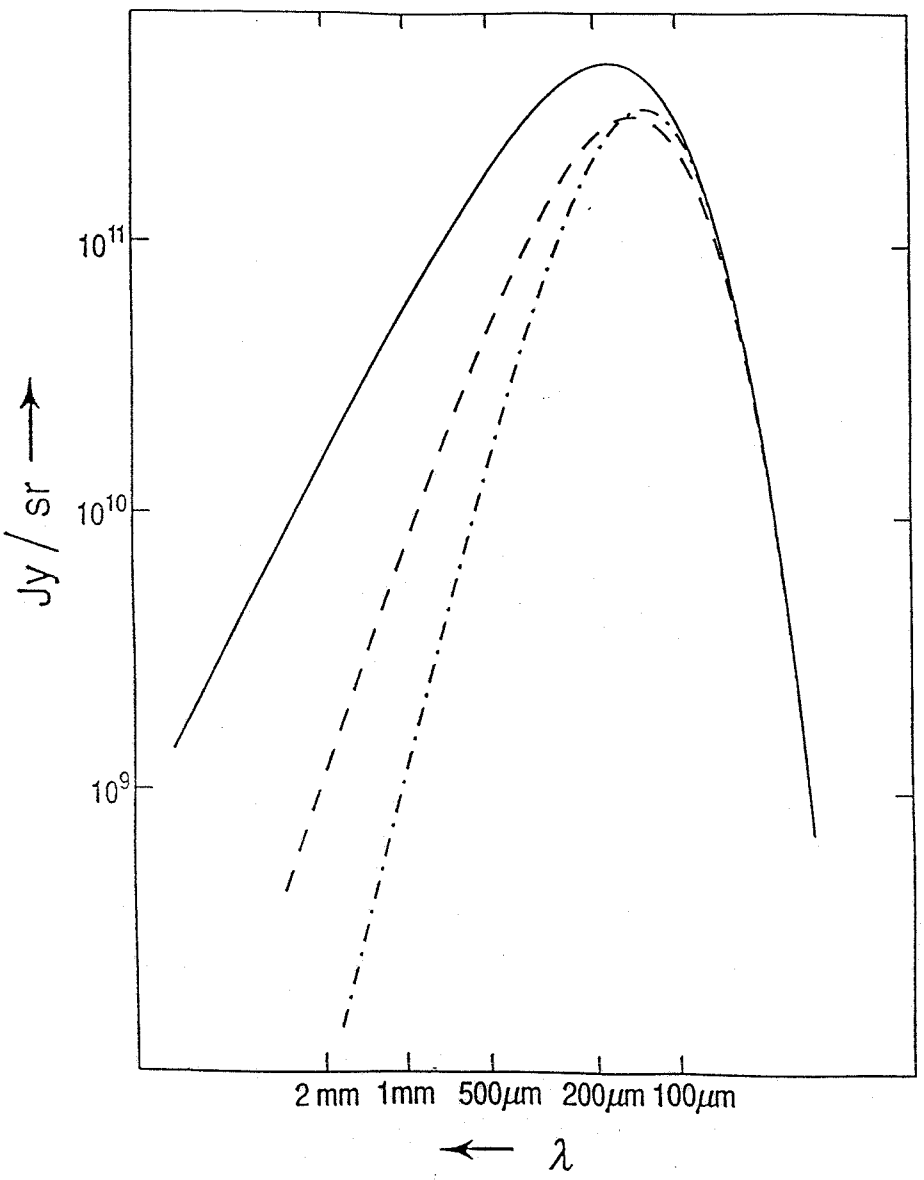

Figure 2.2 Thermal dust emission compared to blackbody radiation (solid curve). The dust emission is taken to have an optical depth of unity at 150 μm and an emissivity which varies with frequency as ν^1 (dashed line) or ν^2 (dashed-dotted line).

of the emissivity, which it might be hoped would help constrain the dust models. The composition of the dust is one factor in determining the dust spectrum. At submillimeter wavelengths, crystalline materials are expected to show a quadratic frequency dependence of their absorption, as are metallic or semimetallic materials (*e.g.*, graphite), understood as absorption by damped harmonic oscillators (such as the free electrons in a metal) (Wooten 1972). An amorphous material will show this same dependence, *i.e.*, λ^{-2},

for different reasons, reflecting the phonon spectrum directly, while amorphous, layered materials, such as amorphous carbon and lattice-layered silicates, show a λ^{-1} dependence because the phonons are limited to two dimensions (Tielens & Allamandola 1987). (Note that graphite, as a layered structure, also has a phonon spectrum with a λ^{-1} dependence, but the absorption is dominated by the free electrons giving the λ^{-2} dependence for the emissivity.) For diffuse radiation from the Milky Way and from other galaxies, observations show a λ^{-2} dependence for $\lambda > 100\,\mu$m. In dense portions of the ISM, observed fluxes suggest that the opacity may vary as λ^{-1} or $\lambda^{-1.5}$ (*cf.* Mathis 1990).

The shape and size distribution of the grains also contribute to the frequency dependence of the emissivity and have been invoked to explain the observed dust emission. Draine & Lee (1984) extended the wavelength range over which an earlier theory of dust composition (Mathis, Rumpl & Nordsieck 1977) could be compared with observations, deriving optical properties for the dust for wavelengths from 300 Å to 1000 μm. This model features a power-law distribution of grain sizes, with individual homogeneous grains composed of either silicate or graphite. Wright (1987) has proposed that the dust grains exhibit a fractal structure resembling twisted branches, the product of the aggregation process in their growth. The resulting open structures are efficient absorbers of submillimeter and far infrared (FIR) radiation and are consistent with a λ^{-1} dependence of the emissivity. One problem with this and other porous grain models is precisely this efficiency, which can leave the grains too cold to explain the observed FIR spectrum of galactic dust (Mathis 1990). Recently Pollack *et al.* (1994) have proposed a model for dust grains in molecular clouds and accretion disks which has much of the carbon in organics rather than graphite, and includes specific information on the mineral composition of the grains. The spectral emissivity index resulting from this model varies, with $\beta \approx 2.5$ between 100 and 650 μm and $\beta \approx 1.5$ between 650 μm and 2.7 mm.

Unfortunately, just as several different mechanisms might explain a given frequency variation of the dust emissivity, making it difficult to determine the particular mechanism involved, so different effects may conspire to prevent an accurate measurement of the frequency variation. In principle, using measurements at several wavelengths the deviation of the observed intensity from a blackbody curve could allow the optical depth of the dust to be derived as a function of frequency from which the frequency dependence of

the emissivity could be extracted. In practice, however, uncertainties in the measurements and about the temperature of the dust (which rarely can be characterized by a single temperature) often result in poorly determined optical depths, particularly as the emission changes from being optically thin to optically thick.

We instead consider the case where the dust emission is taken to be optically thin. As the dust is generally significantly warmer than the cosmic microwave background radiation, we neglect the incident intensity to obtain

$$I_\nu\left(\tau_\nu\right) = S_\nu \tau_\nu = \frac{2h\nu^3}{c^2} \frac{1}{e^{h\nu/kT_{dust}} - 1} \tau_\nu \tag{2.9}$$

where we substitute $B_\nu\left(T_{dust}\right)$ for the source function. If we now make the Rayleigh-Jeans approximation ($h\nu \ll kT_{dust}$) and take the optical depth to vary as ν^β, this becomes

$$I_\nu\left(\tau_\nu\right) \propto \frac{2kT_{dust}}{c^2} \nu^{\beta+2} \tag{2.10}$$

so that the ratio of the observed intensities at two frequencies yields

$$\frac{I_{\nu_1}}{I_{\nu_2}} = \left(\frac{\nu_1}{\nu_2}\right)^{\beta+2}. \tag{2.11}$$

Measurements at longer wavelengths where the dust is more likely to be optically thin and the Rayleigh-Jeans approximation more likely to be valid thus yield a more direct determination of β than measurements for which the effects of dust temperature and finite optical depth must be included in the analysis. However, a substantial and frequency-dependent line flux contribution to broadband flux measurements would produce errors in any derived values of β, so that an understanding of the line flux is important to studies of dust emission and composition.

A simple quantitative estimate may be made of the resulting error in a β value derived from observations at two wavelengths. If we let I_ν^{dust} be the true intensity of the dust continuum and separate the effect of the emissivity variation from all other effects, we may write

$$\frac{I_{\nu_1}^{dust}}{I_{\nu_2}^{dust}} = \left(\frac{\nu_1}{\nu_2}\right)^\beta R_{12} \tag{2.12}$$

where the factor R_{12} is introduced to account for any variation other than the dust emissivity (including the usual ν^2 Rayleigh-Jeans variation). If molecular line emission is responsible for a fraction f_ν of the

observed intensity, with the rest coming from dust, then the actual observed intensity I_ν^{obs} may be expressed as

$$I_\nu^{obs} = I_\nu^{dust} + f_\nu I_\nu^{obs}$$
$$= \frac{1}{(1 - f_\nu)} I_\nu^{dust}. \tag{2.13}$$

We may solve (2.12) for β to obtain

$$\beta = \frac{\log\left(I_{\nu_1}^{dust}/R_{12}I_{\nu_2}^{dust}\right)}{\log\left(\nu_1/\nu_2\right)} \tag{2.14}$$

which in principle allows us to determine β from measured values of I_ν^{dust} and known or assumed values of R_{12}. The change, or error, in β resulting from the use of the actual observed I_ν^{obs} with its molecular emission instead of simply I_ν^{dust} may be found by substituting (2.13) into (2.14) to obtain

$$\Delta\beta = \frac{\log\left[(1 - f_2)/(1 - f_1)\right]}{\log\left(\nu_1/\nu_2\right)}. \tag{2.15}$$

As an example of the sizable changes which might occur, consider the case where molecular emission represents 50% of the emission at a frequency ν_1 but only 10% of the emission at a frequency twice as high, $\nu_2 = 2\nu_1$. Then we find $\Delta\beta = -0.85$ and we would deduce a significantly less steep variation with frequency of the dust emissivity. While this example uses extreme though reasonable values (*cf.* our findings for Orion-KL and IRC +10216 in Chapter 5) which give rather dramatic results, we note that values derived for β are generally the result of fits to multiple points. If the contribution of molecular line emission is similar at several of these points, the overall error will then tend to be reduced (note that $\Delta\beta = 0$ for $f_2 = f_1$).

2.3. Spectral Line Formation

The molecular emission lines which are seen in Figure 1.3 contain a wealth of information about the physical and chemical conditions in these objects. In this section we show how the intensity of a line depends on various parameters (such as temperature). The derived relations play an important part in the analyses of spectra, allowing physical conditions and chemical abundances in the sources to be estimated

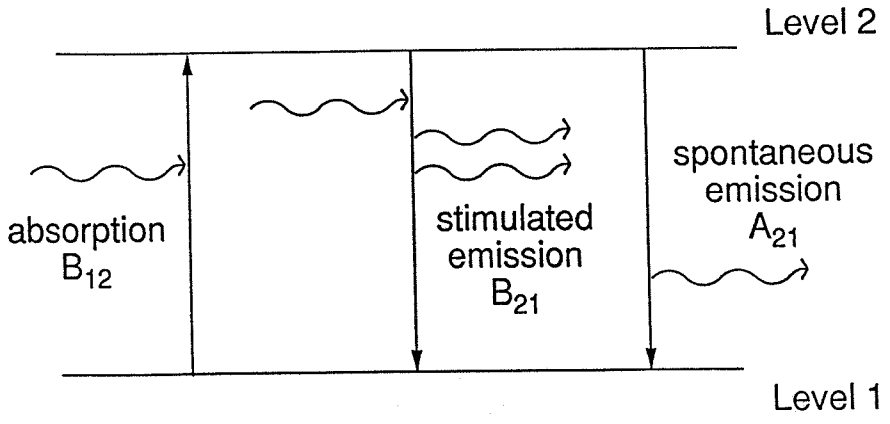

Figure 2.3 Radiative transitions between two energy levels. The relative rates for the transitions are given using the Einstein coefficients.

based upon the observed lines. In addition, these relations may be used to simulate spectral lines given the necessary parameters which determine the emission or absorption.

A. Analysis of a two-level system

We first consider a simple two-level system and the radiative transitions which may occur between the two levels as depicted in Figure 2.3. The emission and absorption coefficients may be written in terms of the Einstein A and B coefficients as

$$j_\nu = \frac{h\nu}{4\pi} n_2 A_{21} \phi(\nu) \tag{2.16}$$

and

$$\kappa_\nu = \frac{h\nu}{4\pi} \left(n_1 B_{12} - n_2 B_{21}\right) \phi\left(\nu\right) \tag{2.17}$$

where $\phi\left(\nu\right)$ is the normalized line profile. Using the principle of detailed balancing, the following relations between the Einstein coefficients are found:

$$g_2 B_{21} = g_1 B_{12} \qquad \text{and} \qquad A_{21} = \frac{2h\nu^3}{c^2} B_{21}, \tag{2.18}$$

where g_1 and g_2 are the degeneracies of the levels. In the two level system we may define an excitation temperature T_{ex} based on the relative population densities n_1 and n_2 by requiring that

$$\frac{n_2}{n_1} = \frac{g_2}{g_1} e^{-h\nu/kT_{ex}}. \tag{2.19}$$

The optical depth of a transition may be found by integrating (2.17), using (2.18) and (2.19) to obtain

$$\tau_\nu = \int \kappa_\nu \, ds = \frac{c^2 A_{21} N_2}{8\pi\nu^2} \left(e^{h\nu/kT_{ex}} - 1 \right) \phi(\nu) \tag{2.20}$$

where we have introduced the concept of the column density (the density integrated along the line of sight) $N_2 = \int n_2 \, ds$. The optical depth is thus seen to be proportional to the Einstein A coefficient and the total population of the upper level along the line of sight. For this two level system, the source function reduces to the Planck function for T_{ex}

$$S_\nu \equiv \frac{j_\nu}{\kappa_\nu} = \frac{2h\nu^3}{c^2} \frac{1}{e^{-h\nu/kT_{ex}} - 1} = B_\nu \left(T_{ex} \right) . \tag{2.21}$$

B. Density considerations

We have thus far ignored collisions, or more generally the means of populating the upper level. We now consider the effects of collisional transitions, again using the simple two-level system. We assume that all collisions are with H_2 and that the system is in steady state, which simply means that the number of transitions into and out of each level must be the same, or

$$n_2 \left(n_{H_2} \gamma_{21} + B_{21} I_\nu + A_{21} \right) = n_1 \left(n_{H_2} \gamma_{12} + B_{12} I_\nu \right) , \tag{2.22}$$

where γ_{ij} is the probability of a collisional transition from the i level to the j level. We define the kinetic temperature T_{kin} by requiring

$$\frac{\gamma_{12}}{\gamma_{21}} = \frac{g_2}{g_1} e^{-h\nu/kT_{kin}} . \tag{2.23}$$

This relation is found using detailed balancing when the populations in the different levels reflect the kinetic temperature. The excitation temperature is thus defined in terms of the level populations, while the kinetic temperature is defined in terms of the collisional rates. Using (2.18) together with these temperature definitions, (2.22) then reduces to the form

$$\frac{I_\nu}{B_\nu \left(T_{ex} \right)} = 1 + \left(\frac{n_{H_2} \gamma_{21}}{A_{21}} \right) \left(1 - e^{h\nu/kT_{ex}} \, e^{-h\nu/kT_{kin}} \right) . \tag{2.24}$$

In the optically thin limit, I_ν is taken to be constant throughout the medium and to have the value of the incident radiation, specified as blackbody radiation of temperature T_{BG}, $I_\nu = B_\nu(T_{BG})$. We then find a

relation between T_{ex}, T_{kin}, and T_{BG} as

$$e^{-h\nu/kT_{ex}} = e^{-h\nu/kT_{BG}} \frac{1 + \left(n_{H_2}\gamma_{21}/A_{21}\right) e^{-h\nu/kT_{kin}} \left(e^{h\nu/kT_{BG}} - 1\right)}{1 + \left(n_{H_2}\gamma_{21}/A_{21}\right) \left(1 - e^{-h\nu/kT_{BG}}\right)} . \tag{2.25}$$

The ratio of the collisional and radiative transition rates $n_{H_2}\gamma_{21}/A_{21}$ is therefore the critical measure in determining the value of T_{ex}. When this ratio is much less than one, the excitation temperature is simply the background temperature, and when it is much greater than one, the excitation temperature becomes the kinetic temperature. In other words, when no collisional transitions take place, the excitation is provided by the incident radiation and the level populations reflect that temperature. When collisional transitions dominate, the level populations reflect the "local" kinetic temperature. Different transitions may therefore be used to determine density variations in observed sources. Lines with large A coefficients, resulting from large dipole moments or higher frequencies, will be observed only from regions with sufficient density to populate their upper levels. Other lines will exhibit emission from more extended and diffuse regions. This discussion holds true as well for the more unusual case where T_{BG} is greater than the kinetic temperature of the medium, *e.g.*, when observing a cold cloud with a warmer cloud or other source behind it. In this case, the line will be seen in absorption, with T_{ex} varying between T_{BG} and T_{kin} as the density increases.

To extend this simple two-level analysis to a many-level molecule, all of the transitions into and out of a given level j must be included in an equation similar to (2.22), yielding

$$\sum_{k \neq j} n_k \left(n_{H_2}\gamma_{kj} + B_{kj} I_\nu + A_{kj}\right) = \sum_{k \neq j} n_j \left(n_{H_2}\gamma_{jk} + B_{jk} I_\nu\right) , \tag{2.26}$$

with the condition that $\sum n_j = n_{total}$. This more general equation includes all possible radiative and collisional transitions between the various states of the molecule. Because of the complexity of the equations and uncertainties in the collisional, and sometimes, radiative, coefficients, practical solutions generally depend on simplifying the equations by making assumptions about the physical conditions.

C. LTE analysis

The equations derived above for the two-level case become applicable for the many-level case if we assume the matter to be in LTE. Under these conditions, the populations of the different energy levels

are determined by the excitation temperature T_{ex} via the Boltzmann factor. Mathematically,

$$\frac{n_j}{g_j} = \frac{n_{total}}{Q\left(T_{ex}\right)} e^{-E_u/kT_{ex}}, \tag{2.27}$$

where $Q\left(T_{ex}\right)$ is the partition function. This is tantamount to assuming a large enough density to populate all levels or simply ignoring the actual means of populating the levels. In particular, we find that the source function is the Planck function for T_{ex} as in (2.21), with the optical depth for a particular transition given by (2.20). To obtain a more convenient expression for the optical depth, we use the total column density $N_T = \int n_{total}\, ds$ in place of the column density in a particular level, converting between the two by means of (2.27). We also make use of the dipole approximation, in which A_{21} may be expressed in terms of the matrix element $|\mu_{21}|^2$ as

$$A_{21} = \frac{64\pi^4\nu^3}{3hc^3}\ |\mu_{21}|^2 = \frac{64\pi^4\nu^3}{3hc^3}\ \frac{\mu^2 S}{g_2}, \tag{2.28}$$

where S/g_2 is the reduced line strength and μ is the dipole moment of the molecule along the appropriate principal inertial axis. The optical depth may then be written as

$$\tau_\nu = \frac{8\pi^3\nu}{3hc}\ \mu^2 S \frac{N_T}{Q\left(T_{ex}\right)} \left(e^{-E_l/kT_{ex}} - e^{-E_u/kT_{ex}}\right) \phi\left(\nu\right). \tag{2.29}$$

For our purposes where the observed material is molecular gas in the ISM, the line profile is generally dominated by the velocity-induced Doppler profile reflecting the kinematics of the gas. It is therefore expedient to convert the line profile from a function of frequency to a function of velocity, as transitions at different frequencies will have the same velocity profile (but different frequency profiles). This assumes, of course, the same gas to be involved in the different transitions; the actual variations between profiles of different transitions can yield information about the excitation conditions of the gas at different velocities and optical depths. We therefore derive the optical depth as a function of velocity, τ_v, for a particular line as

$$\tau_v = \frac{8\pi^3}{3h}\ \mu^2 S \frac{N_T}{Q\left(T_{ex}\right)} \left(e^{-E_l/kT_{ex}} - e^{-E_u/kT_{ex}}\right) \phi\left(v\right), \tag{2.30}$$

where $\phi\left(v\right)$ is the normalized line profile in velocity units. The optical depth of a transition effectively determines the intensity I_ν that will be observed. The LTE approximation results in a constant source

function, so that (2.4) applies with $I_{\nu,obs}$ and $B_\nu\left(T_{ex}\right)$ replacing $I_\nu\left(\tau_\nu\right)$ and S_ν. In the next chapter, we discuss the actual methods of observation and calibration. For the moment we simply note that our observations are done in a differencing mode, where the excess line intensity relative to the background radiation is measured, and the background radiation is again taken to be blackbody radiation at a temperature T_{BG}. Thus, we obtain

$$\Delta I_\nu = I_{\nu,obs} - I_\nu(0) = \left(B_\nu\left(T_{ex}\right) - B_\nu\left(T_{BG}\right)\right)\left(1 - e^{-\tau_\nu}\right) \tag{2.31}$$

as the observed quantity. Again we might equally well have specified the intensity of a particular line as a function of velocity (referred to the line's rest frequency), rather than as a function of frequency. Line intensities are often quoted in units of temperature, with the conversion made utilizing the Rayleigh-Jeans formula $B_\nu^{RJ}\left(T\right) = 2kT/\lambda^2$, so that we define the brightness temperature as

$$T_b = \frac{\Delta I_\nu \lambda^2}{2k} = \frac{h\nu}{k}\left(\frac{1}{e^{h\nu/kT_{ex}} - 1} - \frac{1}{e^{h\nu/kT_{BG}} - 1}\right)\left(1 - e^{-\tau_\nu}\right). \tag{2.32}$$

The brightness temperature is therefore simply a scaled measure of the observed intensity, although under various approximations it can be related to the excitation temperature of the gas. It is this definition, together with (2.30), which we will use in Chapter 4 as the basis for simulating emission line spectra, given a set of column densities and velocity profiles for a suite of molecules.

As was true for the dust emission discussed earlier, we can frequently neglect the background radiation, as the excitation temperatures are generally much higher than 2.7 K. In the limit of $T_{BG} \rightarrow 0$ (or when $T_{BG} \ll T_{ex}$), we may rewrite (2.32) as

$$T_b = T_{ex}\frac{h\nu}{kT_{ex}}\left(\frac{1}{e^{h\nu/kT_{ex}} - 1}\right)\left(1 - e^{-\tau_\nu}\right) \tag{2.33}$$

showing the form of dependence of T_b on T_{ex} and τ (which in turn depends on T_{ex} and additional factors). If the Rayleigh-Jeans approximation ($h\nu \ll kT_{ex}$) is valid, this simply becomes

$$T_b = T_{ex}\left(1 - e^{-\tau_\nu}\right). \tag{2.34}$$

In addition to the simulations where T_{ex} and N_T are used to obtain T_b, we are often interested in the reverse process of deriving information about the excitation conditions and physical parameters from the observed T_b. We first consider the optically very thick and very thin cases, which yield different information about the observed objects and for which different analysis techniques must be used.

For the case of very large optical depths, T_b is independent of τ, so that T_{ex} may be obtained directly from the observations as

$$T_{ex} = \left(\frac{k}{h\nu} \ln \left(\frac{h\nu}{kT_b} + 1 \right) \right)^{-1} \tag{2.35}$$

or in the Rayleigh-Jeans limit, simply T_{ex}= T_b. If the transition is thermalized, so that the excitation temperature reflects the kinetic temperature of the gas, a single observed line can therefore directly measure the cloud temperature. However, precisely because the intensity does not depend on the optical depth, an optically thick transition gives only a lower limit for the column density.

For an optically thin line, as $\tau \rightarrow 0$, we may replace the factor $\left(1 - e^{-\tau}\right)$ by τ in the expressions for T_b. At this point we introduce the integrated line intensity W, or the line intensity integrated over the line profile. This may be done in either frequency or velocity units; unless otherwise noted we will use velocity units, so that we have $W = \int T_b \, dv$. Under the optically thin approximation, integration of (2.33) with τ taken from (2.30) yields

$$W = \frac{8\pi^3}{3k} \nu \mu^2 S \frac{N_T}{Q\left(T_{ex}\right)} e^{-E_u / kT_{ex}}. \tag{2.36}$$

We may rewrite this after taking the natural logarithms of the different terms as

$$\ln \left(\frac{N_T}{Q\left(T_{ex}\right)} \right) - \frac{E_u}{kT_{ex}} = \ln \left(\frac{3kW}{8\pi^3 \nu \mu^2 S} \right) \tag{2.37}$$

where all factors on the right-hand side are in principle either known or observed quantities. For a single line, this yields a relation between the excitation temperature and the column density required to produce the observed integrated intensity (*cf.* the determination of required column density by the SIMCAT computer software as described in §4.7). If two or more lines are observed, a plot of the right-hand side should be linear in E_u, with a slope of $-1/kT_{ex}$ and an intercept of $\ln\left(N_T/Q\left(T_{ex}\right)\right)$. (The software implementation of this method is described in §4.10; an example of this type of plot may be seen in Figure 4.14.) Fits to

the observed integrated intensities done in this manner are known as rotation diagrams and yield values for both the excitation temperature and the column density. Molecular excitation temperatures found in this way are identified as rotation temperatures. We note that this method relies only on the assumptions of low optical depth and negligible background radiation (in addition to the LTE assumption that a single T_{ex} describes the level populations). While some derivations make use of the Rayleigh-Jeans approximation, the rotation diagram technique does not require this condition to be true.

For the optically thick case, the observed quantity which most naturally relates to the physical conditions is the intensity or brightness temperature of the line. Considering (2.24) again, we see that for a thermalized transition with $T_{ex} = T_{kin}$, we obtain simply $I_\nu = B_\nu \left(T_{ex}\right)$, so that the temperature is the parameter of interest. In the optically thin case, where all of the material in the line of sight is assumed to contribute to the intensity, the natural quantity for analysis is the integrated intensity, which depends both upon the temperature and the column density of the gas. These differences are reflected in the analysis presented above and demonstrate the influence of the optical depth on what we observe and what we may deduce from the observations. In both the thin and thick cases, we eliminate the dependence on the line profile, in the thin case by integrating over the profile and in the thick case by removing the dependence upon the optical depth.

For intermediate values of the optical depth, we may return to (2.32) where the observed brightness temperature is seen to depend directly on T_{ex}, N_T, and indirectly upon the line profile function through τ.

In the general case, we may determine the relation between the excitation temperature and the column density required to produce an observed intensity as for the thin case, although the inclusion of the profile function and the optical depth makes the computation less straightforward. If multiple lines of the same species are observed, comparison of the different relations thus obtained may be used to place upper and lower bounds on the excitation temperature and column density of the species.

D. Limitations of LTE analysis

While the LTE approximation makes the analysis of spectral lines more tractable, the use of this approximation may not always be justified for the astronomical objects which we observe. We therefore

list briefly some limitations of the LTE analysis described above.

As noted earlier, the LTE approximation essentially ignores the means by which the higher energy levels are populated. For collisionally maintained populations, the critical density will generally be greater for higher energy levels, so that above some energy level the density will not be sufficient to maintain the population implied by the excitation temperature. Therefore a rotation diagram analysis has a tendency to overestimate the column density by assuming these higher levels are fully populated, while providing a lower bound to the kinetic temperature. However, radiative excitation may also contribute to the level populations. As noted earlier in §2.2, the thermal emission from dust rises with frequency as $\gtrsim \nu^3$. The radiation field may therefore preferentially populate higher energy levels by virtue of its greater intensity at shorter wavelengths. A correct quantitative analysis of a spectral line therefore requires that the source be modeled with both radiative and collisional excitation taken into account, with the emergent spectrum determined by evaluating the radiative transfer equation (2.1) as the medium is traversed. Such radiative transfer models are significantly more computationally burdensome than the LTE approach and can only be done for a limited number of molecules and lines. In addition, the density distribution of the source and the incident radiative field must be modeled, adding to the complexity of this method. A particular advantage may result from such statistical equilibrium calculations, however. The ratios of the intensities of some transitions will be most sensitive to the temperature, while the ratios of other transitions will be most sensitive to density. Observations which take advantage of this behavior by observing the appropriate transitions can therefore yield excellent and largely independent determinations of both the density and temperature of the cloud (*cf.* Jansen, van Dishoeck, & Blake 1993). LTE calculations will, of course, not reveal any density constraints.

Chapter 3

Observations and Calibration Techniques

The CSO spectral line surveys of Orion-KL, Orion-S, IRAS 16293–2422, IRC +10216, VY Canis Majoris, and OH 231.8+4.2 form the basis for our determination of the integrated line flux in these objects. We then compare the observed line flux values with published values of both broadband and narrowband measurements of the continuum flux to evaluate the relative importance of the emission lines as contributors to the total flux observed. The details of the line surveys are presented in the appendices to this thesis, including the precise dates and frequencies of the observations as well as the resulting spectra. The analysis of the line flux contribution for each source is given in Chapter 5, where we also describe the data sets used for comparison. In this chapter, we describe the general techniques we used to perform our observations and to calibrate the data. We also discuss the problems of comparing spectral line observations and flux measurements, including the conversion between the different units of intensity traditionally used in the respective cases of heterodyne spectral line measurements and bolometric continuum observations.

3.1. Observations

We first began the project of carrying out the CSO line surveys in December 1988. Our goal was to extend previous line survey work both to higher frequencies and to a broader range of objects using the then newly commissioned CSO with its high beam efficiency and low-noise 345 GHz facility receiver (Ellison *et al.* 1989). We first concentrated on Orion-KL and IRC +10216, two sources which possess

TABLE 3.1
SUMMARY OF OBSERVING DATES AND SOURCES

Dates	Sources Observed
14 – 20 December 1988 [a]	Orion-KL, Orion-S, IRC+10216
17 – 23 January 1989 [b]	Orion-KL, Orion-S, IRC+10216
19 April – 2 May 1989	IRC+10216, IRAS 16293-2422
12 – 18 January 1990	Orion-KL, Orion-S, IRC+10216
14 – 17 February 1990	Orion-KL, Orion-S, IRC+10216
13 – 19 March 1990	Orion-KL, Orion-S, IRC+10216
10 – 17 July 1990	IRAS 16293-2422
6 – 18 January 1991	Orion-KL, Orion-S, IRC+10216, OH 231.8+4.2, VY CMa
11 – 18 January 1992	IRC+10216,OH 231.8+4.2, VY CMa

[a] All frequencies observed at this time were reobserved at later times.
[b] For this run we had only half nights of observing time; few Orion observations were made and these were later redone.

strong line emission and for which line surveys had previously been published (Johansson *et al.* 1984, Sutton *et al.* 1985, Blake *et al.* 1986), together with Orion-S, a source located 1.5′ south of Orion-KL that we wished to use for comparison. We returned to the CSO at irregular intervals to observe these sources, eventually adding the additional sources IRAS 16293–2422, VY CMa, and OH 231.8+4.2. A total of 10 observing runs were made for the line surveys presented in this thesis, with the data collection continuing until January 1992. Table 3.1 summarizes the dates of the observations and the sources observed at each epoch. During the initial sets of observations, we often found it desirable to repeat observations at given frequencies in order to verify or correct our first observations. In time we developed a routine method of carrying out our observations involving the receiver tuning, LO adjustments, and observing parameters which led to greater consistency and reliability in our results. At the same time, the necessary software was being developed for the sideband deconvolution and line identification and analysis (cf. Chapter 4). Early versions of the software permitted us to deconvolve our data sets as they were collected and identify many of the observed lines in real time. These capabilities were important in allowing us to better judge the reliability and quality of the data and to test our data reduction and calibration techniques.

In many ways, the observations required for a spectral line survey are not very different from those required when making an observation of a particular line. The same basic techniques are used and the same

considerations apply, *e.g.*, pointing, calibration, sensitivity, etc. As observations at different frequencies are to be combined in order to derive the final spectrum, the relative calibration of the data can take on a greater importance in the line survey case; to the extent that the different observations contain redundant data when the frequencies overlap, the individual spectra may be used to evaluate the relative calibration, allowing changes to the observing parameters to be made if needed. Similarly, pointing errors, which cause changes in the lines under observation and degrade the quality of the survey, may be recognized from the data and corrected. In general, the sensitivity of a line survey will be less than that of observations targeting a particular transition simply because of time constraints. Careful planning of the observations for a survey can help ensure an appropriate balance between sensitivity and frequency coverage as well as an efficient use of the telescope time available.

All of the line surveys associated with this work were performed using the 10.4 m CSO telescope located on Mauna Kea, Hawaii. The system has a diffraction-limited beam size of approximately 20″ when averaged over the frequency ranges of our surveys, varying by ∼10% (corresponding to the variation in frequency). The pointing was checked frequently during the observations and was found to be accurate to $\lesssim 5''$. When possible, we optimized the pointing using emission from the source under observation, in some cases retuning the receiver to the frequency of a strong line to verify the pointing, then tuning to the desired frequency for observations. We also used planets and other bright compact sources to check the pointing of the telescope. For Orion-KL, where much of the emission is extended and the different species have distinct spatial distributions, the pointing was particularly critical. For this source we consistently optimized the pointing using bright SO_2 lines, which appear throughout much of the frequency range covered and for which the intensity and line profile change noticeably with pointing variations.

The CSO 345 GHz facility SIS receiver was used throughout the observations. Receiver temperatures were generally in the range 200 – 250 K (SSB), while the system temperatures ranged from 700 – 2000 K (SSB). The atmospheric opacity usually remained below 0.25, but occasionally reached 0.8 (and even higher for some observations of Orion-KL at frequencies near the H_2O line at 325 GHz). Because of the varying brightness of the lines observed in the different sources, the noise level reached and the corresponding integration time varied from source to source. We typically sought to achieve a noise level

of ~80 mK, requiring on-source integration times of roughly 10 – 20 minutes at each frequency. Because of the brightness of the lines in Orion-KL, our typical integration times there were often approximately 5 minutes or less, so that in some cases the time spent tuning the receiver and pointing the telescope became comparable to the time spent collecting survey spectra. The lists of scans given in the appendices make it clear that many of the observations for the different surveys were obtained during a few very productive runs. These were usually the result of good weather (high atmospheric transmissivity), cooperative equipment, and the experience gained during earlier runs.

The facility backend (an acousto-optic spectrometer) was used which had a total bandwidth of 500 MHz and a nominal channel width of 0.49 MHz. Frequency calibration measurements, made by injecting a frequency comb with a spacing of 100 MHz, indicated that the actual resolution was approximately two channels, with variations of less than a few percent over the course of our observations. This corresponds to a channel width of 1 MHz, which is used for the deconvolved SSB spectra (the deconvolution process is discussed at length in Chapter 4). When deconvolution is not performed, the spectra are smoothed to have channel widths of at least 1 MHz depending on the line profiles in the particular source.

The data was calibrated at the time of the observations using the chopper wheel method (Penzias & Burrus 1973, *cf.* discussion below). The atmospheric transmission can vary rapidly with frequency near the ends of the surveys. We have modeled the atmospheric transmission (Grossman 1989) for the two sidebands of the DSB observations and corrected the observed antenna temperatures accordingly. Low order polynomial baselines were removed from the DSB spectra, but no additional corrections are made following the deconvolution. The data are presented as brightness temperatures, corrected for either the extended efficiency of $\eta_{ext} = 0.76$ in the cases of Orion-KL and Orion-S or the main beam efficiency of $\eta_{MB} = 0.60$ in all other cases. In general, the line emission of different species arises from regions of different spatial extent, so that the use of a single correction factor results in under- or over-estimates of the brightness for particular molecules. We estimate the uncertainty in our absolute calibration to be 20%, with the relative calibration over ~1 GHz scales within a given survey closer to ~5%. A more detailed description of the data calibration is given below, with particular consideration given to comparisons of flux measurements and line observations.

A. Selection of LO Frequencies

As described in Chapter 4, the deconvolution process depends on observations which overlap in their frequency coverage. Following Blake *et al.* (1986), we initially set out to obtain a complete set of DSB spectra separated by 250 MHz, *i.e.*, half the backend width. With such a set, most frequencies would appear in four scans, twice in the upper and twice in the lower sideband. Within 250 MHz of each end of the survey, each frequency would be observed a single time. There would also be a 3 GHz range near each end where each frequency would be observed twice, in either the upper or lower sideband only corresponding to the upper or lower end of the frequency range surveyed. This observing scheme provides greater redundancy than a set of scans separated by the full backend width and aids in the deconvolution process. However, stepping by the full backend width does provide complete frequency coverage and allows the deconvolution to be performed provided there is overlap between the upper sideband of some scans with the lower sideband of others. As the surveys progressed, we made several adjustments to our planned sets of scans. We decided to make observations in some cases separated only by $\sim$10 MHz, which presented several advantages. Two such scans give the redundant information required for the deconvolution process over nearly the entire backend width of each scan. (As discussed in Chapter 4, this is most beneficial when the small shift approximately corresponds to the width of the spectral features of interest.) Hence by shifting the LO frequency by 10 MHz at the survey ends, we reduced the range of frequencies observed only once from 250 MHz to 10 MHz. In addition, these small shifts aided us in identifying features as belonging to a particular sideband at the time of the observations, allowing us to more easily compare the data in different scans and verify the relative calibrations, pointing, etc. This was particularly true for the case of Orion-KL, where the line density was so great that a 250 MHz shift often resulted in the shift of equivalent numbers of lines into and out of the band observed. At the other extreme, in the sources with very low line densities where only selected frequencies were observed, these small LO shifts provided all of the data redundancy, as the scans in general did not overlap. An additional advantage of these scans was the ease with which they could be performed. In contrast to larger frequency shifts, which generally required us to retune the receiver and LO chain manually, the smaller shifts could often be accomplished

by issuing a single software command.

A second change in our method was the addition of a greater number of scans with intermediate LO shifts covering the frequencies of the strongest lines. Because of the great dynamic range involved, weak lines in the other sideband are difficult to extract when buried under a strong line. We found that such lines were often visible following the deconvolution but with a greater noise level than the rest of the spectrum. To alleviate this, we developed a procedure whereby the deconvolution was done with the particular scan removed which had led to the excess noise, and the small section of noisy spectrum was replaced with the section resulting from the new deconvolution. The increased frequency coverage enabled this to be done while maintaining approximately the same redundancy as that of the rest of the survey.

Finally, as work on the project progressed, it became clear that conducting complete surveys of several sources was simply impossible within the parameters set by the system performance, desired sensitivity and frequency coverage, and telescope time available, despite the generally excellent performance of the observatory. We therefore chose to obtain only partial surveys in most of our sources, targeting the frequencies corresponding to the strongest expected lines. Using the line catalog software described in Chapter 4, we tried to maximize our productivity by selecting LO frequencies which would give multiple transitions in the two sidebands. Also, given the uncertainties as to the total observing time which would actually be available, we sought to maximize the frequency coverage obtained at intermediate stages of the surveys. In some cases this led us to take spectra separated by 500 MHz first and then to "fill in" the extra scans at 250 MHz intervals later. We also sometimes obtained coverage only in one sideband, shifting the LO frequency by a few GHz after a series of regularly spaced scans. In this manner we could obtain complete frequency coverage in less time, although with reduced redundancy.

Tables and plots in the appendices show the actual frequencies observed and schematically indicate the coverage obtained for the different sources. The methods described above are readily seen as small LO shifts, jumps in the frequencies of the DSB scans, and reduced or increased scan coverage as shown in the plots. The cumulative effect of these efforts was to increase the number of lines observed and the frequency ranges covered in the survey as well as the quality of the data through the judicious selection of observing frequencies.

3.2. Chopper Wheel Calibration

Observations made at the CSO are calibrated using the chopper wheel method first discussed for millimeter astronomy by Penzias & Burrus (1973). The description given here of this method follows the presentation given in an appendix to the CSO Observers Manual (Phillips 1989); other useful discussions of this method of calibration have been given by Kutner & Ulich (1981) and Downes (1989), who includes comparisons between different notations appearing in the literature and temperature scales used.

The use of a chopper wheel, which switches an absorber at ambient temperature into the beam between the receiver and the secondary mirror, allows one to determine the necessary corrections for atmospheric absorption and telescope losses resulting from ambient temperature effects, such as spillover and blockage of the beam. These corrections are automatically made at the CSO as a part of the standard observing procedure and the data is reported on the resulting T_A^* scale. Further corrections may be made for effects such as cold spillover, beam coupling to the source, and sideband gain ratios.

We begin by somewhat arbitrarily defining the beam to have a particular angular size, with power outside of this considered to be spillover. Maps of planets made by scanning the beam across the source show the main beam of the CSO to be an approximately diffraction limited Gaussian beam at these frequencies ($\sim 20''$ at 345 GHz for the 10.4 m diameter primary surface). We then define the following efficiencies: $\eta_{hot} = 1 - f_h$ where f_h is the fraction of power falling on the ground or otherwise absorbed at ambient temperature; $\eta_{cold} = 1 - f_c$ where f_c is the fraction of power falling on the sky but which does not form part of the main beam; and η_{source}, the efficiency with which the source couples to the main beam. We assume that the ambient temperature of the absorber T_{hot} is equal to the ground temperature T_{ground} and the air temperature T_{atmos}, and that all temperatures are large relative to the observing frequency so that the Rayleigh-Jeans approximation ($h\nu/kT \ll 1$) holds. The heterodyne receiver operates in a DSB mode, giving an output voltage proportional to the input power. The input power in turn is proportional to T under our assumptions, so that the output signal may be written as a linear combination of T for the various input signals. Apart from the potentially different input power, we assume the only differences between the upper and lower sidebands are in the atmospheric opacity and in the efficiency of the coupling

to the input radiation. This requires the separation between the sidebands to be small compared to the operating frequency, so that the input power in each sideband may be represented using the same value for T_{hot} and T_{cold}. Letting G be the conversion factor between T_{in} and V_{out}, we obtain the following relation:

$$V_{hot} = G\left[2T_{RX} + T_{hot}\left(\eta_u + \eta_\ell\right)\right] \tag{3.1}$$

where $T_{RX}$is the (DSB) noise temperature of the receiver, the factor of two arises from the DSB nature of the observation, and η_u and η_ℓ are, respectively, the input radiation coupling efficiency for the upper and lower sidebands. The observations are done in a differencing mode, where the voltage looking at the source, V_{source}, is compared to the voltage looking off source, V_{sky}. We may write down expressions for these values, including contributions from the hot (ground) and cold (sky) spillover, the atmosphere (because of its finite opacity), and the source itself, obtaining:

$$\begin{aligned} V_{sky} = G\Big[&2T_{RX} + \left(1-\eta_{hot}\right)T_{ground}\left(\eta_u+\eta_\ell\right) \\ &+\eta_{hot}\left(1-\eta_{cold}\right)T_{atmos}\left(\eta_u\left(1-e^{-\tau_u}\right)+\eta_\ell\left(1-e^{-\tau_\ell}\right)\right) \\ &+\eta_{hot}\eta_{cold}T_{atmos}\left(\eta_u\left(1-e^{-\tau_u}\right)+\eta_\ell\left(1-e^{-\tau_\ell}\right)\right)\Big] \\ = G\Big[&2T_{RX} + T_{hot}\left(\eta_u+\eta_\ell\right) - \eta_{hot}T_{hot}\left(\eta_u e^{-\tau_u}+\eta_\ell e^{-\tau_\ell}\right)\Big] \end{aligned} \tag{3.2}$$

and

$$\begin{aligned} V_{source} = G\Big[&2T_{RX} + T_{hot}\left(\eta_u+\eta_\ell\right) - \eta_{hot}T_{hot}\left(\eta_u e^{-\tau_u}+\eta_\ell e^{-\tau_\ell}\right) \\ &+\eta_{hot}\eta_{cold}\eta_{source}\left(T_u\eta_u e^{-\tau_u}+T_\ell\eta_\ell e^{-\tau_\ell}\right)\Big] \end{aligned} \tag{3.3}$$

where the subscripts u and ℓ identify quantities which are associated with the upper or lower sideband. (Recall that $T_{hot} = T_{ground} = T_{atmos}$).

The first step in the observing procedure is to take a calibration scan which compares the hot load (the ambient absorber) and the sky, storing the quantity $(V_{hot} - V_{sky})/V_{sky}$. The following data scans then compare the source emission with the sky, computing $(V_{source} - V_{sky})/V_{sky}$ and then dividing by the calibration scan to obtain

$$\frac{V_{source} - V_{sky}}{V_{hot} - V_{sky}} = \frac{2\eta_{cold}\eta_{source}\left(T_u\eta_u e^{-\tau_u}+T_\ell\eta_\ell e^{-\tau_\ell}\right)}{\left(\eta_u e^{-\tau_u}+\eta_\ell e^{-\tau_\ell}\right)}. \tag{3.4}$$

The actual quantity stored as the data for the observation is $T_A^* = 2T_{hot}(V_{source} - V_{sky})/(V_{hot} - V_{sky})$. A more transparent expression for T_A^* may be obtained by making the substitution

$$g_u = \frac{2\eta_u e^{-\tau_u}}{(\eta_u e^{-\tau_u} + \eta_\ell e^{-\tau_\ell})} \tag{3.5}$$

and using a similar expression for g_ℓ, which yields

$$T_A^* = \eta_{cold}\eta_{source}\left(g_u T_u + g_\ell T_\ell\right). \tag{3.6}$$

We note that $g_u + g_\ell = 2$, and for the case of equal sensitivities and atmospheric opacity in the two sidebands $g_u = g_\ell = 1$. In this latter case, T_A^* represents the source temperature corrected for the atmosphere and hot spillover, but not for cold spillover and source coupling effects. As the actual source coupling depends on the frequently unknown spatial distribution of the emission, generally applicable values for the product $\eta_{cold}\eta_{source}$ are usually employed.

Sources are typically classified as large, similar, or small compared to the main beam and the appropriate correction factor determined from suitable calibration sources whose emission is well known. For extended sources, $\eta_{cold}\eta_{source}$ may be estimated from measurements of the moon, while the planets may be used to determine the value for sources comparable to the main beam size, with Jupiter and Mars serving as the most useful calibrators. For the CSO 345 GHz receiver system, repeated measurements have yielded values of 0.76 ± 0.03 for the extended efficiency and 0.60 ± 0.10 for the main beam efficiency. Small sources are traditionally corrected using the so-called aperture efficiency, defined as $\eta_{ap} = A_e/A$ where A_e is the effective collecting area and A the geometric area of the antenna. The aperture efficiency and main beam efficiency are therefore quite similar, except that for the aperture efficiency the beam is assumed to be the diffraction function of a uniformly illuminated, perfect telescope instead of a Gaussian beam. Again for the CSO 345 GHz receiver system, a value of 0.40 has been determined for the aperture efficiency with an estimated error of ± 0.10. Kraus (1986) and Rohlfs (1986) present thorough discussions of calibration and general techniques of radio astronomy, and Mangum (1993) presents specific efficiency measurements for the CSO and a general discussion of planetary measurements. A set of secondary

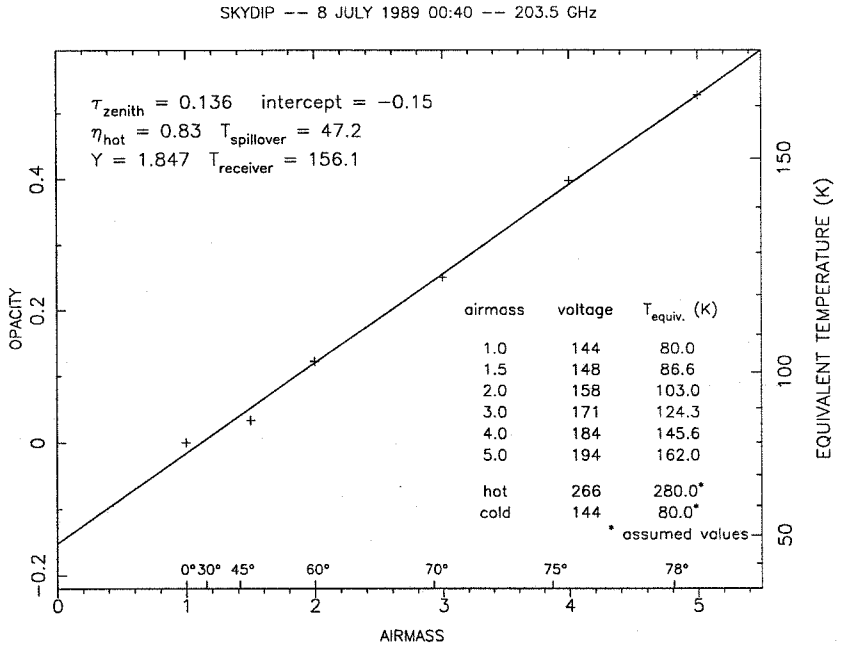

Figure 3.1 Sample skydip data and analysis performed at the CSO prior to the installation of the 225 GHz radiometer. The procedure allows determination not only of the atmospheric opacity, but also the hot efficiency and the receiver noise temperature (DSB) if absorbers at known temperatures (*e.g.*, ambient and liquid nitrogen) are inserted in the beam.

calibrators for submillimeter observations has recently been provided by Sandell (1994), who also discusses general calibration requirements.

When the values of g_u and g_ℓ are not unity, additional corrections are required for atmospheric or receiver sideband imbalance effects. Atmospheric models can be used to determine the values of τ_u and τ_ℓ, provided the specific sky conditions are known. A radiometer located at the CSO measures the optical depth at 227 GHz every 10 minutes, from which the opacity at the observing frequencies can be modeled. Prior to the installation of the radiometer in 1990, we performed "skydips" to directly determine the opacity at the operating frequency. Figure 3.1 shows a sample skydip performed at the CSO (see Groesbeck 1989a for a description of the analysis technique). Except near the edges of the atmospheric window, the atmospheric opacity varies only slightly between the two sidebands and only small corrections are required. The receiver sideband gains are not currently measured at the CSO; where possible we

estimate the values of g_u and g_ℓ using the relative intensities of different observations of the same strong lines. For the survey data, we found the typical gain ratios to vary by less than 15% from unity when a set of consistent tuning procedures was used. During the observations, the tuning of the receiver was done by maximizing its response to the input radiation. We found that placing an ambient temperature absorber in the beam to ensure that the power was similar in both sidebands was helpful in obtaining sideband gain ratios near unity.

3.3. Unit Conversion

The chopper wheel method gives a measurement of the brightness temperature of the source. As noted in Chapter 2, the brightness temperature is simply a scaled measure of the intensity, whose relation to the physical temperature of the source depends upon the optical depth, frequency, etc. The great advantage of the chopper wheel method is that it provides a simple, robust method for calibrating data without making assumptions about the particular source structure. It essentially provides a beam-averaged estimate of the observed intensity, where the particular temperature scale or efficiency correction used (*e.g.*, main beam or extended) determines the extent of the beam over which the average is performed. The use of temperature units for line measurements is in fact a matter of convenience, both for the observations and for interpretation of the source parameters.

Broadband observations, on the other hand, are typically given in units of the flux density S_ν, which is simply the integral of the brightness or intensity over the solid angle of the source

$$S_\nu = \int\int B(\theta, \phi)\, d\Omega. \tag{3.7}$$

The units of flux density are W m^{-2} Hz^{-1}; for radio sources the flux is usually very small so that astronomers use the Jansky (Jy) flux unit, where 1 Jy = 10^{-26} W m^{-2} Hz^{-1}. Because the flux density from an astronomical object is defined as an integral over the solid angle of the source, it should be independent of the telescope used. Of course, different telescopes observing the same source region will detect different input powers because of differences in beam sizes and efficiencies. To obtain the actual flux density, the detected power must be appropriately scaled. The actual corrections required are found

by observing sources with known fluxes, similar to the determination of beam efficiencies when using temperature scales. A useful discussion of flux calibration is given by Sandell (1994) as part of an effort to establish a set of secondary calibration sources at millimeter and submillimeter wavelengths.

What is actually measured in both cases is the input power seen by the receiver, representing the total intensity on the sky weighted by the power pattern and integrated over the beam of the telescope. Hence the use of different units is a reflection of the data processing rather than of the actual measurements, and in principle it is possible to convert between the different units. However, because the temperature scale used depends on an assumed source size while flux density does not, the conversion factor will vary depending upon the source size assumed. We may write the flux density for a source which just fills the main beam as

$$S_\nu = \int\int B(\theta, \phi)\, d\Omega = B_{MB}\Omega_{MB} \tag{3.8}$$

where B_{MB} represents the average intensity across the source. Recalling our definition of brightness temperature, we may write $B_{MB} = 2kT_{MB}/\lambda^2$, while the definition of main beam efficiency leads to $\Omega_{MB} = \lambda^2/A$. Combining these leads to

$$\frac{S_\nu}{T_{MB}} = \frac{2k}{A} \tag{3.9}$$

which has a value of 32.5 Jy/K for the 10.4 m CSO antenna. For the other temperature scales mentioned in connection with chopper calibration, this value should be scaled by the ratio of the efficiencies. Hence, to obtain the flux density for a source filling the main beam, the appropriate conversion factors are 54.2 Jy/K relative to T_A^* and 32.5 Jy/K if the brightness temperature has already been corrected for the main beam efficiency. An additional multiplicative factor of 1.5 relative to T_A^* is required to obtain the flux density for a source which is small compared to the beam and for which the aperture efficiency should be used.

Continuum measurements are generally reported as the observed flux density at a given wavelength; for broadband measurements, an effective wavelength is generally determined from considerations of the variation in detector sensitivity and in expected flux across the instrument's passband. Some model of the source emission must therefore be used to determine the effective wavelength of the observation. In addition, the atmospheric transmission may vary over the range of the measurement passband, thus affecting

the variation in sensitivity, and must enter into this calculation. A significant contribution by the integrated line flux can affect the flux variation, especially if most of the line flux is carried in a few strong lines, and should also be included in determining the effective wavelength when appropriate.

3.4. Frequency Calibration

All of the observations making up the spectral line surveys were performed using the 1024 channel 500 MHz AOS backend at the CSO. The frequency information for a particular observation is given in terms of a reference channel position at the center of the AOS and the channel width. For our line surveys, we were of course interested in the entire bandwidth, making the frequency calibration of utmost importance. While a typical line width of $\sim$10 km s^{-1} represents only a few percent of the 500 MHz width of the AOS, lines can appear at any location in the passband as the observing frequency is varied. Variation in the reference channel appears as a simple shift of the entire band, but a variation of just 1% in the 0.5 MHz channel width will result in an error of 2.5 MHz at the edge of the scan after accumulating over 500 channels. Variations of this magnitude with a time scale of tens of minutes are known to occur during observations, so that an individual scan will not be affected but scans taken at different times will not align properly across the entire band if no corrections are made.

The frequency calibration method used at the CSO provides for the injection of a frequency comb, made up of harmonics at 100 MHz intervals, into the backend for calibration scans. During our initial sets of observations, we found that default values were used for the reference channel and channel width and that changes to these values needed to be made by hand based on the frequency calibration data. A fit to the channel locations of the spikes in the frequency comb data showed the AOS to have very linear properties and enabled us to determine the appropriate channel widths for our different observations. Figure 3.2 shows the effect of making the corrections for a line observed with several LO settings. A description of the correction method used is given in Groesbeck (1989b). Automatic updates to the values were implemented for our later observing runs. The fits to the frequency comb also demonstrated the true resolution of the AOS to be approximately two channels or 1 MHz, as noted earlier.

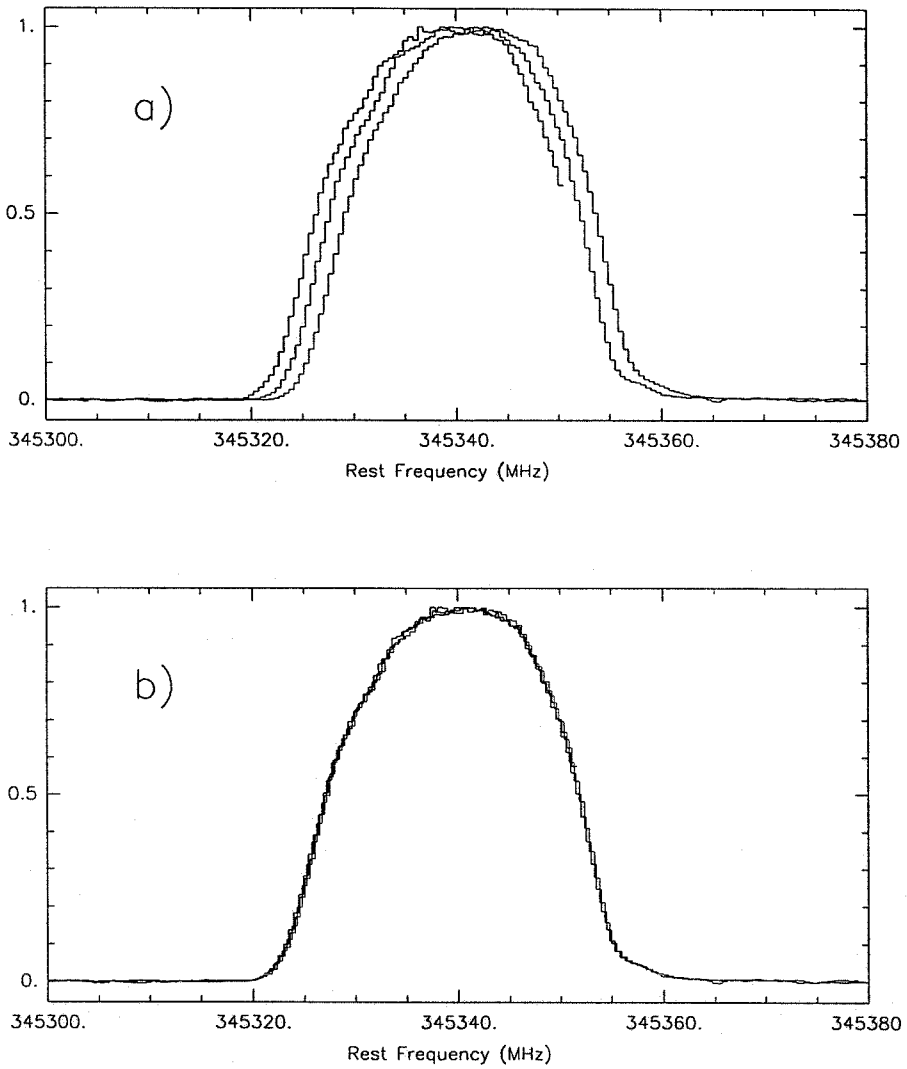

Figure 3.2 Observations of the $H^{13}CN$ J = 4–3 line in IRC +10216 shown *(a)* before and *(b)* after making the frequency calibration corrections described in the text. (The data have been normalized to have unit intensity.) Observations with the line in both the upper and lower sideband are included in this plot. In *(a)*, note that the data end abruptly for one spectrum in which the line fell at the edge of the backend passband. The data have been normalized to unit intensity.

Chapter 4

Data Analysis Programs

In the course of performing the spectral line surveys described in this thesis, it was necessary to write a significant amount of computer software for the data analysis. The first tool developed was an improved means of converting the double sideband (DSB) observations to a single sideband (SSB) format. We also found it prudent to develop an online catalog of molecular lines which greatly simplifies line identification, the selection of observing frequencies, and the analysis of observed lines. This chapter contains a discussion of the methods used and the capabilities of the various programs.

4.1. Heterodyne Observations and the Formation of DSB Spectra

All of our observations were performed using the techniques described in the last chapter with the facility 345 GHz heterodyne SIS receiver at the CSO, which operates in a DSB mode. Figure 4.1 shows a diagram of the main components of a typical heterodyne receiver. The key component is the mixer, in which the radiation from the telescope is combined with radiation from a local oscillator (LO). The mixer has a nonlinear relationship between the input E field of the radiation and its output signal (*e.g.*, voltage), with a term in the output signal proportional to the input power, or the square of the input field. If the signal and LO fields are $E_s \cos(\omega_s t + \delta_s)$ and $E_{LO} \cos(\omega_{LO} t + \delta_{LO})$, with V the output signal, we may write

$$V = \alpha E_{input}^2 = \alpha \left[E_s \cos(\omega_s t + \delta_s) + E_{LO} \cos(\omega_{LO} t + \delta_{LO}) \right]^2 . \quad (4.1)$$

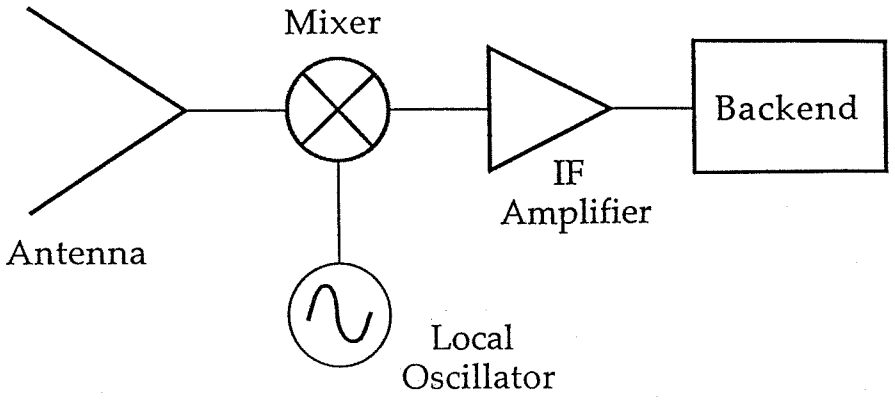

Figure 4.1 Main components of a typical heterodyne receiver. For the astronomical data of this thesis, the RF input comes from the telescope. The mixer downconverts the signal to the much lower intermediate frequency where instrumentation is available to analyze the signal.

Using standard trigonometric identities we may expand this as

$$\begin{aligned} V =& \frac{\alpha}{2}\left(E_s^2 + E_{LO}^2\right) \\ &+ \frac{\alpha}{2}\left[E_s^2\cos(2\omega_s t + 2\delta_s) + E_{LO}^2\cos(2\omega_{LO}t + 2\delta_{LO})\right] \\ &+ \alpha E_s E_{LO}\cos((\omega_s + \omega_{LO})t + \delta_s + \delta_{LO}) \\ &+ \alpha E_s E_{LO}\cos((\omega_s - \omega_{LO})t + \delta_s - \delta_{LO}). \end{aligned} \tag{4.2}$$

The output signal is seen to consist of a DC term, terms at the second harmonics $2\omega_s$ and $2\omega_{LO}$, and terms at the sum and difference frequencies. For submillimeter observations, ω_{LO} is roughly equal to ω_s in practice, making the sum frequency roughly the same as that of the second harmonics (*e.g.*, for our observations at ~350 GHz, the difference between the signal and the LO frequency is ~1.5 GHz). By using appropriate filters, all terms except the desired signal at the difference frequency, called the intermediate frequency or IF, can be eliminated. The receiver output then consists of signals within a range of frequencies determined by the IF passband, which are linearly proportional to the input at frequencies separated from the LO frequency by ω_{IF}.

Frequencies both above and below the injected LO frequency contribute to the IF output, making the receiver sensitive to upper sideband frequencies ($\omega_s > \omega_{LO}$) as well as lower sideband frequencies ($\omega_s < \omega_{LO}$). Such a receiver is said to operate in a double sideband mode and has the property that a

signal from one of the sidebands which appears in the IF output cannot be distinguished from a signal at the corresponding frequency in the other sideband. For this reason, SSB receivers, which are sensitive to only one of the sidebands, are preferred when they are available. The difficulty of building millimeter and submillimeter SSB receivers which have the desired characteristics is such that the great majority of receivers built for astronomical observations are of the DSB variety. In many cases, the resulting DSB spectra contain spectroscopic lines from both sidebands, often blended, so that further processing is necessary before important line parameters can be determined. We describe in the following sections a method for extracting a SSB spectrum from a set of DSB observations. This method allows the information about the individual sidebands to be obtained while still using the available DSB receivers.

4.2. Description of the CLEAN Algorithm for DSB to SSB Conversion

We first give a simplified description of the DSB to SSB conversion algorithm for the simplest case (*e.g.*, noiseless data, unit gain in each sideband, etc.). Figure 4.2 is a schematic depiction of the formation of a DSB spectrum which contains signals from both sidebands. At a given frequency in the IF passband, ν_{IF}, the output will respond to the two frequencies $\nu_{USB} = \nu_{LO} + \nu_{IF}$ and $\nu_{LSB} = \nu_{LO} - \nu_{IF}$. Expressing the signal in units of temperature, we have for this simplest case

$$T_{\nu_{IF}} = T_{\nu_{USB}} + T_{\nu_{LSB}}. \tag{4.3}$$

From a single observation, with no other information than this sum, we are unable to independently determine the values of $T_{\nu_{USB}}$ and $T_{\nu_{LSB}}$.

Figure 4.3 shows how by shifting the LO frequency somewhat, the lines may be made to change their position within the IF band. An upper sideband line at ν_{USB} which appears at ν_{IF} in an observation with LO frequency ν_{LO} will appear at $\nu_{IF} - \Delta\nu$ if the LO frequency is changed to $\nu_{LO} + \Delta\nu$. A lower sideband line which appears first at ν_{IF} will appear at $\nu_{IF} + \Delta\nu$ following the change. The correct sideband for a given line may thus be determined by noting the position of the line in two or more DSB spectra taken at different LO frequencies. Of course, this only works well for relatively uncrowded DSB spectra; in the case of the sample spectrum shown in Figure 4.4, lines from both sidebands are blended to such an extent

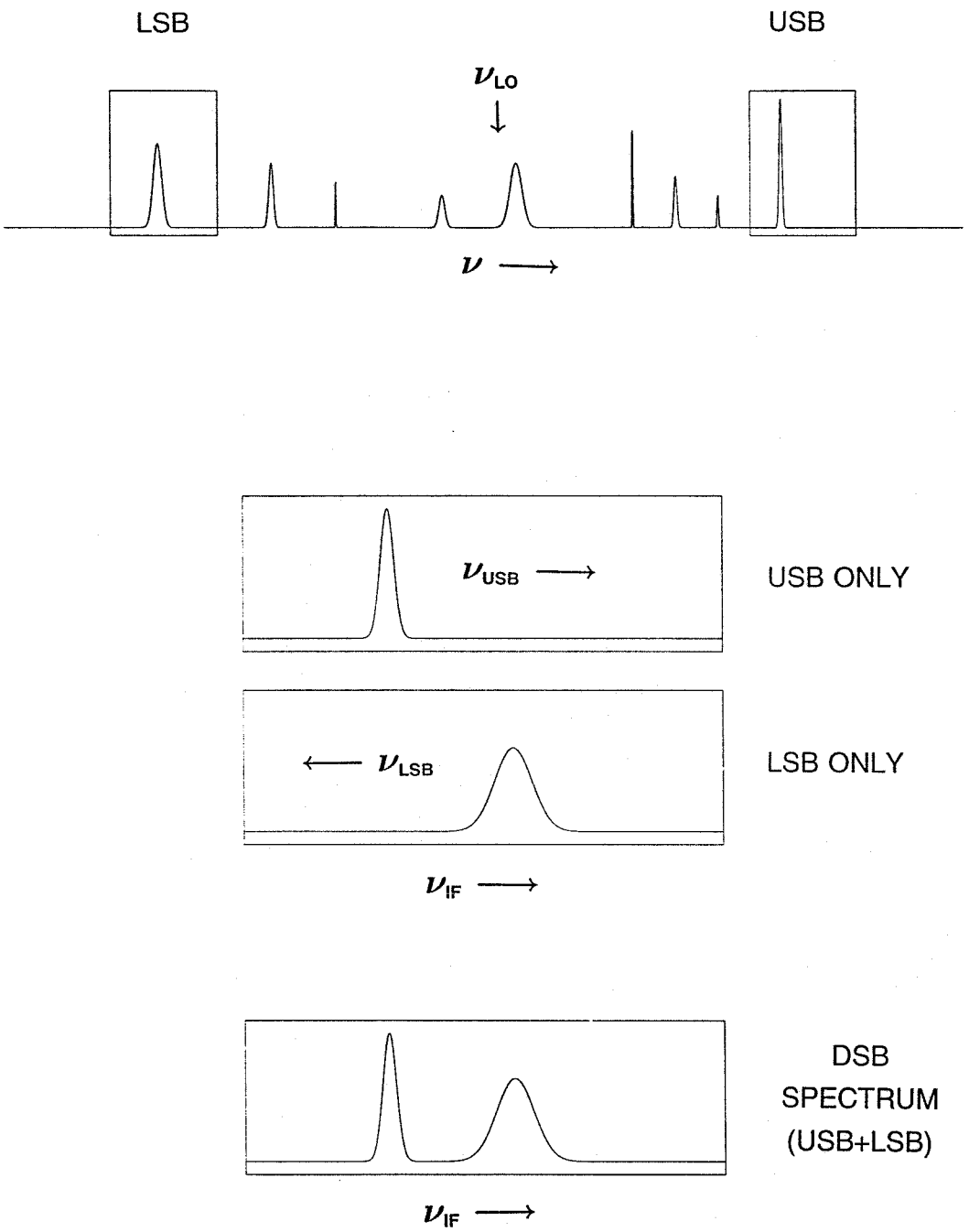

Figure 4.2 Schematic depiction of the formation of a DSB spectrum. A feature which is seen in the final spectrum at ν_{IF} may occur at either $\nu_{USB} = \nu_{LO} + \nu_{IF}$ or $\nu_{LSB} = \nu_{LO} - \nu_{IF}$.

that simply shifting the LO frequency will not enable correct assignments for all of the lines to be made. An additional problem is that while the frequency of a line may be determined in this fashion, blending may still obscure the complete line profile and prevent the integrated intensity and other parameters from being determined accurately.

As shown in Figure 4.5, aligning the observations according to the frequencies of the sidebands rather than by the IF frequencies causes the lines from the aligned sideband to be coincident, and lines from the other sideband to appear shifted by twice the amount of the LO frequency shift. If we then sum (average) the signals from two spectra with the USB frequencies aligned we obtain a spectrum in which the USB lines are unchanged and in which there are two "ghost" images from each of the LSB lines. A similar situation holds for the LSB aligned sum, where ghost images remain from the USB lines. One could equally well add two spectra taken using appropriate LO frequencies by aligning the USB of one spectrum with the LSB of the other; the key is to align the spectra according to the input frequencies. If we adopt the convention that the aligned frequencies are to be called the signal band while the other sideband for each DSB spectrum is to be called the image band, then the temperature at each frequency in the sum is the average of the temperatures at the signal frequency and at the various image frequencies. If the ghost images can be identified and then removed from the sum, the result would be a correct spectrum in SSB format.

The CLEAN algorithm (Hogbom, 1974) developed for radioastronomy aperture synthesis mapping is an iterative scheme for subtracting false images in a similar, albeit two-dimensional, problem. Sutton *et al.* (1985) and Blake *et al.* (1986) used a modification of this algorithm to generate a SSB spectrum representing the Caltech/OVRO spectral line survey of Orion A between 215 GHz and 260 GHz. We have used a similar method (actually somewhat closer to the original CLEAN algorithm) to perform the DSB to SSB deconvolution, but which has reduced the time required to process a typical set of observations by one to two orders of magnitude. The modified algorithm used previously was called SQUEAKY by its authors; we shall use CLEANSB to refer specifically to our algorithm for separating sidebands and CLEAN to refer to the general type of processing done in all of these methods.

The CLEAN algorithm (for mapping) assumes the brightness distribution on the sky can be

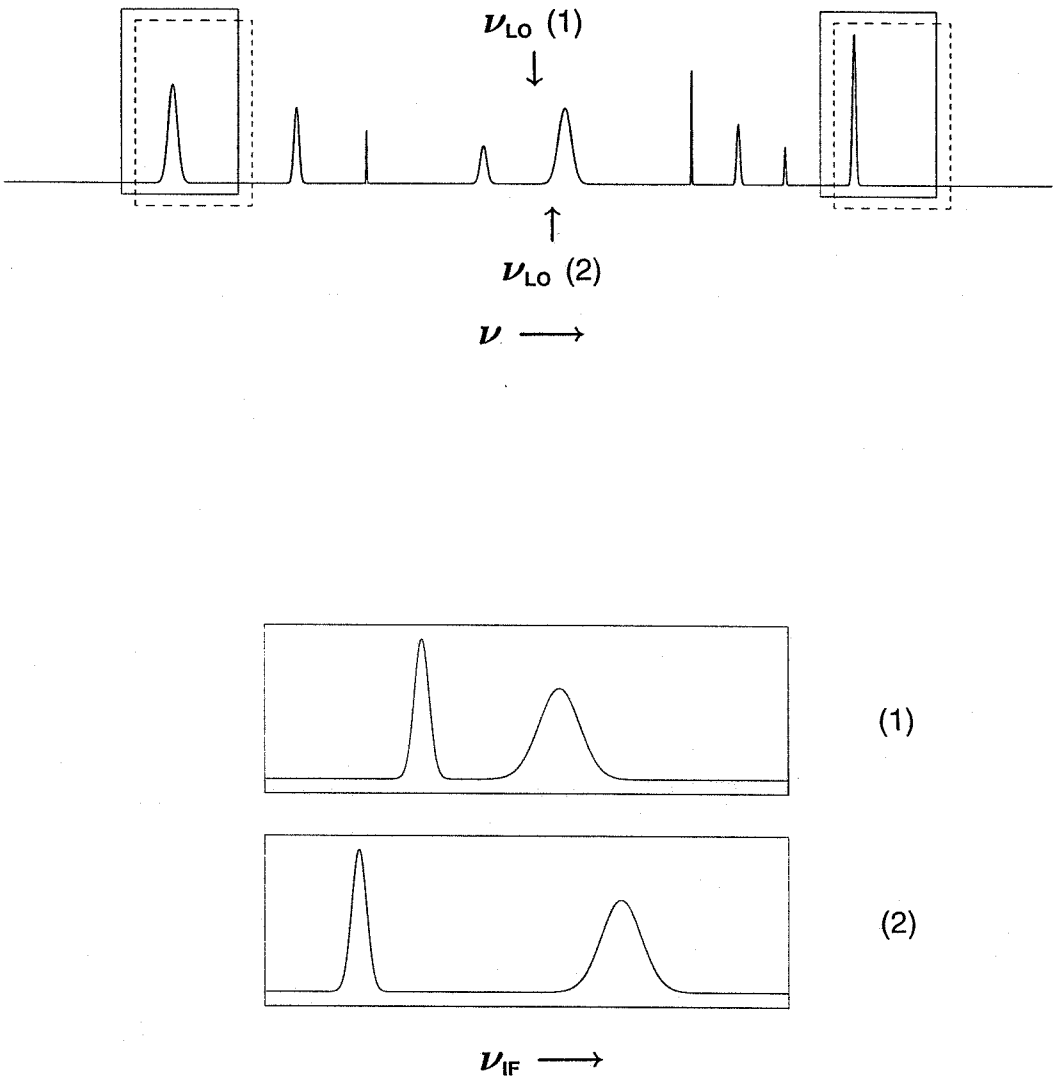

Figure 4.3 DSB spectra for two slightly different LO frequencies. Shifting the LO causes the lines to occur at a different ν_{IF}, allowing the correct sideband to be determined.

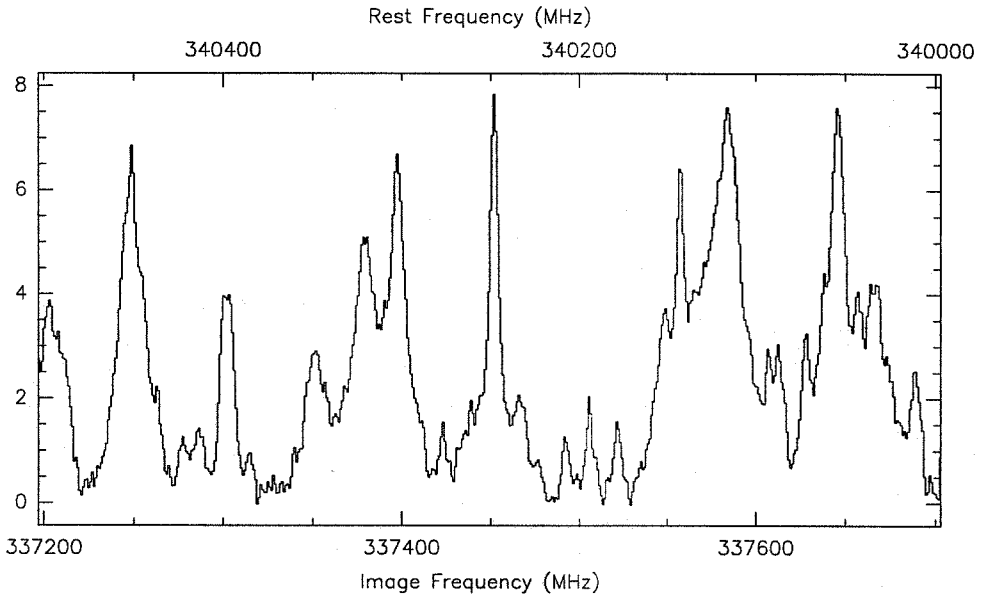

Figure 4.4 Sample DSB spectrum from the CSO Orion-KL survey. The line density is so great that shifting the LO will not clearly indicate the correct sideband assignments for the lines.

represented by a set of point sources. The "dirty" map, resulting from the raw data, is taken to consist of the emission from those sources together with their contributions (via sidelobes) which appear at other points on the sky. An iterative method is used to identify a set of point sources which reproduce the observed data. The strongest peak in the distribution is assumed to correspond to the location of a point source. Some fraction of the peak's value is assigned to the point source, and that amount as well as corresponding sidelobe image amounts are subtracted from the data. This process is repeated until the noise level is reached or some other stopping point (*e.g.*, a certain number of subtractions) is reached. To complete the process of generating a CLEANed map, the resulting set of point sources is usually convolved with a beam representing the map's resolution but with no sidelobes, and then added to the residuals. These last steps serve to produce an image which is more realistic looking and to ensure that any flux remaining in the residuals is not lost.

For the current problem of recovering a SSB spectrum from the DSB data, much the same approach can be used. The addition of the data with the sidebands aligned produces a "dirty" spectrum analogous to

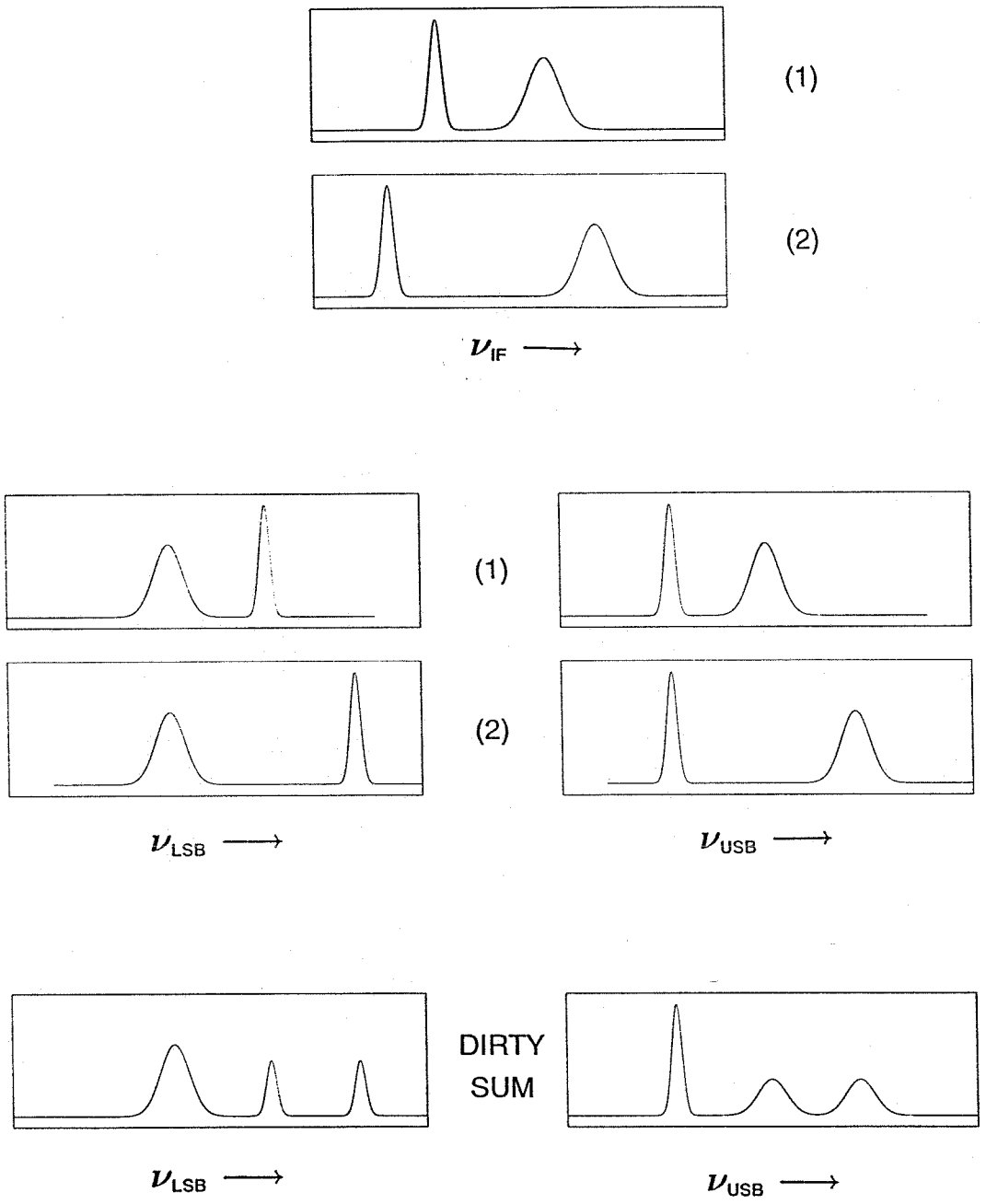

Figure 4.5 Summation of DSB spectra with the sidebands aligned. Lines from the unaligned sideband are separated by twice the amount of the LO shift and appear as ghost images.

the dirty map, with contributions from real lines and their ghost images. A set of lines is identified which reproduces the observed DSB spectra and these are entered in a "clean" spectrum. The spectral resolution of our observations corresponds to a single spectrum channel, making the final convolution unnecessary. The residuals and the clean spectrum are added together to produce a realistic looking spectrum which contains all of the flux from the DSB observations.

It is in performing the subtractions that SQUEAKY diverged from the CLEAN algorithm presented above. In the earlier implementation, all of the peaks above a certain level (chosen as a percentage of the strongest peak) were taken to represent real emission and corresponding amounts were entered in the clean spectrum. The dirty spectrum, however, was only used to find the strongest peaks and hence the frequencies at which the subtractions were to be done; the amounts taken as real emission were subtracted from the observed DSB spectra rather than from the dirty spectrum. Also, the images resulting from the real emission were not computed since they were not subtracted directly. Instead, after each set of subtractions, a new dirty spectrum was constructed from the residuals.

We have done the additional work necessary to determine the interrelations between the channels of the dirty spectrum, permitting the image lines to be subtracted from the dirty spectrum directly. In the traditional application of CLEAN to synthesis mapping, the "point spread function" (PSF) describing the observed emission (including sidelobes) from a point source is the same at all points in the map. In our case, the PSF varies with frequency and must be computed for each channel in the dirty spectrum. However, it takes the simple form of a series of appropriately weighted delta functions which link each frequency with the image frequencies in the DSB observations. We therefore build the dirty spectrum by summing the DSB observations, computing the PSF's at the same time, and do this only once at the outset. The subtractions are then done in place while the clean spectrum is built up. Figure 4.6 shows three stages in the progression of the CLEANing process for the sample spectra shown in previous figures.

While our development of the CLEANSB program was motivated by the requirements of the CSO spectral line surveys, it may also be used to derive a SSB spectrum over a much narrower frequency range (*e.g.*, around a single line of interest). Figure 4.7 shows the different sets of DSB observations appropriate for the two cases.

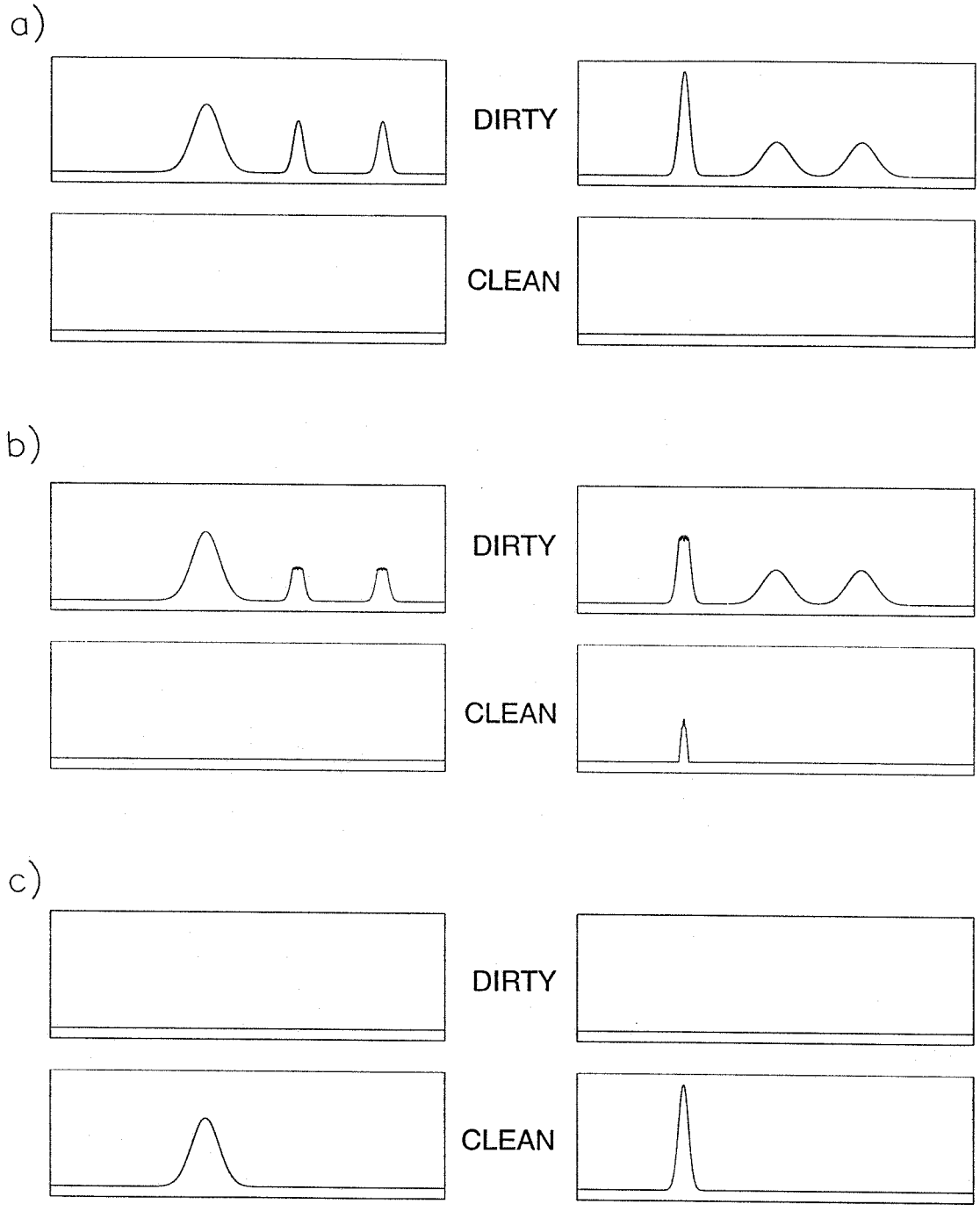

Figure 4.6 Three stages in the CLEANing process. *(a)* The dirty spectrum is formed from the sums of the DSB spectra and the clean spectrum is initially empty. *(b)* Fractional amounts of the peak values are added to the clean spectrum and appropriate amounts are subtracted from the line and its images in the dirty spectrum. Note that no subtractions have yet been performed on the weaker line. *(c)* The iterative subtractions are continued until the residuals in the dirty spectrum are less than the desired limit.

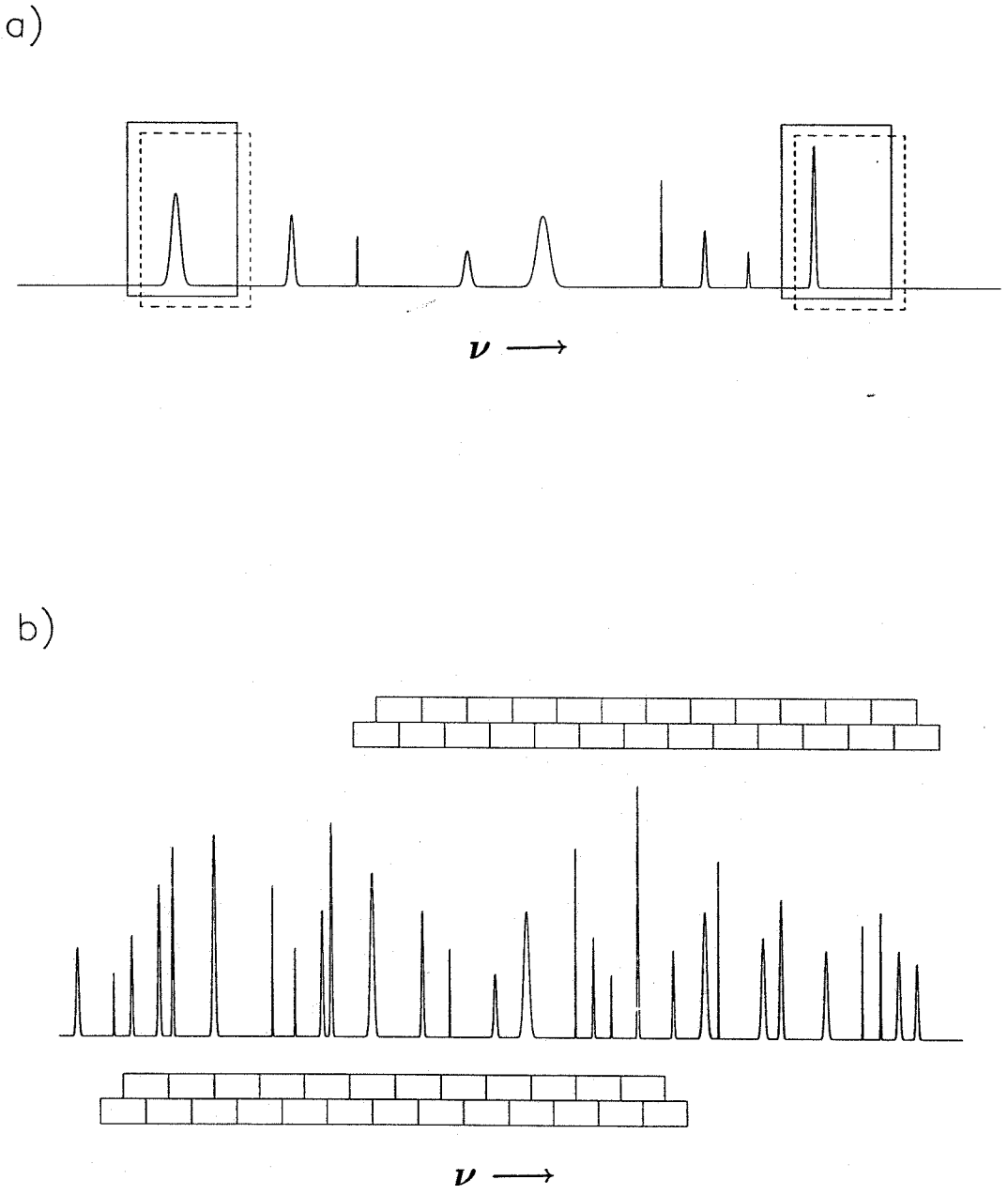

Figure 4.7 Positions of DSB scans for CLEANing a desired spectral range. *(a)* For a narrow range around a specific frequency, two or more scans with slightly shifted LO frequencies are appropriate.*(b)* For a wider range of frequencies, scans separated by half the width of the backend provide complete coverage and several observations of each frequency. Each scan is represented by a pair of boxes showing the frequency coverage, with the boxes above and below the spectrum corresponding to the upper and lower sideband coverage respectively.

For the case of a single line of interest, the LO frequencies of the observations should be shifted by an amount roughly equivalent to the width of the line; a greater shift is preferable when a large range of frequencies is being observed in order to reduce the number of observations needed.

4.3. Analysis of the CLEANSB Algorithm and Program

We now give a more rigorous treatment of the CLEANSB algorithm introducing various complications ignored in the simplified discussion above. These include the discrete nature of the frequency channels in the observations, the noise present in the system, and the potentially different sensitivities in the two sidebands, as well as other potential observational errors such as mispointing, etc.

The clean and dirty spectra are computed at a finite spectral resolution and are treated as a series of channels or bins in an array. The resolution of the clean spectrum is chosen as a function of the resolution of the original observations and also determines how the observations are to be made. In order to preserve the form of the PSF as a series of delta functions, the LO frequencies must be chosen so that the DSB spectra are correctly aligned with respect to the final array. That is, the frequency range of a channel of the clean spectrum, when observed in the signal sideband, must correspond to a frequency range in the image sideband of some other channel in the clean spectrum. This can be accomplished by simply requiring the LO frequencies of the different scans to be separated by an amount equal to an integral or half-integral number of channel widths of the clean spectrum. To construct the dirty spectrum, we first resample the DSB observations at the desired resolution and with the channels aligned with the clean spectrum channels. The channel positions of the clean spectrum are specified by the width of a channel together with a reference frequency, which can be set equal to the LO frequency of one of the scans. This also ensures the other scans will be aligned correctly, provided their LO frequency offsets meet the requirement stated above.

The sensitivity of a DSB receiver commonly exhibits variations between the two sidebands and even within the same sideband. We find that for our data we can successfully treat these variations as a simple change in a gain parameter for each sideband so that (4.3) now becomes

$$T_{\nu_{IF}} = g_s T_{\nu_s} + g_i T_{\nu_{image}} \tag{4.4}$$

(*cf.* (3.6)). Differences in the atmospheric opacities at the signal and image frequencies also produce effective gain variations between the sidebands, and may be treated by inclusion in the gain parameters (*cf.* (3.5)). For the case of equal sensitivity in the sidebands, the gains are unity. If the receiver becomes more sensitive to the signal frequency than to the image frequency, g_s will increase, reaching a maximum value of two when the receiver enters a completely single sideband mode. As noted in the discussion of chopper wheel calibration in Chapter 3, g_s and g_i must satisfy the relation

$$g_s + g_i = 2. \tag{4.5}$$

The sideband gains are not measured at the CSO and vary with the particular settings of the tuning elements. However, by comparing the relative intensities of different observations of the same strong lines, we may estimate the values of g_s and g_i for the scans in which the lines are seen. Determining the actual line intensities can be made difficult when there are overlapping lines. In addition, the gains are not well-constrained for scans in which there are no strong lines. At present, the estimation must be done by the user; future versions of CLEANSB might wish to incorporate an optimization strategy and determine best-fit gain values. Alternatively, there are laboratory methods by which sideband gains can be measured.

As with any receiver, errors are present in the observed data from a number of sources. For the moment, we ignore the source of the errors and simply add an additional component T_{error} to our expression for $T_{\nu_{IF}}$. For each DSB scan we know the relation between ν_s, ν_{image} and ν_{IF} so we may write all of the temperatures explicitly as functions of ν_s, giving

$$T_{\nu_{IF}}(\nu_s) = g_s T_{\nu_s} + g_i T_{\nu_{image}}(\nu_s) + T_{error}(\nu_s). \tag{4.6}$$

It is this expression we will use in summing the observations to form the dirty spectrum. $T_{\nu_{IF}}$ is the only observed quantity, g_s and g_i are estimated as described above, and we wish to determine T_{ν_s} and $T_{\nu_{image}}$.

We want the dirty spectrum to approximate the real spectrum with additional contributions from the ghost images. For each channel in the spectrum, we therefore sum the DSB scans in which that frequency was observed, scaling the observed $T_{\nu_{IF}}$ by $1/g_s$. We also allow the scans to be weighted by different

amounts in the sum. For the dirty spectrum, we therefore obtain

$$T_{\nu_s}^{dirty} = \frac{\sum_j \frac{w^j}{g_s^j} T_{\nu_{IF}}^j(\nu_s)}{\sum_j w^j}$$

$$= \frac{\sum_j w^j T_{\nu_s}^j}{\sum_j w^j} + \frac{\sum_j w^j (g_i^j/g_s^j) T_{\nu_{image}}^j(\nu_s)}{\sum_j w^j} + \frac{\sum_j w^j (1/g_s^j) T_{error}^j(\nu_s)}{\sum_j w^j}$$

$$= T_{\nu_s} + \langle T_{image}^* \rangle + \langle T_{error}^* \rangle \tag{4.7}$$

where the sum is over the appropriate DSB scans, w^j is the weight of the jth scan, and we define

$$\langle T_{image}^* \rangle \equiv \frac{\sum_j w^j (g_i^j/g_s^j) T_{\nu_{image}}^j(\nu_s)}{\sum_j w^j} \tag{4.8}$$

and

$$\langle T_{error}^* \rangle \equiv \frac{\sum_j w^j (1/g_s^j) T_{error}^j(\nu_s)}{\sum_j w^j}. \tag{4.9}$$

Each channel in the dirty spectrum therefore contains the correct value T_{ν_s} plus the scaled average of the image values $\langle T_{image}^* \rangle$ plus the scaled average of the error values $\langle T_{error}^* \rangle$. We note that g_s and g_i are of order unity for the preferred case of approximately balanced sideband gains. If the sensitivity in the signal sideband is too low in a particular scan, the observed value of $T_{\nu_{IF}}$ may be dominated by $T_{\nu_{image}}$ and possibly T_{error}, making the scan less useful in determining T_{ν_s}. This is reflected in (4.7) as g_i/g_s and $1/g_s$ become large. A similar effect may also occur when there is a very strong line in the image sideband with $T_{\nu_{image}} \gg T_{\nu_s}$.

Because of the alignment of frequencies described earlier, each channel in the dirty spectrum is linked to a discrete set of other channels by its own point spread function. For example, if a frequency is included in four DSB scans, then a signal at that frequency will contribute images in the four channels of the image frequencies, just as the value in the channel of the given frequency will have a contribution which is the average of the image values. From (4.7) we can determine the relative strength of an image in a linked channel. A value of T_{ν_s} will be a part of the averaged image values at the linked frequency

ν_{linked} so that we may write

$$\langle T^*_{image}(\nu_{linked})\rangle = \frac{\sum_j w^j (g_i^j/g_s^j) T^j_{\nu_{image}}(\nu_{linked})}{\sum_j w^j}$$

$$= \cdots + \frac{w^k (g_s^k/g_i^k) T_{\nu_s}}{\sum_j w^j} + \cdots \tag{4.10}$$

where the channels are linked by the kth scan and we have interchanged g_s and g_i in changing from ν_s to ν_{linked} as the "signal" frequency. As we build the dirty spectrum, for each channel we keep a list of the linked channels and the relative weights of those channels $w^k_{rel}(\nu_s) = w^k(g_s^k/g_i^k)$, as well as the sum of the weights for the channel itself $w_{tot}(\nu_s) = \sum_j w^j$.

Once the dirty spectrum is entirely constructed, we find the channel having the greatest value. An additional complication is introduced here in that some frequencies (*e.g.*, the upper sideband frequencies of the highest frequency scan) are only observed once. To compensate for this, when the spectrum value at such a frequency is compared to other values to find the largest, it is first multiplied by a scaling factor (0.9 in the current implementation). A large value in such a channel may be the result of a strong line at that frequency or simply the image of a strong line at a different frequency. If it is an image, then at the actual frequency of the line there should be a similarly large value. The multiplication by the scaling factor is an attempt to ensure that if the large value is caused by an image line, then when the values are compared, the value at the actual line frequency will be found to be larger. If the singly-observed frequency corresponds to the strongest line, then the value at the image frequency should have been reduced by the averaging with additional observations.

Having found the peak value, we assume this represents a substantial real signal at that frequency, *i.e.*, that $T^{dirty}_{\nu_s}$ is not dominated by the averages of the image values and errors. We take some fraction of the peak value and add that amount to the clean spectrum

$$\Delta T^{clean}_{\nu_s} = f \cdot T^{dirty}_{\nu_s}. \tag{4.11}$$

At the same time, we need to subtract that amount from the channel in the dirty spectrum as well as the corresponding image amounts in the linked channels. From the discussion above, we see that the correct

amount to subtract in the kth linked channel is

$$\Delta T^{dirty}_{\nu^k_{linked}} = \frac{w^k_{rel}(\nu_s)}{w_{tot}(\nu_s)} \Delta T^{clean}_{\nu_s}. \tag{4.12}$$

The weights need to be computed only once, when the dirty spectrum is first constructed. Subtracting the images consists of performing the indicated multiplication and division and then subtracting the result from the appropriate channel.

Because the weights of the scans and the sideband gains are used to build the dirty spectrum, determining the relative and total weights adds only a slight computational burden to the process. By eliminating the need to frequently recompute the dirty spectrum, the total number of computations required is greatly reduced compared to SQUEAKY. Additional computational savings are realized by sorting the array once and thereafter maintaining the array in sorted form with a very few operations during each subtraction. An advantage of using CLEANSB is that each iteration operates on the peak channel and its images, making it more likely that the subtractions represent a real signal. Because of the burden of recomputing the dirty spectrum for each set of subtractions, the SQUEAKY method performed subtractions not only on the peak channel but also on all channels having a value above a threshold level (set as a fraction of the peak value) before rebuilding the dirty spectrum. By decreasing the threshold level, the analysis could be done more quickly, but at the cost of increasing the probability of errors. We emphasize that the reduction in computing time between CLEANSB and SQUEAKY is typically one or two orders of magnitude for our spectral line surveys. This has permitted us to test our algorithm on simulated data and to experiment as to the best approach and gain factors to use in reducing our real data. The process can also be incorporated as a part of future observations so that the data can be processed and used to make immediate changes in the observing setup if necessary.

4.4. Understanding of Possible CLEANSB Errors

The fundamental assumption of the CLEANSB process is that in each of the observations to be combined, the underlying spectrum is the same so that the ghost images of real signals may be correctly subtracted. Any observational errors which cause this assumption to be violated therefore result in ghost

images being left in the spectrum after the subtractions have all been performed. Adjustments to the sideband gains will correct for calibration errors and variations in the gains which merely change the scaling of the spectrum without causing the shape of the lines to vary. The current method of determining a single gain value for each sideband based on the observed strengths of strong lines minimizes the strength of the ghost images resulting from this type of error, provided the actual gain variations may be accurately represented in this way. Our experience with the data collected for the present work suggests that this representation adequately models the actual variations. Errors which produce changes in the line shapes are more problematic and cause ghosts which cannot be easily removed. These may include the noise present in the spectrum, incorrect baseline removal, as well as mispointing or "rapid" gain variations within the sidebands.

The noise level within the original DSB scans is a function of atmospheric conditions as well as the receiver and back-end noise. For our purposes we consider this to be random noise, which has the effect of making the measurements uncertain to a degree determined by the actual noise level. The measurement of the spectrum will therefore contain errors at some level, with different observations of a given line each having a slightly different profile because of the noise. The noise level in the data therefore sets a limit beyond which no information results from performing additional iterative subtractions. We performed simulations with randomly generated SSB spectra and typical sets of DSB scans similar to those used for our surveys. The performance of our implementation of CLEANSB was tested by adding various levels of Gaussian noise to the different sets of scans, ranging from no noise to half the value of the strongest peaks in the spectrum. For very simple spectra, where very little blending of lines in opposite sidebands occurred, the results of the CLEANSB processing matched the original spectrum to approximately the level of machine precision when no noise was added to the scans. That is, the difference between the original spectrum and the processed spectrum at a given frequency was of the order of 10^{-15} times the value of the spectrum there. As the line density in the spectrum was increased, so that increasing amounts of line overlap occurred, the performance of the CLEANSB algorithm degraded slightly, so that with a line density comparable to that seen in Orion-KL (the source with the greatest known line density at submillimeter wavelengths) the relative differences between the original spectrum and the processed spectrum were of

the order of 10^{-6}. These results change somewhat when the effects of the finite spectral resolution of our data are included, as considered below. However, the performance of CLEANSB still surpasses the limits imposed by the noise levels typically found in observational data, where a dynamic range of 10^4 may be found for the strongest lines but a level of 10^2 would be a more typical limit required for the majority of a spectrum. Equally important, no additional structure was added to the processed spectra when subtractions were continued to a level below the noise in the simulated data. We are therefore confident that the presence of noise in the data imposes a limit to the accuracy with with which the clean spectrum may be known, but does not cause the algorithm to fail or to add excess noise to the final result. As noted earlier, once the subtractions have been completed, we add the residuals to the clean spectrum. This produces a final spectrum with an appropriate noise level which contains any remaining signals (but also the corresponding ghost images) if the subtractions were halted too soon.

Since CLEANSB represents the spectrum as a series of channel values which may be thought of as delta functions, it is best suited to finding the variations in spectra, and performs less well when deconvolving a flat, broad signal. Baselines are therefore removed from the observed DSB scans before these are processed with CLEANSB. For all of the sources in this thesis, the spectra consist of emission lines; however, the algorithm may be used to process spectra containing absorption lines or a combination of emission and absorption lines. In all cases, baselines should be removed so that the lines appear as departures from the zero signal level. Errors made in removing the baselines may result in increased numbers of ghost images left in the final processed spectrum; these are not caused by the CLEANSB processing, but rather are the result of errors in the data used by CLEANSB.

Mispointing of the telescope may occur during the observations, so that the same line in different scans may exhibit different profiles resulting from source structure on scales similar to the magnitude of the pointing variations. Again, the resulting ghosts left in the final spectrum are the result of data errors rather than processing errors in CLEANSB.

As noted above, for the data used in this thesis, the sideband gains were found to be adequately modeled as a single value for each of the two sidebands. The determination of these values is done before the actual CLEANSB processing, but like the baseline removal is necessary to the algorithm's

implementation. If the gain were found to vary within the sidebands, the construction of the dirty spectrum could include channel dependent gain values for each scan. When incorrect values of the gains are used, either because a variation should be included or because errors were made in determining the values, there will again be ghosts in the final spectrum resulting from data errors.

While the above discussion concerns errors found in the data before the CLEANSB processing, these errors must be included when considering the use of CLEANSB. If the baselines cannot be reliably determined, or the mispointing is severe enough that drastic variations in the line shapes are seen, the processing of the data by CLEANSB will result in a SSB spectrum containing many ghosts. These artifacts, while caused by errors in the data and not the result of processing errors, may make it preferable to utilize the DSB scans directly. Note, however, that the DSB scans will themselves contain these errors, so that comparison of the scans would imply the different line profiles were the result of emission at other frequencies.

A source of error directly attributable to the CLEANSB processing results from the finite spectral resolution of the DSB scans together with the necessary alignment of the channels in the construction of the dirty spectrum. The DSB spectra must be resampled at the desired resolution, with the resampled frequencies aligned in all of the scans. Since the channel widths in the DSB spectra can vary, this is done using an integration over the frequency range of the desired channel. A rectangular integration is used for speed and simplicity, which we have tested in the following manner. The first tests were done with aligned channels in the simulated SSB spectra, the associated DSB scans, and the resulting CLEANSB spectra, with the results noted above. When the channels in the DSB scans were set to have varying widths typical of the scans in our surveys, the relative differences between the simulated and processed spectra increased to 10^{-6} for the simple spectrum and 10^{-4} for the densest spectrum. The resampling is therefore sufficiently accurate to process typical submillimeter observations; problems resulting from strong lines with a larger dynamic range occur at easily determined frequencies and can be readily identified. Additional measures can then be taken to correct the resulting spectrum at those frequencies. In most cases, a frequency where a ghost image occurs will have been observed in several different scans. If a strong line occurs at the corresponding frequency in the opposite sideband in one of the scans and is found to be the cause of the

problem, the other scans containing that section of the spectrum can be processed with the offending scan removed and the resulting segment free of ghosts can be used in the final spectrum.

A second problem associated with the channel alignment problem results from the difference between the Doppler shifts for frequencies in the two sidebands. When there is a relative velocity between the source and the observer, frequencies in the source spectrum will be observed at Doppler shifted frequencies in the observer's frame of reference. However, the orbital motion of the Earth produces variations in the source velocity relative to the observer; thus, for observations made at different epochs, spectral features in the source spectrum will not be aligned if we work in the observer's frame of reference. When we work in the reference frame of the source, however, the construction of the dirty spectrum as given above with the simple PSF composed of delta functions is not strictly correct. The magnitude of the Doppler shift is proportional to frequency, and hence varies between, and even within (though to a lesser extent), the two sidebands. The result is a small misalignment between the assumed frequencies and the channels of the reconstructed spectrum as in the following example. We consider a sample scan whose upper sideband is centered at 345 GHz in the source's frame of reference, with a center IF of 1.5 GHz in the observer's frame of reference, when the relative velocity is 30 km s^{-1} (source and observer moving apart). The signal frequency of 345 GHz will be Doppler shifted by 34.5 MHz, while the image frequency of 342 GHz will be shifted by 34.2 MHz. If the desired resolution of the final spectrum is 1 MHz, the resampled channels in the two sidebands will then be misaligned by 0.3 channel widths. That is, an integration of the DSB spectrum from 345.000 to 345.001 GHz in the upper sideband will correspond to the range 341.9987 to 341.9997 GHz in the lower sideband. To preserve the simple form of the PSF and the resulting speed gain, the present implementation ignores this misalignment, treating the spectrum as though there were no Doppler shift and using the same value for the channels from 345.000 to 345.001 GHz and from 341.999 to 342.000 GHz. The resulting error in the lower sideband is easily seen to be $\Delta T_{Doppler} = (v_{rel}/c)2\nu_{IF} \times (dT/d\nu)$ where v_{rel} is the relative velocity and the spectrum is assumed to be linear on the scale of the frequency misalignment. The significance of this systematic error depends on the values of the slope of the spectrum, the spectrum itself, and the IF in use. Furthermore, as the amount of the misalignment will change over the IF passband, another consideration is the width of this passband. For

our surveys, the above numbers represent typical frequencies and velocities and except for the steepest line edges, the errors thus introduced are less than the noise level in the scans. For the very steep lines, such as those in IRC +10216, the systematic misalignment produces a recognizable line profile in the resulting ghosts. (The ghost image profile is that of the line derivative, with one side positive and one side negative for most lines.) We have treated these ghosts following the method given above, where at the necessary frequencies, we have processed the data separately with particular scans removed as needed to eliminate the ghost images. While this method has proven satisfactory for the present configuration, modifications to the resampling procedure and a finer sampling grid may be required in future uses.

To consider the overall effect of errors in the subtraction process, independent of their source, we return to (4.7). While the correct values of T_{ν_s} and $\langle T^*_{image} \rangle$ at all frequencies are not known *a priori*, for our purposes of analysis we may assume that these have the correct values (in other words, all of the error is contained in $\langle T^*_{error} \rangle$). At each step in the iteration, we would like the amount added to the clean spectrum to be less than the remaining signal at that frequency, thereby building up the spectrum in stages. Imposing this condition in (4.11) and (4.7) gives

$$\Delta T^{clean}_{\nu_s} = f \times (T_{\nu_s} + \langle T^*_{image} \rangle + \langle T^*_{error} \rangle) < T_{\nu_s} \tag{4.13}$$

which reduces to

$$\langle T^*_{image} \rangle + \langle T^*_{error} \rangle < \frac{1-f}{f} \cdot T_{\nu_s}. \tag{4.14}$$

Choosing a smaller value of f therefore increases the likelihood that this condition will be met, at the cost of increasing the total number of subtractions which need to be performed. From (4.14) it might seem that values of T_{ν_s} smaller than $\langle T^*_{error} \rangle$ could be correctly found. However, as the noise level in the data is reached, we find $T_{\nu_s} \sim \langle T^*_{error} \rangle \sim \langle T^*_{image} \rangle$, with the result that an incorrect peak channel is often found and the subtractions are performed on noise rather than on a real signal.

For the traditional CLEAN application to interferometer data, Schwarz (1978) has shown that for $0 < f < 2$ the residuals will converge to zero. For more general applications, the CLEAN algorithm may not converge (Cornwell 1989). Note that when $1 < f < 2$ the value in a particular channel of the dirty spectrum will oscillate between positive and negative values, with the absolute magnitude decreasing to

zero. The corresponding channel in the clean spectrum will exhibit decreasing oscillations about its final limiting value, in contrast to the monotonic tendency for $f < 1$, and (4.14) must be modified. We have performed limited tests with different values of f, finding convergence for all values between 0 and 2. In general, we found that values of f in the range of 0.1 – 0.2 worked best for the data in our surveys, representing a compromise between the desired speed and accuracy.

For the standard usage of CLEANSB with $f < 1$, (4.14) shows that minimizing $\langle T^*_{image} \rangle$ and $\langle T^*_{error} \rangle$ will help reduce errors resulting from incorrect subtractions, as would be expected. These averages can be minimized in different ways, and have subtly different effects because of their definitions. Improving the quality of the observations and avoiding the possible pitfalls outlined above will minimize the value of $\langle T^*_{error} \rangle$. Care should be taken so that building the dirty spectrum does not increase the error level significantly beyond the noise present in the original data. While $\langle T^*_{error} \rangle$ represents any errors in the data, $\langle T^*_{image} \rangle$ represents real signals which occurred in the opposite sideband in the different scans. Its value is insensitive to the quality of the observations, but depends on the particular LO settings used. In general, increasing the number of times a particular frequency is observed will bring $\langle T^*_{image} \rangle$ closer to the average value of the spectrum in the possible ranges of the opposite sidebands. Particularly for frequencies which coincide with a strong line from the opposite sideband in a particular scan, it may be advantageous to make additional observations which include that frequency. However, we note that if $\langle T^*_{error} \rangle$were zero, T_{ν_s} at the peak channel would be greater than $\langle T^*_{image} \rangle$for gains of order unity, making (4.14) true for $f < 0.5$. It is only because $\langle T^*_{error} \rangle$ has a finite value that minimizing $\langle T^*_{image} \rangle$ reduces the final amount of error.

4.5. Practical Application of CLEANSB to Our Surveys

The nominal resolution of our observations done at the CSO is approximately 0.5 MHz and varies slightly (by $\sim$ 1%) between different scans, particularly those taken during different observing sessions. Spectra taken of an injected frequency comb show the actual resolving capability of the system to be approximately 1 MHz. We therefore chose the final resolution to be 1 MHz, and made observations with LO frequencies which are separated by an integral number of MHz.

When SQUEAKY was first used by Sutton *et al.*(1985), the separation between adjacent scans was

taken to be a full backend width. This provided the maximum possible continuous frequency coverage for a given number of scans, with each frequency observed in two scans, once in the lower sideband and once in the upper sideband. During the course of the Caltech OVRO line survey of Orion, it became apparent that a set of scans with greater redundancy would be preferable. The separation between scans was therefore changed to half the backend width by Blake *et al.*(1986), making it possible to observe each frequency twice in the upper sideband and twice in the lower sideband. Of course, the redundancy of the observations is reduced at the ends of the frequency range covered and where any gaps in the frequency coverage occur. Following Blake *et al.*, we chose LO frequencies separated by 250 MHz for our observations with the CSO backend width of 500 MHz. This scheme provides frequency coverage as shown in the example of Figure 4.7 and was used in the cases where continuous frequency bands were observed. To provide redundancy near the ends of the frequency bands, additional observations were taken with much smaller LO shifts, typically 20 MHz. We also found it helpful during the course of our surveys to take scans with these smaller LO shifts in regions where severe line crowding occurred. These additional scans allowed us to more readily identify the lines in these crowded regions and to determine their intensities, as required to estimate the sideband gains. In addition, this permitted us to use particular lines to check the quality of the scans as we observed. We also made additional observations in the regions around the very strongest lines to minimize $\langle T^*_{image} \rangle$ as discussed in the previous section. In practice, we obtained better results by processing some frequencies separately with a particular scan removed as we did for the steepest lines. We found that the slight differences in the profiles of the strongest lines as seen in different scans resulted in ghost images being left in the clean spectrum otherwise. For these sections, the additional observations provided important redundancy to compensate for the removed scans. (For more discussion of the selection of LO frequencies, see Chapter 3. Tables showing the complete set of LO frequencies are given in the Appendices.)

We observed selected frequency regions in some sources rather than performing complete surveys because of time limitations. Nevertheless, we often used CLEANSB to process scans taken with different LO frequencies in order to obtain SSB data. This also assured us that we had assigned the emission lines to the correct frequencies by eliminating the sideband ambiguity. In all cases, whether for surveys or selected

regions, we have found the CLEANSB processing to give good results, with noise levels matching that expected from the observations.

4.6. Line Identification Programs

A second programming effort was undertaken in conjunction with our line surveys performed at the CSO in order to speed the process of line identification and analysis. To this end we have produced an online catalog of molecular lines which may be quickly searched by frequency or by species. A program called SIMCAT is used to specify the search parameters and to display the information from the catalog in a variety of formats. In addition, SIMCAT can perform LTE computations for line intensities and optical depths and may be used to produce simulated spectra from these computations. An associated program described below in §4.10 has also been written to carry out a rotation diagram analysis based upon observed transitions from a given species. These programs are now available at the CSO and have been used extensively in the course of performing the spectral line surveys of this thesis, as well as by other researchers.

The original motivation in writing the line catalog programs was to be able to readily identify the frequently numerous lines which appeared in the DSB scans as we observed. In particular, during our earliest observations of Orion-KL it became clear that a real-time identification of the observed lines (which were often blended) would provide a means of verifying the pointing, receiver tuning, and frequency settings used. Two catalogs of line information were available on the CSO computers, but neither was in a form which facilitated its use for an easy and quick method of identifying lines. We therefore converted the data from these catalogs into a more accessible format and wrote the necessary programs to select and display the appropriate information.

The first catalog we used was the Submillimeter, Millimeter, and Microwave Spectral Line Catalog which is actively maintained at JPL and for which the data is now available via ftp over the Internet. A description of this catalog is given by Poynter & Pickett (1985) and documentation is also available with the data. The line lists for the different species included in this catalog are stored in separate files; with over 200 species now included, this storage format simplifies studies involving a particular molecule but

greatly complicates searches for any line near a given frequency. An important feature of this catalog is the inclusion of the rotation-spin partition function for each of the listed species. The JPL catalog thus contains *consistently* defined partition functions, state degeneracies, and line strengths which are necessary for performing the LTE calculations described in the next section. For our online catalog we have combined the data for all species into a single file with the transitions given in frequency sorted order. Each transition also includes a link telling where the next transition of the same species may be found in the catalog. This is used by the program in order to read only the relevant transitions for faster display.

The second catalog which we used was an unpublished compilation by F. J. Lovas (1984) of molecular transition data, which had been obtained at the time of the earlier OVRO line surveys of Orion-KL (Sutton *et al.* 1985, Blake *et al.* 1986). An addition to this list containing higher frequency transitions as well as data for some new species was transmitted to us during the course of this work (F. J. Lovas 1990). No partition function information was included in this catalog so that the list of transitions was used only for line identification purposes. The Lovas listing included fewer species than the JPL catalog; however it did include several astronomically interesting species which were not contained in the JPL catalog (*e.g.*, $^{34}SO_2$ and $C^{17}O$).* We have put the transition information into a linked list similar to that used for the JPL catalog. However, the information included for each transition and the format of the data are sufficiently different for the two catalogs that we have kept them as two separate data files, with no attempt made to merge them.

The initial effort resulted in a program called LINECAT, which has served for several years at Caltech and the CSO as the standard means of identifying lines and looking up frequencies. This program utilizes both the JPL and Lovas catalogs, although because of the different formats the two are accessed separately. This program served as the basis for developing the SIMCAT program with its additional capabilities. It allows the transition information contained in the catalogs to be selectively displayed, restricted to specific molecules and/or frequencies selected by the user. An example of the display format is shown in Figure 4.8.

* We note that during the course of this work, the data for $^{34}SO_2$ was added to the JPL catalog. This exemplifies the dynamic nature of the JPL catalog, which is being updated as new data become available.

Molecule	Transition	Intensity (log)	E lower (cm-1)	Freq Error	Frequency (MHz)	
CS	7 - 6	-1.17	34.32	0.10	342883.000	obs
H2CS	10 010 - 9 0 9	-2.57	51.52	0.68	342944.369	
Si-29-O	8 - 7	-0.78	40.05	0.59	342979.109	
H2CS	10 2 9 - 9 2 8	-2.66	88.18	0.59	343319.645	
H2C-13-O	5 1 5 - 4 1 4	-1.76	31.14	0.08	343325.467	
H2CS	10 3 8 - 9 3 7	-2.30	133.82	0.79	343408.119	
H2CS	10 3 7 - 9 3 6	-2.30	133.82	0.78	343412.325	
H2CS	10 2 8 - 9 2 7	-2.66	88.21	0.59	343810.755	
SO	8 8 - 7 7	-1.87	49.32	0.07	344310.612	obs
SO2	5 5 1 - 6 4 2	-4.62	40.72	0.01	345148.952	
SO2	13 212 - 12 111	-2.87	53.11	0.02	345338.543	
SO	3 2 - 1 2	-5.89	3.10	0.04	345704.555	
CO	3 - 2	-3.61	11.53	0.06	345795.989	obs
H2CO-18	5 0 5 - 4 0 4	-2.20	23.12	0.29	345881.382	

Figure 4.8 Sample display of information from the LINECAT line catalog. A frequency sorted list of transitions is displayed, including such information as the species names, the quantum numbers of the transitions, and the energy of the lower state above the ground state.

In addition to the listing of lines, the program is capable of plotting the positions of lines along a frequency axis. For the case of DSB observations, the program can generate a plot showing the relative positions of lines in each sideband for a given LO frequency and backend width. This has proven important in selecting observing frequencies which allow lines of interest to be observed simultaneously in the upper and lower sidebands while avoiding any line overlap. A sample DSB plot including lines from both sidebands is shown in Figure 4.9. We used LINECAT to select the observing frequencies used in our spectral line surveys, both to avoid problems of line overlap and to maximize the number of lines observed in the sources for which we were unable to perform complete surveys.

4.7. LTE Calculations of Intensity and Opacity

Once the information in the line catalogs was easily accessible, it became clear that having the program do the calculations needed to compare the catalog information with observed data would save the user from repeating the same calculations many times and would insure consistency in the performance of the analysis. The JPL line catalog includes an intensity value for each transition which together with the partition function for the species may be converted into the line strength and used in LTE calculations of opacity or brightness temperature. We used the LINECAT program as a base and added the capability to perform a variety of calculations for the lines in the JPL catalog, as well as the ability to generate a

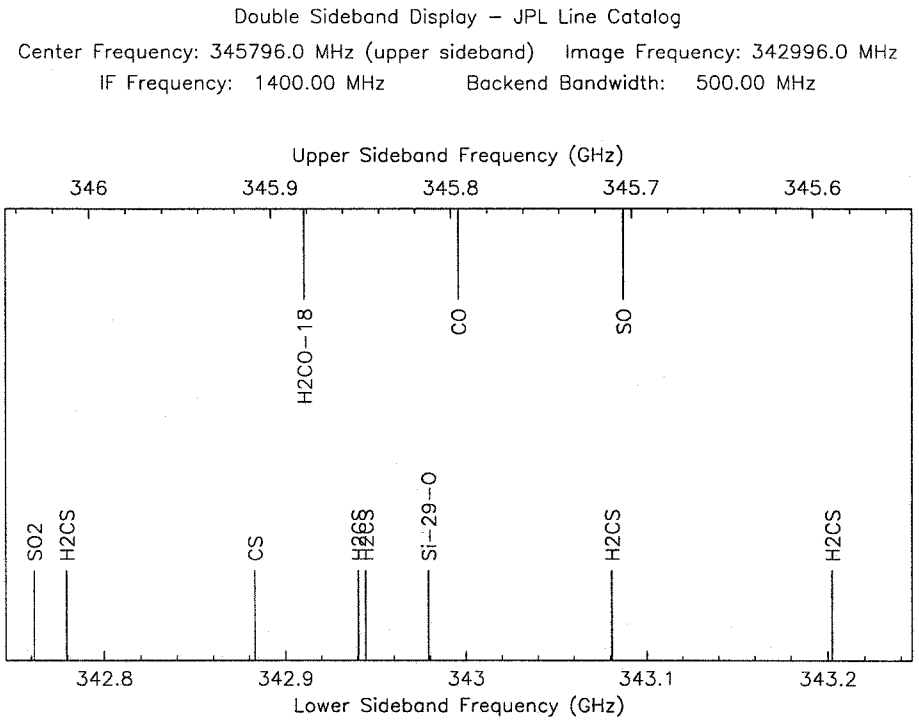

Figure 4.9 Sample DSB format plot from the LINECAT line catalog. Lines from the selected sideband are shown as solid tick marks while lines from the other sideband are shown as dashed tick marks. Using these plots, LO frequencies can be selected to avoid line overlap problems.

simulated spectrum using these calculations. The resulting program, called SIMCAT, has been available at Caltech and the CSO for the past year. In this section, we describe the various calculations which may be carried out within SIMCAT. A description of the method for producing simulated spectra is given in the next section.

The partition functions for the various species are contained in a separate file from the transition listing. For each species, the logarithm of the partition function is stored for the following temperatures: 300K, 225K, 150K, 75K, 37.5K, 18.75K, and 9.375K. It is possible to display the partition function values within the program and to plot them graphically. In addition, a power-law fit to the partition function is made for each species which is used as needed in other calculations. Figure 4.10 shows the partition function values and fit for the CO molecule and the resulting plot from SIMCAT.

The intensity value given for each transition in the JPL line catalog is based on the integral of the absorption cross section over the width of the line. The actual value stored is the logarithm of I_{cat}, the

a)

Partition function for CO as a function of temperature

9.375 K	18.75 K	37.5 K	75 K	150 K	225 K	300 K
3.74	7.12	13.90	27.45	54.58	81.71	108.87

Fit to partition function Q(T) = alpha * Tbeta**

alpha = 0.41210 beta = 0.97552

b)

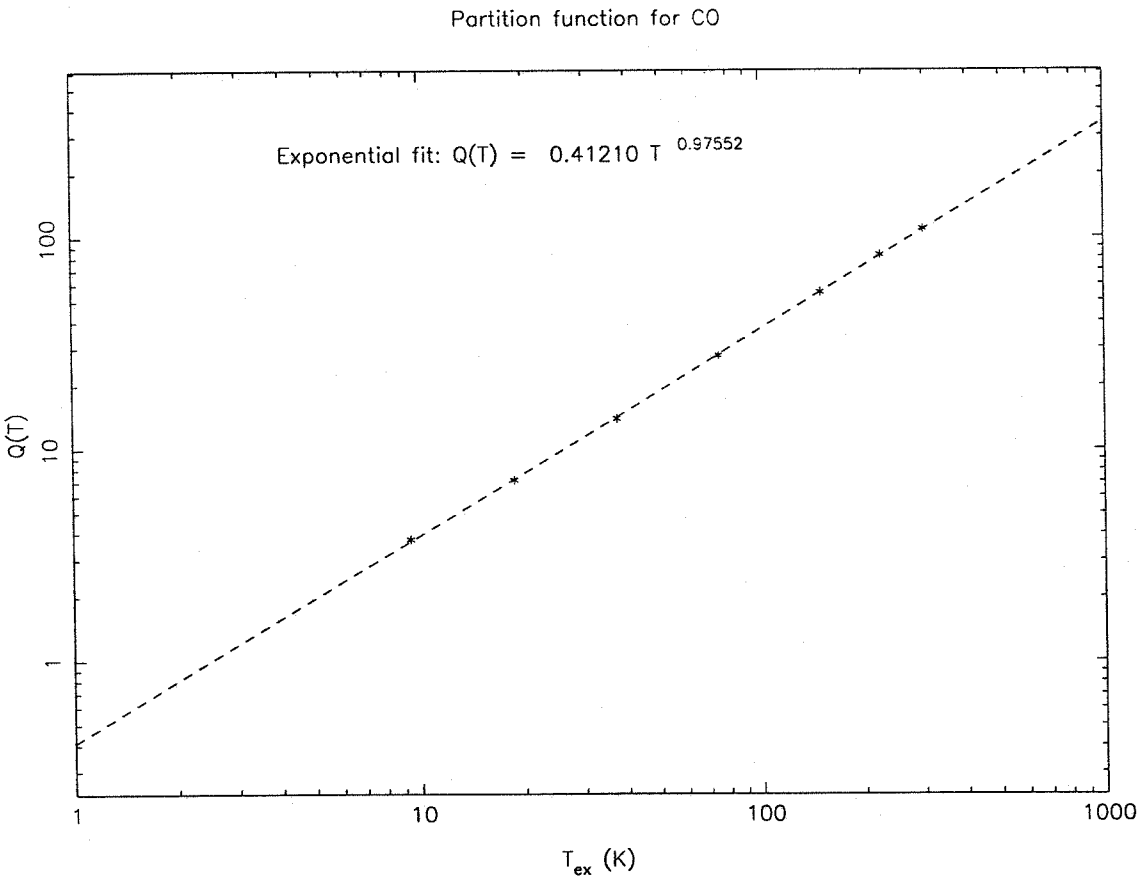

Figure 4.10 Display and plot of CO partition function from SIMCAT. *(a)* The values of the partition function from the JPL line catalog are displayed together with the parameters from the power-law fit. *(b)* The plot of the partition function includes the data points from the catalog (∗) and the fit (the dashed line).

intensity calculated for a temperature of T_0 = 300K. This is defined as

$$I_{cat} = \frac{8\pi^3}{3h}\frac{\nu}{c}\mu^2 S \frac{1}{Q(T_0)}\left(e^{\frac{-E_l}{kT_0}} - e^{\frac{-E_u}{kT_0}}\right) \tag{4.15}$$

where ν is the line frequency, μ is the dipole moment, S the line strength appropriate for the transition, E_l and E_u are the energies of the lower and upper states respectively, and $Q(T_0)$ is the value of the partition function at 300K. The value of I_{cat} is given in units of nm^2 MHz. We again note the advantage of using data from a single catalog so that the definitions of the line strength and partition function are consistent. In the standard display from SIMCAT, the value of $\mu^2 S$ is extracted from I_{cat} and displayed. The dipole moments for the various species are given in the written documentation available with the catalog data but are not included in the data files. Since μ appears in all of the conversions in the combination $\mu^2 S$, the actual value of μ itself is not needed for the computations. Comparison of (4.15) with (2.30) shows that for a given column density N_T and excitation temperature T_{ex}, the optical depth τ_v in a particular transition may be obtained from I_{cat} as

$$\tau_v = \frac{c}{\nu} N_T I_{cat} \frac{Q(T_0)}{Q(T_{ex})} \frac{e^{\frac{-E_l}{kT_{ex}}} - e^{\frac{-E_u}{kT_{ex}}}}{e^{\frac{-E_l}{kT_0}} - e^{\frac{-E_u}{kT_0}}} \phi(v) \tag{4.16}$$

where $\phi(v)$ is the profile function in terms of velocity. Note that all conversions described in this section are done under the assumption of LTE and use the derivations of §2.3. Within the program, the user may specify the values of N_T and T_{ex} for any desired molecules together with a spectral linewidth Δv in km s^{-1}. The program will compute and display τ_v from (4.16), taking $\phi_v = 1/\Delta v$ (corresponding to a rectangular line shape of width Δv).

Using the same parameters (N_T, T_{ex}, and Δv) the program will also compute the brightness temperature T_b and integrated intensities $W = \int T_b\, dv$ for a transition in a "thin" approximation and a "thick" approximation. For the optically thin case, we first compute W_{thin} using the definition of T_b from §2.3, replacing $(1 - e^{-\tau})$ by τ and taking T_{BG} = 0, thereby neglecting any background radiation. Using

(4.16) together with $h\nu = E_u - E_l$ and $\int \phi(v)\,dv = 1$ then gives W_{thin} in terms of the catalog intensity as

$$W = \int \frac{h\nu}{k}\left(\frac{1}{e^{h\nu/kT_{ex}}-1}\right)\tau_v\,dv$$

$$= \frac{hc}{k}N_T I_{cat}\frac{Q(T_0)}{Q(T_{ex})}\int \frac{1}{e^{h\nu/kT_{ex}}-1}\,\frac{e^{\frac{-E_l}{kT_{ex}}}-e^{\frac{-E_u}{kT_{ex}}}}{e^{\frac{-E_l}{kT_0}}-e^{\frac{-E_u}{kT_0}}}\,\phi(v)\,dv$$

$$= \frac{hc}{k}N_T I_{cat}\frac{Q(T_0)}{Q(T_{ex})}\,\frac{e^{\frac{-E_u}{kT_{ex}}}}{e^{\frac{-E_l}{kT_0}}-e^{\frac{-E_u}{kT_0}}}. \qquad (4.17)$$

In the thin approximation, the entire column density is assumed to contribute to the integrated intensity; hence W_{thin} is proportional to N_T and is independent of Δv. The value of $T_{b,thin}$, which does depend on Δv, is then found as $T_{b,thin} = W_{thin}/\Delta v$.

When computing W_{thick} and $T_{b,thick}$, the value of τ_v from (4.16) is found with $\phi(v) = 1/\Delta v$ and then used together with the specified values of T_{ex} and T_{BG} in the definition of T_b to obtain

$$T_{b,thick} = \frac{h\nu}{k}\left(\frac{1}{e^{h\nu/kT_{ex}}-1}-\frac{1}{e^{h\nu/kT_{BG}}-1}\right)\left(1-e^{-\tau_v}\right). \qquad (4.18)$$

The integrated intensity is then computed as $W_{thick} = T_{b,thick} \times \Delta v$. The integrated intensities may also be displayed in units of K MHz using the approximate conversion $W(\text{K MHz}) = W(\text{K km s}^{-1}) \times \nu/c$.

The above conversions from the catalog intensity use the specified column density, excitation temperature, and rectangular linewidth to compute an opacity or line intensity for a particular transition. In many cases, a brightness temperature or upper limit may be known for a transition and an interesting question is what column density would be required to produce the known value. We have therefore included in the program the ability to compute and plot the required column density as a function of excitation temperature. The user may specify any of the following: τ, $T_{b,thin}$, W_{thin}, $T_{b,thick}$, or W_{thick}. For each transition to be displayed (restricted by the selected frequency range and set of species) the column density obtained by solving for N_T in the appropriate equation above is computed while T_{ex} is allowed to vary. If the rectangular linewidth has not been specified for the molecule, then a default value of 1 km s^{-1} is used in the computations. The required column density is first computed at the temperatures for which the partition function is explicitly given and displayed as shown in the sample of Figure 4.11.

a)

Molecule	Transition	Frequency (MHz)	E upper (K)	E lower (K)	mu^2 S (D^2)
CO	3 - 2	345796.0	33.19	16.60	0.036

Column density required for tau = 1
as a function of excitation temperature

9.375 K	18.75 K	37.5 K	75 K	150 K	225 K	300 K
0.5867E+16	0.6506E+16	0.1339E+17	0.3821E+17	0.1289E+18	0.2739E+18	0.4734E+18

Calculated with no background radiation and delta v = 1.00 km/s

b)

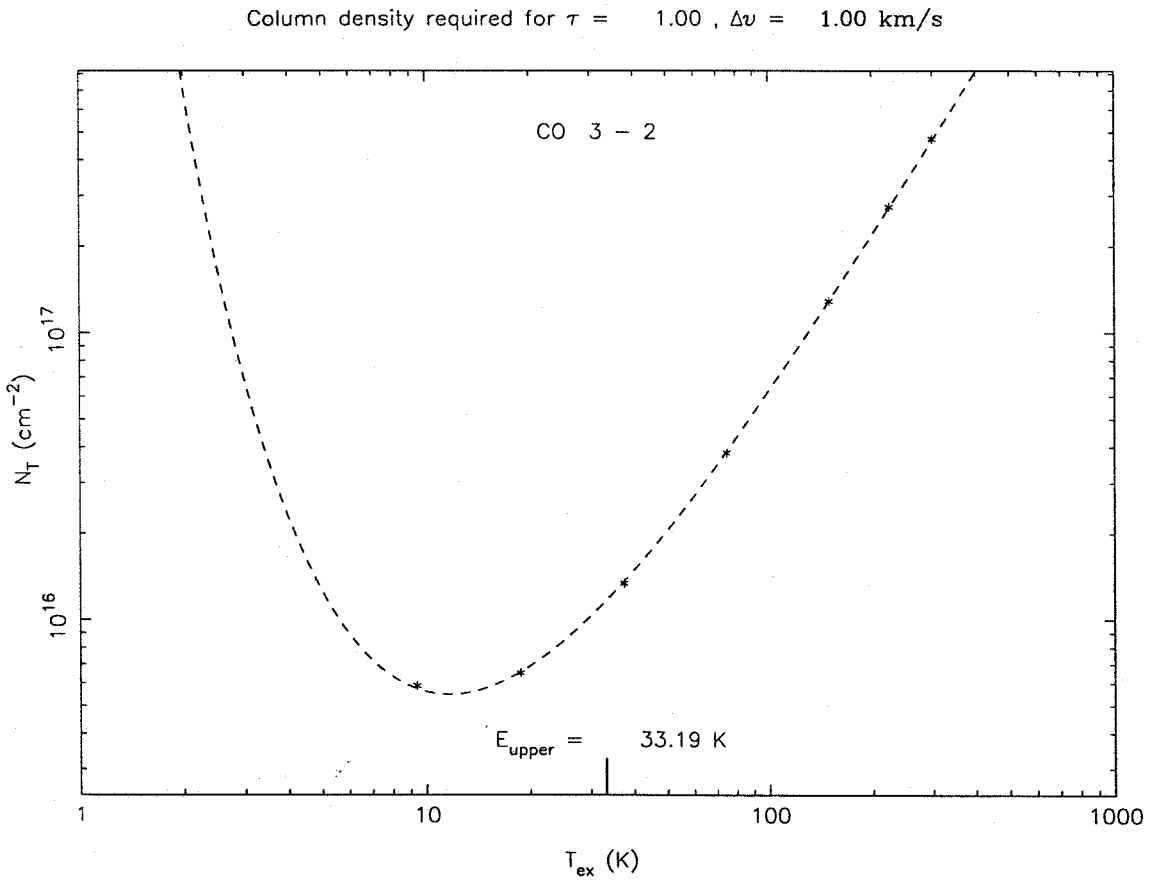

Figure 4.11 Sample display and plot showing required column density. *(a)* The required column density is computed using the partition function values from the catalog and displayed to the user's screen. *(b)* The plot of the required column density shows the values derived from the stored partition function (*) and also the values obtained using the power-law fit to the partition function (the dashed line).

If a plot is requested, the fit to the partition function is used and the required column density is plotted for temperatures up to 1000 K as also shown in Figure 4.11.

4.8. Generation of Simulated Spectra

In addition to a list of the line intensities resulting from a given set of species together with their column densities, etc., we wished to generate simulated spectra from such a set, with the user able to specify the velocity distribution of the column density for each molecule included in the set. While the assumption of LTE in the calculations clearly limits the accuracy of the resulting spectrum, this represents a first step towards modeling the emission from a region containing a variety of molecules. We are unaware of any other means presently available to derive a simulated spectrum which allows a large suite of molecules and different excitation temperatures to be included.

To construct a simulated spectrum, the user first must specify the frequency range of interest. The spectra computed by SIMCAT are represented as brightness temperatures in channels whose width is given by the frequency resolution of the simulation (also specified by the user). For each molecule to be included, the excitation temperature and column density are used just as before. However, the actual distribution of the column density as a function of velocity is specified, rather than taking $\phi_v = 1/\Delta v$ as before. The shape of the distribution is given in a file containing a normalized (unit width and area) line shape and a scaling factor is used to specify the actual width of the line in velocity. This approach allows a single file to be used for molecules which exhibit different widths. Several standard files have been generated and are included in the program for Gaussian, Lorentzian, and other types of profiles.

The actual method used by the program to obtain the simulated spectrum is similar to the calculation of optical depth given in the previous section. For a given molecule, a normalized optical depth is computed as

$$\tau_{norm} = \frac{c}{\nu} N_T I_{cat} \frac{Q(T_0)}{Q(T_{ex})} \frac{e^{\frac{E_l}{kT_{ex}}} - e^{\frac{E_u}{kT_{ex}}}}{e^{\frac{E_l}{kT_0}} - e^{\frac{E_u}{kT_0}}} \tag{4.19}$$

for each transition within the specified range. The velocity distribution described above is scaled by this value and resampled on the grid of the simulated spectrum channels. An optical depth spectrum with the same resolution as the simulated spectrum is thus constructed for each species, where the optical depth

in a given channel is the sum of the optical depths in all of the transitions of that species which overlap that frequency. The optical depth in each channel is then converted to a brightness temperature using (2.32) with the line frequency ν taken to be the frequency of the channel. Most velocities of interest in molecular line observations are small compared to c, so the error introduced by this approximation to ν_{line} is unimportant. This method allows us to sum the optical depths rather than the brightness temperatures, as is necessary to avoid overestimating the emission from overlapping optically thick lines. We have found this to be important, particularly for the case of hyperfine splitting of lines of great optical depth.

Since the different molecular species are allowed to have different temperatures, it is not feasible to sum the optical depths resulting from all of the included species. The conversion from optical depth to brightness temperature is made for each species separately, and the resulting spectra are summed to form the overall simulated spectrum. This overestimates the emission at frequencies where lines of different species overlap when the optical depths are significant. Our experience with the simulations suggests that such overlaps are relatively rare and that this is not usually a significant problem in practice. In any case, accurate simulations in these cases would require more detailed modeling than the LTE approximations used by the program.

The simulated spectrum obtained in this way may be saved and later restored together with the accompanying molecule list. Smoothing of the spectrum is possible by convolving with a response function or by resampling on a coarser grid. A sample plot of a simulated spectrum before and after smoothing is shown in Figure 4.12. Double sideband plots which show the contribution from each sideband together with the sum are also available. If desired, the spectrum can be plotted with tick marks and labels for the transitions included in the simulation.

4.9. Integrated Line Flux Considerations

Several additional capabilities have been added to the SIMCAT program for the purpose of studying the total integrated line flux. The simplest of these is the ability to sum the integrated intensities W_{thin} and W_{thick} obtained as in §4.7 over a specified frequency range with subsums reported at a specified resolution. These sums may be done in units of K MHz or K km s^{-1} and utilize the current list of

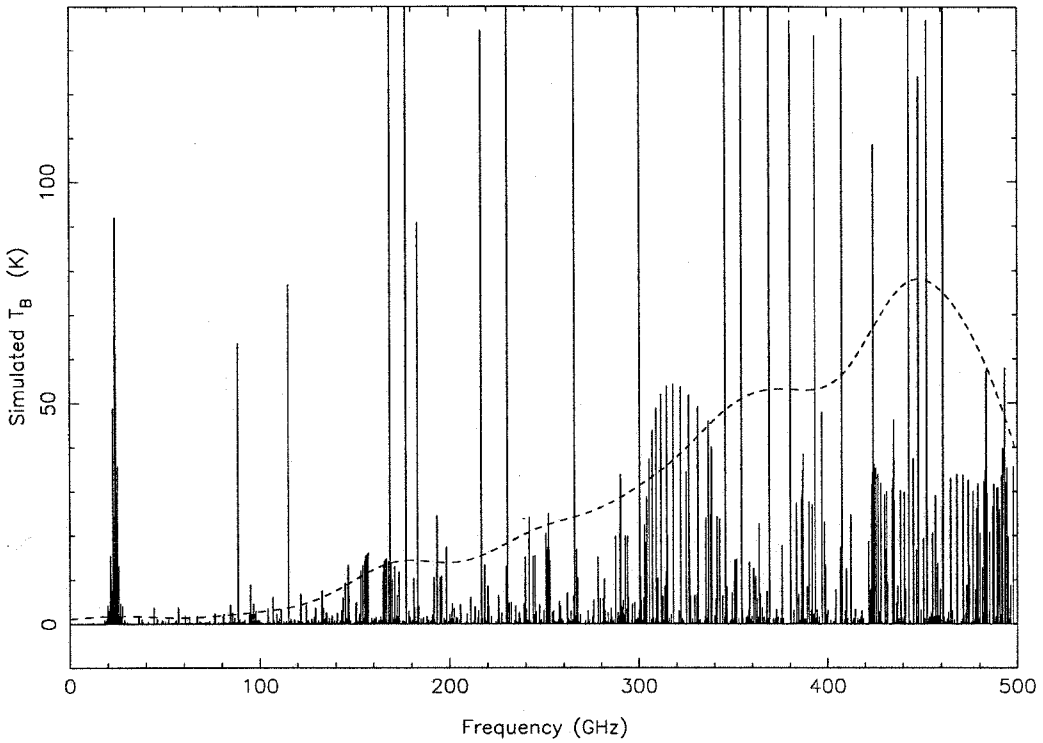

Figure 4.12 Simulated spectrum obtained using SIMCAT. The spectrum as it is originally computed is shown as the solid trace. The spectrum is then convolved with a 50 GHz Gaussian and multiplied by 100 to obtain the dashed trace.

molecular species with their column densities, etc. The integrated intensity from a simulated spectrum may be similarly summed using a straightforward integration over the current spectrum. These capabilities have been combined with the smoothing capability to investigate the temperature and frequency dependence of the line flux for certain molecular abundances. A list of molecules, together with column densities, linewidths, and profiles, must be specified. The user selects the frequency range and resolution in the usual manner and additionally sets a range of temperatures and the temperature step size to be used. The program loops through the range of temperatures, each time setting the excitation temperature of all of the included molecules to be the current temperature step. The simulated spectrum is generated and the sums are computed for the simulated spectrum and the thin and thick cases. If a smoothing method has been chosen, the sum is also computed for the smoothed spectrum. The resulting output is a two-dimensional array of integrated intensity with frequency and excitation temperature as the axes. Contour plots can then

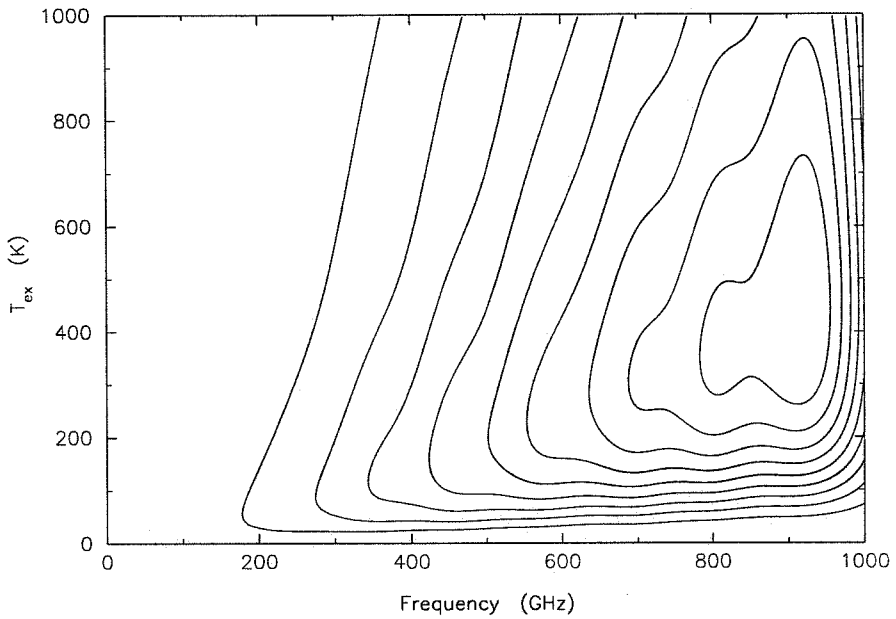

Figure 4.13 Sample contour plot showing integrated line flux as a function of frequency and excitation temperature. SIMCAT is used to compute the spectrum at a series of excitation temperatures; these are then smoothed by convolution with a 100 GHz Gaussian and combined to obtain the above contours. (The sharp drop near 1000 GHz occurs because the spectrum is simulated only for frequencies below 1000 GHz.)

be made as shown in Figure 4.13 to reveal the regions having the greatest line flux and the temperature dependence of the flux. A number of these plots are shown in the next chapter for the different sources considered in this thesis.

4.10. RD Program

The rotation diagram analysis described in §2.3 requires information from the line catalog concerning the transition and the observed line intensities. One of the output formats of SIMCAT writes the necessary transition information to a file. This file is used in turn as input to a companion program (called RD) which will perform the rotation diagram analysis and plot the results. By selecting a single molecule in SIMCAT and also limiting the frequency and energy ranges used, the appropriate transitions may be included in the file. The user can then edit the file, inserting the observed intensities of the transitions as well as the

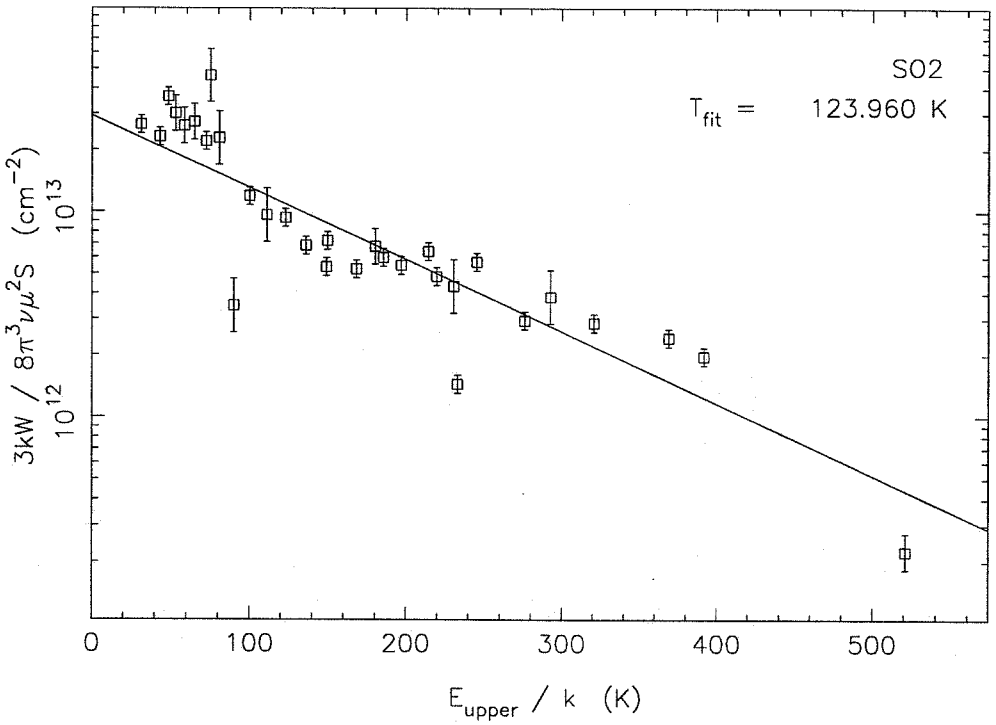

Figure 4.14 Sample rotation diagram from the RD program. The data are taken from the CSO line survey of Orion-KL.

relative uncertainties in the data. It is possible to separate the observed lines into different sets (*e.g.*, for lines observed at different telescopes) and to fit the different sets separately in addition to the complete set. Upper limits to observed intensities may also be entered in the file; these values are not included in the fitting process but are plotted for comparison with the data and the resulting fits. The RD program derives a rotation temperature and a column density for each set of data and writes these to an output file. The rotation temperature is obtained directly from the fit to the data; the column density, however, depends on the value of the partition function at the derived temperature in addition to the actual fit. We emphasize once again the need to use consistently defined parameters for these calculations. The information written by SIMCAT therefore includes the partition function from the catalog. Once the data have been fit, plots showing the data and the resulting fits can be easily made. For each set of points, the user can choose to show the data, the error bars, and the fit to that set, as well as the overall fit resulting from all of the data. A sample plot is shown in Figure 4.14.

Chapter 5

Survey and Line Flux Results

5.1. Overview of the Surveys

With the advent of large ground-based telescopes and sensitive receivers at millimeter and submillimeter wavelengths, spectral line surveys have become an important method of studying the chemical and physical conditions in astronomical sources. Because of the large amount of observing time required to perform complete surveys, these have typically been performed for the brightest, and hence best-studied, sources, such as Orion-KL (Johansson *et al.* 1984, Sutton *et al.* 1985, Blake *et al.* 1986, Jewell *et al.* 1989, Turner 1989, Greaves & White 1991, Ziurys & McGonagle 1993), Sgr B2 (Cummins, Linke & Thaddeus 1986, Turner 1989, Sutton *et al.* 1991), and IRC +10216 (Avery *et al.* 1992, Johansson *et al.* 1984). Using data from the OVRO spectral line survey of Orion-KL, Sutton *et al.* (1984) demonstrated that 40 – 60% of the total flux observed from Orion-KL in the range 230 – 260 GHz was contributed by molecular emission lines. We initiated the current project to evaluate the contribution of the integrated line flux to the total flux in other sources and to study the frequency dependence of this contribution in general. The availability of the very sensitive facility heterodyne receiver at the CSO made it possible to perform spectral line surveys of several sources in the 330 – 360 GHz atmospheric window to determine the actual line flux there. Ideally, complete surveys would provide the line information for each of the sources over the spectral range desired. However, in order to complete the data collection within a reasonable amount of

time, it was necessary to make targeted observations at a limited number of frequencies for some sources. Especially for the weaker sources, where the lines may be an order of magnitude or more weaker than in Orion-KL, the telescope time which would be required to obtain complete surveys to a proportionally greater sensitivity is simply not practical. In order to obtain meaningful estimates of the total line flux, we instead observed selected frequency ranges where the strongest lines might be expected.

We wished to include a variety of sources representative of different types of astronomical objects of interest to millimeter and submillimeter astronomers. We therefore chose to observe two well-studied sites of star formation, Orion-KL representing a high-mass star-forming region and IRAS 16293–2422 representing a low-mass star-forming region. For Orion-KL, we performed a complete survey from 325 – 360 GHz, while for IRAS 16293–2422 our observations included roughly 50% of the 330 – 360 GHz range. For comparison with Orion-KL, we also observed Orion-S, located 1.5′ south of IRc 2 in the OMC-1 molecular ridge, providing another example of star formation in a region with similar initial physical conditions. In addition to the above star-forming regions, the objects surveyed by us include three evolved stars with circumstellar shells of gas and dust. A complete survey from 330 – 358 GHz was performed for IRC +10216, together with limited observations of VY Canis Majoris and OH 238.1+4.2. The line flux contribution to the total flux for all of these sources is discussed individually in the sections which follow. The actual survey data, including plots of the spectra and tables giving the observed line parameters, are given in the appendices of this thesis.

In previous chapters we have described our observing procedures, including the calibration techniques and data reduction methods used. We made observations at the CSO during a total of 10 sessions between December 1989 and January 1992 (the dates and sources observed for each session were given earlier in Table 3.1). We initially concentrated on the surveys of Orion-KL and the nearby source Orion-S, as well as the survey of IRC +10216, knowing that these would require the greatest amount of time. The observations of these sources also provided useful information when selecting the frequencies to observe in other sources. As the survey work progressed, we made observations of the other sources, attempting to maximize the amount of data gathered by considering the atmospheric transmission and the source positions in the sky. Eventually we obtained observations at over 200 LO frequencies for Orion-KL and over

100 LO frequencies for IRC +10216. For Orion-S, we soon determined that our initial intent to obtain a complete survey matching that of Orion-KL was impractical, and we observed only at selected frequencies, eventually performing observations using approximately 45 LO frequencies for our survey. The total number of LO frequencies observed in the other sources was approximately 45 in IRAS 16293–2422 and approximately 25 in both OH 231.8+4.2 and VY Canis Majoris.

5.2. Evaluation of the Integrated Line Fluxes

Our observations provide us with a measurement of the integrated line flux in these sources, but with the exception of the two Orion sources, they do not allow us to determine the total flux for comparison. We therefore use published flux values, particularly a consistent set of broadband flux values which includes all of the sources except for Orion-KL and Orion-S (Sandell 1994). For both Orion sources, the continuum emission was sufficiently strong that we could estimate its value as the average continuum offset of the baselines which were removed from the observed spectra. Additional flux values used for comparison are given in the discussions of the individual sources below.

We follow a multistep procedure for evaluating the contribution of the integrated line flux to the total flux for each of the objects. We first determine the integrated line flux averaged over the frequency range of the observations based on the lines detected by the surveys. For the sources where the frequency coverage of the observations is incomplete, we derive upper and lower bounds for the average line flux over the canonical range of 330 – 360 GHz based upon the observed lines. Following this determination, we extrapolate to low line intensities and estimate the flux contribution from lines too weak to be detected in our survey, again for the observed frequency range and the 330 – 360 GHz range. Finally, we use simulations to estimate the importance of the line flux contribution at frequencies up to 1000 GHz. Each of these steps is described in greater detail below. Following the analysis of the individual sources, we give a summary of our findings and comment on general trends and the possibility of applying these results to other sources.

The initial phase of this project consisted of obtaining the line surveys in their final form, and included making the observations, using CLEANSB to separate the sidebands, and identifying the observed

lines. In some cases, the observations do not permit the sideband separation to be performed, generally in cases where no confusion or line blending resulted from the DSB observations and the sideband separation was not warranted. From the observed spectrum, we are able to derive an average line flux value by summing the intensities of the observed lines and averaging over the actual frequency range covered. For the complete surveys of Orion-KL and IRC +10216, this number provides a reasonable estimate of the line flux in the 330 – 360 GHz atmospheric window. For the other surveys with less complete frequency coverage, we generally chose to observe those frequencies where the strongest lines would be expected to occur. This initial value of the average line flux is therefore likely to be an overestimate of the average value for the entire window. We may obtain a lower limit by averaging our total observed line flux over the entire window. The two values thus obtained differ by a factor of approximately 2 to 3 for the cases with the least frequency coverage; these turn out to be the cases where the contribution of the line flux is least significant.

After determining the flux contribution from detected lines, we next estimate the contribution from lines which are too weak to be detected by our surveys. Despite their low intensity, these lines may contribute a significant amount of integrated flux when summed together. Following SBMP we model the distribution of line intensities with a power-law fit, and extrapolate the observed distribution to lower intensities. To derive the power-law fit, we use the integrated line intensities W and plot the total number of observed lines having at least the given intensity versus the intensity value. Letting this quantity be $N_>(W)$, we note that it is simply the integral of the number density of lines at a given intensity $n_{lines}(W)$

$$N_>(W) = \int_W^\infty n_{lines}(W')\, dW'. \tag{5.1}$$

For an assumed power-law distribution with $N_>(W) = aW^b$, we must have $n_{lines}(W) = -baW^{b-1}$ (we will assume $b < 0$ in order to have more weak lines than strong lines). In their fit to the line intensity distribution for Orion-KL, SBMP used the line density per logarithmic interval. Letting their density be $\tilde{n}_{lines}$, we find that $\tilde{n}_{lines} \propto W n_{lines}(W) \propto W^b$, so that the power-law index b we derive is directly comparable to theirs. If our derived distribution holds for all intensities, we may determine the flux contributed by lines weaker

than a given intensity $F_<(W)$ as

$$F_<(W) = \int_0^W W' n_{lines}(W')\, dW' = -\frac{baW^{b+1}}{b+1}\,. \tag{5.2}$$

We may use this expression to estimate the required correction to the observed line flux to account for undetected weak lines. We typically observe a roll-off in the observed line distribution, suggesting a possible undercounting of lines at the lowest detected intensities. We may determine a value W_{min} such that we believe that all of the lines with integrated intensities greater than W_{min} are detected. From (5.2) we may then obtain the total line flux for intensities between W_{min} and the maximum observed intensity W_{max} as

$$F_<(W_{max}) - F_<(W_{min}) = -\frac{ba}{b+1}(W_{max}^{b+1} - W_{min}^{b+1}) \tag{5.3}$$

which will be approximately equal to the total observed line flux depending upon the degree to which the fit corresponds to the actual line distribution and the severity of the undercounting of weak lines. (The total observed line flux may be corrected to include only the flux from lines within the same intensity limits W_{min} to W_{max} if desired for the comparison.) The ratio

$$\frac{F_<(W_{min})}{F_<(W_{max}) - F_<(W_{min})} = \frac{1}{\left(\frac{W_{max}}{W_{min}}\right)^{b+1} - 1} \tag{5.4}$$

gives the fractional amount which should be added to the flux within the limits as a correction for undetected weak lines. As weaker lines are detected, W_{max}/W_{min} increases and the fractional correction will be reduced; as the steepness of the slope increases, b becomes more negative, approaching -1, and the fractional correction increases, becoming infinite for the case $b = -1$. Indeed, any value of b less than -1 would yield an infinite flux contribution from weaker lines when integrated to zero intensity and thus cannot be extrapolated indefinitely.

There is some correlation between the slope of the line intensity distribution and the types of species responsible for the bulk of the line emission. Simple linear rotors possess fewer total lines and will tend to produce less steep distributions when compared with symmetric or asymmetric tops. While the actual slope found in a given source will depend on the excitation and the amounts of the specific molecules which are present, we may be able to obtain a rough estimate for the slope which we expect for a particular

type of source with a given chemistry based upon the slopes found in extensive line surveys. This estimate can then be used to estimate the total line flux based upon observations of only a few of the strongest lines, when a fit to the line distribution is not possible.

We have chosen to use the integrated intensities W for our fit as these provide a more direct means of estimating the line flux from weak lines than using the line intensity alone and reduces the dependence of the estimate on any assumed line profiles. (Note that a line with a Lorentzian profile has an integrated intensity $\sim$ 50% greater than a Gaussian line having the same intensity and the same width at half the maximum intensity.) Provided the integrated intensities used in the fit accurately reflect the actual flux from the observed lines, the estimated flux derived from such a fit is independent of the line profiles. The power-law fits for the different sources are performed as linear fits using the logarithms of $N_{>,obs}(W)$ and W and displayed in the following sections. As there are more weak lines, an unweighted fit is dominated by the points at lower intensities. We have experimented with different weighting functions, finding only slight variations in the resulting fits when a sufficient number of lines were observed as in the larger surveys. For the less complete surveys where fewer lines were observed, the fits were poorly constrained yielding rather uncertain estimates for the flux contribution from weak lines. We have specified the integrated intensity W in units of K MHz for the purposes of evaluating the line distribution; these are the units most directly related to the contribution of the lines to the total flux. However, there is no significant difference between the current results and fits and estimates obtained using units of K km s^{-1}.

Finally, we use simulations to extend our comparison of the line flux and the total flux to additional frequencies outside the range of our data. Our observations were all made in the frequency range between 325 and 360 GHz, and hence provide information on the integrated line flux only in that range. For Orion, we may refer to the previous findings of SBMP concerning the line flux between 230 and 260 GHz. Some additional information is available for the remaining sources, particularly the results of previous line surveys of IRC +10216, but this information is limited to lower frequencies. We have therefore used the capability of the SIMCAT program, described in the previous chapter, to simulate the emission line spectra for the various sources at frequencies up to 1000 GHz. These simulations are done using column densities and excitation temperatures for the molecular species determined from our surveys and other data as indicated in

the discussions of the individual sources below. The simulated spectra are first generated with a resolution of 1 MHz and then smoothed by convolution with Gaussians of different widths in order to obtain the contribution resulting from line emission in broadband measurements. We have also performed simulations to evaluate the combined temperature and frequency dependence of the line emission as described in §4.9.

5.3. Estimation of Errors in the Flux Comparisons

As described in the previous section, we determine the contribution of line flux to the total observed flux, with our line surveys providing the measurements of the line flux. For the two Orion sources, we also determine the continuum flux from our observations, taking the total flux to be the sum of the measured line and continuum fluxes. We use the broadband measurements of Sandell (1994) to obtain the total flux for the remaining sources. The dominant source of uncertainty in the derived ratio of the emission line flux to the total flux varies by source depending on the frequency range observed and how the value for the total flux was obtained. We first consider general issues of calibration and uncertainty in our flux comparisons, afterward discussing specifics associated with individual sources, particularly Orion-KL and Orion-S.

In most cases, we simply compute the ratio of two numbers (the line flux and the total flux) which have uncorrelated errors. If the errors are statistical in nature, a simple consideration of error propagation shows that the uncertainty in the derived ratio satisfies

$$\frac{\sigma_R^2}{R^2} = \frac{\sigma_L^2}{L^2} + \frac{\sigma_F^2}{F^2}, \tag{5.5}$$

where $R = L/F$ is the computed ratio of the line flux L and the total flux F, and R, L, and F have the associated uncertainties σ_R, σ_L, and σ_F, respectively. The total flux values reported by Sandell which we use for our comparisons have typical statistical uncertainties quoted of ~5% (the precise values for each source are given in the individual sections below), not including an additional ~5% which should be added to the total error estimates resulting from the uncertainty in the absolute flux densities of the planets used for calibration. The total uncertainty in our flux calibration is estimated to be 20%, resulting from a combination of possible errors in the chopper wheel calibration, gain ratios, pointing, etc. Observations of the same lines at different epochs showed variations of less than this value; since the strongest lines which

determine to a large degree the line flux value were generally observed multiple times, allowing more precise determinations of their integrated flux, we are confident that this is a reasonably accurate estimate of the statistical uncertainty in our measured line flux values. Using (5.5) with these values ($\sigma_F/F = 0.10$ and $\sigma_L/L = 0.20$) yields a relative uncertainty for the derived ratios of $\sigma_R/R = 0.22$. However, we find that other, non-statistical, effects can lead to significantly larger uncertainties in our values.

Perhaps the most obvious example of a non-statistical effect results from the incompleteness of some of the line surveys. As discussed above, in these cases we assign upper and lower limits to the ratio of the line flux to the total flux. These limits differ by as much as a factor of 3 for the surveys of VY CMa and OH 231.8+4.2, with the limit values retaining the inherent ~20% calibration uncertainties as well. A related effect results from the disparity between the specific frequency range included in the line measurements (with equal sensitivity at all frequencies) and the specific frequency response of any broadband measurements used for comparison. Unfortunately, this effect is greatest when it is of most interest, *i.e.*, when the contribution of the lines is largest, as the emission from a smooth continuum source can easily be modeled. A sophisticated estimate of the magnitude of the resulting uncertainty would require a knowledge of the broadband frequency response function in order to appropriately scale an estimated or measured emission line spectrum. Alternatively, an estimate can be made of the uncertainty in a determination of the broadband flux that would be measured by an instrument having the same responsivity function as the line survey measurements. We use this latter method, considering the apparent variation in the broadband fluxes when compared to smooth continuum emission, and conclude that the additional uncertainty in the broadband values used for comparison is likely to be 5–10% in most cases, making the total statistical uncertainty approximately 25%. This value is likely to be larger for IRC +10216 because of the large line contribution to the total flux and the sharp variation in the line flux resulting from the few very strong lines. However, the existence of an independent narrowband measurement of the continuum flux allows a separate comparison between the line flux and the total flux (*cf.* the discussion in §5.7 below and the spectrum shown in Appendix C).

Our directly observed line flux serves as a lower limit to the actual line flux (again with the same overall calibration uncertainties). We estimate the amount of flux contributed by undetected weak

lines using the power-law extrapolation described previously. This method represents a purely empirical approach with large uncertainties; the most that can be stated unequivocally is that, again subject to calibration uncertainties, the flux from weak lines lies somewhere between zero and an amount sufficient that line emission would account for all of the flux observed from the source. The line intensity distributions we derive have fairly similar slopes, with fairly small formal statistical errors, which may suggest that our estimates are at least resonable. However, lacking *a priori* knowledge of the true line intensity distribution, we are unable to place hard limits on or even make accurate error estimates of the flux contained in undetected lines.

We again note that our extrapolation method makes use of the integrated line intensities observed rather than the peak line intensity, and thus does not depend on the assumption of a particular line profile or width. Of course, it does depend on the specific baseline or reference levels used to determine the actual integrated intensities. For the Orion-KL spectra, the large line density meant that the true baseline level was often obscured (*cf.* Figure 5.1 below), even to the extent that one could not rule out the possibility that the apparent underlying continuum emisison was in fact simply the result of the overlapping emission of numerous lines. In the other sources surveyed, the narrower lines and lower line densities allowed the baselines to be more readily determined, also making it appear unlikely that line emission could be responsible for apparent continuum emission. Particularly for Orion-S, where we observed a significant continuum offset together with rather widely separated molecular lines, the appearance of the spectrum seems incompatible with extended wings of the line emission being responsible for the smooth offset. This in turn suggests that for Orion-KL there is also true continuum emission at some level, albeit a level which is difficult to determine precisely. In our determination of the baselines for the Orion-KL spectra, we were conservative in assigning flux to the emission lines, *i.e.*, we selected the highest continuum offset level consistent with the data. The line flux value therefore represents a lower limit to the true line flux, as it is possible that some of the continuum offset is in fact the result of the overlapping line emission.

For both of the Orion sources, we directly compare the line flux we measure with the total flux we measure, thereby eliminating uncertainties associated with the relative calibration between different telescopes and observations, differences in pointing, or different frequency sensitivities. Indeed, this

method allows us to directly measure the quantity of interest, namely the ratio of the line flux to the total flux. Of course, the measurement gives direct information about this ratio only over the frequency range observed and for the particular beamsize used, but those limitations would also apply for other less direct comparisons. Because of the difficulty in determining the baseline level, and the fact that our observation techniques are not optimized for continuum emission, we estimate an uncertainty of 15% in the overall determination of the relative contribution of the line flux to the total flux for both Orion sources. In addition, particularly for Orion-KL, the value found should be regarded as a lower limit, as noted above.

In summary, then, the ratios of line flux to total flux determined from our measurements have various uncertainties associated with them. Possible calibration errors and comparison with uncertain broadband values lead to estimated uncertainties of 15% for the Orion sources and 25% for the other sources. However, larger uncertainties are associated with the incomplete frequency coverage, which we treat by assigning upper and lower limits for the line flux contribution, and with the unknown emission from weak lines, which we estimate by extrapolation of the line intensity distribution. The overall result is that we are able to determine lower limits with uncertainties associated with calibration errors; we can estimate the unknown emission from weak lines and in unobserved frequency regions, but cannot assign truly firm upper limits. Additional information specific to the individual sources may be found in the sections below.

5.4. Orion-KL Results

A. Source Description

The Orion-KL region is located within the much larger Orion molecular cloud complex which is the subject of a recent review by Genzel & Stutzki (1989). As the nearest cloud (at a distance of about 450 pc) showing recent and ongoing high-mass star formation, the Orion molecular cloud offers unique opportunities for investigating interstellar matter and star formation and has been extensively studied. Extended molecular emission has been found in two large clouds, Orion A and B, that each extend over several degrees on the sky. The brightest source at 2 μm within the cloud is the Becklin-Neugebauer object (BN), discovered in 1967 (Becklin & Neugebauer 1967), while a more extended bright infrared nebula (Orion-KL) was discovered in that same year by Kleinmann & Low (1967) about 10″ south of BN.

Subsequent infrared observations, beginning with those of Rieke, Low, & Kleinmann (1973), have detected a number of compact sources within the region around BN and Orion-KL, which is known as the BN-KL region or OMC-1; the most luminous of these sources are BN and the additional infrared source IRc2 which is located at the center of Orion-KL. At millimeter and submillimeter wavelengths, the brightest gas and dust emission is roughly centered on IRc2. Single-dish mapping at 400 μm with a 35″ beam (Keene, Hildebrand, & Whitcomb 1982) resolve the continuum emission into two peaks, one coincident with IRc2 and the other approximately 90″ south of IRc2, corresponding to Orion-S (*cf.* the discussion below). A quite similar structure is observed for NH_3 by Batrla *et al.* (1983). Interferometer observations by Mundy *et al.* (1986) further resolve the emission into several discrete regions of ~10″ size, both for continuum and CS line emission. Higher resolution single-dish continuum maps at 1.3 mm (Mezger, Wink, & Zylka 1990) also detect individual condensations within OMC-1; when the observations are smoothed to a resolution of 21″, the resulting emission again shows similar peaks at Orion-KL and Orion-S.

Our single-dish observations for the Orion-KL spectral line survey were centered on a nominal source position of $\alpha(1950) = 05^h32^m47^s$, $\delta(1950) = -05°24'21''$ chosen to coincide with the earlier survey carried out at OVRO by Sutton *et al.* (1985) and Blake *et al.* (1986). A source velocity of $v_{LSR} = 9\,\mathrm{km\ s^{-1}}$ was used while making the observations and to establish the rest frequency scale. Because of the large amount of time required for the observations even for a single position, no mapping was performed. However, as was the case for the OVRO survey, emission from individual subsources may be distinguished in the data by their characteristic line profiles. We follow Blake *et al.* (1987) in identifying the different subsources as the "hot core," the "plateau," the "extended ridge," and the "compact ridge," and adopt their derived parameters for the different emission components for simulations as will be shown below. We briefly mention some of the distinctions between the components here; for the simulated spectra considered below we treat each subsource separately. The extended ridge gas consists of the quiescent clouds near Orion-KL, running roughly SW to NE, and displays rather narrow line emission ($\Delta v \sim 4\,\mathrm{km\ s^{-1}}$). Analysis of the line emission yields rotation temperatures of ~60 K and densities of $\sim 10^5\ \mathrm{cm^{-3}}$ for the gas in the extended ridge. The compact ridge source is located ~10″ SW of IRc2, again exhibits rather narrow line emission ($\Delta v \sim$ 3-5 $\mathrm{km\ s^{-1}}$), but appears significantly warmer and denser than the extended ridge with the emission

arising from a more spatially compact region. There is also a chemical differentiation between the extended ridge, which shows mainly emission from simple molecules (diatomics and triatomics) and the compact ridge, which exhibits significant emission from complicated oxygen-rich molecules (*e.g.*, HCOOH, CH_3OH, $HCOOCH_3$, and CH_3OCH_3). These differences are suggestive of an interaction between the plateau gas outflowing from IRc2 and the quiescent cloud in which the compact ridge gas is compressed and heated, with its chemical composition changing as well (*cf.* Johansson *et al.* 1984 and Irvine & Hjalmarson 1984). The plateau gas is characterized by substantially greater line widths ($\Delta v \gtrsim 20 - 25\,\mathrm{km\ s^{-1}}$) than the ridge gas, with densities $\sim 10^6$ $\mathrm{cm^{-3}}$ and temperatures of ~95-150 K. A variety of molecules are observed to exhibit emission from the plateau source, with emission thought to arise from small dense clumps of matter embedded in the outflow as well as from the boundaries of the cavity where the outflow is decelerated by the surrounding dense molecular cloud. Finally, the hot core itself is a very compact region located immediately adjacent to IRc2 which exhibits significantly higher temperatures (~150-300 K) and densities ($\sim 10^8$ $\mathrm{cm^{-3}}$), with line widths of $\sim 5 - 10\,\mathrm{km\ s^{-1}}$.

B. Observed Line Flux

The data from the CSO spectral line survey of Orion-KL are presented in Appendix A of this thesis, with a more detailed analysis to be published separately (Schilke *et al.* 1994). In this section we summarize some of the key findings from the survey, particularly those related to evaluating the contribution made by the rich emission line spectrum to broadband flux measurements. Over 200 scans were used in assembling the spectrum for our survey, covering frequencies ranging from 325 to 360 GHz. A total of 801 transitions have been detected in the spectrum. Of these, 617, or 77%, have been identified with 26 distinct chemical species. We were unable to identify any transitions of known species corresponding to the remaining 184 lines. The observed line information is given as a series of tables in Appendix A, showing the intensities as well as the frequencies and the identified species for the detected lines. By far the strongest line is the CO J = 3–2 line located roughly at the center of the spectral scan, for which the brightness temperature is nearly three times greater and the integrated intensity nearly four times greater than that observed for any other line. However, the numerous strong and broad lines of SO_2 scattered throughout the survey when summed

TABLE 5.1

SIGNIFICANT FLUX CONTRIBUTIONS BY SPECIES FOR ORION-KL

Species [a]	N_{lines}	$\int T_{MB}\, d\nu$ (K MHz)	Relative Contribution (% of Total Line Flux)
SO_2†	71	10396.8	28.2
SO_2	37	9623.1	26.1
CO†	4	5392.6	14.6
CO	1	4884.7	13.3
SO†	14	4813.7	13.1
SO	6	3920.5	10.6
CH_3OH†	106	4196.5	11.4
CH_3OH	75	4029.9	10.9
HCN†	4	2492.8	6.8
HCN	1	1578.9	4.3
$HCOOCH_3$	211	1446.5	3.9
SiO†	3	911.4	2.5
CH_3CN†	35	898.5	2.4
HCO^+ †	3	771.2	2.1
CS†	3	535.7	1.5
CH_3OCH_3	82	406.9	1.1
U-lines	184	1625.2	4.4

[a] Values for species marked with a † also include the contributions of all transitions detected from isotopomers and vibrationally excited states. In some cases entries are made separately for the main species and for all of the variants together, *e.g.*, SO_2† and SO_2 are both shown.

contribute a total integrated intensity approximately twice as great and represent the largest fraction of the integrated line flux attributed to a single species. The species for which the greatest numbers of lines were detected include CH_3OH, CH_3OCH_3, and $HCOOCH_3$ (many of these lines are blended transitions). Of these, only CH_3OH has a sufficient number of bright lines to contribute a significant fraction of the total line flux (the emission for these asymmetric rotors arises mainly from the compact ridge and hence the lines are rather narrow). Other species which contribute significant fractions of the total line flux include SO, HCN, and CH_3OH. Table 5.1 shows the number of lines detected and the contribution to the integrated line flux for the most important species in the CSO line survey of Orion-KL.

For Orion-KL and Orion-S we were able to directly compare the integrated line emission with the continuum emission detected in our observations. Because of the strong level of continuum emission, the original DSB spectra of Orion contained both emission lines and a non-zero baseline offset as in Figure 5.1. Before the CLEANSB program was used, the baseline was subtracted, leaving only the emission lines. The actual baseline subtracted was determined by fitting a low-order polynomial to sections of the spectrum

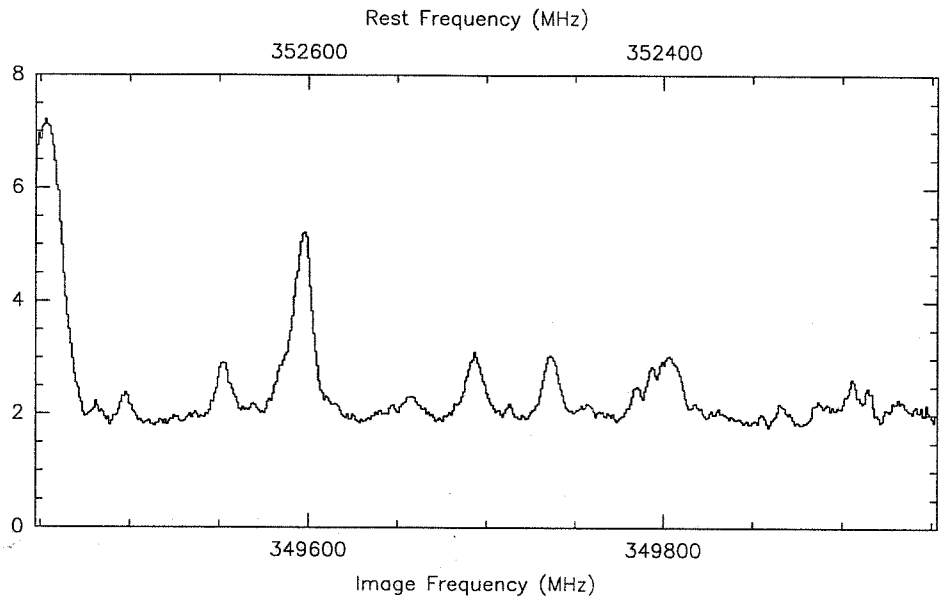

Figure 5.1 DSB observation of Orion-KL showing a typical baseline offset caused by the underlying continuum emission. Despite the comparatively weak line emission in this scan as compared with most of the Orion-KL data, the determination of the actual baseline level is still made difficult by the large line density. The temperature scale shown is appropriate for line emission in a single sideband, while the continuum emission is present in both sidebands. The baseline offset of $\sim$2 K therefore corresponds to a value of $\sim$1 K in each sideband.

where line emission was not seen. For much of the Orion data, the line density was sufficiently great that it became difficult to determine the correct baseline to subtract. Typically the DSB spectra contained only very few sections obviously free of line emission, and these were generally too narrow to clearly indicate the shape of the baseline. We therefore subtracted only flat baselines from the spectra unless there was a clear trend in the data, using the minima between lines to estimate the continuum level when no line-free sections were found.

For each scan, we have determined the apparent continuum level by taking the average value of the subtracted baseline. Combining the results from all of the scans yields a measurement of the true continuum, free from significant line emission. As noted by SBMP, using the same observations to determine both the line and continuum flux is the preferred method of comparing the two, as this eliminates the complications which arise when trying to compare data between different telescopes. This allows a direct measurement

of the quantity of interest, that is, the relative amount contributed by the integrated line emission to the total flux observed.

In the frequency range of our survey, the resulting value for the continuum emission is 1.1 K on the uncorrected T_A^* scale. The integrated line flux, when averaged over the range of frequencies observed, is very nearly as great, with a value of 1.0 K. We estimate the uncertainty in the continuum value to be 15% in addition to the overall calibration uncertainty of 20%, largely the result of the difficulty in accurately determining the appropriate baselines. Since the positioning of the baselines also determines the line intensities, a similar uncertainty applies to the observed line flux. The integrated line flux therefore represents 48% of the total flux that would be observed with a broadband detector covering the range of our survey. This is, in fact, a lower limit to the line contribution since it is based only on lines detected in the survey and does not include contributions from undetected weak lines. In addition, we were conservative in our fitting of baselines in the scans where the continuum level was obscured by line emission so the actual line intensities may have been somewhat higher. Since the data cover the entire frequency range from 325 to 360 GHz, no corrections are required to obtain the average line flux as they are for the other surveys which have incomplete frequency coverage. Thus one half of the total flux measured for Orion-KL in this frequency range is the result of observed molecular transitions. This is similar to, although somewhat greater than, the 30-40% attributed to observed lines in the 230 GHz region by SBMP.

C. Extrapolation for Weak Lines

In Figure 5.2 we plot the distribution of the observed lines as a function of the integrated intensity. At the highest intensities, the shape of the distribution is dominated by the individual line intensities because of the low number of lines; at the lowest intensities, the distribution appears to roll over, most probably because numerous weak lines at these intensities are simply not detected or recognized in the survey. Also shown in the figure is a fit derived over the intermediate range of intensities 10 K MHz $< W <$ 250 K MHz which includes over 400 lines. The fit to the observed distribution yields a power-law index of $b = -0.84$ and would require the line flux to be increased by 30–40% to account for the undetected weak lines, resulting in a line flux contribution of some 60-70% of the total flux observed. The power-law index

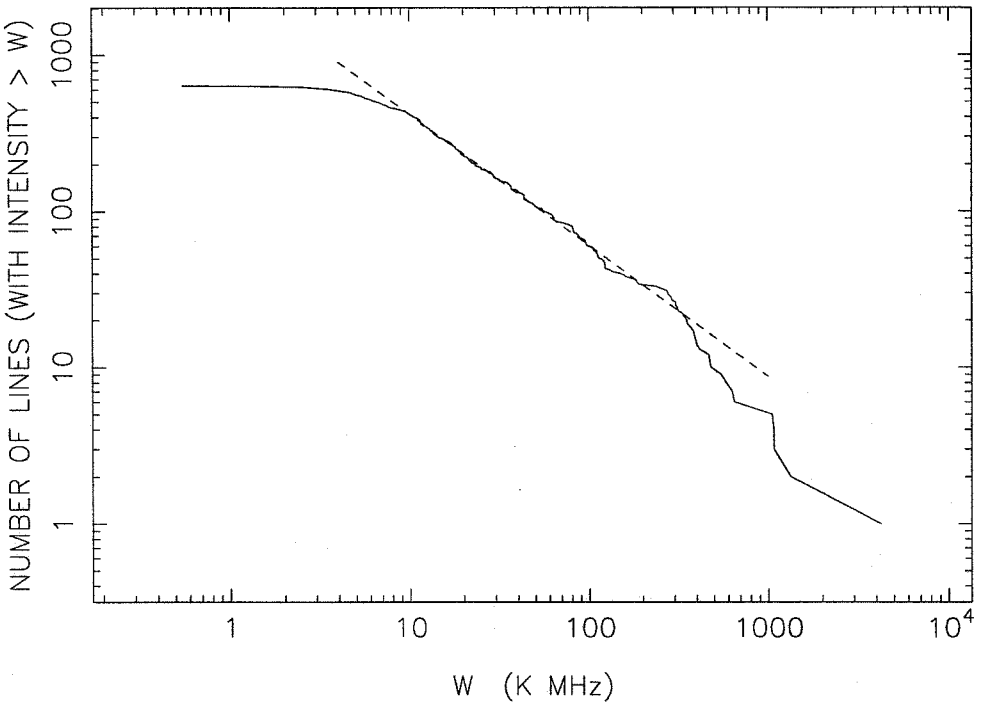

Figure 5.2 Distribution of observed integrated line intensities from the Orion-KL line survey. A power-law fit is shown with a slope of −0.84 as discussed in the text.

we derive is similar to that found by SBMP (−0.8) using a process of counting lines per logarithmic interval. Their distribution was derived for line brightness, however, rather than integrated intensity, so that the correction for undetected weak lines depended upon the assumed line widths. SBMP found that the contribution of the integrated line emission would be increased to 45–60% of the total flux detected when the line distribution was extrapolated in this manner.

D. Comparison with Additional Flux Measurements

The above comparison between the observed line and continuum flux values is made directly between values derived from the same set of observations, thereby eliminating the uncertainties of accounting for different efficiencies, beam sizes, etc. which arise for comparisons between different data sets. However, to obtain a more complete picture of the line contribution to the flux, we wish to compare our derived flux values with other published results.

We have already mentioned, of course, the line and continuum flux comparison of SBMP, who

derive from their data a total flux of 86 Jy at a wavelength of 1.3 mm (and a line flux of 25 Jy). They also derive a fit to the total flux in a 0′.6 beam using a 400 μm measurement (1500 Jy) from Keene *et al.* (1982) and 1 mm data (128 Jy after correction for a different beam size) from Elias *et al.* (1978). From this fit they obtain a frequency dependence for the total flux of $\nu^{2.7}$. Greaves & White (1991, hereafter GW) note that this fit agrees well with more recent measurements at shorter wavelengths with higher spatial resolution: 66.7 Jy at 1.3 mm with 21″ resolution (Mezger *et al.* 1990) and 243 Jy at 800 μm with 15″ resolution (value from White *et al.*, quoted by GW). GW conclude that the total flux over this range shows little variation for beamsizes between 15″ and 30″, with the original fit of SBMP providing a useful estimate of the total flux at these wavelengths. While the above value from Mezger *et al.* is taken from their uncorrected mapping data, they suggest that their broadband data includes a contribution from molecular lines amounting to some 40% of the observed flux. Based upon their line survey of Orion-KL from 257 to 273 GHz, GW report a significantly smaller contribution from the lines than either SBMP or Mezger *et al.*, with the integrated line flux representing some 13% of the total flux as estimated from the SBMP fit. However, they note that this estimate is dependent upon the assumed source size for the line emission and becomes 40% for a source size of $\sim$10″. The strong dependence upon source size results from the use of different data sets to determine the line flux and the total flux, making the relative values dependent upon the beam efficiency and coupling to the source.

Our measurements of the total flux agree well with the SBMP fit if we assume the emission region is small compared to the beam. With an aperture efficiency of 40% appropriate for a small source, we obtain a total flux value of 171 Jy, in good agreement with the 186 Jy predicted at 870 μm. It therefore seems likely that the majority of both the line flux and the total flux derives from the central $\lesssim$10″. Mezger *et al.* (1990) model the observed emission from Orion-KL using a 100 K dust envelope some 14″ in size surrounding a hot (200 K) inner core 9″ in size, with the inner core the dominant source of dust emission at submillimeter and millimeter wavelengths. Although mapping data were not obtained during our survey, it was clear from our pointing data that the line emission of several species, such as that of SO_2 and CH_3OH, arose from compact regions. In view of the importance of these species to the total line flux observed, this is consistent with a small effective source size for line emission. The contribution of the integrated line

TABLE 5.2

SIMULATION PARAMETERS FOR ORION-KL BY SUBSOURCE

Species	T_{ex} (K)	N_T (cm^{-2})	ΔV (km s^{-1})	Velocity Profile
		HOT CORE		
CO	200	1.0×10^{19}	10.5	Gaussian
SO	200	1.7×10^{15}	10.9	Gaussian
SO_2	200	2.0×10^{15}	6.9	Gaussian
HDO	164	4.4×10^{15}	9.1	Gaussian
H_2CO	166	2.2×10^{15}	12.7	Gaussian
HNCO	182	4.8×10^{14}	9.1	Gaussian
HCN	200	2.5×10^{16}	12.6	Gaussian
DCN	200	5.9×10^{13}	11.7	Gaussian
HC_3N	312	1.3×10^{14}	10.0	Gaussian
CH_3CN	274	6.5×10^{14}	10.3	Gaussian
C_2H_3CN	154	1.5×10^{14}	8.6	Gaussian
C_2H_5CN	200	8.2×10^{14}	11.4	Gaussian
CH_3OH	200	1.0×10^{17}	10.0	Gaussian
NH_3	200	2.0×10^{17}	10.0	Gaussian
CS	200	1.0×10^{15}	10.0	Gaussian
H_2S	200	5.0×10^{17}	10.0	Gaussian
H_2O	200	1.0×10^{18}	10.0	Gaussian
		PLATEAU		
CO	100	6.5×10^{18}	50	Gaussian
CS	100	1.2×10^{15}	23	Gaussian
OCS	100	2.8×10^{15}	19	Gaussian
SiO	100	1.5×10^{15}	34	Gaussian
SO	100	2.8×10^{16}	28	Gaussian
SO_2	100	2.8×10^{16}	25	Gaussian
HCN	100	1.5×10^{16}	27	Gaussian
HC_3N	100	1.8×10^{14}	29	Gaussian
H_2S	100	5.0×10^{15}	23	Gaussian
HDO	100	9.0×10^{14}	35	Gaussian
H_2CO	100	1.7×10^{15}	42	Gaussian

flux observed by GW would then be similar to the 40–50% level found by SBMP and the present work and in agreement with the preliminary finding by SBMP that data from the 247–263 GHz spectral scan by Blake *et al.* (1986) showed increased line emission relative to the 215–247 GHz data analyzed by SBMP.

E. Simulated Spectra

We also utilize simulated spectra obtained from SIMCAT (*cf.* §4.8) to estimate the significance of the integrated line emission to total broadband flux measurements at other frequencies. We have performed the simulations for the various subsources of Orion-KL separately, using the values from Blake *et al.*

TABLE 5.2 – *Continued*

Species	T_{ex} (K)	N_T (cm^{-2})	ΔV (km s^{-1})	Velocity Profile
		COMPACT RIDGE		
OCS	75	1.0×10^{15}	3.7	Gaussian
HDO	90	1.9×10^{14}	2.0	Gaussian
CH_3CN	101	9.6×10^{13}	4.0	Gaussian
CH_3OH	146	3.5×10^{16}	3.3	Gaussian
H_2CO	90	5.0×10^{15}	3.8	Gaussian
H_2CS	116	4.8×10^{14}	4.1	Gaussian
CH_3OCH_3	63	3.0×10^{15}	3.6	Gaussian
HCOOH	90	1.5×10^{14}	3.9	Gaussian
		EXTENDED RIDGE		
C I	20	7.5×10^{17}	5.0	Gaussian
CO	60	1.5×10^{19}	4.3	Gaussian
CN	60	1.0×10^{15}	4.4	Gaussian
NO	60	1.5×10^{16}	4.0	Gaussian
C_2H	60	1.6×10^{15}	4.0	Gaussian
CH_3C_2H	52	1.0×10^{15}	3.8	Gaussian
NH_3	60	1.5×10^{17}	7.0	Gaussian
CS	20	7.5×10^{14}	4.4	Gaussian
HCO^+	20	7.0×10^{14}	3.6	Gaussian
HCS^+	60	1.6×10^{13}	4.0	Gaussian
HCN	20	1.5×10^{15}	3.5	Gaussian
DCN	20	5.1×10^{12}	3.5	Gaussian
HNC	20	1.6×10^{14}	3.3	Gaussian
DNC	20	2.3×10^{12}	3.3	Gaussian
HC_3N	60	4.0×10^{13}	3.3	Gaussian
C_3H_2	20	2.6×10^{13}	7.0	Gaussian
HNCO	35	6.5×10^{14}	4.3	Gaussian
SO	20	2.8×10^{14}	3.4	Gaussian
HC_5N	20	7.0×10^{12}	4.0	Gaussian

(1987) and van Dishoeck *et al.* (1993). Table 5.2 gives the actual column densities, temperatures, and Gaussian linewidths used in the simulations. In Figure 5.3, we show the resulting spectra after they have been smoothed by convolution with a 100 GHz (FWHM) Gaussian. While the different chemical compositions of the subsources lead to differences between the spectra of the different components, the largest effect appears to reflect their different temperatures. The higher temperature regions (the hot core and the plateau) display significantly brighter emission, particularly at higher frequencies where the cooler components (the compact and extended ridge) do not populate the higher-energy levels involved in many of the transitions. The emission lines from the hot core and especially the plateau also display greater

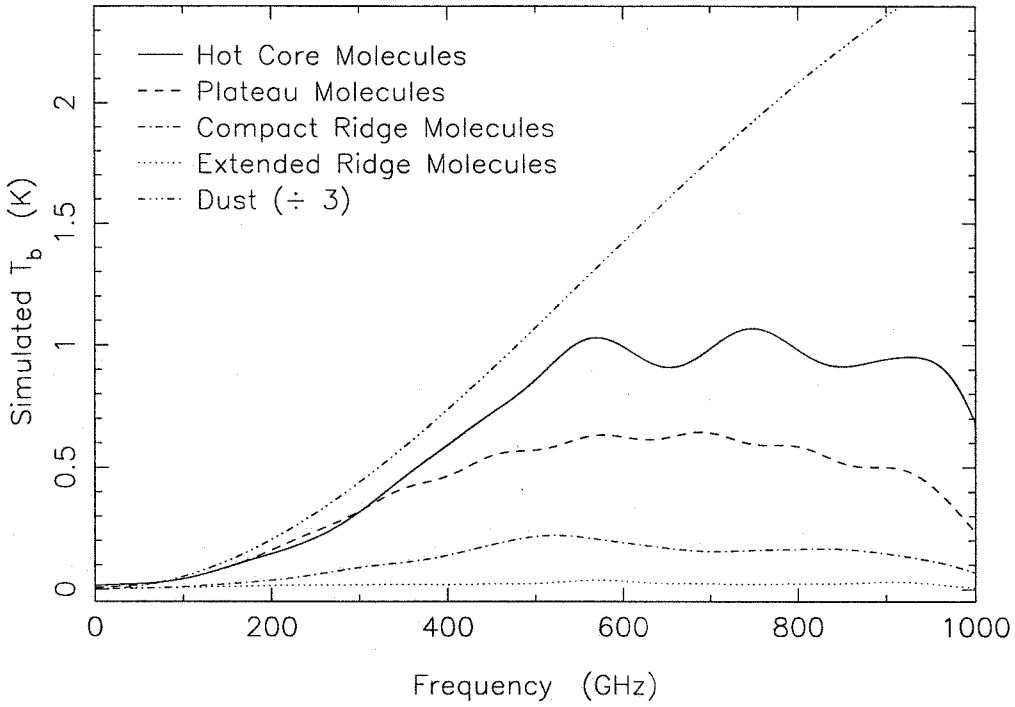

Figure 5.3 Simulated spectra for the different components of Orion-KL, together with a model dust spectrum assuming an emissivity index of 2.0, a temperature of 200 K, and an optical depth of unity at 350 μm. The dust spectrum has been divided by 2 before plotting to facilitate comparison with the molecular emission. Details of the simulations are given in the text.

linewidths; for optically thick lines, this results in greater integrated intensities in the lines. A simple model for dust emission using an emissivity index of 2.0, an optical depth of unity at 350 μm, and a temperature of 200 K is also shown in Figure 5.3. The parameters for the dust model are adopted from Mezger *et al.* (1990), who discuss briefly the problem of the sensitivity of broadband measurements to molecular line emission. While they do not give specific details of their analysis, they estimate a correction for integrated line emission at 1.3 mm of ~40% for the Orion-KL region (their FIR 1 region), citing SBMP and also their own preliminary investigations. The absolute scaling of the simulated dust spectrum is determined from our observed continuum value of 1.8 K (after correction for η_{MB}) at 350 GHz.

The simulated dust emission has been divided by a factor of 3 before plotting in order to facilitate comparison with the smoothed molecular emission spectra. While simply adding together the spectra for the different components may not be appropriate, the figure suggests that the combined molecular emission

would produce a line flux comparable to the continuum flux over a large range of frequencies. The results shown previously in Table 5.1, where the bulk of the observed line flux is carried in lines of a relatively few species, suggest that simulations such as these may give reasonably accurate estimates of the line flux and its variation with frequency, since weaker and unidentified lines are responsible for a small percentage of the total line flux.

The apparent decrease in line emission near 1000 GHz results from the convolution process; the original simulated spectra cut off sharply at 1000 GHz because the online data for SIMCAT extend only that far. Nevertheless, the spectrum for each of the subsources has flattened out or indeed started to decrease at frequencies above the 700–800 GHz range. By contrast, the dust emission shown in Figure 5.3 rises dramatically until the optical depth approaches unity and continues to increase even beyond that point. The clear implication of these results is that molecular line emission will make less of a contribution to the total observed flux for observations at frequencies above ~700 GHz. As noted in Chapter 2, LTE analysis tends to overestimate the populations of high energy levels by assuming that all levels are fully populated as implied by the excitation temperature. In turn this may lead to an overestimate of the line emission in transitions from these high energy levels, which generally correspond to higher frequency lines. Hence, the use of LTE assumptions for the simulations is likely to yield a spectrum which is too bright at higher frequencies rather than too weak. It therefore appears likely that more accurate estimates of the emission spectrum would support the above conclusion that at frequencies above ~700 GHz the total flux is dominated by the continuum dust emission, with molecular line emission contributing a diminishing amount as the frequency continues to increase. The line emission appears to make the most significant contribution to the total flux between 300 and 500 GHz, which is consistent with the somewhat higher percentage contribution found in the present survey relative to the OVRO survey. In particular, the near confluence of the strong emission lines from CO, HCN, and SO_2 which are seen in our survey leads to a peak in the simulated emission line spectra near 350 GHz when the smoothing is done using a narrower convolving function.

We also show comparisons of the above dust model with the simulated spectra for the hot core and the plateau sources separately in Figure 5.4. The simulated molecular spectrum in each case has been

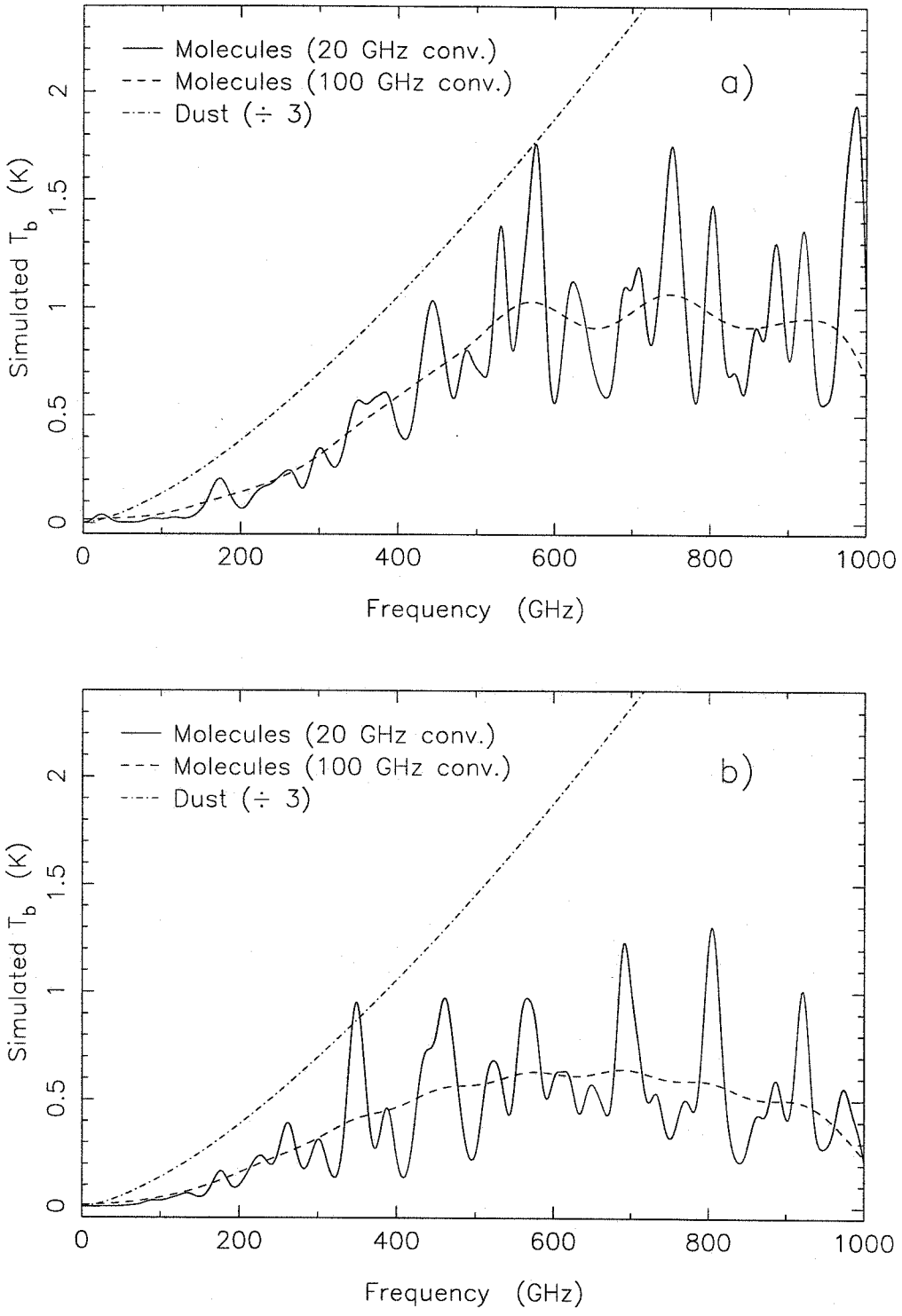

Figure 5.4 Simulated molecular emission spectrum for *(a)* the Orion-KL hot core and *(b)* the Orion-KL plateau compared with a model dust spectrum as before. The line emission has been convolved with a 20 GHz Gaussian and with a 100 GHz Gaussian before plotting.

convolved with a 20 GHz Gaussian and with a 100 GHz Gaussian (recall that the spectra are first generated with 1 MHz resolution). When convolved with the narrower Gaussian, the spectra show a significant amount of structure, evidence of the underlying narrow lines which are the source of the integrated line flux. The differences between the spectra of the two components reflect the differences in excitation temperature and chemical abundances used for the simulations. The largest peaks in the plateau spectrum may be ascribed to the various CO lines throughout the range, while some of the additional large peaks seen for the hot core arise from bands of CH_3OH, for instance. The structure seen in the simulated spectra when smoothed to resolutions of $\sim$20 GHz is indicative of the potential for variation in the ratio of the integrated line emission to the continuum flux depending upon the actual frequency response of an observing system. In light of this variation, we note that the spectral passband for the data of Keene *et al.* extended from 300 to 800 μm, with the atmospheric transmission determining the spectral response between these two limits. They identify the 350 and 450 μm atmospheric windows as the predominant sources of the actual detected radiation, with a flux-weighted mean wavelength of $\sim$400 μm derived assuming a spectrum proportional to $\nu B(\nu, T)$. For comparison, the set of filters discussed by Duncan *et al.* (1990) have bandwidths ranging from 30 to 220 GHz, with typical bandwidths of 70 – 110 GHz (flux measurements using the 850 μm filter, with a 30 GHz passband, and the 800 μm filter, with a 101 GHz passband, are used below for comparisons with our observed line emission for IRAS 16293–2422 and the evolved stars).

Of course, our simulation results are based on molecular parameters derived for the most part from observations below 300 GHz and for beam sizes of 20″–30″. Observations at higher frequencies and/or with smaller beams which probe regions with higher excitation temperatures or greater column densities would be expected to yield somewhat different results. To consider the effects of varying excitation temperature, we performed simulations as described in §4.9 for each of the subsources using the same molecular column densities as before. The excitation temperature was set to be the same for all of the species and the simulated spectrum was then generated and smoothed (again by convolution with a 100 GHz Gaussian). This process was repeated for temperatures between 5 and 995 K at intervals of 10 K. In Figure 5.5 we show the resulting flux contours as functions of frequency and temperature for the different subsources. Some features corresponding to strong lines or bands of emission remain visible in

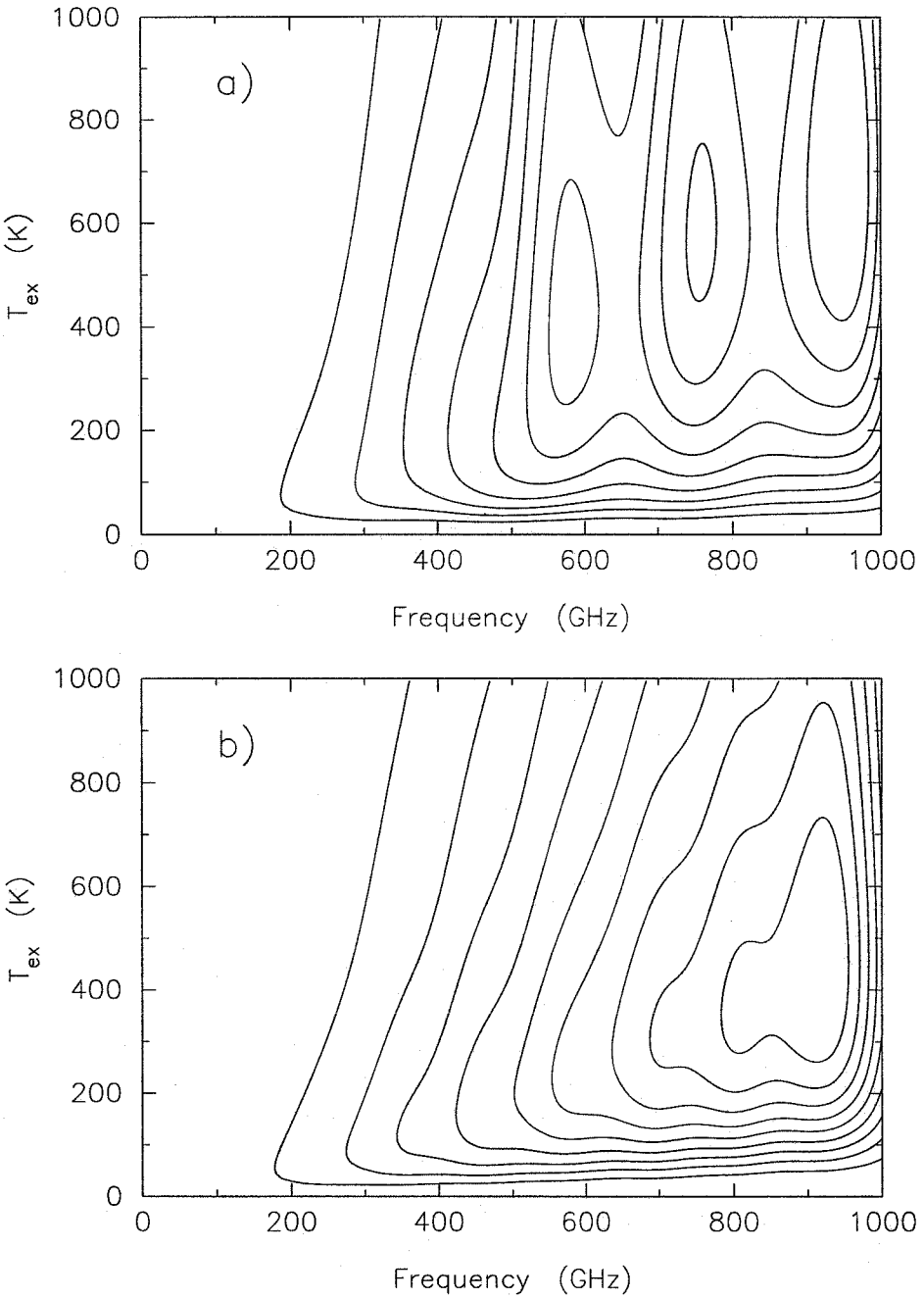

Figure 5.5 Contours of the simulated molecular line emission for *(a)* the Orion-KL hot core and *(b)* the Orion-KL plateau as a function of frequency and excitation temperature. The spectrum is simulated and smoothed by convolution with a 100 GHz Gaussian for a given excitation temperature; the contours represent the brightness temperature of the emission. A cut at the frequency of a given transition would show the line's brightness as a function of excitation temperature, while a cut at a particular temperature value would show the smoothed spectrum obtained for that temperature. Contour lines are at intervals of 15.7 K for *(a)* and 13.8 K for *(b)*, corresponding to 10% of the peak value in each case.

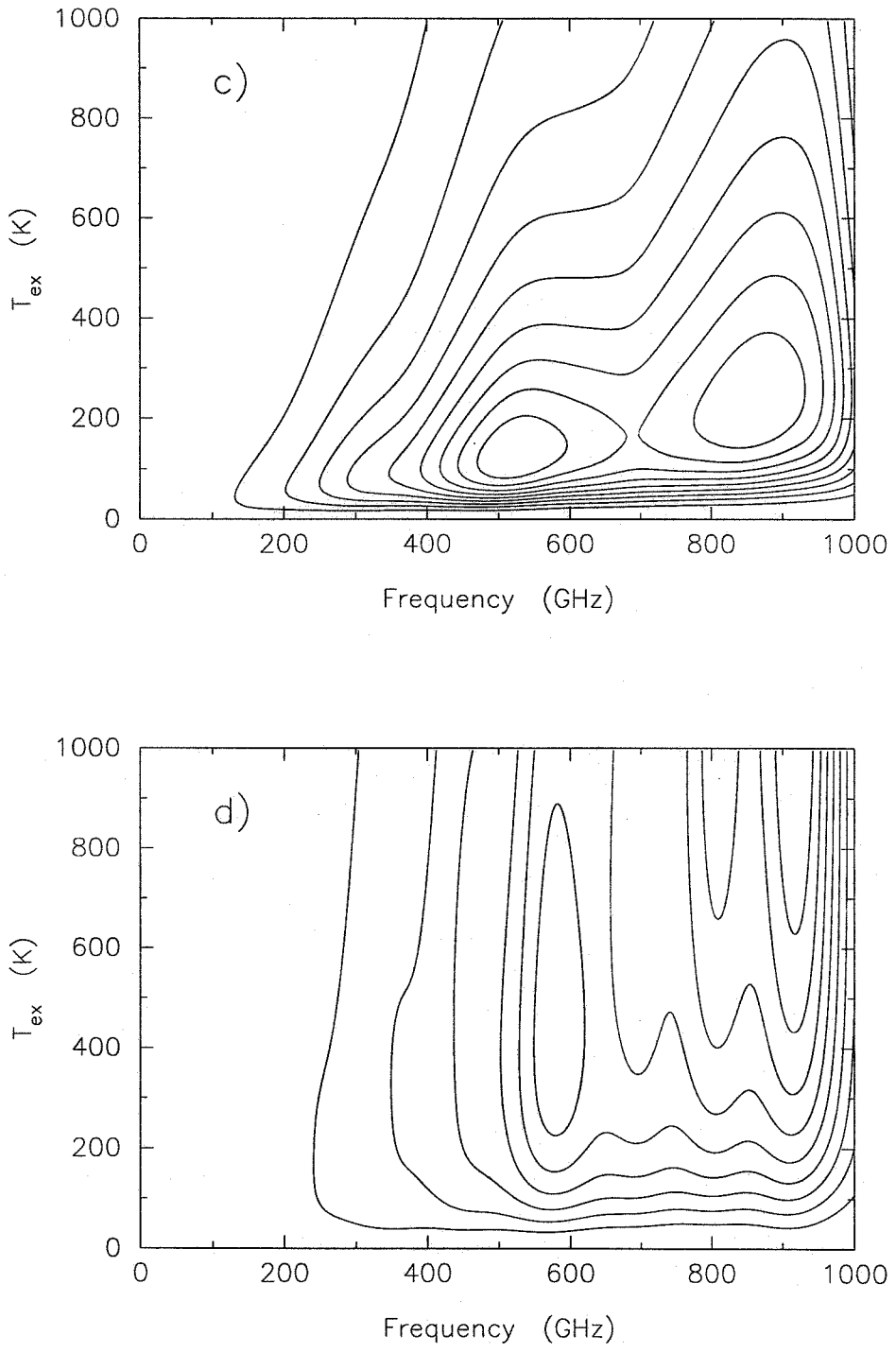

Figure 5.5 – *Continued.* Simulated molecular line emission for *(c)* the Orion-KL compact ridge and *(d)* the Orion-KL extended ridge as before. Contour lines are at intervals of 2.44 K for *(c)* and 2.74 K for *(d)*.

the plots. The smoothed spectrum for a given excitation temperature may be obtained by making a cut in the frequency direction through the surface at that particular temperature. In general the peak flux for a given excitation temperature occurs at higher frequencies as the temperature increases. However, a very substantial increase in temperature above 200 K would be required before the line flux would continue to rise with frequency up to or beyond 1000 GHz. Changes in the observed chemistry would undoubtedly be associated with such a large variation in temperature, so that the use of a constant set of molecular column densities is unrealistic. The results nevertheless suggest that continuum emission will remain the dominant contributor of flux at high frequencies even as hotter gas is probed by new observations. Over smaller temperature ranges, *e.g.*, an increase from 10 K to 100 K, a simple change in temperature has a fairly small effect on the chemistry of the source when compared with such considerations as the presence of outflows and shocks, or the object's evolutionary state (van Dishoeck, 1993). In the remaining sections of this chapter, we include simulations for each of the observed sources over the same range of temperatures, *i.e.*, 5 to 995 K. While the use of a constant set of molecular parameters for the simulations over such an extreme range of temperatures is unrealistic, the results provide useful insight into the effects of varying temperatures on the spectra that are observed. For example, depending upon the amount of smoothing performed, the variation of the integrated intensity of a single line or of a group of lines may be seen. As our interest is in the effects over broad frequency intervals, we present only the smoothed results with some comments on the particular lines or species which may be causing the variation.

F. Summary

The contribution of the integrated line flux to the total observed flux in the CSO spectral line survey of Orion-KL from 325 to 360 GHz was found to be approximately 50%, or slightly greater than the 40% found by SBMP for the OVRO line survey from 215 to 247 GHz. Both of these measurements refer only to detected lines, and are thus lower limits; in addition, the derived values have estimated uncertainties of $\sim$15%. The direct comparison of the observed line and continuum emission as detected by a single set of observations eliminates potential complications related to different beam sizes, pointing, and calibration which can arise when comparing observations between telescopes.

An extrapolation of the observed line intensity distribution in order to account for undetected weak lines suggests that the line emission may be responsible for as much as 60% of the total flux in this work. The observed line distribution, with $N_>(W) \propto W^{-0.84}$, is similar to that found in the earlier lower frequency survey. Our derived total flux value of 171 Jy agrees well with a fit to published measurements of the total flux at other frequencies if we assume that the bulk of the flux arises from a compact region. Simulated spectra computed for the different regions, *i.e.*, the hot core, plateau, compact ridge and extended ridge regions, indicate that the relative contribution of the integrated line emission to the total flux will decrease substantially at frequencies above 700 GHz as the line flux will level off or decrease while the continuum emission will continue to rise steeply. Finally, simulations carried out for different excitation temperatures suggest that this pattern will continue as observations are made at higher frequencies or with smaller beam sizes which probe hotter regions. One important implication of these results is that total flux values at mid- and far-infrared wavelengths ($\lambda < 400\,\mu$m) are likely to reflect the true continuum flux, with no significant contribution from molecular line emission. Hence, such measurements should give an accurate depiction of the frequency dependence of dust emissivity. Unfortunately, it becomes more difficult to extract this information because the Rayleigh-Jeans assumptions may no longer be valid, making the effects of potentially large optical depths and uncertain dust temperatures more important to the overall frequency dependence of the total flux. As was discussed in §2.2, estimates of the emissivity index β derived from a mix of short and long wavelength observations will give values for β which are too low if the long wavelength total flux values include increased flux from emission lines. If we take the contribution of the line emission to be 60% at 870 μm and 10% at 450 μm, the value for β derived from uncorrected flux measurements could be too low by as much as 1.2, although the inclusion of additional points at other wavelengths will tend to reduce that error. The model of Mezger *et al.* (1990) for the continuum emission from Orion-KL utilizes flux values at 1.3 mm which have been corrected for the effects of line flux and incorporates two dust components, with temperatures of 100 K and 200 K, which have significant optical depths at shorter wavelengths. The value of $\beta = 2$ for the dust emissivity index obtained from their model thus appears to have been been derived taking the above concerns into account and is unlikely to be significantly in error.

As described in the remaining sections of this chapter, we find this same pattern of reduced line emission relative to the total flux at shorter wavelengths in all of our sources, although in some cases the significance of the line emission is small even at longer wavelengths. In sources where we find the contribution of the line emission to be significant, this pattern leads to underestimates of β unless corrected flux values are used.

5.5. Orion-S Results

A. Source Description

Located approximately 1.′5 south of Orion-KL is Orion-S, another molecular condensation within OMC-1, which has also been identified by various authors as a separate emission peak and referred to as the southern peak (Keene *et al.* 1982), S6 (Batrla *et al.* 1983), CS3 (Mundy *et al.* 1986), and FIR 4 (Mezger *et al.* 1990). It was first noted as an active star formation region based on observations of NH_3 lines (Ziurys *et al.* 1981) and 400 μm continuum maps (Keene *et al.* 1982). Interferometer maps at 95 GHz reveal a compact ($10'' \times 4''$) emission source (Mundy *et al.* 1986). Observations of SiO emission suggested the presence of a bipolar outflow associated with this source (Ziurys & Friberg 1987). High velocity wings are also seen in the CO J = 7–6 line (Schmid-Burgk *et al.* 1989), while observations of the CO J = 2–1 transition towards Orion-S have demonstrated the highly collimated and extended nature of the bipolar outflow (Schmid-Burgk *et al.* 1990). Recent interferometer maps of several molecular lines have shown that the molecular abundances are somewhat depleted in the compact core of Orion-S (McMullin, Mundy, & Blake 1993). Relative to the fractional abundances found towards the components of Orion-KL, the chemistry in Orion-S appears to resemble most closely that of the quiescent gas in the extended ridge. This has been interpreted to suggest that Orion-S is at an earlier stage of chemical and physical evolution than the condensations in the Orion-KL region and that the Orion-S outflow has not yet had a significant impact on the molecular abundances there (McMullin *et al.* 1993).

Our observations were centered on a nominal source position of $\alpha(1950) = 05^h32^m46.13^s$, $\delta(1950)$ = -05°26′01″ using the same source velocity (v_{LSR} = 9 km s^{-1}) as assumed for Orion-KL. The survey data are shown in reduced SSB form in Appendix A, with tables listing the lines detected and their intensities.

The most striking differences between the spectra of Orion-KL and Orion-S are the reduced number of lines detected, the narrower line widths seen towards Orion-S and the near absence of SO_2 emission towards Orion-S. As discussed below, the integrated line emission and the contribution of the lines to the total flux are therefore greatly reduced relative to the Orion-KL case.

B. Observed Line Flux

The spectrum of Orion-S obtained from the CSO spectral line survey is presented in Appendix A; a more detailed exposition of the survey will be published separately (Groesbeck, Phillips, & Blake 1994b). As was done above for Orion-KL, we summarize here the survey data as it relates to the integrated line flux. A total of 43 scans were combined to yield the final survey spectrum, which partially covers the frequency range from 325 to 360 GHz. Time constraints coupled with the weaker emission from this source made it imperative to select particular frequencies for observation, particularly those at which strong emission and/or particular species were observed towards Orion-KL. Choosing to observe these frequencies had the dual benefits of increasing the likelihood that the majority of the line flux would be included in our observations (for the case where strong emission was also observed towards Orion-S) and of allowing distinguishing characteristics of the two sources to be observed (for the case where strong emission was not detected towards Orion-S). Hence we have particular scans which include frequencies corresponding to the CH_3OH band near 338 GHz and the SO_2 band near 358 GHz, for example. Some 63% of the band between 330 and 360 GHz is included in our final set of combined observations, with the particular scan information given in Appendix A. Appendix A also contains tables showing the particular lines detected in the Orion-S survey and giving transition and intensity information. A total of 78 spectral features, identified with 108 molecular transitions, were detected, with only 2 features remaining unidentified. We believe that more sensitive observations would be likely to detect additional lines, including features which would not be identifiable with known transitions. All of the species for which emission was observed in Orion-S were also seen in Orion-KL.

The lines in Orion-S are generally weaker and much narrower than the corresponding lines in Orion-KL, thus yielding a much reduced integrated line flux. For example, while the CO J = 3–2 line has

TABLE 5.3

SIGNIFICANT FLUX CONTRIBUTIONS BY SPECIES FOR ORION-S

Species [a]	N_{lines}	$\int T_{MB}\, d\nu$ (K MHz)	Relative Contribution (% of Total Line Flux)
CO †	3	1313.2	48.9
CO	1	1148.6	42.8
CH_3OH	27	264.4	9.8
HCO^+ †	2	226.2	8.4
HCN †	3	220.3	8.2
CS †	2	141.9	5.3
CN	10	119.7	4.5
SO †	3	95.0	3.5
H_2CO †	2	91.6	3.4
C_2H	2	88.8	3.3
SO_2	19	44.1	1.6
CH_3OCH_3	24	5.8	0.2
U-lines	2	1.7	0.1

[a] Values for species marked with a † also include the contributions of all transitions detected from isotopomers and vibrationally excited states. For CO, entries are shown both for the main species and for all of the variants together.

a roughly comparable peak temperature (118 K as compared to 144 K), the integrated area is reduced by a factor of 4 (995 K km s^{-1} versus 4178 K km s^{-1}). Even greater reductions occur in the integrated areas of lines from other molecules which exhibited broad emission in Orion-KL, *e.g.*, HCN, CS, SiO, and SO. The near absence of SO_2 emission in Orion-S results in an integrated line flux from this species which is reduced by two orders of magnitude; since SO_2 emission is responsible for ~28% of the integrated line flux in Orion-KL this is of tremendous significance for the total line flux in Orion-S. Table 5.3 shows the contributions of the most significant species to the integrated line flux as seen by our survey.

As was the case for Orion-KL, the survey data permit a direct comparison between the detected line flux and the continuum flux as determined from the average baseline offset. In general, the baselines were somewhat easier to determine for these observations because of the reduced line emission. We deduce an uncorrected continuum emission value of 0.8 K, with the same uncertainty as before (15% in addition to the overall calibration uncertainty estimated at 20%). The average integrated line flux over the range of observed frequencies is found to be 0.11 K, so that the integrated line flux represents 12% of the total flux detected by our observations.

This value may be taken to be an upper limit for the line flux contribution that would be detected

in a complete survey because the observations are chosen to include the regions of strongest line emission. It is therefore unlikely that a continuous survey, including frequency ranges where no strong lines occur, would have the same average line emission. Instead, the line emission would be likely to be reduced when averaged over a broader range of frequencies, although this depends on the particular frequencies included, of course. By comparison, the continuum emission is relatively insensitive to the particular frequencies observed within the fairly limited range of our survey. We may deduce a lower limit by assuming that no additional line flux would be detected in such a survey, simply scaling the observed average line flux by the relative frequency coverage. For the present survey data, this yields a value of 0.07 K for the line flux averaged over the entire 330–360 GHz window, or 8% of the total flux observed. Considering the upper and lower limits thus found, we may conclude that the molecular emission lines contribute ~10% to the total flux for Orion-S at these wavelengths.

As was noted above, this value is greatly reduced when compared to the line flux for Orion-KL because of the narrower, weaker lines and because of the absence or near absence of various species, most notably SO_2. The comparison of line flux and continuum emission has the advantage of being a direct comparison utilizing the same data, and while the frequency coverage of the survey is incomplete, the rather low value for the line flux contribution results is fairly well constrained.

C. Extrapolation for Weak Lines

We again estimate the contribution of undetected lines by extrapolating a power-law fit to the line distribution as a function of the integrated intensity. We plot the observed line distribution in Figure 5.6 together with a fit to the data over the range of 2–100 K MHz (including nearly 50 detected lines) which gives a power-law index of $b = -0.59$. The fit is significantly flatter than our fit to the Orion-KL line distribution, although this may in part reflect a general undercounting of weak lines which might result from the bias of our observations towards strong lines. Extrapolating this flatter distribution would suggest that the observed line flux should be increased by only ~7% to account for undetected lines. Thus our estimate of the line flux contribution would not be significantly changed from the above value of ~10%.

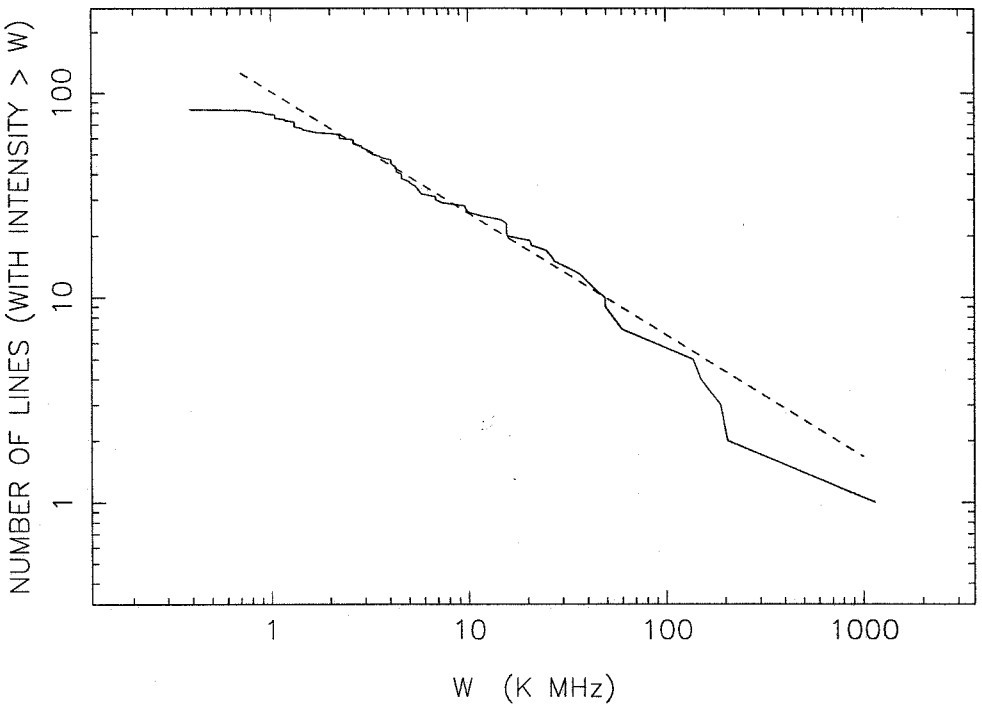

Figure 5.6 Distribution of observed integrated line intensities from the Orion-S line survey. A power-law fit is shown with a slope of −0.59 as discussed in the text.

D. Comparison with Additional Flux Measurements

As part of their single-dish mapping of the OMC-1 region, Mezger *et al.* (1990) have made 1.3 mm observations of Orion-S (FIR 4 in their notation). When their observations are smoothed to 21″ resolution, they obtain a total broadband flux of ∼25 Jy towards Orion-S. The 400 μm observations of Keene *et al.*(1982) give a value of 900 Jy in a 35″ beam. A simple fit to these values yields a spectral index of 3 for the total flux from Orion-S. Additional data is available at 3 mm from interferometer maps by Mundy *et al.* (1986), where the flux from Orion-S (their CS3) is 0.6 Jy for a 10″×4″source size. They estimate that 20%–50% of the dust emission is recovered by the interferometer observations; a total flux of 2 Jy, corresponding to 30% recovery, agrees very well with the simple fit to the 1.3 mm and 400 μm data. From this fit, we obtain an estimated total flux of 83 Jy at 870 μm, which compares well with our total observed flux of 74 Jy (again assuming a small source as for Orion-KL).

As noted before, Mezger *et al.* estimate a correction for integrated line emission at 1.3 mm of ∼40%

TABLE 5.4

SIMULATION PARAMETERS FOR ORION-S

Species	T_{ex} (K)	N_T (cm^{-2})	ΔV (km s^{-1})	Velocity Profile
CO	200	1.5×10^{18}	10.0	Gaussian
^{13}CO	50	1.0×10^{17}	6.0	Gaussian
CS	50	5.0×10^{14}	6.0	Gaussian
SiO	50	1.5×10^{13}	6.0	Gaussian
SO	50	6.5×10^{14}	6.0	Gaussian
^{34}SO	50	5.5×10^{13}	6.0	Gaussian
CN	50	6.0×10^{14}	6.0	Gaussian
NO	50	2.0×10^{15}	6.0	Gaussian
HCN	50	2.0×10^{14}	6.0	Gaussian
$H^{13}CN$	50	2.0×10^{13}	6.0	Gaussian
$HC^{15}N$	50	2.8×10^{12}	6.0	Gaussian
HCO^+	50	2.0×10^{14}	6.0	Gaussian
$H^{13}CO^+$	50	1.3×10^{13}	6.0	Gaussian
HCS^+	50	1.5×10^{13}	6.0	Gaussian
C_2H	50	8.0×10^{14}	6.0	Gaussian
H_2CO	50	4.0×10^{14}	6.0	Gaussian
$H_2{}^{13}CO$	50	1.1×10^{13}	6.0	Gaussian
H_2CS	53	1.5×10^{14}	6.0	Gaussian
CH_3CN	50	2.0×10^{13}	6.0	Gaussian
CH_3OCH_3	48	4.8×10^{14}	6.0	Gaussian
CH_3OH	62	2.3×10^{15}	6.0	Gaussian
SO_2	75	1.9×10^{14}	6.0	Gaussian

for the Orion-KL region (their FIR 1 region). They also estimate a correction of ~30% for the Orion-S region (their FIR 4), noting only that the confusion of line emission with broadband dust emission occurs to a lesser extent there and is not a problem in cooler regions or outside the emission peaks. Given our findings above, the 30% correction for Orion-S appears likely to be an overestimate, although we do not have observational data at 1.3 mm to verify this.

E. Simulated Spectra

We again perform simulations of the molecular emission spectrum for Orion-S, using the simulation parameters shown in Table 5.4. Our observations allowed us to construct rotation diagrams for CH_3OH, CH_3OCH_3, H_2CS, and SO_2, and we have used the resulting rotation temperatures and column densities for those species. Typical excitation temperatures of 45–65 K were found, with SO_2 somewhat warmer; these are consistent with previous molecular temperatures (Menten *et al.* 1988, McMullin *et al.* 1993) and dust

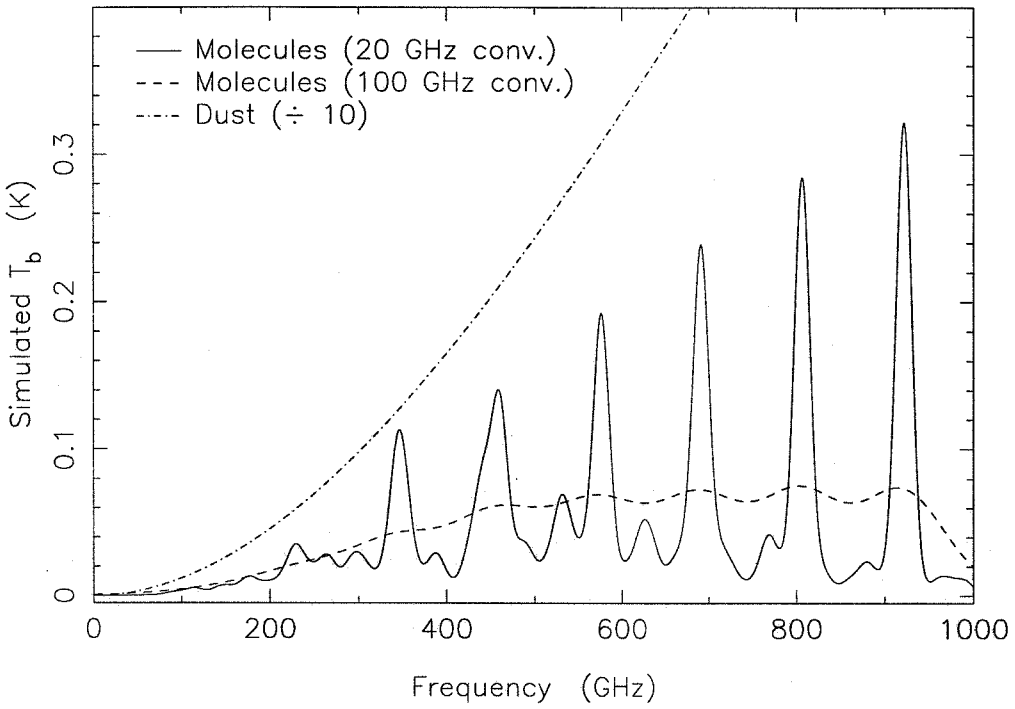

Figure 5.7 Simulated molecular emission from Orion-S convolved with a 20 GHz Gaussian and with a 100 GHz Gaussian and compared with a model dust spectrum assuming an emissivity index of 2.0, a temperature of 65 K, and an optical depth of unity at 200 μm. The dust spectrum has been divided by 10 before plotting to facilitate comparison with the molecular emission. Details of the simulations are given in the text.

temperatures (Keene *et al.* 1982, Mundy *et al.* 1986, Mezger *et al.* 1990) found for this source. For the remaining molecules (except CO), we have derived the column density required to give the integrated line intensity observed by us (*cf.* §4.7), assuming an excitation temperature of 50 K and a Gaussian velocity profile with a FWHM of 6 km s^{-1}. The CO J = 3–2 line observed by us is not consistent with an excitation temperature of 50 K, but requires significantly warmer gas to attain the observed brightness. We have therefore derived the required column density assuming a rotation temperature of 200 K for CO. While the bulk of the gas appears to be cooler, it seems likely that some fraction of the material is warmer, with CO the only molecule having a sufficient optical depth to produce significant emission at the higher temperature. As before, we plot the results of the simulation after convolving the spectrum with a 20 GHz and a 100 GHz Gaussian together with a model dust spectrum for comparison; these are shown in Figure 5.7. The large peaks in the molecular spectrum as convolved with the 20 GHz Gaussian result from the

regularly spaced CO lines, sometimes blended with the smaller peaks which occur mostly where lines of HCN, HCO^+, and CH_3OH are found. The dust spectrum shown assumes a dust temperature of 65 K, an optical depth of unity at 200 μm, and an emissivity index of $\beta = 2$, taken from from Mezger *et al.* (1990), with the absolute scaling determined by the 1.3 K (after correction for η_{MB}) continuum emission observed by us at 350 GHz. For comparison with the simulated molecular emission, the dust spectrum shown has been divided by a factor of 10 before plotting. As was the case for Orion-KL, the dust emission continues to rise more dramatically than the line emission, particularly when the line emission is averaged over a broad frequency range. While varying excitation temperatures would lead to some change in the line spectrum, including increased emission at higher frequencies, the overall scaling of the molecular emission is roughly fixed by our spectral line survey. Hence it seems unlikely that a realistic molecular spectrum could be constructed which would represent more than $\sim$10% of the dust emission within the range of a typical broadband measurement.

In Figure 5.8 we plot contours of the smoothed emission spectrum obtained as before from our simulations as a function of frequency and temperature. As was the case for our observational data and the simulated spectrum, the emission is dominated by the strong lines of CO, with the individual lines distinguishable to some extent in the plot despite the smoothing. (Again the steep decrease in emission seen near 1000 GHz reflects the convolution process rather than a real decrease; this serves to further highlight the CO J = 8–7 line near 920 GHz.) There tends to be a steeper increase with temperature as the frequency increases, which can be understood in terms of the variation of the intensity of individual lines with temperature (*cf.* §2.3, particularly (2.29) and (2.33)). The intensity of a transition reaches a maximum value at a temperature which is determined in part by the variation of the population in the upper state; this first increases as the temperature becomes sufficient to populate the upper level, then decreases as the total population is spread among ever more states as the temperature continues to increase. For the CO lines which are the dominant source of emission here, the temperature at which the maximum line emission occurs increases with increasing frequency, simply as a result of the higher frequency lines involving levels of higher excitation. Again we emphasize that these simulations assume conditions of LTE, so that all levels are assumed to be fully populated in accord with the excitation temperature.

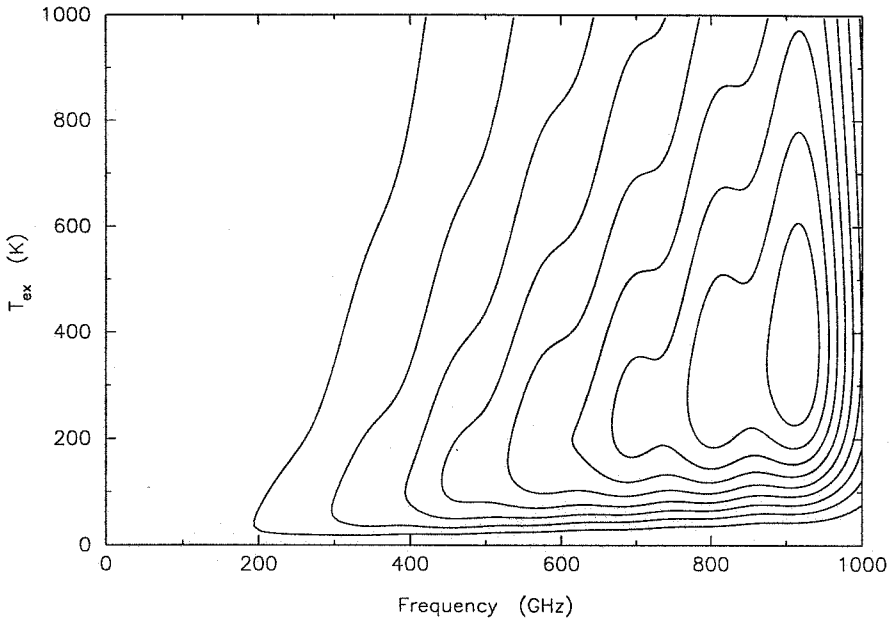

Figure 5.8 Contours of the simulated molecular line emission for Orion-S as a function of frequency and excitation temperature. The spectrum is simulated and smoothed by convolution with a 100 GHz Gaussian for a given excitation temperature; the contours represent the brightness temperature of the emission as before. Contour lines are at intervals of 1.67 K.

The contours of Figure 5.8 indicate that for the given molecular column densities, there can be substantial variation in the integrated line emission for varying temperatures, particularly at frequencies above ~600 GHz. However, we have taken the CO to have an excitation temperature of 200 K for our simulations in Figure 5.7, which corresponds roughly to the maximum emission for these frequencies. We also note that those regions with greater densities and higher temperatures will also tend to have greater dust opacities, so that the dust emission will also be increased. It therefore seems unlikely that the contribution of molecular emission to the total flux would be found to greatly exceed the 10% level found here, even as higher frequency observations are made with smaller beamsizes.

F. Summary

The integrated line emission from Orion-S is found to be much less than that from Orion-KL, while the continuum emission is reduced by a lesser amount. The overall result is that the contribution of molecular line emission to broadband flux measurements is only ~10% for the 330–360 GHz window, as

found by direct comparison of the continuum and line emission detected by our survey. A number of factors contributing to the reduced line emission have been noted, including the nearly absent or greatly reduced emission from particular species (most notably SO_2) and the reduced brightness temperatures and greatly reduced line widths in general, particularly for species which had exhibited emission from the Orion-KL plateau. The line distribution as a function of intensity appears to be less steep than for Orion-KL, so that the estimated correction for undetected weak lines is also reduced and would only produce an increase of $\lesssim$10% in the total line flux. Simulations of the molecular emission compared with a simple model dust spectrum suggest that the contribution of the integrated lines is unlikely to increase at other frequencies.

5.6. IRAS 16293–2422 Results

A. Source Description

IRAS 16293–2422 was chosen as an example of a low-mass star-forming region in contrast to the Orion-KL region of high-mass star formation. At a distance of 160 pc (Lada 1991), this source has been found to possess a rich molecular line emission spectrum together with relatively strong dust continuum emission at millimeter and submillimeter wavelengths. Both single-dish and interferometric observations of IRAS 16293–2422 have been made to study the physical and chemical processes associated with star formation (Walker *et al.* 1986, 1988, 1990, Mundy, Wootten & Wilking 1990, Mundy *et al.* 1992). These have resulted in the detection of two millimeter dust continuum sources, each with an apparent mass of $\sim$0.5 $M_\odot$, and a complex molecular outflow pattern involving at least four distinguishable lobes. Extensive studies of the chemistry of this source using data from the present line survey combined with lower frequency data are presented by Blake *et al.* (1994) and van Dishoeck *et al.* (1994). With the exception of the optically thick and self-absorbed CO J = 3–2 transition, we find typical line widths of 4–5 km s^{-1}, *i.e.*, similar to the quiescent regions of Orion-KL and Orion-S. In fact, the spectrum we obtain is quite similar in overall appearance to the Orion-S spectrum, although the actual line intensities are significantly lower. Based upon the observed lines and derived parameters, van Dishoeck *et al.* conclude that qualitatively the physical and chemical regimes which can be distinguished in IRAS 16293–2422 are similar to those found in high-mass star-forming regions, and that the chemical composition in a star-forming region depends

more on the age of the object than its mass. We also note that Blake *et al.* identify IRAS 16293–2422 as "the low mass counterpart to Orion-KL" because of its frequent use as a comparison source and its rich line spectrum.

The observations for the IRAS 16293–2422 survey were centered on a nominal source position of $\alpha(1950) = 16^h29^m20.90^s$, $\delta(1950)$ = -24°22′13″. A source velocity of v_{LSR} = 4 km s^{-1} was assumed when making the observations and for the plots shown in the presentation of the data in Appendix C.

B. Observed Line Flux

Our observations of IRAS 16293–2422 cover some 50% of the range between 330 and 360 GHz, with the observing frequencies again selected to preferentially include those regions expected to exhibit the strongest line emission. The actual survey data are presented in Appendix C and, together with additional observations at mostly lower frequencies, form the basis for analyses of the chemistry in this source by Blake *et al.* (1994) and van Dishoeck *et al.* (1994). A total of 44 scans were combined to yield the SSB spectrum; compared with the Orion-S survey, the frequency coverage is somewhat reduced, despite the comparable number of scans, because there is a slightly greater overlapping among the scans. The actual frequency ranges of the two surveys are somewhat different, although in both cases we include particular frequencies around strong lines. The actual scan frequencies and the particular lines detected are listed in tables in Appendix C. We detect a total of 65 lines, of which 62 have been identified with 15 distinct chemical species. The remaining 3 spectral features have not been identified with known transitions of any species.

The relative flux contributions and numbers of lines detected for the most important species (in terms of flux) are given in Table 5.5. This provides some quantitative indication of the similarity between the spectra of Orion-S and IRAS 16293–2422, although of course the different frequency ranges of the surveys prevent an exact comparison between the detected transitions. The lines of SO and, to a lesser degree, SO_2 are somewhat more prominent in IRAS 16293–2422 than in Orion-S, but otherwise the reported percentages of Table 5.5 are nearly the same as those for Table 5.3.

We again obtain the average flux attributable to line emission over the range of our survey by

TABLE 5.5

SIGNIFICANT FLUX CONTRIBUTIONS BY SPECIES FOR IRAS 16293–2422

Species [a]	N_{lines}	$\int T_{MB}\, d\nu$ (K MHz)	Relative Contribution (% of Total Line Flux)
CO †	2	376.5	48.2
CO	1	328.7	42.0
SO †	5	97.3	12.4
SO	3	91.9	11.8
HCO^+ †	2	82.2	10.5
CH_3OH	20	54.8	7.0
HCN †	2	49.4	6.3
CS †	2	39.1	5.0
SO_2	13	26.0	3.3
H_2CO	1	22.5	2.9
U-lines	2	5.3	0.7

[a] Values for species marked with a † also include the contributions of all transitions detected from isotopomers and vibrationally excited states. For CO and SO, separate entries are shown for the main species and for all of the isotopomers together.

summing the integrated line intensities. In units of main beam temperature (after correction for η_{MB}), the lines contribute an average of .052 K, corresponding to a flux value of 1.7 Jy. As before, this constitutes a probable upper limit for the average line flux, given our bias towards frequencies with strong emission. Assuming that no other lines are present in the 330–360 GHz band yields a lower limit of 0.85 Jy for the line flux.

The continuum emission from IRAS 16293–2422, and from the remaining sources considered below, is considerably weaker than the emission from Orion-KL or Orion-S and was not detected by our observations (which were optimized for line detection). We must therefore evaluate the relative contribution of the molecular line emission by comparing our average line flux with published values (given below) for the total flux, rather than having the direct comparison as we did for the Orion sources.

C. Extrapolation for Weak Lines

We again perform a power-law fit to the observed distribution of lines as a function of integrated intensity with the results shown in Figure 5.9. We have included all lines having an integrated intensity $W > 2$ K MHz in our fit, but find little change in the fit parameters even when the entire range of line intensities is utilized. The derived fit gives a power-law index of $b = -0.72$ for the distribution, intermediate

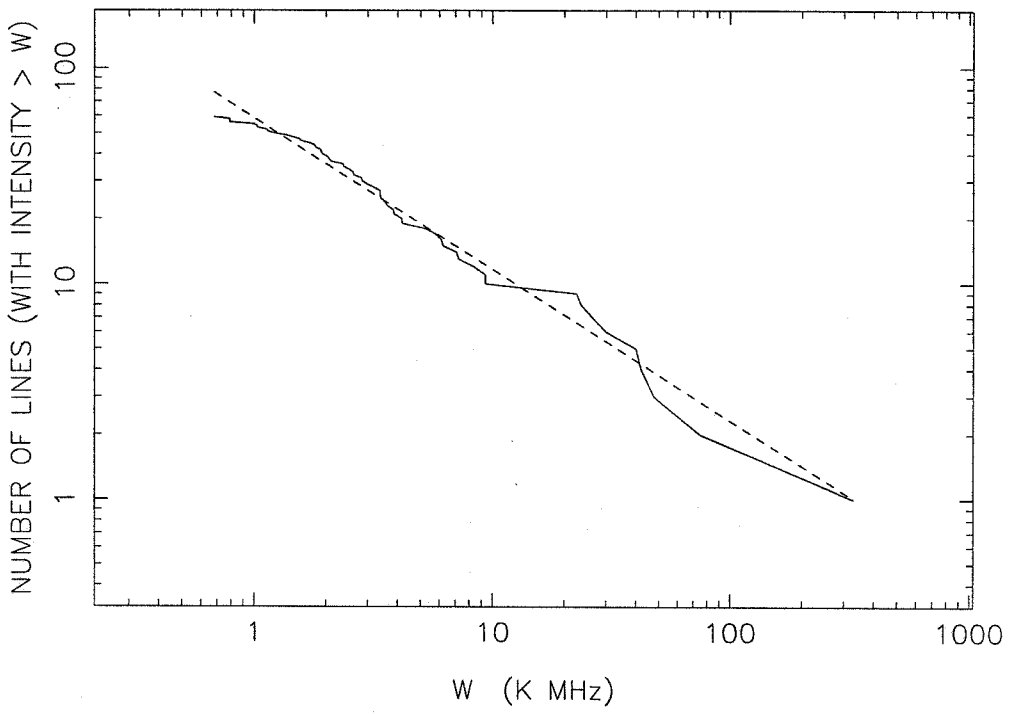

Figure 5.9 Distribution of observed integrated line intensities from the IRAS 16293–2422 line survey. A power-law fit is shown with a slope of -0.72 as discussed in the text.

between the two Orion sources. Extrapolating the fit to weak intensities suggests that our detected line flux may need to be increased by ~20% to account for undetected weak lines, giving a range between 1.0 and 2.0 Jy for the line flux based upon the upper and lower limits derived above.

D. Comparison with Additional Flux Measurements

As noted above, our observations did not detect the continuum emission for any of the remaining sources so that we must compare our derived line flux in each case with other broadband measurements of the total flux. Fortunately, a consistent set of observed flux densities including data for all of these sources (IRAS 16293–2422, IRC +10216, VY CMa, and OH 231.8+4.2) is presented by Sandell (1994) in his study of possible calibration sources for submillimeter observations. The data include flux densities observed at wavelengths between 2 mm and 350 μm, with beamsizes which are usually ~18″. Of particular interest, given the frequency range of our surveys, are the measurements at 800 and 850 μm, with beamwidths of 16.5″ and 17.5″ and filter bandwidths of 101 and 30 GHz respectively.

The observed total flux values for IRAS 16293–2422 are 17.3 ± 0.9 Jy at 850 μm and 21.1 ± 0.5 Jy at 800 μm; based on a simple power-law fit to the entire data set we find the total flux to vary as $\nu^{2.7}$. We adopt the total flux value of 17 Jy at 350 GHz resulting from this fit for comparison to the value for the line flux as found from our spectral observations in the 330–360 GHz window. As derived above, the average emission line flux in this range contributes between 1 and 2 Jy, representing between 6 and 12% of the total flux. The emission line contribution to the total flux observed from both IRAS 16293–2422 and Orion-S is therefore ~10%, significantly less than the ~60% value we obtain for Orion-KL. This appears to give additional support to the proposal that the chemistry, and hence the resulting line emission, in star-formation regions may be more strongly dependent upon the age of the objects than upon their masses. If this is verified in additional sources, it may then be possible to estimate the approximate correction for line emission needed for broadband total flux measurements of other objects based upon their evolutionary state without the need for extensive line observations.

E. Simulated Spectra

We have performed simulations of the molecular line emission spectrum as before, this time using the molecular parameters for IRAS 16293–2422 found by Blake *et al.* (1994) and van Dishoeck *et al.* (1994) and which are shown in Table 5.6. This table also includes upper limits derived by these authors for several molecules, particularly "heavy" and more complex molecules such as CH_3CHO and C_2H_5CN. A simulated spectrum was generated and smoothed in the usual way for the observed molecular column densities and a second simulation was performed using only the derived upper limits. In Figure 5.10 we show the spectrum for the observed column densities after convolution with a 20 GHz and a 100 GHz Gaussian, together with a model dust spectrum for comparison. The dust is taken to have a temperature of 65 K, with an emissivity index of $\beta = 1.5$ and an optical depth of unity at 75 μm, adapted from Mundy *et al.* (1992). The absolute scaling of the dust spectrum is chosen to give a value of 17 Jy at 350 GHz as found above. The dust spectrum has been divided by a factor of 10 before plotting so that it may more easily be compared to the molecular emission. We also show the comparison of the molecular spectra obtained for the observed column densities and for the upper limits after each has been convolved with

TABLE 5.6

SIMULATION PARAMETERS FOR IRAS 16293-2422

Species	T_{ex} (K)	N_T (cm^{-2})	ΔV (km s^{-1})	Velocity Profile
CO	20	2.0×10^{19}	13.0	Gaussian
^{13}CO	20	3.3×10^{17}	13.0	Gaussian
$C^{18}O$	20	1.8×10^{16}	4.0	Gaussian
HCO^+	80	2.0×10^{14}	3.0	Gaussian
$H^{13}CO^+$	80	3.0×10^{12}	2.7	Gaussian
$HC^{18}O^+$	80	5.0×10^{11}	2.0	Gaussian
DCO^+	29	4.0×10^{12}	1.9	Gaussian
HCN	20	6.0×10^{13}	6.0	Gaussian
$H^{13}CN$	21	1.0×10^{12}	5.8	Gaussian
HNC	20	2.0×10^{13}	4.0	Gaussian
DCN	13	5.0×10^{11}	2.4	Gaussian
DNC	14	2.0×10^{12}	2.1	Gaussian
CN	34	6.0×10^{12}	1.1	Gaussian
C_2H	30	6.0×10^{13}	1.8	Gaussian
C_3H_2	24	1.0×10^{13}	1.7	Gaussian
H_2CO	89	2.0×10^{14}	4.0	Gaussian
CH_3OH	94	8.0×10^{14}	4.3	Gaussian
CH_3CN	222	2.0×10^{13}	4.0	Gaussian
CH_3C_2H	80	1.1×10^{14}	4.0	Gaussian
CH_2CO	80	3.0×10^{13}	4.0	Gaussian
HNCO	80	3.0×10^{13}	4.0	Gaussian
CS	80	2.3×10^{14}	4.0	Gaussian
$C^{34}S$	32	1.0×10^{13}	3.5	Gaussian
SO	124	7.9×10^{14}	4.2	Gaussian
^{34}SO	80	3.5×10^{13}	4.3	Gaussian
SiO	65	2.0×10^{13}	4.5	Gaussian
^{29}SiO	65	1.0×10^{12}	4.5	Gaussian
HCS^+	236	4.0×10^{12}	4.0	Gaussian
OCS	210	3.4×10^{15}	5.5	Gaussian
$OC^{34}S$	200	6.3×10^{13}	5.2	Gaussian
$O^{13}CS$	200	5.6×10^{13}	5.5	Gaussian
H_2S	60	3.0×10^{14}	4.6	Gaussian
H_2CS	63	3.7×10^{13}	3.8	Gaussian
SO_2	95	2.9×10^{14}	4.6	Gaussian
$HN^{13}C$ [a]	20	1.0×10^{12}	4.0	Gaussian
HCOOH [a]	80	6.0×10^{13}	4.0	Gaussian
NH_2CN [a]	80	2.0×10^{12}	4.0	Gaussian
HCO [a]	80	2.0×10^{13}	4.0	Gaussian
CH_3CHO (A) [a]	80	1.0×10^{13}	4.0	Gaussian
CH_3CHO (E) [a]	80	1.0×10^{15}	4.0	Gaussian
C_2H_5OH [a]	80	8.0×10^{13}	4.0	Gaussian
NH_2CHO [a]	80	8.0×10^{12}	4.0	Gaussian
CH_2NH [a]	80	8.0×10^{13}	4.0	Gaussian
C_2H_3CN [a]	80	1.0×10^{15}	4.0	Gaussian
C_2H_5CN [a]	80	2.0×10^{14}	4.0	Gaussian
CCCO [a]	80	2.0×10^{14}	4.0	Gaussian
CCCS [a]	80	7.0×10^{14}	4.0	Gaussian
SiS [a]	80	8.0×10^{12}	4.0	Gaussian

[a] Species not detected; upper limit is shown and used in separate simulation.

a 20 GHz Gaussian, together with the model dust spectrum (again divided by 10) in Figure 5.10. The molecular emission from IRAS 16293–2422 can be seen from these comparisons to be roughly comparable to 10% of the dust emission, depending upon the particular frequency range considered, and as for the sources previously considered, drops well below the dust spectrum for observations at higher frequencies. It is interesting to note the increased emission at lower frequencies in the simulation using the upper limits. The many lines from the generally heavier and more complex species combine to give a rather smooth spectrum peaking below 200 GHz despite the assumed excitation temperature of 80 K for these molecules. As a result of the many states available, transitions at higher frequencies exhibit weaker emission because the populations in the corresponding levels are low. Thus we see that lower frequency observations are best suited for detection of these molecules and that their contribution to the integrated line flux will in general be unimportant for frequencies above 350 GHz.

We also show the results of our simulations using different excitation temperatures in Figure 5.11. As was the case for Orion-S, features can be seen at the frequencies of the individual CO transitions, while the apparent drop in emission for frequencies near 1000 GHz again is an artifact resulting from the convolution process. Since temperatures greater than 200 K must be reached before the average line flux continues to increase well past 700 GHz, it seems unlikely that the average line contribution will significantly increase beyond the ~10% level found by us, even as regions of higher temperature and greater densities are probed. We note that the CO column density used for our simulations is derived using optically thin $C^{17}O$ observations (Blake *et al.* 1994); the LTE calculations do not allow the self-absorption we observe to be included in our simulated spectrum and tend to overestimate the emission in the CO lines.

F. Summary

The spectrum of IRAS 16293–2422 is found to be rather similar in appearance to that of Orion-S over the range of our surveys, with the various species responsible for approximately the same percentage of the total line flux in each of the two sources, although the emission from SO lines as compared to lines of other species appears to be somewhat enhanced in IRAS 16293–2422 relative to Orion-S. This similarity supports previous suggestions that similar physical and chemical regimes are found in both high-

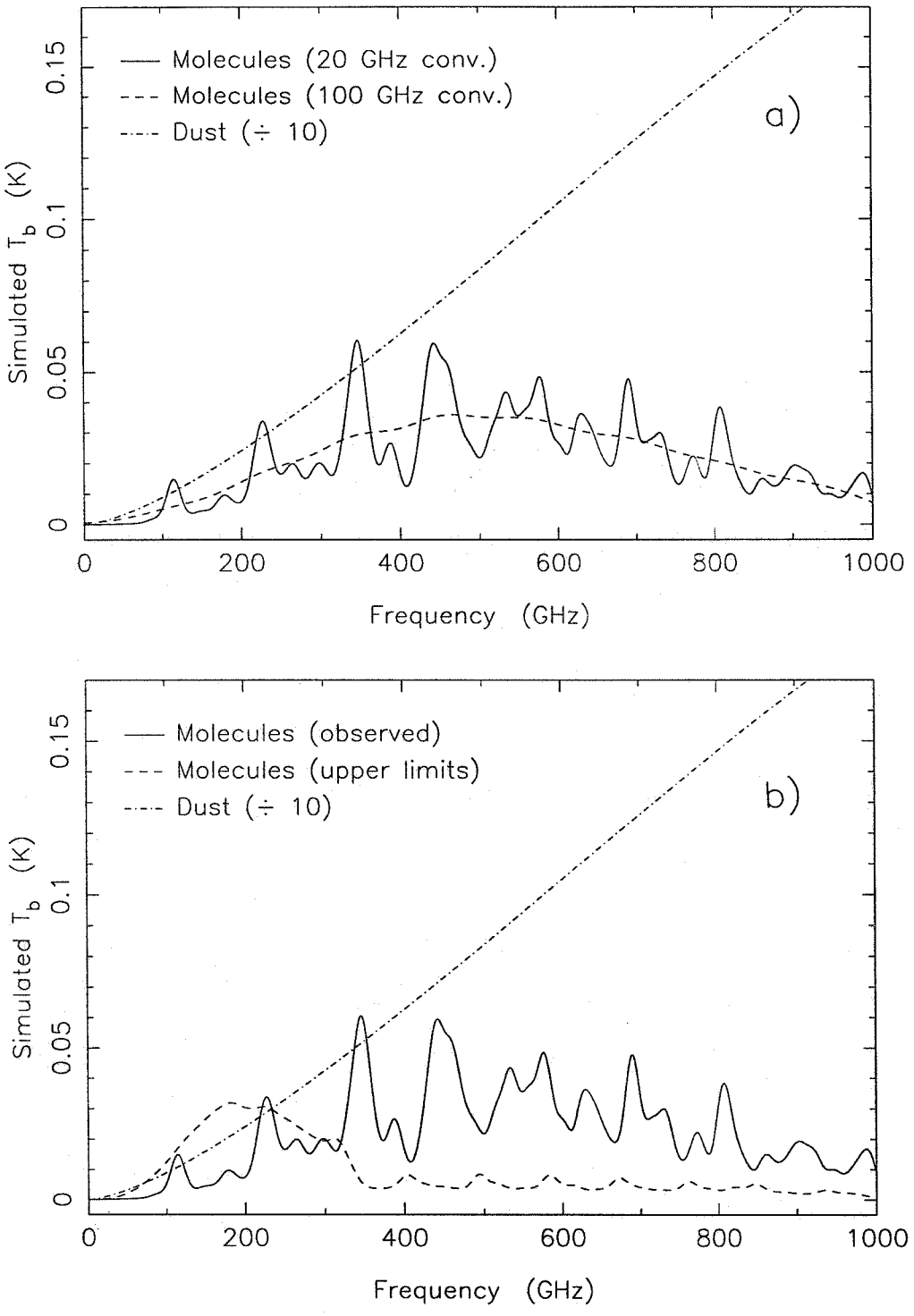

Figure 5.10 Simulated molecular emission spectrum for IRAS 16293–2422 compared with a model dust spectrum as before. *(a)* The line emission for the observed column densities after convolution with a 20 GHz Gaussian and with a 100 GHz Gaussian. *(b)* The line emission for the observed column densities and for the derived upper limits are shown separately after convolution with a 20 GHz Gaussian.

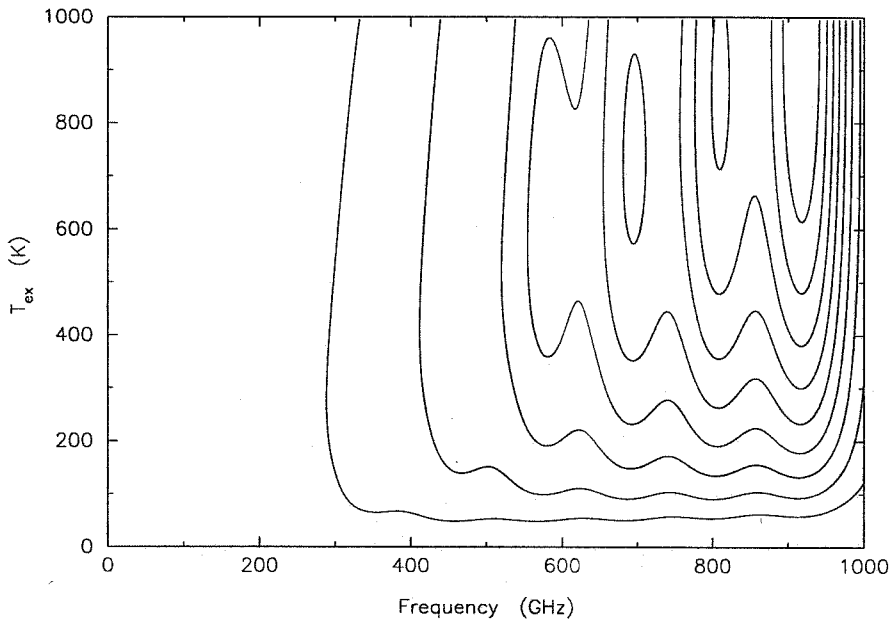

Figure 5.11 Contours of the simulated molecular line emission for IRAS 16293–2422 as a function of frequency and excitation temperature. The spectrum is simulated and smoothed by convolution with a 100 GHz Gaussian for a given excitation temperature; the contours represent the brightness temperature of the emission as before. Contour lines are at intervals of 4.7 K.

and low-mass star-forming regions and that the chemistry in star-forming regions is heavily dependent upon the age of the source, since both Orion-S and IRAS 16293–2422 are believed to be at a relatively early evolutionary state. Also similar to the Orion-S results is the finding that the integrated line emission contributes only $\sim$10% of the total line flux over the range of our survey, with simulations showing that this value is unlikely to increase significantly at other frequencies. The distribution of the line intensities observed in our survey suggests that the detected line flux should perhaps be increased by some 20% to account for undetected weak lines. Finally, our simulations show that emission from heavy molecules peaks at low frequencies ($\lesssim$ 200 GHz), as expected from considerations of the level populations.

5.7. IRC +10216 Results

A. Source Description

The carbon star IRC +10216 with its extended circumstellar shell of gas and dust has been the subject of extensive study at infrared and millimeter wavelengths. First noted as a bright object at 5 and 2 μm by Becklin *et al.* (1969), it exhibits variations in its intensity with a period of ~650 days. The CO J = 1–0 and 2–1 line emission is detected out to a radius of $\gtrsim$200″(Huggins, Olofsson, & Johansson 1988), and the CO emission for rotational lines up to J = 6–5 has been extensively modeled (*e.g.*, Kwan & Linke 1982, Sahai 1987). Kwan & Linke find the dust in the shell maintains a relatively warm temperature of ~100 K out to a radius of 10^{17} cm (corresponding to a distance of ~33″at the estimated source distance of 200 pc), while the gas cools more rapidly in the flow and has a temperature of ~15 K at that distance. Based upon infrared observations of CO, Sahai & Wannier (1985) suggest that an inner envelope of size $\lesssim$6″ is significantly warmer (~200 K). The gas reaches its terminal expansion velocity of $\sim$ 15 km s^{-1} within 8 stellar radii (10^{15} cm or 0.2″at the estimated distance of 200 pc). The chemistry of the source is generally understood in terms of a "freeze-out" model (McCabe *et al.* 1979) where near equilibrium abundances in the warm inner regions are frozen as the gas cools in the outflow and are modified by photochemistry in the outer portions of the envelope (*e.g.*, Glassgold *et al.* 1987). A rich spectrum of emission lines has been observed from this source, with many species detected either only in this source or first seen here (*e.g.*, SiCC, Thaddeus, Cummins, & Linke 1984; NaCl, AlCl, KCl, AlF, Cernicharo & Guélin 1987). Spectral line surveys have previously been performed for this source (Johansson *et al.* 1984, Avery *et al.* 1992) including an unpublished survey using the 30m IRAM telescope from which several detections of unusual species have been made (*cf.* Cernicharo *et al.* 1991). The observed line shapes are indicative of the roughly symmetric expanding shell, displaying parabolic line shapes in the optically thick case and doubly peaked or flat lines in the optically thin case, depending upon the relative sizes of the beam and the emitting region (Morris 1975, Oloffson *et al.* 1987). These line shapes allow a distinction to be made between optically thin and optically thick line emission in the case of spherical symmetry. Because of its nearness and bright emission, IRC +10216 has come to serve in many ways as the standard

evolved star for reference, in much the same way that Orion serves as the standard hot core region. In each case, the source may not be a typical member of that class of sources, but has been extensively observed and studied and provides a useful reference for comparison.

A source position of $\alpha(1950) = 09^h45^m14.80^s$, $\delta(1950) = 13°30'40''$ was assumed for the observations of IRC +10216, together with a source velocity of $v_{LSR} = -26\,\mathrm{km\ s^{-1}}$.

B. Observed Line Flux

The data from the CSO spectral line survey of IRC +10216 are presented in Appendix B of this thesis; a more complete analysis is being published separately (Groesbeck, Phillips, & Blake 1994a). The SSB spectrum derived from our survey extends continuously from roughly 330 to 358 GHz, and represents the combination of some 107 individual DSB scans. We detect a total of 56 spectral lines, of which 2 remain unidentified while the remainder are identified with 8 molecules (and their isotopomers) which have previously been detected towards IRC +10216.

The compressed view of the spectrum plotted in Appendix B shows a relatively few strong lines, not unlike the spectra for Orion-S and IRAS 16293–2422, but a closer inspection reveals that in IRC +10216 it is a different set of particular species which exhibit strong emission. The expanded view of the IRC +10216 spectrum also reveals completely different line shapes as well as a clearly different chemistry in the source. We find that the CO J = 3–2 transition is the strongest line observed, as it has been in all of the sources discussed thus far. However, the HCN J = 4–3 transition has nearly the same intensity and the corresponding line of $H^{13}CN$ is half as strong and is in fact stronger than any of the remaining lines. In addition, we detect emission from a number of vibrationally excited states of HCN. The combination of these lines from the different HCN variants, particularly the very strong emission from HCN and $H^{13}CN$, is responsible for 40% of the total line flux observed in our survey, while the combined CO emission accounts for 28% of the total line flux. Table 5.7 gives these values and the proportion of the line flux contributed by other species which exhibit significant line emission. Notable by their absence are SO, SO_2, CH_3OH, H_2CO and HCO^+, all of which were among the significant flux contributors for the star-forming regions previously considered.

TABLE 5.7

SIGNIFICANT FLUX CONTRIBUTIONS BY SPECIES FOR IRC +10216

Species [a]	N_{lines}	$\int T_{MB}\, d\nu$ (K MHz)	Relative Contribution (% of Total Line Flux)
HCN †	11	1720.1	40.3
HCN	1	987.5	23.1
$H^{13}CN$	1	520.9	12.2
CO †	2	1202.5	28.1
CO	1	1106.8	25.9
CS †	4	390.6	9.1
CS	1	346.3	8.1
SiS †	8	323.3	7.6
SiS	1	232.9	5.5
C_2H	4	251.1	5.9
SiCC	14	196.9	4.6
SiO †	3	116.3	2.7
U-lines	2	7.1	0.2

[a] Values for species marked with a † also include the contributions of all transitions detected from isotopomers and vibrationally excited states. In some cases, separate entries are shown for individual species as well, *e.g.* entries are shown for HCN, $H^{13}CN$, and for all variants of HCN together.

The observations of IRC +10216 have been corrected for the main beam efficiency ($\eta_{MB} = 0.76$), with the sum of the integrated line intensities averaging 0.15 K over the entire range of the survey, equivalent to a flux of 4.9 Jy, which then represents our upper limit for the average line flux. Our survey nearly covers the canonical range of 330–360 GHz, so that the lower limit derived by averaging only the observed line emission over the full 30 GHz range is only slightly less, with a value of 4.6 Jy. We find that 80% of the line flux is contained in the seven strongest lines which are plotted separately in Figure B1.4; since we do not expect any additional lines of comparable strength to be found in the remaining portion of the window, the actual value of the integrated line flux is likely to be closer to the lower limit. A further result of the concentration of the flux in so few lines is that the actual contribution of lines to broadband measurements is critically dependent upon the actual frequency response of the system.

We were again unable to evaluate the intensity of the continuum emission from our spectroscopic heterodyne observations. Comparisons of our observed line flux to both broadband and narrowband total flux measurements are given below.

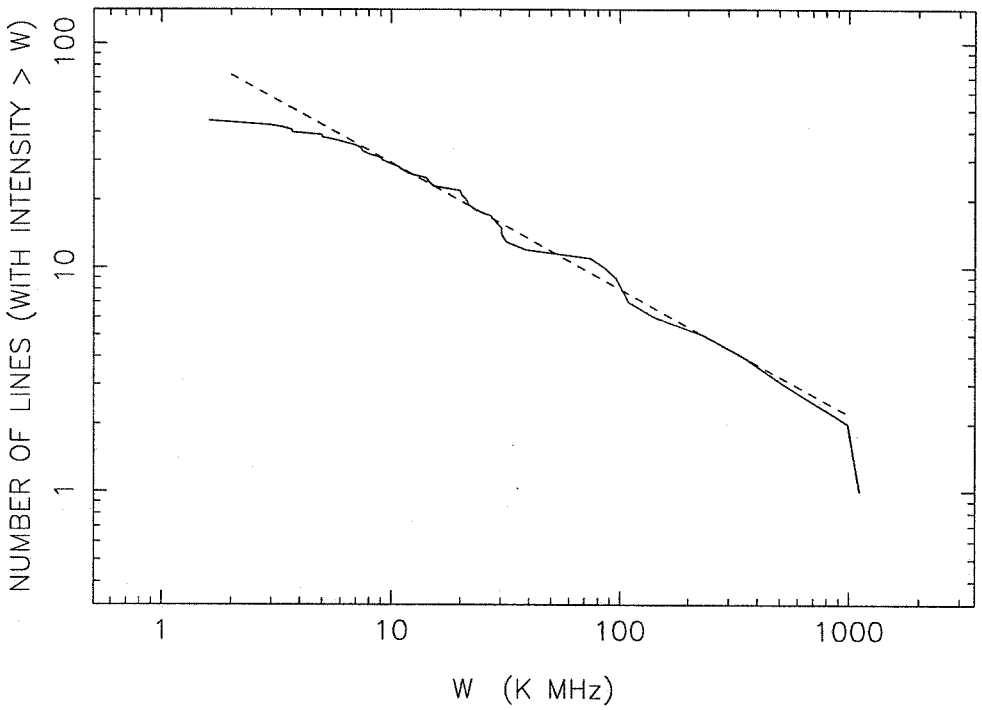

Figure 5.12 Distribution of observed integrated line intensities from the IRC +10216 line survey. A power-law fit is shown with a slope of −0.56 as discussed in the text.

C. Extrapolation for Weak Lines

As noted above, the vast majority of the flux is carried by rather few spectral lines. This is indicative of a less steep line intensity distribution, which is indeed what we derive from our fitting process. The observed line distribution is plotted in Figure 5.12 together with our fit which has a power-law index of −0.56. To perform the fit, we have selected those lines which satisfy 10 K MHz$< W <$ 400 K MHz, as the data suggest a possible undercounting of lines at lower integrated intensities. The relatively shallow slope of the distribution leads to a lower contribution from weak lines, so that an increase of only some 8–10% to the detected line flux is warranted to correct for undetected lines. Hence, the total line flux for IRC +10216 averaged over the 330–360 GHz range is found to be ∼5 Jy.

D. Comparison with Additional Flux Measurements

We first consider the total broadband flux measurements of Sandell (1994) as discussed earlier. Data are reported for the maximum and minimum phases of the variable emission from IRC +10216, with the

flux at 850 μm listed as 6.5 ± 0.4 Jy at the maximum and 4.9 ± 0.4 Jy at the minimum. The corresponding flux values at 800 μm are somewhat lower, 5.9 ± 0.4 Jy and 4.5 ± 0.3 Jy, despite the shorter wavelength. In view of the clearly substantial contribution of molecular line emission and its dependence upon the particular frequency range considered, it seems likely that the narrower bandwidth of the 850 μm filter (*cf.* the earlier comments in §5.3) may result in a higher average line flux contribution if it corresponds to a range containing several strong lines.

We found no evidence for variation in the intensity of our observed line emission as a function of the varying continuum emission. The variation between the intensity of a particular line as observed at different epochs was comparable to the variation observed during a single observing session. We therefore assumed a constant intensity for all of the lines for our analysis, including the reconstruction of the SSB spectrum. In any case, it is clear from a comparison of our derived line flux of ~5 Jy and the values listed above that the line flux contribution to the total broadband flux is quite substantial at these frequencies.

A spectral line survey of IRC +10216 from 339.6 to 364.6 GHz with considerably less sensitivity than the present work was recently published by Avery *et al.* (1992), who estimate a line flux density of ~4.3 Jy in a 30 GHz band centered around 354 GHz. A narrowband heterodyne measurement by Sandell is also quoted by Avery *et al.*, which gave a flux value of 1.9 Jy (at the minimum phase) where the observing parameters were chosen so that both sidebands were free of discernible line emission.

Considering the various reported flux values, we believe that at the phase corresponding to the minimum total flux, line emission is responsible for $\gtrsim$ 65% of the total flux from IRC +10216 in the 330 – 360 GHz range, while this contribution may be reduced to ~50% at the phase of maximum total flux. It seems likely that this value will vary significantly for different frequency ranges (*cf.* our simulated spectrum for IRC +10216 when convolved with a 20 GHz Gaussian as shown below).

At longer wavelengths (1.3 mm), Walmsley *et al.* (1991) have presented continuum measurements made with a 50 GHz bolometer passband (210 – 260 GHz). Using estimates of the line emission based upon a 10 GHz section of the unpublished IRAM spectral line survey together with their own sum of known strong lines, they suggest that line emission contributes ~0.5 Jy to their total observed value of ~1.5 Jy. We believe their estimate of the flux from strong lines is too low, as it does not include the

emission from several transitions ($H^{13}CN$ J = 3–2 and SiS J = 12–11, 13–12, and 14–13) which are likely to have comparable and probably greater intensities than four of the five specific lines mentioned by them. We estimate that including these additional lines would increase their total line flux estimate to 0.8 Jy, or approximately half of the total flux. It would also be more consistent with our finding that the line flux is dominated by the emission from the strongest lines.

We note that additional measurements at 400, 450, and 900 μm presented by Sopka *et al.* (1985) yield observed total fluxes of 32, 29, and 9 Jy respectively in somewhat larger beams (37″ at 400 μm and 47″ at 450 and 900 μm). An emissivity index of β = 1.2 with a required optical depth of unity at 10 μm gave the best fit to their data and other published flux values; however, our finding that more than half of the total flux at 870 μm is contributed by line emission suggests that their uncorrected 900 μm total flux value may be significantly too large. As described by Groesbeck *et al.* (1994), correcting their long wavelength flux for the line emission leads to a better agreement between the relative values of their observed fluxes and the overall emissivity index which was derived from data over the entire range from 50 to 1000 μm.

Finally, we return to the data from Sandell (1994), specifically considering the observations at both shorter and longer wavelengths than those mentioned above. Our simulations (described below) suggest that substantial corrections for line flux contributions may be needed for all longer wavelength broadband observations, while the required corrections will be relatively minor at shorter wavelengths. Fitting the complete data set without corrections leads to a value of approximately 0 for β, as though the dust were optically thick even at millimeter wavelengths. This indicates that the broadband values at long wavelengths are too high, which may be explained as the result of included line emission.

E. Simulated Spectra

In Table 5.8 we list the usual set of molecular parameters used in our simulations. The velocity line profiles for the different molecules are listed as thick, thin, or flat, and correspond to the optical depths of the observed transitions. As noted above, for a spherically symmetric expanding shell such as that seen here, optically thick lines display parabolic line shapes while optically thin emission can produce a

TABLE 5.8
SIMULATION PARAMETERS FOR IRC +10216

Species	T_{ex} (K)	N_T (cm^{-2})	ΔV (km s^{-1})	Velocity Profile [a]
CO	42	2.0×10^{18}	25	Thick
^{13}CO	42	5.0×10^{16}	25	Thin
CS	28	3.0×10^{15}	25	Thick
^{13}CS	28	1.1×10^{14}	25	Flat
$C^{34}S$	28	1.5×10^{14}	25	Flat
SiO	29	3.5×10^{14}	25	Thick
^{29}SiO	29	1.9×10^{13}	25	Thin
^{30}SiO	29	1.1×10^{13}	25	Thin
SiS	75	3.8×10^{15}	25	Thick
^{29}SiS	75	2.1×10^{14}	25	Thin
^{30}SiS	75	1.2×10^{14}	25	Thin
$Si^{34}S$	75	1.8×10^{14}	25	Thin
SiCC	106	3.7×10^{14}	25	Flat
CN	10	6.2×10^{14}	25	Thin
C_2H	16	4.6×10^{15}	25	Thin
HCN	30	2.8×10^{16}	25	Thick
$H^{13}CN$	30	2.8×10^{14}	25	Thick
HC_3N	11	4.0×10^{15}	25	Flat
HC_5N	11	1.4×10^{16}	25	Flat

[a] Thick and thin profiles correspond to parabolic or doubly- peaked line shapes; see text.

doubly-peaked profile if the shell is spatially resolved or a flat-topped profile if it is not resolved by the beam. For our simple LTE modeling of the emission we give the velocity profile of the column density, with the actual appearance of a transition depending upon the optical depth which is computed in the course of the simulations. The thick, thin, and flat line profiles listed therefore correspond to parabolic, doubly-peaked, or flat-topped distributions of the column density as a function of velocity for the various molecules. The column densities and rotation temperatures used are derived by combining our data with lower frequency observations, particularly those of Kahane *et al.* (1988, 1992), using the rotation diagram technique (see Groesbeck *et al.* 1994a for details). In addition, we have taken the parameters for HC_3N and HC_5N, which are not detected in our survey, from the previous line survey of Johansson *et al.* (1984).

Figure 5.13 shows the resulting simulated spectrum in the usual way, after convolution with a 20 GHz Gaussian and a 100 GHz Gaussian. We also show model dust spectra for two values of the emissivity index, $\beta = 1.0$ and $\beta = 1.5$. In each case we have assumed an optical depth of unity at 10 μm (Sopka *et al.*,

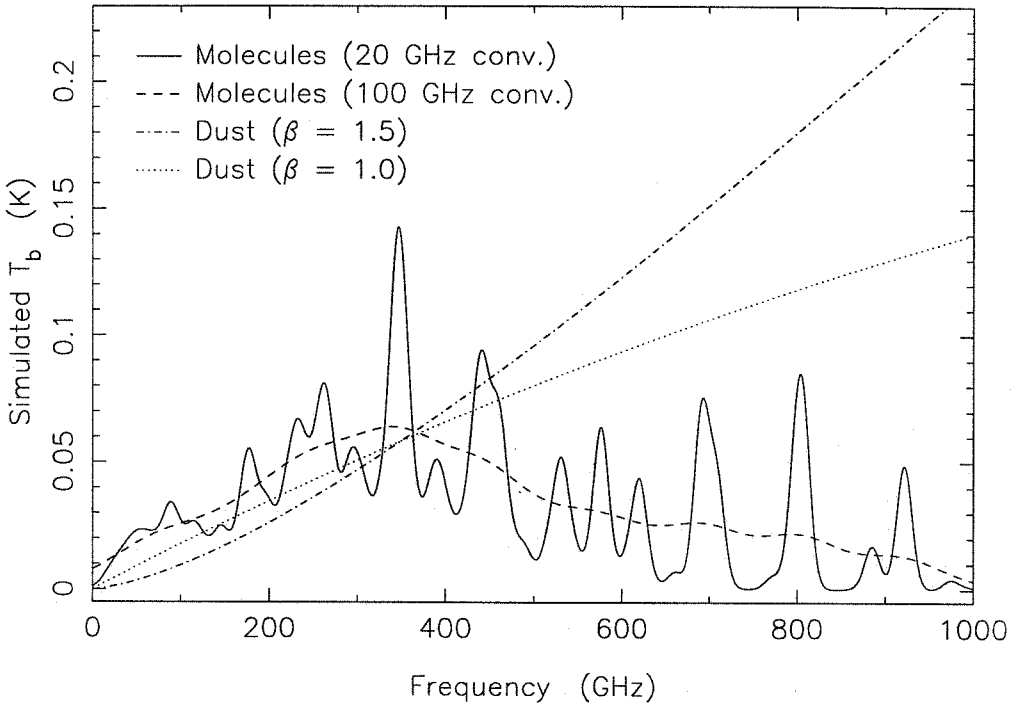

Figure 5.13 Simulated molecular emission from IRC +10216 convolved with a 20 GHz Gaussian and with a 100 GHz Gaussian and compared with model dust spectra for two different values of the emissivity index β. For each of the dust spectra plotted, we assume a temperature of 100 K, and an optical depth of unity at 10 μm, with $\beta = 1.5$ in one case and $\beta = 1.5$ in the other. Details of the simulations are given in the text.

1985) and a temperature of 100 K (Kwan & Linke, 1982), with the absolute scaling set by the narrowband measurement of Sandell giving a value of 1.9 Jy at 350 GHz. The two values of β have been chosen to represent the typical range quoted for the emissivity index (*cf.* §2.2) with the value of 1.2 found by Sopka *et al.* falling approximately midway between them.

In the simulations as well as in our observations, the line flux from IRC +10216 is dominated by the emission from the strongest lines. The structure which is seen in the simulated molecular emission is indicative of this dependence on the locations of the strongest lines, particularly CO and HCN. Hence the region of our observations, where emission from several strong lines is seen over a fairly narrow range of frequencies, corresponds to a peak in the molecular emission for IRC +10216 as it generally has for the sources previously considered. Also similar to our findings for other sources is the clear implication that at higher frequencies ($\nu > 600$ GHz), the relative contribution of line emission to the total flux becomes

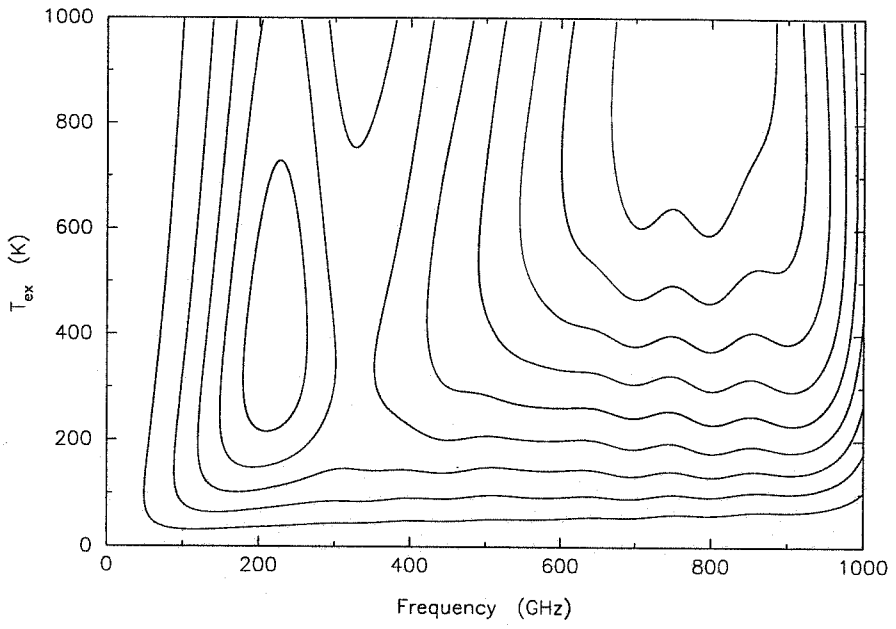

Figure 5.14 Contours of the simulated molecular line emission for IRC +10216 as a function of frequency and excitation temperature. The spectrum is simulated and smoothed by convolution with a 100 GHz Gaussian for a given excitation temperature; the contours represent the brightness temperature of the emission as before. Contour lines are at intervals of 7.1 K.

much less important. We therefore suggest that the value of 1.2 found for β by Sopka *et al.* may be too low because the 900 μm flux value used has not been corrected for line emission and is probably too large. However, since their fit includes a number of flux measurements at shorter wavelengths where corrections for line emission will be small, the overall change in the emissivity index will tend to be rather small. It is also interesting to note that the simulated line emission exceeds the model dust emission at essentially all frequencies below ~300 GHz, suggesting that significant corrections to the observed flux values will be required throughout this range.

We have also simulated the emission line spectrum using the same column densities but with different excitation temperatures, as has been done for the other sources previously considered. The resulting contour plot is shown in Figure 5.14. The local maximum visible near 200 GHz for temperatures between 200 and 700 K occurs because the catalog information for HC_5N extends only up to a frequency

of 263 GHz (the J = 99–98 line with E_u = 632 K); the column density is sufficiently large that the LTE calculations yield sizable populations in these highly excited states, and hence a sharp drop occurs in the simulated emission above the cutoff frequency. Otherwise, over the range of temperatures below 200 K, the apparent effect of an increase in temperature is to increase the overall strength of the emission, without producing any great change in the appearance of the smoothed spectrum. Indeed, the contours suggest that for temperatures in that range and even higher, the spectrum is fairly flat at frequencies above 300 to 500 GHz. Thus the contribution of the line flux is likely to drop at shorter wavelengths, even as observations at higher frequencies or with smaller beamsizes probe hotter gas.

F. Summary

We have performed a complete spectral line survey of IRC +10216 over the range 330.2 – 358.1 GHz. The different lines and species observed clearly show a different chemistry than was seen towards the star-forming regions, but one which nevertheless produces a large line flux in this case. The integrated line emission represents ∼5 Jy, or ∼50 – 65% of the total flux observed at these frequencies, depending on the phase of the variable continuum emission. The actual line flux was dominated by the emission present in the strongest observed lines, in accord with the relatively flat distribution of line intensities having a slope of −0.56 which was found.

This finding of a substantial flux contribution from the integrated line emission may at first appear surprising, particularly given the very sparse line spectrum relative to that of Orion-KL. The very broad lines, however, carry significant amounts of flux, particularly the strongest lines which display optically thick emission. We also point out that several very strong lines are found within the particular frequency range observed by us, and that a significant amount of structure in the molecular emission will exist over scales of ∼20 – 30 GHz depending upon the relative frequencies of the strong lines.

Based upon our simulations, the contribution of the molecular line emission is significant for all frequencies below ∼300 GHz, but drops rapidly above ∼600 GHz. At these higher frequencies, the average line emission drops off in intensity while the dust continuum emission continues to rise. Taken as a whole, our findings suggest the possibility that the emissivity index β, as derived from observations over wide

ranges of frequencies, may need to be increased.

5.8. VY CMa Results

A. Source Description

VY CMa was chosen as an additional star with a circumstellar shell of gas and dust, but having different characteristics from IRC +10216. Located at a distance of some 1500 pc (Lada & Reid 1978), it displays an oxygen-rich chemistry, with strong maser emission from OH, H_2O and SiO (Turner *et al.* 1970; Wilson, Barrett, & Moran 1970; Buhl *et al.* 1974). (A second oxygen-rich star, OH 231.8+4.2, was also observed for this study; those observations are discussed in the next section.) VY CMa has the appearance of a bipolar nebula, most likely the result of an increased density of circumstellar material in the equatorial plane which allows only the poles to be illuminated (Morris 1981). Knapp, Sandell, & Robson (1993, hereafter KSR) suggest that the star itself is a long period variable (~870 d), with the irregular variations seen in optical light the result of structure in the surrounding circumstellar material (Wallerstein 1978).

The observed molecular transitions indicate a speed for the outflowing material of $35 - 40\,\mathrm{km\ s^{-1}}$ (the CO J = 3–2, SiO J = 8–7, and HCN J = 4–3 lines all have full widths in excess of 50 $\mathrm{km\ s^{-1}}$ as can be seen in the line plots of Appendix C), but the complex lineshapes seen do not lend themselves to the straightforward analysis which can be used in the case of spherical symmetry to distinguish optically thin and thick lines. The observed line profiles instead suggest a pronounced departure from spherical symmetry, in agreement with the above findings. Fewer molecules are detected in our survey of VY CMa than in IRC +10216, with such carbon-containing species as CS, CN, and CCH absent, while SiO exhibits quite strong emission at nearly the same intensity as the CO line with readily detectable emission from its isotopomers ^{29}SiO and ^{30}SiO. A total of six molecules are detected via their line emission, namely CO, SiO, HCN, HCO^+, SO, and SO_2. Plots of the actual line spectra observed by us are presented in Appendix C together with tables showing the transition intensities. Comparison of continuum spectral measurements for IRC +10216 (Sopka *et al.* 1985) and VY CMa (KSR) suggests that the shell of VY CMa is cooler, as the peak of the radiation is at $\sim 20\,\mu$m as compared with $\sim 10\,\mu$m for IRC +10216. For reference, the radiation from the other evolved star observed by us, OH 231.8+4.2, peaks near $42\,\mu$m (KSR), indicating

that it is in turn cooler than VY CMa.

Our observations were centered on a nominal source position of $\alpha(1950) = 07^h20^m54.60^s$, $\delta(1950) = -25°40'12''$. A source velocity of v_{LSR} = 18.7 km s^{-1} was assumed for the observations and is used for the line plots of VY CMa appearing in Appendix C.

B. Observed Line Flux

Among the spectral line surveys considered in this thesis, those of VY CMa and OH 231.8+4.2 are the most limited in terms of the range of frequencies covered. In part this is because their line emission is the least intense among the various sources, so that we chose to concentrate on a smaller set of detectable molecular lines in each case. This approach led to a similar set of observations for each of these two sources, particularly given their relative proximity to each other on the sky which allowed us to observe them using a single tuning of the receiver for each frequency by merely slewing the telescope between the sources. Our selected frequencies amounted to some 30% of the frequency range between 330 and 360 GHz, contained in a number of short segments, with approximately the same specific frequencies observed in the two sources.

In VY CMa, we detect strong line emission from CO, SiO, HCN, and SO, as well as weaker emission from HCO^+ and SO_2. The SiO J = 8–7 line actually has a peak temperature greater than that of the CO J = 3–2 line, although its integrated intensity is slightly less as a result of its somewhat narrower line profile. Each of these two lines is responsible for approximately 30% of the total integrated line flux detected in our observations. Table 5.9 gives the relative proportions of the line flux in our observations contributed by various species. A total of 11 lines are detected, with no unidentified lines included in our data.

As for the other sources with incomplete frequency coverage, we derive both upper and lower limits for the integrated line flux. The upper limit is obtained by averaging the integrated line intensity over the range of frequencies observed by us, and the lower limit by averaging over the entire 330–360 GHz range instead. These correspond to assuming that the same average line emission would be found in the unobserved portion of the window to obtain the upper limit or that no additional lines would be found

TABLE 5.9
SIGNIFICANT FLUX CONTRIBUTIONS BY SPECIES FOR VY CANIS MAJORIS

Species	N_{lines}	$\int T_{MB}\, d\nu$ (K MHz)	Relative Contribution (% of Total Line Flux)
SiO [a]	3	208.8	38.4
SiO	1	155.6	28.7
CO	1	163.2	30.0
HCN	1	84.8	15.6
SO	2	64.5	11.9

[a] Includes all isotopomers, *i.e.*, SiO, ^{29}SiO, and ^{30}SiO.

to obtain the lower limit. Given our attempt to include strong lines in our observations, the remainder of the nominal frequency range is unlikely to contain the same average intensity as that observed by us. Conversely, it is certain to contain at least some line emission, although the actual amount is likely to be relatively small. In this case, because the observed frequencies amount to only 28% of the window, the upper limit is three times greater than the lower limit so the actual line flux remains rather uncertain. Converting our average main beam temperatures yields an upper limit of 2.1 Jy and a lower limit of 0.6 Jy for the line flux; we expect the actual value to be closer to the lower limit.

We did not detect the continuum emission from this source in our heterodyne observations. Instead, we compare the above values with published total broadband flux values below.

C. Extrapolation for Weak Lines

Given the rather few lines actually detected, it is difficult to draw reliable conclusions about the distribution of line intensities. We plot the observed distribution and perform the same type of power-law fit as before, including all of the observed lines in the fit. The result is a power-law index of -0.51, as shown in Figure 5.15. Extrapolating the derived fit to zero intensity suggests that the total line flux observed by us be increased by 10% in order to account for weak lines within our frequency range which were not detected. However, this correction is highly dependent upon the value of the power-law index, as shown by (5.2) and (5.4). It is somewhat difficult to assess the uncertainty in the fit for such a limited number of data points, particularly as the observed line distribution itself would likely show significant changes as more lines were detected. However, we note that the derived value is similar to that found for IRC +10216. The emission from VY CMa and IRC +10216 are also similar in that strong line emission

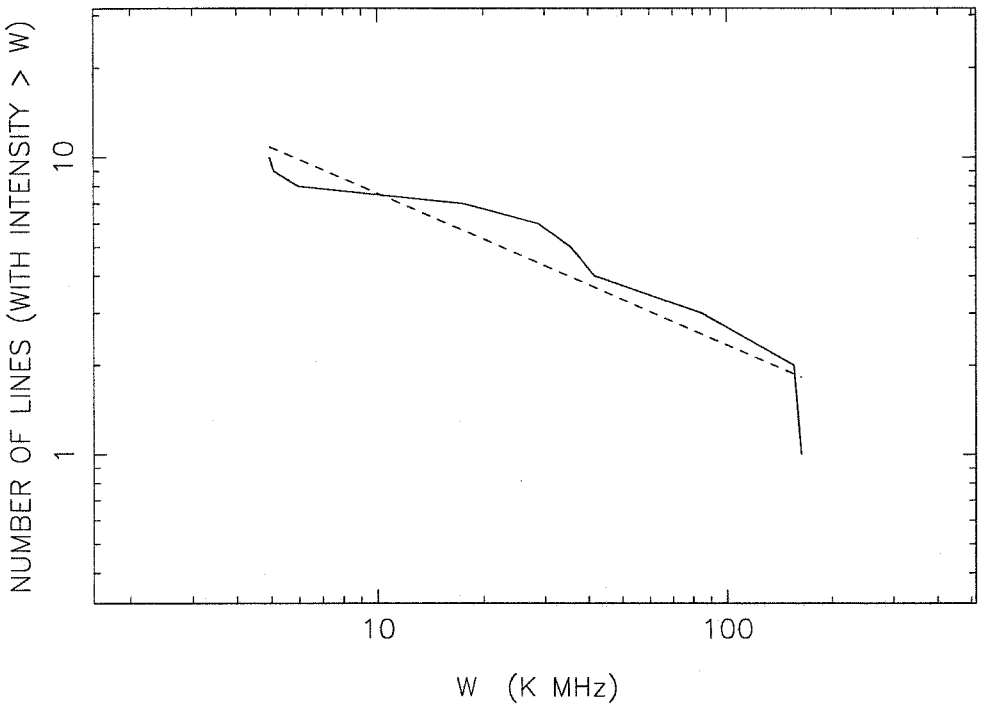

Figure 5.15 Distribution of observed integrated line intensities from the VY CMa line survey. Because of the relatively few lines detected, any fit to the data is rather uncertain. We show a fit to the entire data range which yields a slope of −0.51.

from a few species dominates the observed line flux, while emission from "complex" species which would have more numerous lines is reduced or absent. Thus we believe the actual line distribution is likely to be well represented by a power-law model with an index of ~ -0.5 or -0.6, so that the correction for undetected weak lines will be fairly small.

D. Comparison with Additional Flux Measurements

We again compare our line flux with the observed broadband flux values from Sandell (1994), particularly the 800 and 850 μm values. KSR present the same observational data in somewhat greater detail, with their Table 5 showing the extent to which the measured fluxes varied between observing dates. The averaged values for both the 800 and 850 μmmeasurements are 2.2 Jy, with a formal uncertainty of 0.2 Jy quoted by Sandell. According to KSR, the CO J = 3–2 line is expected to contribute 0.3 Jy to the flux measured with the 850 μm filter. They conclude that this can explain the slight bump they find in their data at this wavelength, and also that spectral line emission is therefore unlikely to contribute significantly to the

TABLE 5.10
SIMULATION PARAMETERS FOR VY CANIS MAJORIS

Species	T_{ex} (K)	N_T (cm^{-2})	ΔV (km s^{-1})	Velocity Profile
SO	150	5.0×10^{14}	50	Gaussian
SO_2	150	4.0×10^{14}	50	Gaussian
CO	150	1.0×10^{18}	70	Gaussian
SiO	150	2.0×10^{14}	50	Gaussian
^{29}SiO	150	5.0×10^{13}	50	Gaussian
^{30}SiO	150	3.0×10^{13}	50	Gaussian
HCN	150	9.0×10^{13}	50	Gaussian
HCO^+	150	4.0×10^{12}	50	Gaussian

total flux at submillimeter wavelengths as the contribution of the strongest line is fairly small. However, as we have seen in several sources already, the CO line may represent only 30% of the total line emission in the 330 – 360 GHz range, and this is indeed what we find even considering only the lines detected from our limited survey. Since the SiO J = 8–7 line has approximately the same integrated intensity as the CO line, these two lines alone would give a value of ~0.6 Jy for the line emission if we adopt their value for CO, in agreement with the lower limit found above. Our upper limit would correspond to having line emission responsible for nearly the entire observed flux. We interpret these data to imply a contribution of the lines of $\gtrsim$30% to the observed total flux at these wavelengths, taking our lower limit as approximately correct.

A model fit to their submillimeter observations by KSR yields a spectral index of 2.6 and an emissivity index for the dust of 0.9. This fit would predict a value of 1.7 Jy at 850 μm, in reasonable accord with the value of 1.6 Jy obtained by subtracting our lower limit for the line flux. Based upon our simulations of the line emission shown below, it seems likely that the other data of KSR will have smaller line contributions. Thus their model appears to reasonably describe the continuum emission from VY CMa and is consistent with a 30% line flux contribution at 850 μm.

E. Simulated Spectra

In Table 5.10 we show the molecular parameters used in our simulations of the VY CMa molecular emission. We have assumed a temperature of 150 K and derived the required column densities for each

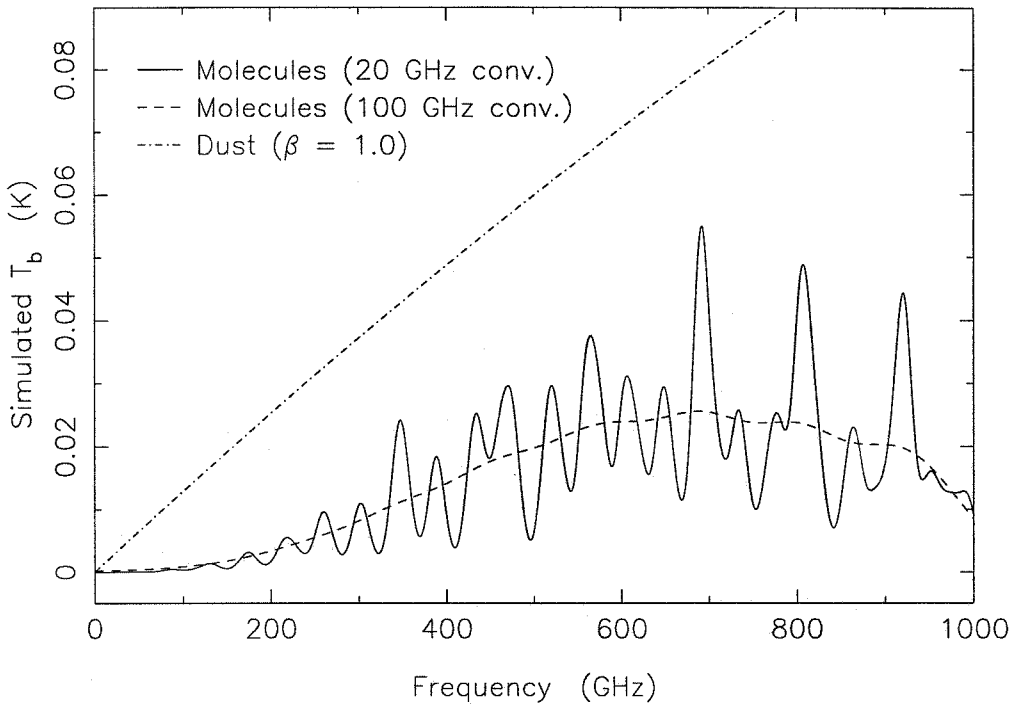

Figure 5.16 Simulated molecular emission from VY CMa convolved with a 20 GHz Gaussian and with a 100 GHz Gaussian and compared with a model dust spectrum. The molecular spectrum is obtained using parameters derived from our observational data; the dust spectrum shown assumes a temperature of 150 K, an optical depth of unity at 10 μm, and β = 1.0 for the emissivity index. Details of the simulations are given in the text.

of the species we observe as described in §4.7, adopting a width of 50 km s^{-1} for the line profiles with the exception of CO for which we use 70 km s^{-1}. The rather high temperature was deliberately chosen to see whether the line emission would become important at higher frequencies. This spectrum can be compared with the contour plot below to assess the effects of varying the temperature. While the observed lines exhibit somewhat irregular line profiles, we have used Gaussian profiles as a simple approximation. Particularly given our limited observational data, the simulations are intended only as indicators of very general trends and care should be taken not to assign great significance to specific details. The simulated spectrum we calculate is convolved with a 20 GHz Gaussian and a 100 GHz Gaussian and plotted in Figure 5.16 together with a model dust spectrum whose temperature of 150 K and emissivity index of 1.0 are taken from KSR. The absolute scaling of the dust model shown is chosen to give a flux of 1.6 Jy at 350 GHz obtained using our lower limit as the line flux and a value of 2.2 Jy for the total flux.

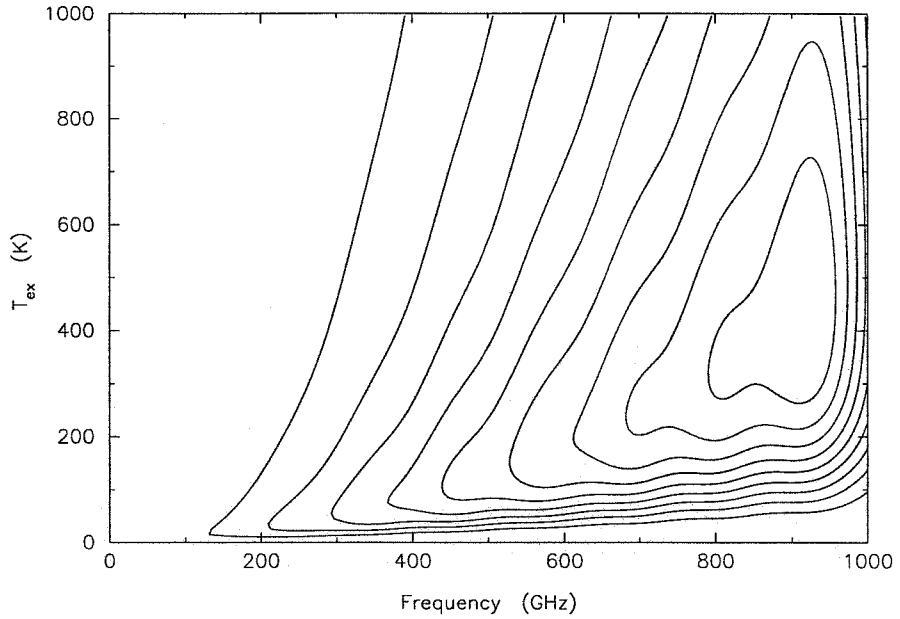

Figure 5.17 Contours of the simulated molecular line emission for VY CMa as a function of frequency and excitation temperature. The spectrum is simulated and smoothed by convolution with a 100 GHz Gaussian for a given excitation temperature; the contours represent the brightness temperature of the emission as before. Contour lines are at intervals of 0.36 K.

The structure seen in the molecular spectrum results from the strong lines of CO and SiO, with the largest peaks occurring where two of the lines are close together. Even for the relatively warm excitation temperature used, the spectrum begins to decrease at frequencies above 700 GHz when averaged over a large bandwidth. The greatest contribution of the emission lines to the total flux would appear to occur for frequencies between 300 and 600 GHz; the line flux contribution within this range is only moderate, with the peak near 350 GHz corresponding to a ~35% contribution, while outside this range any contribution appears likely to be fairly small.

The contours of line emission based on our simulations at different excitation temperatures are shown in Figure 5.17. As before, we can see slight indications of the presence of particularly strong lines, in this case corresponding to the peaks of Figure 5.16 where both CO and SiO emission was combined. For increasing temperatures up to 400 K, the emission spectrum shows a shift of the largest intensity to

higher frequencies and an overall increase in the strength of the spectrum. It seems unlikely, however, that the line flux contribution we expect at other wavelengths would change dramatically, given the results of our observations in the 330 – 360 GHz range.

F. Summary

While our data permit the entire flux density seen at 850 μm in broadband observations to be ascribed to line emission, this seems rather unlikely. Instead, we believe our lower limit of a ~30% contribution of the line flux to the total flux is a more realistic estimate. The greater uncertainty in our determination of the line flux contribution for this source relative to the others we have considered reflects the reduced frequency coverage of the observations.

Our results for VY CMa are in several ways similar to those for IRC +10216. In both, we find a rather flat line intensity distribution, with the strongest lines seen dominating the total line flux. While the relative molecular abundances are clearly different in the two sources based on the observed spectra, in each case the CO J = 3–2 line contributed some 30% of the total line flux, with HCN approximately the same strength in IRC +10216 and SiO approximately the same strength here. The broad line profiles observed clearly contribute to the large line fluxes seen for both sources. However, the overall contribution of the lines in IRC +10216 appears to be significantly more than in VY CMa. This may result from several factors, including the different distances of these sources. As the molecules cool more quickly with radius than the dust (Kwan & Linke, 1982), the observed line flux contribution will generally decrease as the source becomes smaller than the beam, particularly at higher frequencies where the warmer gas is more important. The different chemistries and molecular abundances and different physical conditions in the sources will also cause the line flux contribution to vary.

5.9. OH 231.8 +4.2 Results

A. Source Description

As noted above, OH 231.8+4.2 was chosen together with VY CMa as an oxygen-rich evolved star for comparison with the carbon-rich circumstellar shell of IRC +10216. OH 231.8+4.2 and VY CMa

are located within some 15 degrees of each other on the sky; thus we were able to conveniently observe both stars at the same LO settings. In general, switching between observations of VY CMa and of OH 231.8+4.2 could be accomplished simply by repointing the telescope and adjusting the LO frequency without the requirement of manually retuning the receiver. The observations for the OH 231.8+4.2 survey were centered on a source position of $\alpha(1950) = 07^h39^m59.00^s$, $\delta(1950) = -14°35'41''$, with a source velocity of $v_{LSR} = 30\,\mathrm{km\ s^{-1}}$ used for the observations. As shown by the figures of Appendix C, the full width of the CO J = 3–2 line is observed to be nearly 200 km s^{-1}; a full width of 100 km s^{-1} has been observed for the OH maser profile (Turner 1971; Morris & Bowers 1980). OH 231.8+4.2 is located at a distance of 1400 pc, roughly the same distance as VY CMa but several times more distant than IRC +10216.

Like VY CMa, OH 231.8+4.2 exhibits OH, H_2O and SiO maser emission (Morris & Knapp 1976; Bowers & Morris 1984; Barvainis & Clemens 1984). A relatively rich molecular emission spectrum has been observed from the circumstellar shell, with 13 molecules known in the outflow (Morris *et al.* 1987). We detect emission from six molecules, the same number as in VY CMa, with the difference that the CS J = 7–6 line is seen towards OH 231.8+4.2 while the HCO^+ J = 4–3 line is not detected. (Note that the HCO^+ line may be partially obscured by the nearby SO_2 line.) The observed line spectra from the two sources may be compared using the plots and tables of Appendix C; we note here simply that the SO_2 emission is much stronger and the SiO emission is much weaker in OH 231.8+4.2 than was seen in VY CMa, suggestive of a different chemical environment.

The continuum spectrum for OH 231.8+4.2 peaks near 42 μm (KSR), indicating that this object is cooler than VY CMa which is in turn cooler than IRC +10216 as noted above.

B. Observed Line Flux

As noted above, our survey of OH 231.8+4.2 was similar in scope to that of VY CMa. The data are presented in Appendix C, with plots and tables displaying the actual lines detected in this source. The frequency coverage was again approximately 30% of the entire 330 – 360 GHz range in a number of discontinuous segments chosen to include particular molecular lines.

TABLE 5.11

SIGNIFICANT FLUX CONTRIBUTIONS BY SPECIES FOR OH 231.8+4.2

Species	N_{lines}	$\int T_{MB}\, d\nu$ (K MHz)	Relative Contribution (% of Total Line Flux)
SO_2	14	189.8	47.7
CO [a]	2	159.7	40.1
CO	1	114.8	28.8
SO	2	27.7	6.9
HCN	1	13.3	3.4
CS	1	4.8	1.2
SiO	1	3.0	0.8

[a] Includes CO and ^{13}CO.

The actual spectra observed in the two sources are somewhat different, which is reflected in the varying contributions of different species to the total line flux, with the values for OH 231.8+4.2 shown in Table 5.11. While the CO J = 3–2 line again contributes some 30% of the detected line flux, in this source the corresponding ^{13}CO line is one third as strong whereas in VY CMa it was not detected. The SO_2 emission lines are also much stronger in this source, and together they contribute almost half of the total line flux as compared with at most a few percent in VY CMa. On the other hand, the SiO emission which was so strong in VY CMa is absent here. The overall number of species detected is rather similar in both sources, although the relative abundances of the species are clearly different.

We compute upper and lower limits for the line flux in the usual manner, obtaining values of 1.3 Jy and 0.4 Jy respectively. The rather large uncertainty is again the result of our limited frequency coverage; however, we again expect the actual value to be closer to our lower limit. In that regard, we note that our observations include nearly all of the SO_2 lines within the 330–360 GHz range. These values are compared below to broadband flux measurements, since we did not detect the continuum emission in our observations.

C. Extrapolation for Weak Lines

Many of the comments made above for VY CMa about fitting the line intensity distribution apply in this case as well. The rather small number of detected lines makes the fitting itself less accurate, and also raises the question of whether the limited data reflect an actual line distribution. This latter question may be particularly significant here, where numerous lines of SO_2 were detected; the particular lines observed

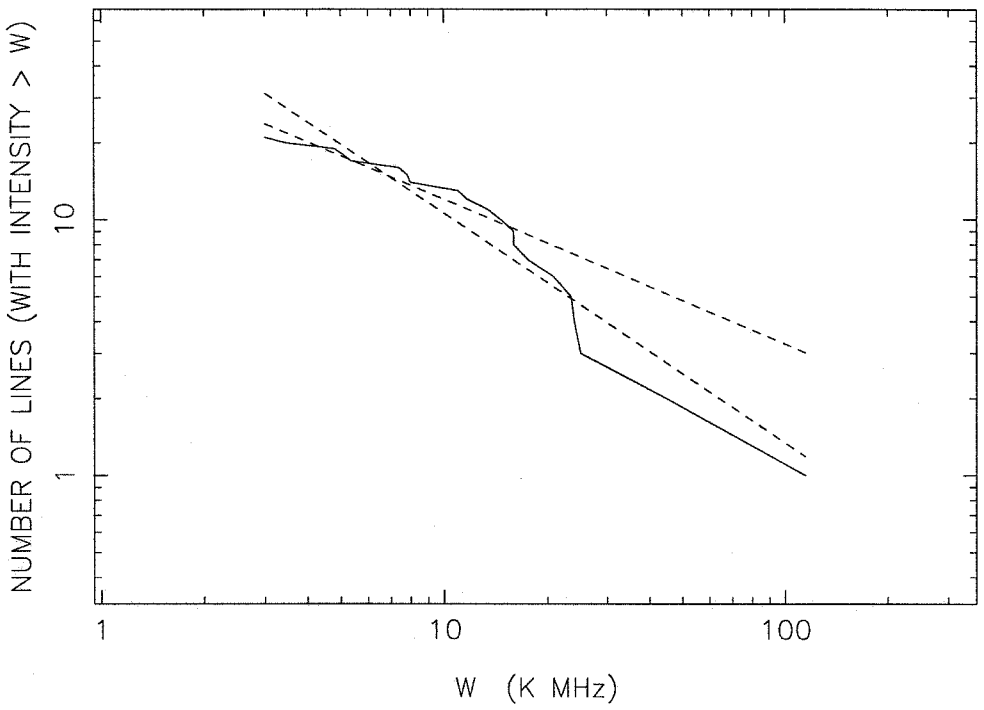

Figure 5.18 Distribution of observed integrated line intensities from the OH 231.8+4.2 line survey. Because of the relatively few lines detected, any fit to the data is rather uncertain. We show two fits, one a fit to all of the data and one a fit to the observed lines with $3 < W < 20$. These result in derived slopes of -0.89 and -0.57 respectively.

determine to some extent the fit we obtain.

The usual plot of the observed line intensities is shown in Figure 5.18. In addition, two fits to the distribution are plotted in order to show the uncertain nature of such a fit in this case. The first includes all of the data and yields a power-law index of -0.89, while the second fit is limited to the range of values $3 < W < 20$ and yields a value of -0.57 for the index. Since the line flux correction depends strongly on the power-law index of the line intensity distribution, these two fits give vastly different results. In the very steep case, the extrapolation to zero intensity actually would suggest that weak undetected lines contribute nearly double the observed line flux so that our above flux values should be tripled. As this seems unlikely, we conclude that the line distribution is not accurately reflected by the limited data available. The second fit produces an estimated correction of 23% to the observed line flux which appears to be more reasonable but is hardly more well-determined. We therefore use the upper and lower limits derived earlier without

TABLE 5.12

SIMULATION PARAMETERS FOR OH 231.8+4.2

Species	T_{ex} (K)	N_T (cm^{-2})	ΔV (km s^{-1})	Velocity Profile
CO	40	5.0×10^{17}	50	Gaussian
^{13}CO	40	2.0×10^{17}	50	Gaussian
SO	70	2.0×10^{15}	25	Gaussian
CS	70	1.2×10^{13}	20	Gaussian
SiO	70	4.0×10^{12}	20	Gaussian
HCN	40	9.0×10^{12}	25	Gaussian
SO_2	40	1.3×10^{15}	20	Gaussian

correction, adopting 0.5 Jy (somewhat greater than the lower limit) as a rough estimate of the line flux.

D. Comparison with Additional Flux Measurements

The broadband flux observed for OH 231.8+4.2 by Sandell throughout the submillimeter range is approximately the same as that found for VY CMa. At 800 and 850 μm, the observed fluxes are 2.6 ± 0.2 Jy and 2.2 ± 0.1 Jy, respectively. As was the case for VY CMa, a more complete analysis of the data and more detailed listings of the observed values are given by KSR, who derive an emissivity index of 0.85, essentially the same as for VY CMa.

Our upper and lower limits are somewhat reduced relative to our values for VY CMa and therefore give somewhat lower values for the contribution of the line emission to the total flux. Our overall estimate of 0.5 Jy for the line flux corresponds to ~20% of the total flux instead of the 30% found for VY CMa. The uncertainty in both of these values is rather large, however. The simulated spectra discussed below suggest that the line contribution is reduced in OH 231.8+4.2 at other wavelengths as well.

E. Simulated Spectra

We perform the usual set of simulations for OH 231.8+4.2 using the molecular parameters given in Table 5.12. We have adopted cooler excitation temperatures (40 or 70 K) for the molecules, selecting the one for which the required column density is nearer its minimum value. The column densities are again chosen as required by our observations. Figure 5.19 shows the resulting spectrum after convolution with a 20 GHz Gaussian and a 100 GHz Gaussian, and a model dust spectrum for comparison. The dust

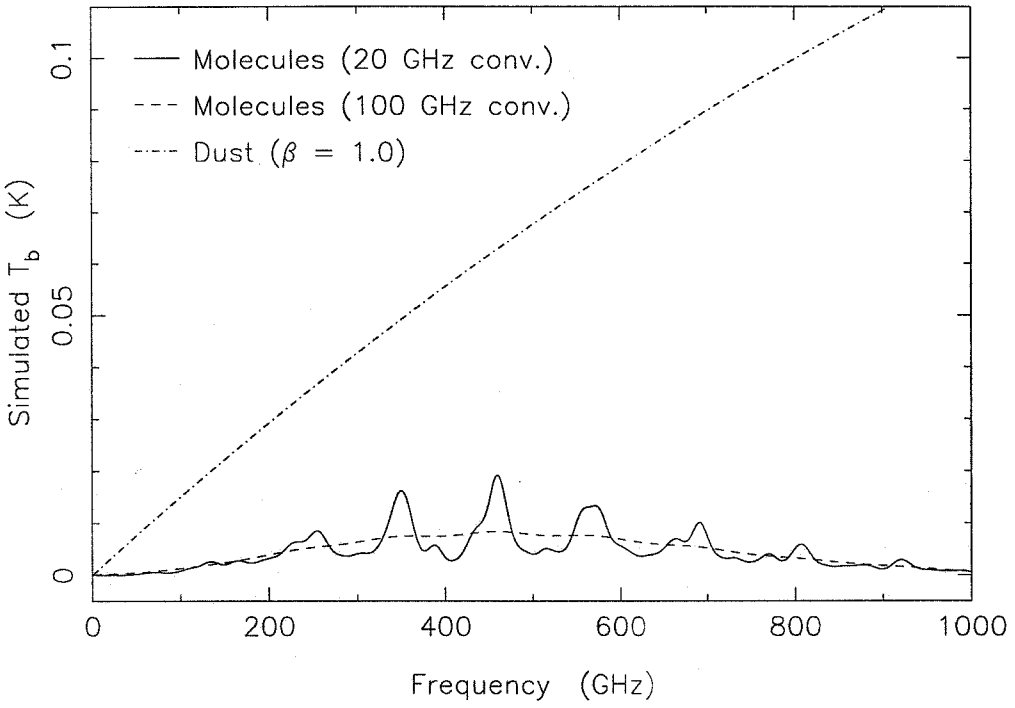

Figure 5.19 Simulated molecular emission from OH 231.8+4.2 convolved with a 20 GHz Gaussian and with a 100 GHz Gaussian and compared with a model dust spectrum. The molecular spectrum is obtained using parameters derived from our observational data; the dust spectrum shown assumes a temperature of 100 K, an optical depth of unity at 10 μm, and β = 1.0 for the emissivity index. Details of the simulations are given in the text.

emissivity index is taken to be 1.0, with an optical depth of unity at 10 μm, and the temperature is assumed to be 100. The absolute scaling is set to give a flux of 1.7 Jy at 350 GHz, using our estimate of 0.5 Jy for the line flux and a value of 2.2 Jy for the total flux. We note that for frequencies below the peak of the blackbody curve where the emission is thin, changes in the dust temperature have little effect on the shape of the spectrum. Thus the particular spectrum shown would vary only slightly even if the dust were taken to have a temperature of 40 K.

The simulated molecular spectrum shown in Figure 5.19 has its peak at a lower frequency than the VY CMa simulation of Figure 5.16, largely because of the cooler temperatures assumed for the molecules. In particular, the CO J = 4–3 line which can be distinguished near 460 GHz represents the peak of the emission in this source. The general appearance of the spectrum is also smoother; this results from the SO_2 emission which is distributed over lines at many frequencies instead of only at regular intervals as is

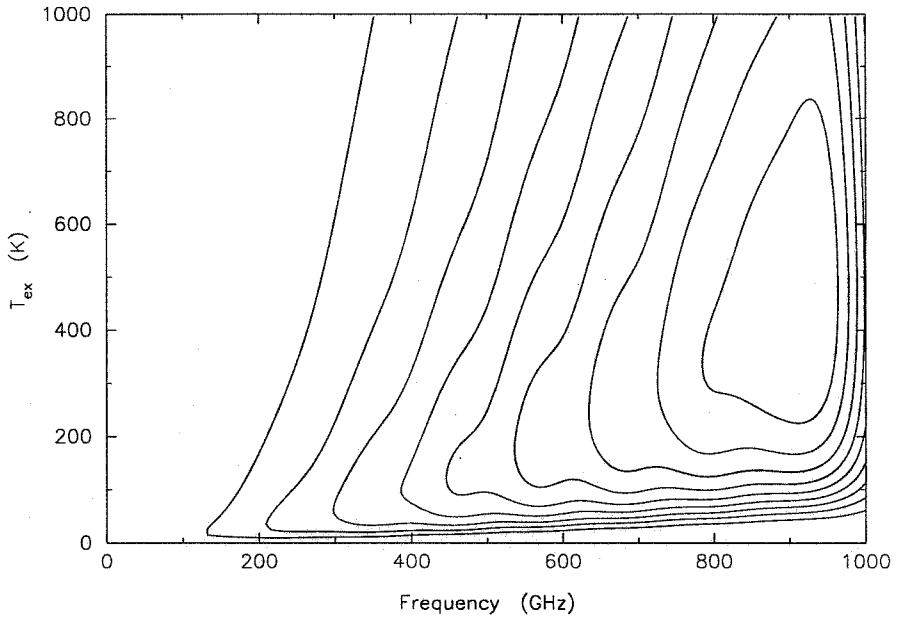

Figure 5.20 Contours of the simulated molecular line emission for OH 231.8+4.2 as a function of frequency and excitation temperature. The spectrum is simulated and smoothed by convolution with a 100 GHz Gaussian for a given excitation temperature; the contours represent the brightness temperature of the emission as before. Contour lines are at intervals of 0.22 K.

the case for the simple linear rotors.

We display the contours of the simulated line emission as a function of frequency and temperature in Figure 5.20. The usual results are also seen here: the frequency of the peak intensity increases with increasing temperature, while at frequencies above the peak intensity, the main effect of an increase in the temperature is to produce stronger emission without greatly changing the general shape of the spectrum. Particularly as the envelope of OH 231.8+4.2 is known to be relatively cool (KSR), these simulations indicate that the line flux will reach its maximum at frequencies below 500 GHz, so that the percentage of the total flux contributed by the line emission will be small at higher frequencies, as has been generally the case for all of the sources considered.

F. Summary

While the specific transitions which were detected in our line survey of OH 231.8+4.2 were different

from those seen in the VY CMA survey, the overall results concerning the integrated line flux in the two sources are rather similar. In this case we estimate the line flux to be $\gtrsim$20% of the total flux observed in broadband measurements; while this is slightly less than was deduced for VY CMa the actual contribution is rather uncertain because of the limited frequency coverage of the survey. The CO J = 3–2 line is again responsible for $\sim$30% of the line flux; however ^{13}CO and SO_2 are important sources of flux in OH 231.8+4.2, while SiO is not important. The broadband fluxes measured for the two sources are rather similar, and in both cases an emissivity index of $\sim$1 is derived by KSR by fitting the data over a wide range of frequencies. Our simulations indicate that the maximum contribution of the line emission to the total flux is likely to be the 20–30% found from our surveys, and that the contribution will be less at other frequencies. This is especially true at higher frequencies for OH 231.8+4.2, where the cool temperature of the envelope gives reduced line flux values while the dust emission continues to rise.

5.10. Summary of Results

The analysis of the molecular emission line contribution to the total flux observed for the individual sources considered above permits us to identify some general principles relating to the importance of the line emission. The surveys clearly show that in some cases, half or more of the total 870 μm flux observed from an object may be the result of integrated line emission, verifying the earlier results of SBMP. We discuss here some practical considerations regarding the relative magnitude of the line emission and some of the general results and implications of our surveys, particularly the trends which were observed in several different sources.

The first principle concerning the importance of the integrated line flux consists of a statement of the obvious, namely that the line emission will contribute a significant amount of flux only when strong, bright lines with large velocity widths are observed. Of course, what constitutes a bright line will vary with the particular source under consideration, so this does not actually give any specific information. One point which is of interest is that the line width is in fact only important for optically thick lines. The integrated intensity of an optically thin line is independent of the actual velocity profile, since the entire cloud is sampled by the observed radiation. Hence, one measure of the line brightness of a source would be the

optical depths observed, although the integrated intensity of an optically thick line is less than would be observed for the same material with a sufficiently broad profile to give optically thin emission. In any case, the empirical evidence is that the line emission contributes significantly to the total flux for the sources having the brightest and broadest line emission, which is in general associated with large opacities.

As a related point, it is clear from our findings for IRC +10216 that a relatively few bright lines may be sufficient to produce significant line flux. Thus while the compressed view of the Orion-KL survey with its confusion-limited spectrum showing strong line emission throughout the entire band is visually more impressive than the comparatively sparse spectrum for IRC +10216, the lines in IRC +10216 contribute a greater percentage of the observed total flux in the range of our surveys. Of course, the significance of the line emission in the IRC +10216 case may be more dependent upon the particular frequencies involved, as the inclusion or exclusion of the few important lines becomes critical to the average line flux.

Any set of observations will detect only lines above some minimum value, and thus we can measure only the flux contained in lines stronger than this minimum intensity. The amount of flux which might be contributed by the integrated emission in the possibly numerous weak lines is potentially significant. We follow SBMP in modeling this by assuming a power-law distribution of line intensities and deriving fits to the observed distributions. As discussed earlier, a power-law distribution with an index of -1 or less would correspond to an infinite amount of flux contained in weak lines if extrapolated to zero intensity. The derived power-law index is in fact critical in evaluating the total line flux, as the extrapolated contribution of undetected lines can range from nearly zero to infinity for an index within the allowed range between 0 and -1. Particularly for sources with few detected lines, it is difficult to determine an accurate value for this index, and perhaps even more difficult to determine how accurate a particular value might be. Empirically we have found, however, that values between -0.6 and -0.8 were typical for the observed sources, with some correlation between the complexity of the observed molecules and a steeper variation. Based on our fits, the amount of flux in undetected weak lines was found to be between 10% and 30% of the actual detected flux, with the larger value corresponding to the steeper fits.

Particularly for the flatter distributions, the strongest lines observed dominated the line flux. The simulations based on our derived molecular parameters tended to show the effects of these lines as local

peaks in the emission. As a large part of the flux is carried by relatively few species, this suggests that simulations which give good results for the dominant species will give reasonably correct models for the emission line flux, without requiring a complete set of molecular column densities, line profiles, and excitation temperatures to be determined for all species which might be present.

Another important consideration which will have an impact on the relative contribution of line emission to the total flux concerns the distance to the source and the observed spatial distributions of the molecules and the dust. For example, in IRC +10216 the dust remains warm out to a greater distance from the central star than does the gas. Hence as the beam size of the observations varies, the coupling of the molecular emission to the beam will vary in a different manner than the continuum emission, leading to changes in the relative strengths of the two kinds of emission. For a constant beam size of $\sim$20″, as in our observations and simulations, the effect is manifested as a variation with frequency as follows: the warmer dust continues to show an increase in emission with increasing frequency well beyond the 1000 GHz limit shown, while the generally cooler molecular gas displays a decrease in its smoothed emission beyond a frequency of $\sim$600 GHz. Hence changes in the percentage of the total flux contributed by molecular lines will be seen as observations are made with different telescopes having different beam sizes at different frequencies. Care must therefore be taken when estimating the significance of the line flux for different observing parameters than those for which it has been determined.

Turning now to specific findings from our surveys, the relative contribution of the molecular line emission to the total flux over the 330–360 GHz range was found to vary between $\sim$10 and $\sim$65% for the sources we observed. Table 5.13 gives a brief summary of the total flux and line flux values obtained for each source. We show the lower limits for the line flux derived for the different sources; we also show an estimated value for the emissivity index β which we derive after correcting the broadband flux measurements for the line flux contribution shown. These simple estimates are based solely on the flux variation and do not include modeling of the sources (*e.g.*, morphology, optical depth, etc.). Hence the values given here should be considered as general indicators for comparison only. The detailed studies of the individual sources cited below should be referred to in conjunction with our findings regarding the line flux contribution for more complete information. For Orion-KL and Orion-S, our derived index of

TABLE 5.13

SUMMARY OF LINE SURVEY FLUX RESULTS

Source	Frequency Range (GHz)	Coverage Achieved [a] (%)	Line Flux [b] (Jy)	Total Flux [c] (Jy)	Contribution of Line Flux (%)	Emissivity Index β [d]
Orion-KL	325–360	100	85	171 [e]	50	2.0 [f]
Orion-S	330–360	63	5.7	74 [e]	8	2.0 [f]
IRAS 16293–2422	330–360	50	0.9	17	5	1.0 [g]
IRC +10216	330–358	100	4.6	7.0 [h]	65	1.4 [i]
VY CMa	330–360	30	0.6	2.2	27	1.0 - 1.5 [j]
OH 231.8+4.2	330–360	30	0.5	2.2	23	1.0 - 1.5 [j]

[a] Fraction of the stated frequency range which was included in the observations.

[b] Values shown are the lower limits for the line flux (see the individual source discussions for details).

[c] Except as noted, the total flux values are taken from Sandell (1994).

[d] Estimated values for β after line flux corrections are made.

[e] Total flux values for Orion-KL and Orion-S are obtained from our observations.

[f] Based on data from Mezger *et al.* (1990).

[g] Based on data from Sandell (1994) and Mundy *et al.* (1992).

[h] Estimate based on our derived line flux and narrowband measurement of Sandell cited by Avery *et al.* (1992).

[i] Based on data from Sandell *et al.* (1994) and Sopka *et al.* (1985).

[j] Uncertain because of large spread in possible line flux correction; based on data from Sandell *et al.* (1994) Knapp *et al.* (1993).

β = 2.0 agrees with the previous determination by Mezger *et al.* (1990); their analysis made use of an estimated correction for line flux as described earlier. Mundy *et al.* (1992) estimated an emissivity index of 1.0 for IRAS 16293–2422. Given the relatively small contribution of the emission lines to the flux, it is not surprising that we also obtain β = 1.0 for this source. For IRC +10216, we find a value of 1.4 for β, slightly greater than the value of 1.2 derived by Sopka *et al.* (1985). The increase may be traced directly to our correction for line flux, but is relatively small because the previous result was fairly well constrained by a number of short wavelength measurements. In fact, the main effect of our correction was to bring the 870 μm flux values into better agreement with the overall fit as discussed previously. For VY CMa and OH 231.8+4.2, the great uncertainty in the line flux correction leads us to give instead an approximate range for β. Knapp *et al.* (1993) estimate the dust emissivity to vary approximately as β = 1 in each of these sources; this value falls at the lower end of our estimated range. If the line flux at 870 μm is significantly greater than our minimum value, then the estimated value for β would also be significantly greater. We note that in all cases, an increased flux contribution from the lines over the 330–360 GHz range would lead to larger changes in the value of β than we have observed here.

Different species were found to be the most significant flux contributors in the different sources. The CO J = 3–2 line at 345 GHz near the center of the frequency range was usually found to be the strongest line in terms of both brightness temperature and integrated intensity, making it the most important line for the total flux in nearly all cases. However, we note that towards IRC +10216 the HCN J = 4–3 line at 354 GHz was nearly as strong, while towards VY CMa the SiO J = 8–7 line at 347 GHz was actually brighter but had a slightly lower integrated intensity. In other cases, while no individual line had an intensity comparable to the CO line, the overall flux contribution from several lines observed from a single species was found to exceed that of CO, *e.g.*, SO_2 in Orion-KL was responsible for roughly twice as much flux as CO. Combining the emission from isotopomers, we find that HCN is responsible for 40% of the line flux from IRC +10216 compared to 28% for CO, SiO contributes 38% compared to 30% for CO in VY CMa, and SO_2 contributes 48% compared to 40% for CO in OH 231.8+4.2. By contrast, the CO emission in Orion-S and IRAS 16293–2422 was responsible for 49% and 48%, respectively, of the total line flux observed for each source, with no other species responsible for more than 12% of the line flux. Hence the different physical and chemical environments in the various sources lead to very different emission patterns. One very crude estimate of the line flux at this frequency from a source which has not been extensively observed would be to consider the type of source and to scale the CO emission in that source according to our findings in these surveys. Thus for an active high-mass star-forming region with observable hot cores and large line densities such as Orion-KL, one would assume the observed CO line emission to represent perhaps 15% of the total line flux, while for a significantly younger object such as Orion-S or IRAS 16293–2422 that figure would change to nearly 50%. However, without additional survey data we are unable to accurately assess the reliability of this method; it might also prove difficult to select the proper figure for sources which do not match closely one of the types observed by us.

A quite general trend which emerged from our work was the tendency of the simulated molecular spectra to first increase and then decrease with frequency, with the particular frequency where the turnover occurs determined to a large extent by the temperature of the gas. We found this to be true in all cases, independent of the relative importance of the line emission to the total flux. This tendency is easily understood in terms of the populations in the various levels involved in the different transitions, but the

simulations provide a clear demonstration and quantitative estimation of the actual frequency dependence of the spectra which has not been available before. This behavior, coupled with the increase of the dust continuum emission with increasing frequency up to well past 1000 GHz, leads to a significant decrease in the contribution of molecular emission lines at frequencies above the turnover point which is generally in the range of 700 GHz or lower. Our simulations of the line emission as a function of both frequency and temperature suggest that this pattern will continue even as warmer gas is probed by higher frequency observations with smaller beam sizes.

A second pattern which is apparent in the simulations is the frequent presence of a local peak in the molecular emission at a frequency near 345 GHz which corresponds to our observed frequencies. It might be suspected that this is the result of a selection effect, *i.e.*, since our observations detect species which exhibit emission in this frequency range, using parameters derived from our observations will yield an emission peak there. This is true, of course, although the extent to which this affects the accuracy of the overall spectrum is unclear. There are two potential dangers apparent, which are the possibility of leaving out an important species which does not have a line within our range of frequencies, and the possibility of selecting a specific component of gas within the source having the appropriate excitation to yield emission in our range while ignoring warmer or colder gas which might yield line emission at a different set of frequencies. As an example of this latter effect, the different CO emission lines in IRC +10216 reflect the temperatures of the regions where each becomes optically thick (*cf.* Sahai, 1987). For the lower J lines, this occurs at a greater distance from the central source where the gas is cooler, and hence the brightness temperature of the emission lines increases with increasing J (although this may be altered by consideration of the relative sizes of the beam and the emission region). An example of the former effect may be seen in the simulations performed for IRAS 16293–2422. When the simulation is done using the upper limits derived from the observations, significantly increased emission is derived for lower frequencies where the species involved are wont to display emission. This is typical of what would be expected for heavier, more complex molecules, while light molecules such as hydrides might display emission at higher frequencies. Inasmuch as the simulations are probably more interesting at higher frequencies, where observing is generally more difficult, the possible emission from light species might

seem to be a greater problem. This is somewhat mitigated by the general interest in such lines, which have often been the target of specific observations, as some information concerning the possible abundances of the species in question may be available. The preferred solution to both types of problems is to make use of observations at multiple wavelengths in order to better constrain the molecular parameters. Particularly for carefully chosen sets of observations, this will reduce the problem of missing species whose transitions fall outside the observed regions. Although the simulations use LTE calculations, and hence are limited to the use of a single temperature, it is possible to obtain useful results even when multiple components are present in a source. One could select the parameters which give the best results for a particular frequency range of interest; alternatively one could perform multiple simulations as was done for Orion-KL, and if necessary devise an appropriate combination of the resulting spectra. Finally, the judicious use of upper limits on molecular column densities can provide useful insights into where the available data are unable to accurately constrain the simulated spectra.

Having addressed this issue at some length, we point out that for our purposes of evaluating the integrated line flux the simulations appear to give fairly reliable results. In particular, we do not believe that the integrated line emission at higher frequencies will be significantly greater than the results of our simulations. The overall trend of a decreasing relative contribution from the line flux above 600 GHz seems unlikely to change. We also note that a number of lines appear within the nominal 330–360 GHz range which often display quite strong emission, such as transitions of CO, CS, SiO, SiS, SO, SO_2, HCN, H_2CO, and CH_3OH. Since the lines of these species occur at different frequency spacings, the window around 345 GHz actually provides a tremendous and somewhat unique opportunity to observe all of these lines, and it is not entirely surprising that the average line intensity shows a peak there.

Finally, the combination of our observed spectra and simulations both for a single set of parameters and for varying temperatures suggest that in at least some cases, derived values of β, the emissivity index of the dust, will be too small unless corrections are made for the contribution of line emission to the different flux measurements. However, we find that the two sources which require the greatest correction for line emission (Orion-KL and IRC +10216) have been extensively observed at many wavelengths, and that fits to the total flux data are generally well constrained by shorter wavelength data where the corrections for

line flux are less significant. Indeed, Mezger *et al.* (1990) estimate corrections for the line flux in their 1.3 mm observations of Orion-KL in modeling the dust emission. The observed flux at 900 μm of Sopka *et al.* (1985) appears to require a substantial correction, given our finding that over half of the total flux at 870 μm results from line emission; however, the result of making this correction is to improve the agreement between that data point and the general fit to data between 50 and 1000 μm. The effects of a significant contribution from line emission to the total flux on a derived value of β will be greatest in the case where few observations are available with some (*e.g.*, at long wavelengths) requiring sizeable corrections and others (*e.g.*, at short wavelengths) requiring essentially no correction.

Chapter 6

Summary

6.1. Summary of Results

We have performed several extensive spectral line surveys for star-forming regions (Orion-KL, Orion-S, and IRAS 16293–2422) and circumstellar shells (IRC +10216, VY CMa, and OH 231.8+4.2). For each of the sources considered, we have compared the integrated line flux as determined from the line surveys with the total flux observed for the source, obtained either from our own observations or from published values for the total flux. These surveys have also greatly extended the emission line data available for these sources.

We have developed and implemented a variant of the CLEAN algorithm for the purpose of deconvolving double sideband observations. Our analysis of this algorithm has demonstrated its ability to generate an accurate representation of the underlying single sideband spectrum and the more than tenfold improvement in speed we obtained through our modifications. We have also developed a line catalog program which includes the unique capability of performing LTE simulations of line spectra involving many molecules over extensive frequency ranges. The catalog program also provides a means of planning and selecting observing frequencies, identifying observed lines, and analyzing the observed line emission in a consistent manner.

The integrated line emission has been found to be responsible for between 10 and 65% of the total

flux in the different sources, with different molecules responsible for significant fractions of the line flux in different sources. The brightest sources, Orion-KL and IRC +10216, were found to have the greatest contributions from lines, while the star-forming regions of Orion-S and IRAS 16293, both of which are thought to be in the early stages of star-formation, exhibited the lowest proportions of line flux in the observed total fluxes. Our simulations of the molecular emission for the derived source parameters in general showed a peak in the line contribution to the total flux in the range between 300 and 600 GHz, with reduced values both above and below this range, but more particularly at higher frequencies where the dust emission continues to increase. Hence the overall effect of correcting observed total flux values is to increase the emissivity index derived for a source (the spectral energy distribution becomes steeper because of the greater reduction in the continuum flux that is required at longer wavelengths). For sources where the line flux is never a significant contributor to the flux, any corrections to the derived value of β would be small, while larger corrections would of course result in larger changes in the value of β. However, we note that in some cases, a sufficient number of measurements exist at frequencies where the line flux contribution is small to constrain the value of β in spite of the line flux corrections which may be required at other wavelengths. We find this to be true for IRC +10216 and Orion-KL, where the 1.3 mm value for Orion-KL used in the fit has in fact been corrected for line emission. For both of these sources, the use of corrected values for the continuum flux improves the overall fit without dramatically changing the derived value of β.

6.2. Suggestions for Possible Future Work

The techniques developed during the course of this work will permit future line surveys to be carried out more easily, as much of the planning, line identification, and line analysis work may now be done using the software and techniques described in this thesis. As higher frequency and more sensitive receivers continue to become available, it will become possible to extend this work yet further in the number and types of sources considered and in the frequency ranges surveyed. The analysis of the line flux contribution as a function of frequency can then be compared to the results of our simulations. A number of additional comparisons between different sources will also be possible using the data thus

collected, and improved source models may be constructed. This may allow accurate estimates of the line spectrum and integrated line flux to be made based on simulations for a wider variety of sources. It may eventually be possible to classify different sources according to the observed molecular lines, identifying certain evolutionary phases of star formation with specific patterns of molecular emission for example. Our data, while limited, suggest a distinction between the physical and chemical regimes typified by Orion-S and Orion-KL which might be confirmed by observations including line surveys of additional sources.

Such future line surveys of additional objects would be well complemented by carefully calibrated narrowband observations aimed at determining the continuum flux in regions chosen to be free of line emission. Again as new receivers become available, such observations may be made at a range of wavelengths which has not been possible heretofore. Particularly for Orion-KL, where it is difficult to find a line-free region, the information in the line catalogs and the simulation capabilities will be helpful in determining the optimum frequencies for such measurements.

Further refinements in the software techniques may be contemplated, such as experimenting with different deconvolution methods besides the CLEAN method. The line catalog program will probably need to have additional species added as spectral line data become available. In addition, it may be possible to combine the LTE simulations of the present catalog software, which have the great advantage of speed and simplicity and allow large numbers of species and transitions to be included, with more complete simulations which take into account the physical conditions present in the sources.

References

Avery, L. W. *et al.* 1992, *Astrophys. J. (Suppl.)*, **83**, 363.

Barvainis, R. & Clemens, D. P. 1984, *Astron. Jour.*, **89**, 1833.

Batrla, W., Wilson, T.L., Bastien, P., & Ruf, K. 1983, *Astron. Astrophys.*, **128**, 129.

Becklin, E. E., Frogel, J. A., Hyland, A. R., Kristian, J., & Neugebauer, G. 1969, *Astrophys. J. (Letters)*, **158**, L133.

Becklin, E. E., & Neugebauer, G. 1967, *Astrophys. J.*, **147**, 799.

Blake, G. A., Sutton, E. C., Masson, C. R., & Phillips, T. G. 1986, *Astrophys. J. (Suppl.)*, **60**, 357.

Blake, G. A., Sutton, E. C., Masson, C. R., & Phillips, T. G. 1987, *Astrophys. J.*, **315**, 621.

Blake, G. A., van Dishoeck, E. F., Jansen, D. J., Groesbeck, T. D., & Mundy, L. G. 1994, *Astrophys. J.*, **428**, 680.

Bowers, P. F. & Morris, M. 1984, *Astrophys. J.*, **276**, 646.

Buhl, D., Snyder, L. E., Lovas, F. J., & Johnson, D. R. 1974, *Astrophys. J. (Letters)*, **192**, L97.

Cernicharo, J. & Guélin, M. 1987, *Astron. Astrophys.*, **183**, L10.

Cernicharo, J. & Guélin, M., Kahane, C., Bogey, M., Demuynck, C., & Destombes, J. L. 1991, *Astron. Astrophys.*, **246**, 213.

Cheung, A. C., Rank, D. M., Townes, C. H., Thornton, D. D., & Welch, W. J. 1968, *Phys. Rev. Lett.*, **21**, 1701.

Cheung, A. C., Rank, D. M., Townes, C. H., Thornton, D. D., & Welch, W. J. 1969, *Nature*, **221**, 626.

Cornwell, T. J. 1989, in *Diffraction-Limited Imaging with Very Large Telescopes*, eds. D. M. Alloin & J.-M. Mariotti (Dordrecht:Kluwer), p. 53.

Cox, P., & Mezger, P. G. 1989, *Astron. Astrophys. Rev.*, **1**, 49.

Cummins, S. E., Linke, R. A., & Thaddeus, P. 1986, *Astrophys. J. (Suppl.)*, **60**, 819.

Douglas, A. E., & Herzberg, G. 1941, *Astrophys. J.*, **94**, 381.

Downes, D. 1989, in *Diffraction-Limited Imaging with Very Large Telescopes*, eds. D. M. Alloin & J.-M. Mariotti (Dordrecht:Kluwer), p. 53.

Draine, B. T., & Lee, H. M. 1984, *Astrophys. J.*, **285**, 89.

Dunham, T. Jr. & Adams, W. S. 1937, *Pub. Am. Astr. Soc.*, **9**, 15.

Elias, J. H., *et al.* 1978, *Astrophys. J.*, **220**, 25.

Ellison, B. N. & Miller, R. E. 1987, *Int'l. J. IR & MM Waves*, **8**, 608.

Ellison, B. N., Schaffer, P. L., Schaal, W., Vail, D., & Miller, R. E. 1989, *Int'l. J. IR & MM Waves*, **10**, 937.

Genzel, R., & Stutzki, J. 1989, *Ann. Rev. Astron. Astrophys.*, **27**, 41.

Glassgold, A. E., Mamon, G. A., Omont, A., & Lucas, R. 1987, *Astron. Astrophys.*, **180**, 183.

Greaves, J. S., & White, G. J. 1991, *Astron. Astrophys. Suppl.*, **91**, 237.

Groesbeck, T. D. 1989a, *CSO Observers Manual, Appendix 1, Section 2*

Groesbeck, T. D. 1989b, *CSO Observers Manual, Appendix 1, Section 3*

Groesbeck, T. D., Phillips, T. G., & Blake, G. A. 1994a, *Astrophys. J. (Suppl.)*, **94**, 147.

Groesbeck, T. D., Phillips, T. G., & Blake, G. A. 1994b, in preparation.

Grossman, E. N. 1989, AT – Atmospheric Transmission Software, Airhead Software, 2069 Bluff St., Boulder, CO 80304

Hildebrand, R. H. 1983, *Quart. J. Roy. Astron. Soc.*, **24**, 267.

Hogbom, J. 1974, *Astrophys. J. (Suppl.)*, **15**, 417.

Huggins, P. J., Olofsson, H., & Johansson, L. E. B. 1988, *Astrophys. J.*, **332**, 1009.

Irvine, W. M., & Hjalmarson, Å. 1984, *Origins of Life*, (Dordrecht:Reidel).

Jansen, D. J., van Dishoeck, E. F., & Black, J. H. 1993, *Astron. Astrophys.*, **282**, 605.

Jewell, P. R., Hollis, J. M., Lovas, F. J., & Snyder, L. E. 1989, *Astrophys. J. (Suppl.)*, **70**, 833.

Johansson, L. E. B. *et al.* 1984, *Astron. Astrophys.*, **130**, 227.

Kahane, C., Gomez-Gonzalez, J., Cernicharo, J., & Guélin, M 1988, *Astron. Astrophys.*, **190**, 167.

Kahane, C., Cernicharo, J., Gomez-Gonzalez, J., & Guélin, M 1992, *Astron. Astrophys.*, **256**, 235.

Keene, J., Hildebrand, R. H., & Whitcomb, S. E. 1982, *Astrophys. J. (Letters)*, **252**, L11.

Kleinmann, D. E., & Low, F. J. 1967, *Astrophys. J. (Letters)*, **149**, L1.

Knapp, G. R., Sandell, G., & Robson, E. I. 1993, *Astrophys. J. (Suppl.)*, **88**, 173. (KSR)

Kooi, J. W., Chan, M., Bumble, B., Leduc, H. G., Schaffer, P. L., & Phillips, T. G. 1994b, *Int'l. J. IR & MM Waves*, in press.

Kooi, J. W., Chan, M., Phillips, T. G., Bumble, B., & Leduc, H. G. 1992, *IEEE Trans. Microw. Theory Tech.*, **40**, 812.

Kooi, J. W., Walker, C. K., Leduc, H. G., Hunter, T. R., Benford, D. J., & Phillips, T. G. 1994a, *Int'l. J. IR & MM Waves*, **15**, 477.

Kraus, J. D. 1986, *Radio Astronomy, 2nd edition*, (Powell, Ohio:Cygnus-Quasar Books).

Kutner, M. L., & Ulich, B. L. 1981, *Astrophys. J.*, **250**, 341.

Kwan, J. & Linke, R. A. 1982, *Astrophys. J.*, **254**, 587.

Lada, C. J. 1991, in *The Physics of Star Formation and Early Stellar Evolution*, eds. C. J. Lada & N. D. Kylafis (Dordrecht:Kluwer), p. 329.

Lada, C. J. & Reid, M. J. 1978, *Astrophys. J.*, **219**, 95.

Lovas, F. J. 1984, private communication.

Lovas, F. J. 1990, private communication.

Mangum, J. G. 1993, *Pub. Astron. Soc. Pacific*, **105**, 117.

Mathis, J. S. 1990, *Ann. Rev. Astron. Astrophys.*, **28**, 37.

Mathis, J. S. 1993, *Rep. Prog. Phys*, **56**, 605.

Mathis, J. S., Rumpl, W., & Nordsieck, K. H. 1977, *Astrophys. J.*, **217**, 425.

McCabe, E. M., Smith, R. C., & Clegg, R. E. S. 1979, *Nature*, **281**, 263.

McKellar, A. 1941, *Publ. Dom. Astr. Obs.*, **7**, 251.

McMullin, J. P., Mundy, L. G., & Blake, G. A. 1993, *Astrophys. J.*, **405**, 599.

Menten, K. M., Walmsley, C. M., Henkel, C., & Wilson, T. L. 1988, *Astron. Astrophys.*, **198**, 253.

Mezger, P. G., Wink, J. E., & Zylka, R. 1990, *Astron. Astrophys.*, **228**, 107.

Morris, M. 1975, *Astrophys. J.*, **197**, 603.

Morris, M. 1981, *Astrophys. J.*, **249**, 572.

Morris, M., & Bowers, P. F. 1980, *Astron. Jour.*, **85**, 724.

Morris, M., Guilloteau, S., Lucas, R., & Omont, A. 1987, *Astrophys. J.*, **321**, 888.

Morris, M., & Knapp, G. R. 1976, *Astrophys. J.*, **204**, 415.

Mundy, L. G., Scoville, N. Z., Bååth, L. B., Masson, C. R., & Woody, D. P. 1986, *Astrophys. J. (Letters)*, **304**, L51.

Mundy, L. G., Wootten, H. A., & Wilking, B. A. 1990, *Astrophys. J.*, **352**, 159.

Mundy, L. G., Wootten, H. A., Wilking, B. A., Blake, G. A., & Sargent, A. I. 1992, *Astrophys. J.*, **385**, 306.

Olofsson, H., Johansson, L. E. B., Hjalmarson, Å., &Ngueyen-Q-Rieu. 1982, *Astron. Astrophys.*, **107**, 128.

Penzias, A. A., & Burrus, C. A. 1973, *Ann. Rev. Astron. Astrophys.*, **11**, 51.

Phillips, T. G. 1988, *Astr. Lett. & Comm.*, **26**, 293.

Phillips, T. G. 1989, *CSO Observers Manual Appendix 1, Section 1*

Phillips, T. G., Huggins, P. J., Neugebauer, G., & Werner, M. W. 1977, *Astrophys. J. (Letters)*, **217**, L161.

Phillips, T. G., & Keene, J. 1992, *Proc. IEEE*, **80**, 11.

Pollack, J. B., Hollenbach, D., Beckwith, S., Simonelli, D. P., Roush, T, & Fong, W. 1994, *Astrophys. J.*, **421**, 615.

Poynter, R. L., & Pickett, H. M. 1985, *Appl. Optics*, **24**, 2235.

Rieke, G. H., Low, F. J., & Kleinmann, D. E. 1973, *Astrophys. J. (Letters)*, **186**, L7.

Rohlfs, K. 1986, *Tools of Radio Astronomy*, (Berlin:Springer-Verlag).

Sahai, R. 1987, *Astrophys. J.*, **318**, 809.

Sahai, R., & Wannier, P. G. 1985, *Astrophys. J.*, **299**, 424.

Sandell, G. 1994, private communication.

Schilke, P., Groesbeck, T. D., Phillips, T. G., & Blake, G. A. 1994, in preparation.

Schmid-Burgk, J., Densing, R., Krugel, E., Nett, H., Roser, H. P., Schafer, F., Schwaab, G., van der Wal, P., & Wattenbach, R. 1989, *Astron. Astrophys.*, **215**, 150.

Schmid-Burgk, J., Gusten, R., Mauersberer, R., Schulz, A., & Wilson, T. L. 1990, *Astrophys. J. (Letters)*, **362**, L25.

Schwarz, U. J. 1978, *Astron. Astrophys.*, **65**, 345.

Snyder, L. E., Hollis, J. M., Zuckerman, B., & Palmer, P. 1969, *Phys. Rev. Lett.*, **22**, 679.

Sopka, R. J., Hildebrand, R., Jaffe, D. T., Gatley, I., Roellig, T., Werner, M., Jura, M., & Zuckerman, B. 1985, *Astrophys. J.*, **294**, 242.

Sutton, E. C., Blake, G. A., Masson, C. R., & Phillips, T. G. 1984, *Astrophys. J. (Letters)*, **283**, L41. (SBMP)

Sutton, E. C., Blake, G. A., Masson, C. R., & Phillips, T. G. 1985, *Astrophys. J. (Suppl.)*, **58**, 341.

Sutton, E. C., Jaminet, P. A., Danchi, W. C., & Blake, G. A. 1991, *Astrophys. J. (Suppl.)*, **77**, 255.

Swings, P. & Rosenfield, L. 1937, *Astrophys. J.*, **86**, 483.

Thaddeus, P., Cummins, S. E., & Linke, R. A. 1984, *Astrophys. J. (Letters)*, **283**, L45.

Tielens, A. G. G. M. 1989, in *IAU Symp. 135 Interstellar Dust*, eds. L. J. Allamandola & A. G. G. M. Tielens (Dordrecht:Kluwer), p. 239.

Tielens, A. G. G. M. & Allamandola, L. J. 1987, in *Interstellar Processes*, eds. D. J. Hollenbach & H. A. Thronson, Jr. (Dordrecht:Reidel), p. 397.

Townes, C. H. 1954, *J. Geophys. Res.*, **59**, 198.

Turner, B. E. 1971, *Astrophys. Lett.*, **8**, 73.

Turner, B. E. 1989, *Astrophys. J. (Suppl.)*, **70**, 539.

Turner, B. E., Buhl, D., Churchwell, E. B., Mezger, P. G., & Snyder, L. E. 1970, *Astron. Astrophys.*, **4**, 165.

van Dishoeck, E. F. 1993, private communication.

van Dishoeck, E. F., Blake, G. A., Draine, B. T., & Lunine, J. I. 1993, in *Protostars and Planets III*, eds. E. H. Levy, J. I. Lunine, & M. S. Matthews (Univ. of Arizona Press:Tucson), p. 163.

van Dishoeck, E. F., Blake, G. A., Jansen, D. J., & Groesbeck, T. D. 1994, in preparation.

Walker, C. K., Carlstrom, J. E., Bieging, J. H., Lada, C. J., & Young, E. T. 1990, *Astrophys. J.*, **364**, 173.

Walker, C. K., Kooi, J. W., Chan, M., LeDuc, H. G., Carlstrom, J. E., & Phillips, T. G. 1992, *Int'l. J. IR & MM Waves*, **13**, 785.

Walker, C. K., Lada, C. J., Young, E. T., Maloney, P. R., & Wilking, B. A. 1986, *Astrophys. J. (Letters)*, **309**, L47.

Walker, C. K., Lada, C. J., Young, E. T., & Margulis, M. 1988, *Astrophys. J.*, **332**, 335.

Wallerstein, G., H. 1978, *Observatory*, **98**, 224.

Walmsley, C. M., Chini, R., Keysa, E., Steppe, H., Forveille, T., & Omont, A. 1991, *Astron. Astrophys.*, **248**, 555.

Weinreb, S., Barret, A. H., Meeks, M. L., & Henry, J. C. 1963, *Nature*, **200**, 829.

Wilson, W. J., Barrett, A. H., & Moran, J. M. 1970, *Astrophys. J.*, **160**, 545.

Wooten, B. J. 1972, *Optical Properties of Solids*, (New York:Academic Press).

Wright, E. L. 1987, *Astrophys. J.*, **320**, 818.

Ziurys, L. M., & Friberg, P. 1987, *Astrophys. J. (Letters)*, **314**, L49.

Ziurys, L. M., Martin, R. N., Pauls, T. A., & Wilson, T. L. 1981, *Astron. Astrophys.*, **104**, 288.

Ziurys, L. M., & McGonagle, D. 1993, *Astrophys. J. (Suppl.)*, **89**, 155.

Appendix A

Spectral Line Surveys of Orion-KL and Orion-S

Spectral line surveys have proven to be effective methods of gathering data for molecular transitions at millimeter and submillimeter wavelengths (see Hjalmarson 1989 and references to individual surveys below.) Among their advantages when compared to observations of individual lines are the increased number of lines detected, both within a given species and from a greater variety of species, and the consistency in calibration and processing of all transitions seen. Line identifications are apt to be more certain because the presence of a species may be confirmed by the detection of several transitions. Surveys also allow the entire observable chemistry of sources to be investigated at once rather than piecemeal. They provide a large data set which can be confidently used to derive physical parameters without additional uncertainties introduced because of relative calibration errors. Finally, they provide an unbiased look at spectral lines within the frequency range observed and may result in serendipitous detections.

As millimeter- and submillimeter-wave telescopes and receivers have become available, a number of surveys have been carried out in the brightest and richest sources of molecular lines. The Orion hot core region is perhaps the most thoroughly studied and observed source, and serves as a reference source for molecular clouds. Surveys of Orion have been completed for the frequency ranges 72–91 GHz (Johansson *et al.* 1984), 70–115 GHz (Turner 1989), 150–160 GHz (Ziurys & McGonagle 1993), 215–247 GHz (Sutton *et al.* 1985), 247–263 GHz (Blake *et al.* 1986), 257–273 GHz (Greaves & White 1991), and 330–

360 GHz (Jewell *et al.* 1989). Extensive surveys have also been performed for Sgr B2, another example of a high-mass star formation region, over the ranges 70–115 GHz (Turner 1989), 70–150 GHz (Cummins *et al.* 1986), and 330–355 GHz (Sutton *et al.* 1991), and for IRC +10216, which serves as a reference for circumstellar shells, over the ranges 72–91 GHz (Johansson *et al.* 1984) and 340–365 GHz (Avery *et al.* 1992). An unpublished survey of IRC +10216 has been carried out covering large regions of the spectrum between 80 and 250 GHz, from which several detections of new and unusual molecules have been made (*cf.* Cernicharo *et al.* 1991). Lower frequency surveys have been conducted for the dark cloud TMC-1 over the ranges 22–24 GHz and 36–50 GHz (Kaifu *et al.* 1987) and 18.5–21.5 GHz (Irvine *et al.* 1988).

Given the success of previous line surveys, particularly the Caltech OVRO survey of Orion-KL (Sutton *et al.* 1985, Blake *et al.* 1986), we began a program at the Caltech Submillimeter Observatory to extend the surveys both to the higher frequencies made possible by the new facility and to a wider range of objects. Our initial efforts concentrated on Orion-KL and IRC +10216, two sources which had been extensively studied before and which were known to possess rich emission spectra. At the same time, we intended to perform a complementary survey of the young stellar object Orion-S located 1′.5 south of Orion-KL. It soon became apparent that for a complete spectral survey of Orion-S to be meaningful, it would have to achieve a much greater sensitivity level than a survey of Orion-KL. We therefore decided to make a limited number of observations toward Orion-S, at frequencies chosen based upon the complete survey being performed of Orion-KL. In this appendix we present the deconvolved SSB spectra obtained for Orion-KL over the 325–360 GHz range and for Orion-S in the selected frequency ranges, with the spectra of IRC +10216 and the other sources we observed presented in additional appendices. We also comment on the contribution of the observed lines to broadband flux measurements. Complete analyses of the various surveys will be published separately as noted for each source.

A1. The CSO Orion-KL Spectral Line Survey

A1.1. Overview

The Orion-KL region has been extensively studied (see the review by Genzel & Stutzki 1989) as

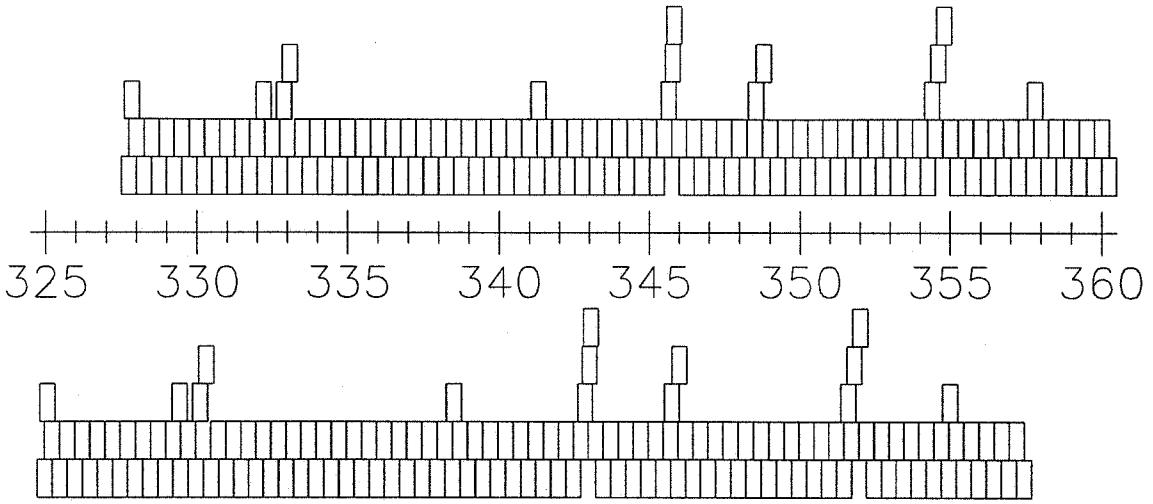

Figure A1.1 Frequency coverage of the Orion-KL observations. Each DSB observation is represented by a pair of boxes: one showing the frequency range in the upper sideband and one showing the range of the lower sideband.

the nearest, brightest example of a high-mass star forming region. Previous line surveys had been done at lower frequencies revealing a spectrum of extraordinary richness, where at many frequencies the line density was so great as to occupy the entire baseline. Beginning in December 1988, we undertook to survey the entire atmospheric window around the CO J = 3-2 line at 345 GHz, eventually covering the range from 325 to 360 GHz. Chapter 3 of this thesis gives details of the general observing procedures and calibration methods used while Chapter 4 contains a description and analysis of the deconvolution method used to obtain the spectrum in single sideband form from the double sideband observations. The spectra were generally taken at spacings of 250 MHz, or half the backend width. Additional spectra were sometimes obtained using smaller LO shifts, particularly around very strong lines or near regions of reduced coverage (*e.g.*, at the ends of the range included in the survey). Table A1.1 lists the actual center frequencies in both sidebands for all of the scans used in constructing our final spectrum, while Figure A1.1 shows the frequency coverage thus obtained.

Our spectrum is in general agreement with the DSB spectra (when converted to main beam temperatures) presented by Jewell *et al.* (1989) whose observations cover the range from 330 to 360 GHz, although our sensitivity to weak lines is much greater. This is largely the result of our significantly

TABLE A1.1

CENTER FREQUENCIES OF OBSERVATIONS FOR THE CSO ORION-KL SPECTRAL LINE SURVEY

USB Center (GHz)	LSB Center (GHz)	Date Observed	USB Center (GHz)	LSB Center (GHz)	Date Observed
327.750	324.950	12 January 1991	335.750	332.950	16 March 1990
327.850	325.050	12 January 1991	335.760	332.960	16 March 1990
328.000	325.200	12 January 1991	336.000	333.200	16 March 1990
328.240	325.440	12 January 1991	336.240	333.440	16 March 1990
328.250	325.450	12 January 1991	336.250	333.450	16 March 1990
328.500	325.700	12 January 1991	336.490	333.690	16 March 1990
328.740	325.940	12 January 1991	336.500	333.700	16 March 1990
328.750	325.950	12 January 1991	336.750	333.950	16 March 1990
329.000	326.200	12 January 1991	336.990	334.190	16 March 1990
329.250	326.450	12 January 1991	337.000	334.200	16 March 1990
329.490	326.690	12 January 1991	337.250	334.450	16 March 1990
329.500	326.700	12 January 1991	337.490	334.690	16 March 1990
329.750	326.950	12 January 1991	337.500	334.700	16 March 1990
329.990	327.190	12 January 1991	337.740	334.940	16 March 1990
330.000	327.200	12 January 1991	337.750	334.950	16 March 1990
330.250	327.450	12 January 1991	337.760	334.960	16 March 1990
330.500	327.700	12 January 1991	338.000	335.200	17 March 1990
330.740	327.940	12 January 1991	338.250	335.450	17 March 1990
330.750	327.950	12 January 1991	338.500	335.700	17 March 1990
331.000	328.200	12 January 1991	338.750	335.950	11 January 1991
331.240	328.440	12 January 1991	338.990	336.190	17 March 1990
331.250	328.450	12 January 1991	339.000	336.200	17 March 1990
331.500	328.700	17 January 1991	339.250	336.450	11 January 1991
331.740	328.940	12 January 1991	339.480	336.680	17 March 1990
331.750	328.950	12 January 1991	339.500	336.700	17 March 1990
332.000	329.200	16 January 1991	339.750	336.950	11 January 1991
332.010	329.210	16 January 1991	340.000	337.200	17 March 1990
332.220	329.420	17 January 1991	340.240	337.440	17 March 1990
332.250	329.450	17 January 1991	340.250	337.450	17 March 1990
332.500	329.700	13 January 1991	340.490	337.690	17 March 1990
332.750	329.950	13 January 1991	340.500	337.700	17 March 1990
332.890	330.090	15 March 1990	340.750	337.950	17 March 1990
332.900	330.100	15 March 1990	341.000	338.200	17 March 1990
333.100	330.300	15 March 1990	341.250	338.450	17 March 1990
333.250	330.450	15 March 1990	341.300	338.500	14 March 1990
333.500	330.700	15 March 1990	341.310	338.510	14 March 1990
333.750	330.950	15 March 1990	341.500	338.700	14 March 1990
333.760	330.960	15 March 1990	341.740	338.940	14 March 1990
334.000	331.200	15 March 1990	341.750	338.950	14 March 1990
334.250	331.450	15 March 1990	341.990	339.190	14 March 1990
334.500	331.700	15 March 1990	342.000	339.200	14 March 1990
334.750	331.950	15 March 1990	342.010	339.210	14 March 1990
334.990	332.190	15 March 1990	342.250	339.450	14 March 1990
335.000	332.200	15 March 1990	342.260	339.460	14 March 1990
335.240	332.440	16 March 1990	342.500	339.700	14 March 1990
335.250	332.450	16 March 1990	342.510	339.710	14 March 1990
335.500	332.700	16 March 1990	342.750	339.950	14 March 1990
335.510	332.710	16 March 1990	342.760	339.960	14 March 1990

TABLE A1.1 - *continued*

USB Center (GHz)	LSB Center (GHz)	Date Observed	USB Center (GHz)	LSB Center (GHz)	Date Observed
343.000	340.200	14 March 1990	351.000	348.200	19 March 1990
343.260	340.460	14 January 1991	351.250	348.450	18 March 1990
343.500	340.700	18 March 1990	351.260	348.460	18 March 1990
343.510	340.710	18 March 1990	351.500	348.700	19 March 1990
343.750	340.950	14 January 1991	351.750	348.950	16 February 1990
344.000	341.200	18 March 1990	351.760	348.960	16 February 1990
344.010	341.210	18 March 1990	352.000	349.200	16 February 1990
344.240	341.440	14 January 1991	352.010	349.210	16 February 1990
344.250	341.450	14 January 1991	352.250	349.450	16 February 1990
344.500	341.700	14 January 1991	352.260	349.460	16 February 1990
344.750	341.950	14 January 1991	352.500	349.700	16 February 1990
344.760	341.960	14 January 1991	352.750	349.950	16 February 1990
345.000	342.200	12 January 1990	352.760	349.960	16 February 1990
345.250	342.450	18 January 1991	353.000	350.200	16 February 1990
345.500	342.700	12 January 1990	353.010	350.210	16 February 1990
345.650	342.850	13 January 1990	353.250	350.450	18 January 1991
345.796	342.996	12 January 1990	353.260	350.460	18 January 1991
345.850	343.050	13 January 1990	353.500	350.700	18 January 1991
346.000	343.200	13 January 1990	353.750	350.950	18 January 1991
346.250	343.450	13 January 1990	354.000	351.200	14 February 1990
346.500	343.700	13 January 1990	354.250	351.450	14 February 1990
346.750	343.950	14 January 1990	354.260	351.460	14 February 1990
347.000	344.200	14 January 1990	354.400	351.600	15 February 1990
347.250	344.450	14 January 1990	354.500	351.700	14 February 1990
347.500	344.700	14 January 1990	354.510	351.710	14 February 1990
347.750	344.950	14 January 1990	354.600	351.800	16 February 1990
348.000	345.200	14 January 1990	354.800	352.000	18 March 1990
348.250	345.450	15 January 1990	355.000	352.200	18 March 1990
348.500	345.700	15 January 1990	355.010	352.210	18 March 1990
348.540	345.740	17 January 1990	355.250	352.450	18 March 1990
348.550	345.750	17 January 1990	355.500	352.700	18 March 1990
348.750	345.950	18 January 1990	355.520	352.720	18 March 1990
348.750	345.950	18 January 1990	355.750	352.950	18 March 1990
348.800	346.000	17 January 1990	356.000	353.200	18 March 1990
348.810	346.010	17 January 1990	356.010	353.210	18 March 1990
349.000	346.200	18 January 1990	356.250	353.450	18 March 1990
349.010	346.210	18 January 1990	356.500	353.700	13 January 1991
349.250	346.450	18 January 1990	356.740	353.940	13 January 1991
349.260	346.460	18 January 1990	356.750	353.950	13 January 1991
349.500	346.700	19 March 1990	357.000	354.200	13 March 1990
349.750	346.950	18 March 1990	357.010	354.210	13 March 1990
349.760	346.960	18 March 1990	357.250	354.450	13 March 1990
350.000	347.200	18 January 1991	357.260	354.460	13 March 1990
350.250	347.450	18 March 1990	357.500	354.700	13 March 1990
350.260	347.460	18 March 1990	357.510	354.710	13 March 1990
350.500	347.700	19 March 1990	357.750	354.950	13 January 1991
350.750	347.950	18 March 1990	357.800	355.000	13 January 1991
350.760	347.960	18 March 1990	358.000	355.200	13 January 1991

TABLE A1.1 - *continued*

USB Center (GHz)	LSB Center (GHz)	Date Observed	USB Center (GHz)	LSB Center (GHz)	Date Observed
358.250	355.450	13 January 1991	359.250	356.450	13 January 1991
358.490	355.690	13 January 1991	359.500	356.700	13 January 1991
358.500	355.700	13 January 1991	359.740	356.940	13 January 1991
358.750	355.950	13 January 1991	359.750	356.950	13 January 1991
359.000	356.200	13 January 1991	360.000	357.200	13 January 1991
359.010	356.210	13 January 1991	360.240	357.440	13 January 1991
359.240	356.440	13 January 1991	360.250	357.450	13 January 1991

TABLE A1.2

CSO ORION-KL SPECTRAL LINE SURVEY
SUMMARY OF OBSERVING DATES AND FREQUENCIES

Dates	Frequencies [a] (GHz)
1990 January 12–18	342–349.5
1990 February 14–16	349–355
1990 March 13–19	330–344, 346.5–357.5
1991 January 11–18	325–333, 336–337, 338.5–345.5
	350–351, 353–354, 355-360

[a] Approximate frequency ranges covered during each observing session.

higher main beam efficiency (0.6 as compared with $\lesssim$0.3) together with the lower system noise temperatures obtained with the CSO.

The observations of Orion-KL were made during a total of six periods between 1988 December and 1991 January at the 10.4m CSO telescope on Mauna Kea, Hawaii. All of the frequencies observed during the first two observing runs (1988 December and 1989 January) were later reobserved, so that the observations included in the present data set were all made during the final four observing periods. Table A1.2 gives a summary of the observing dates and the approximate frequency ranges covered during each period. The overlapping nature of the observations resulted in many frequencies being observed at more than one epoch. The telescope had a FWHM beamwidth of 20″ averaged over the range of frequencies in the survey. Pointing was checked frequently by observing planets; in addition we used the strong emission from SO_2 lines throughout the survey to consistently optimize our pointing on the source itself. Throughout the observations, the pointing was found to be accurate to $\lesssim 5''$.

We used the facility SIS receiver (Ellison *et al.* 1989) for all observations, obtaining receiver temperatures of typically 200 - 250 K (SSB) and system temperatures ranging from 700 to 2000 K (SSB). The atmospheric opacity was usually less than 0.25, reaching 0.8 on occasion and even higher for the observations near the H_2O transition at 325 GHz. The facility backend (an acousto-optic spectrometer) was used which had a bandwidth of 500 MHz and a nominal channel width of 0.49 MHz. The SSB spectrum is reconstructed with a channel width of 1.0 MHz, which approximately matches the actual resolution of the backend as determined from frequency calibration measurements.

The chopper wheel method as described in Chapter 3 was used to calibrate the data as the observations were made, and low order polynomial baselines were removed from the DSB spectra. In many cases, the majority of the spectrum was occupied by emission lines, making it possible only to remove a constant or possibly linear baseline. As noted in Chapter 5, the removed baselines have been used to evaluate the continuum emission from Orion-KL giving results consistent with published values. The data presented here have been corrected for an extended efficiency of $\eta_{ext} = 0.76$ as found from observations of the moon (however, see the footnote below regarding the line tables). The complicated nature of the Orion-KL region, with different molecules and transitions exhibiting emission from several subsources of different sizes makes it impossible for a single correction to yield accurate line brightness temperatures in all cases. The main beam efficiency was found to be $\eta_{MB} = 0.60$ from planetary measurements, so that multiplying the present results by 1.27 will yield main beam temperatures.

A1.2. Results

We present here the final spectrum obtained together with a brief summary of the survey results concerning the integrated line flux. A detailed analysis of the survey, including consideration of the individual species and transitions detected as well as addressing the chemistry of the source, will be published separately (Schilke *et al.* 1994).

Figure A1.2 shows a compressed view of the reduced single sideband spectrum obtained from our observations. The resulting spectrum covers the frequency range from 325 to 360 GHz continuously, with a noise level of ~90 mK in main beam brightness temperature units over most of the band. Some

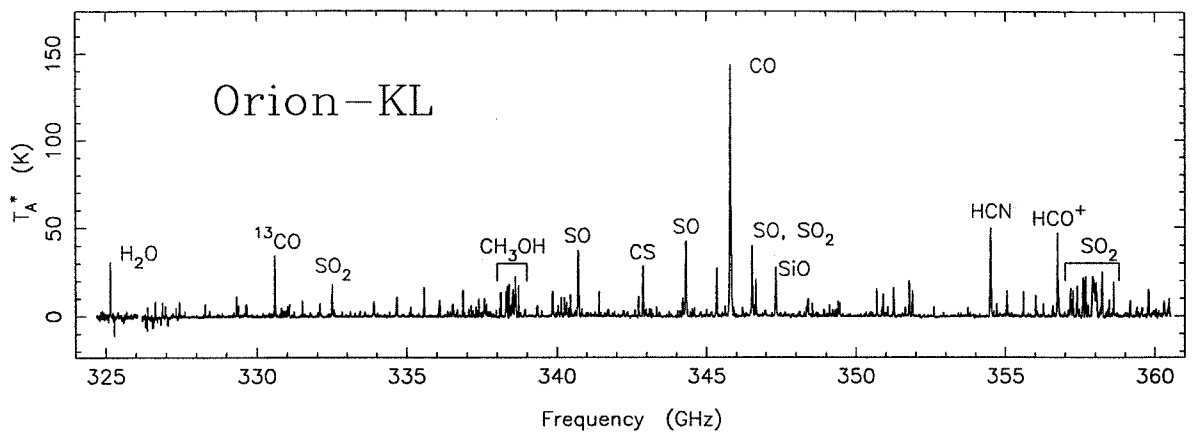

Figure A1.2 A compressed view of the CSO spectral line survey of Orion-KL.

characteristics are readily apparent, such as the much larger intensity of the CO J = 3–2 line at 345 GHz compared to any other line, the appearance of transition "bands" from particular molecules (*e.g.*, CH_3OH near 338 GHz and SO_2 near 358 GHz), the increasing number of lines as weaker intensities are probed, and the overall complexity and richness of the spectrum, which in many places is confusion limited, *i.e.*, the baseline is completely occupied by line emission. Significantly higher noise levels are seen at the lowest frequencies included in our survey; these result from the large atmospheric opacity caused by the H_2O line at 325 GHz. An expanded view of the spectrum is presented in Figure A1.3 with vertical ticks and labels showing the detected lines and "ghosts" which remain in the spectrum. The frequency scale is determined assuming a source velocity of 9 km s^{-1}; note that in previous surveys, lines have been found to exhibit emission from several velocity components.

A total of 801 lines have been detected in the survey, of which 184, or 23%, could not be identified with transitions of any known species. The remaining 617 lines have been identified with 26 distinct chemical species. Table A1.3 lists the spectral lines detected, showing the frequency and corresponding species (where identified) of each line. More detailed information about the lines, including quantum numbers and intensities, is given in Tables A1.4 through A1.21.* Following the reconstruction of the SSB

* Work on this survey is continuing, particularly efforts to identify the molecules and transitions responsible for the unidentified lines. These tables are the working versions in preparation for the detailed chemical analysis by Schilke *et al.* (1994), and the intensity values given therein are not corrected for the extended efficiency. For the purposes of determining the integrated line flux, we have corrected all intensities for the extended efficiency of 0.76, and this is reflected in the plots of the spectrum. We also

spectrum, 34 ghost images were found which could not readily be eliminated and which remain in the spectrum. Because of the severe line overlap problem resulting from the large line density and broad lines, it is possible that some of the unidentified lines may in fact be ghosts.

The most straightforward comparison of the emission line flux with the continuum emission may be made by integrating over the reduced SSB spectrum to obtain the line flux and fitting baselines to the original DSB spectra to obtain the continuum flux. By making the comparison based on a single unified data set, we eliminate sources of error such as relative calibration, pointing variations, and beam size effects which arise when comparing measurements from different telescopes. The resulting values (in uncorrected T_A^* units averaged over the frequency range of the survey) are 1.1 K for the continuum offset and 1.0 K for the integrated lines. The integrated line flux thus represents 48% of the total flux detected in our survey, somewhat greater than the ~40% found by Sutton *et al.* (1984) for the OVRO survey. By far the greatest contribution of any single line comes from the CO J = 3–2 transition, which by itself represents some 13% of the line flux. The 36 SO_2 lines detected in the survey are responsible for the greatest amount of flux from any single species, representing ~26% of the line emission, with most of this flux coming in the band of lines near 358 GHz. Other species which give significant flux contributions include SO (11%), CH_3OH (11%), and HCN (4% of the total line flux). Of these, only SO_2 and CH_3OH have large numbers of observed lines, resulting from the band emission noted earlier. The species which are observed to have the largest numbers of detected lines, $HCOOCH_3$ with 211 and CH_3OCH_3 with 82 (of course, many of these are blends of transitions), are responsible for 26% and 10%, respectively, of the total number of lines seen, but only 4% and 1% of the flux. It thus appears that the bulk of the line flux is carried in the strongest lines emitted by relatively few species; hence simulations may be able to give reasonable estimates for the line flux using relatively few parameters which may be readily determined from observations. Further discussion of the comparison between the integrated line flux and the continuum flux is given in Chapter 5.

---

note that with regard to the total integrated line flux, the identification of individual lines is relatively unimportant, particularly as the strongest lines are securely identified, allowing us to determine which molecules are most important to the flux.

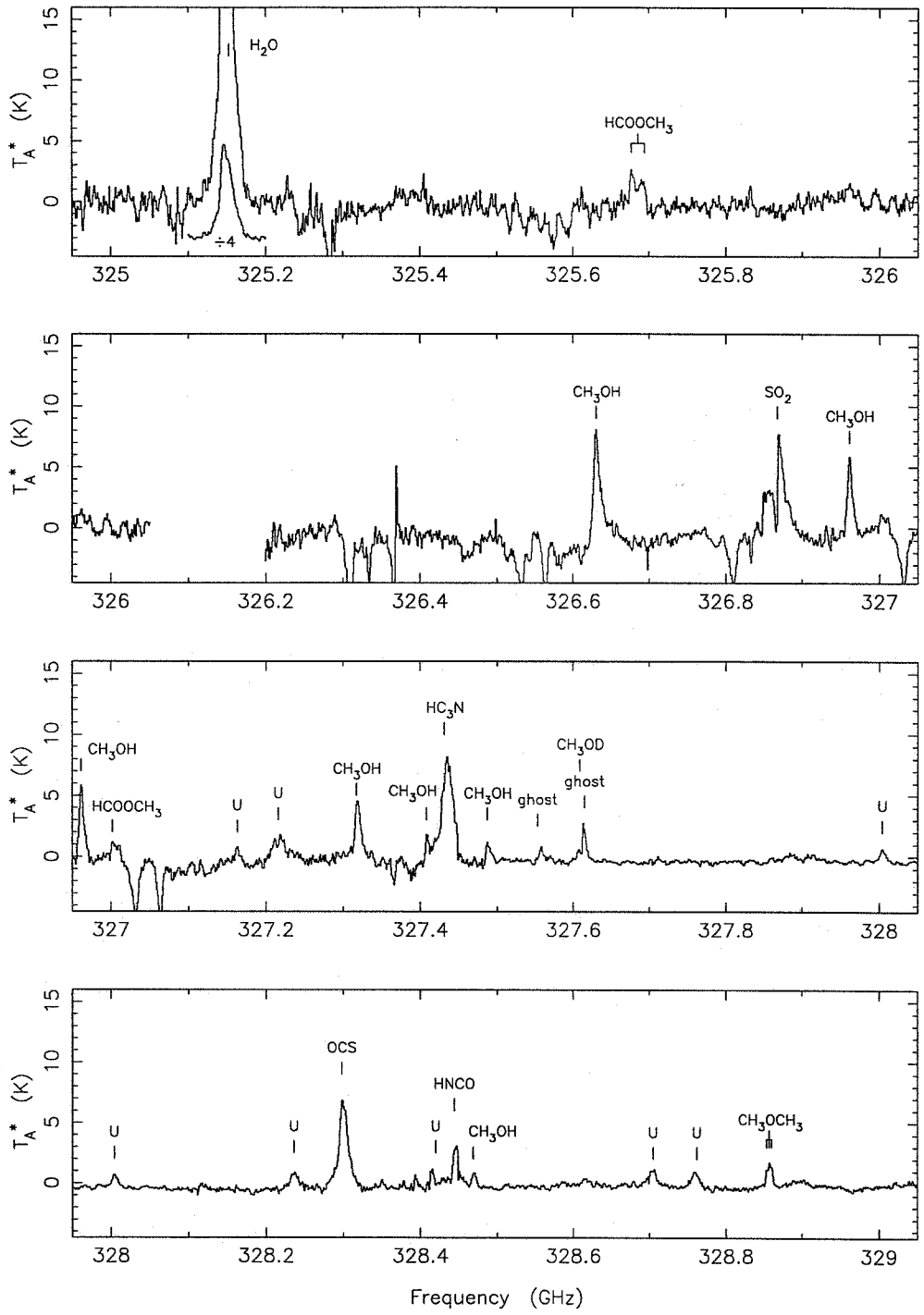

Figure A1.3 Spectrum of Orion-KL from 325 to 360 GHz. The data have been corrected by the extended beam efficiency of 0.76. The rest frequency scale has been established using a v_{LSR} of 9 km s^{-1}. Tick marks show the rest frequencies of identified transitions.

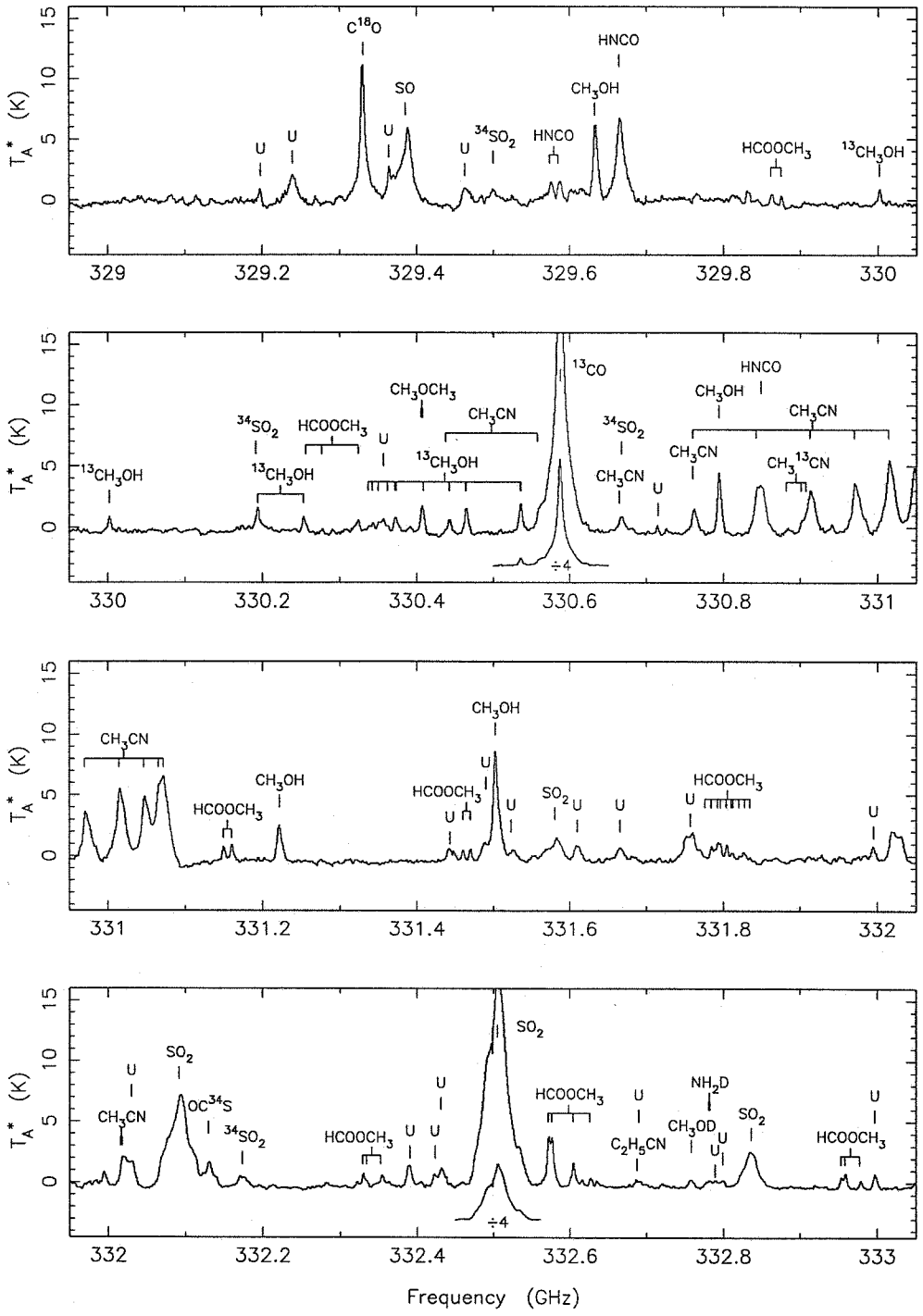

Figure A1.3 — *Continued*

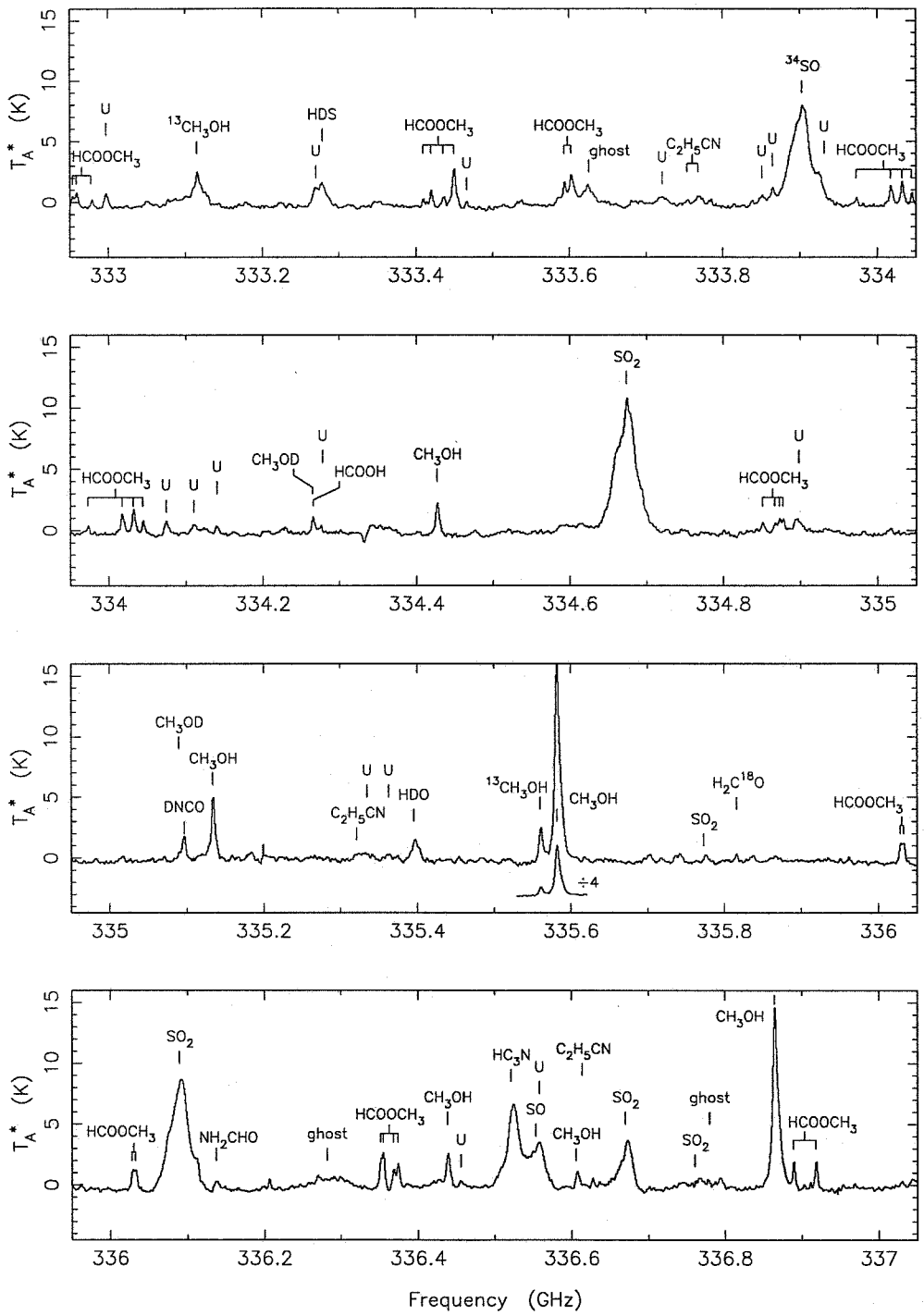

Figure A1.3 — *Continued*

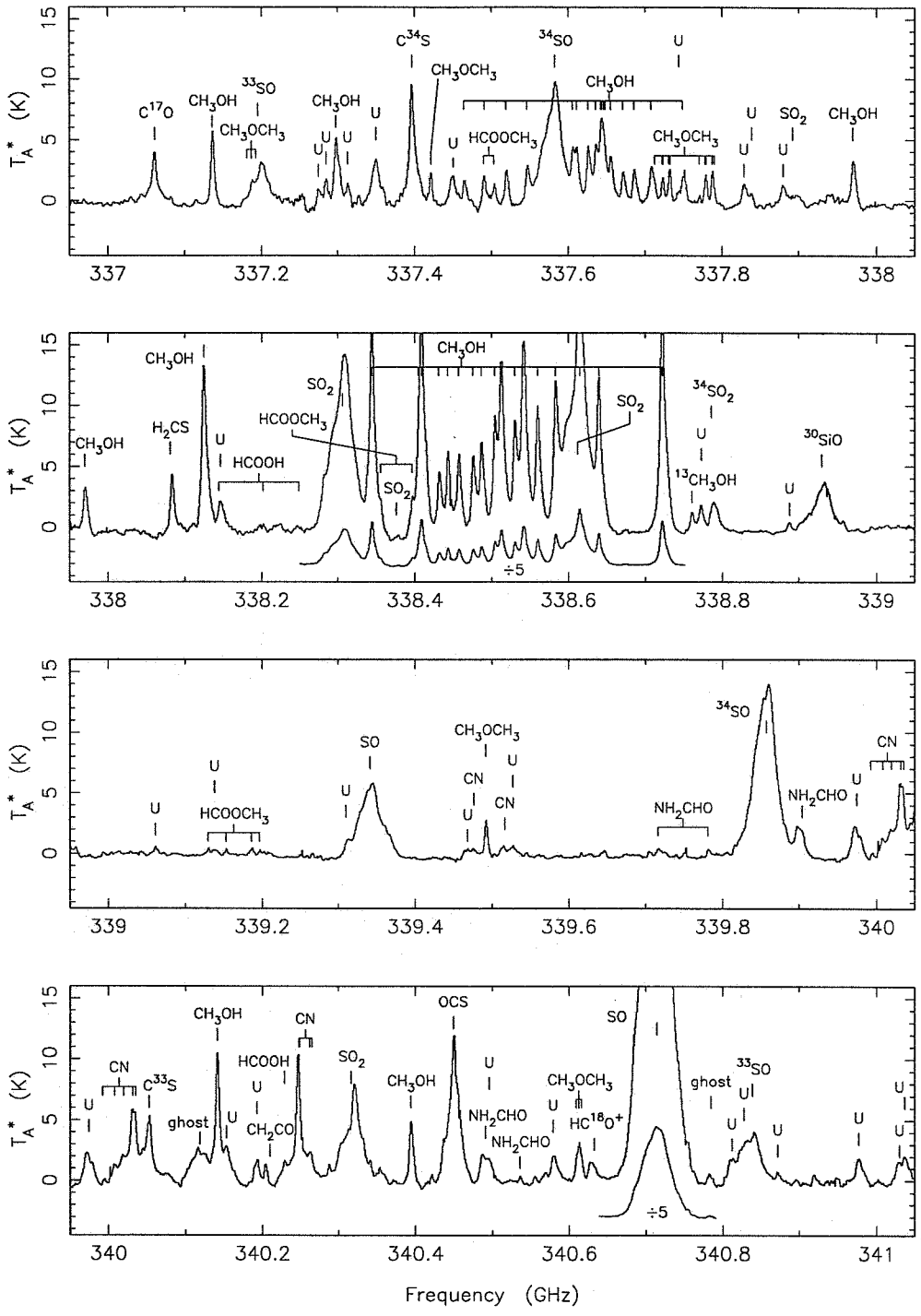

Figure A1.3 — *Continued*

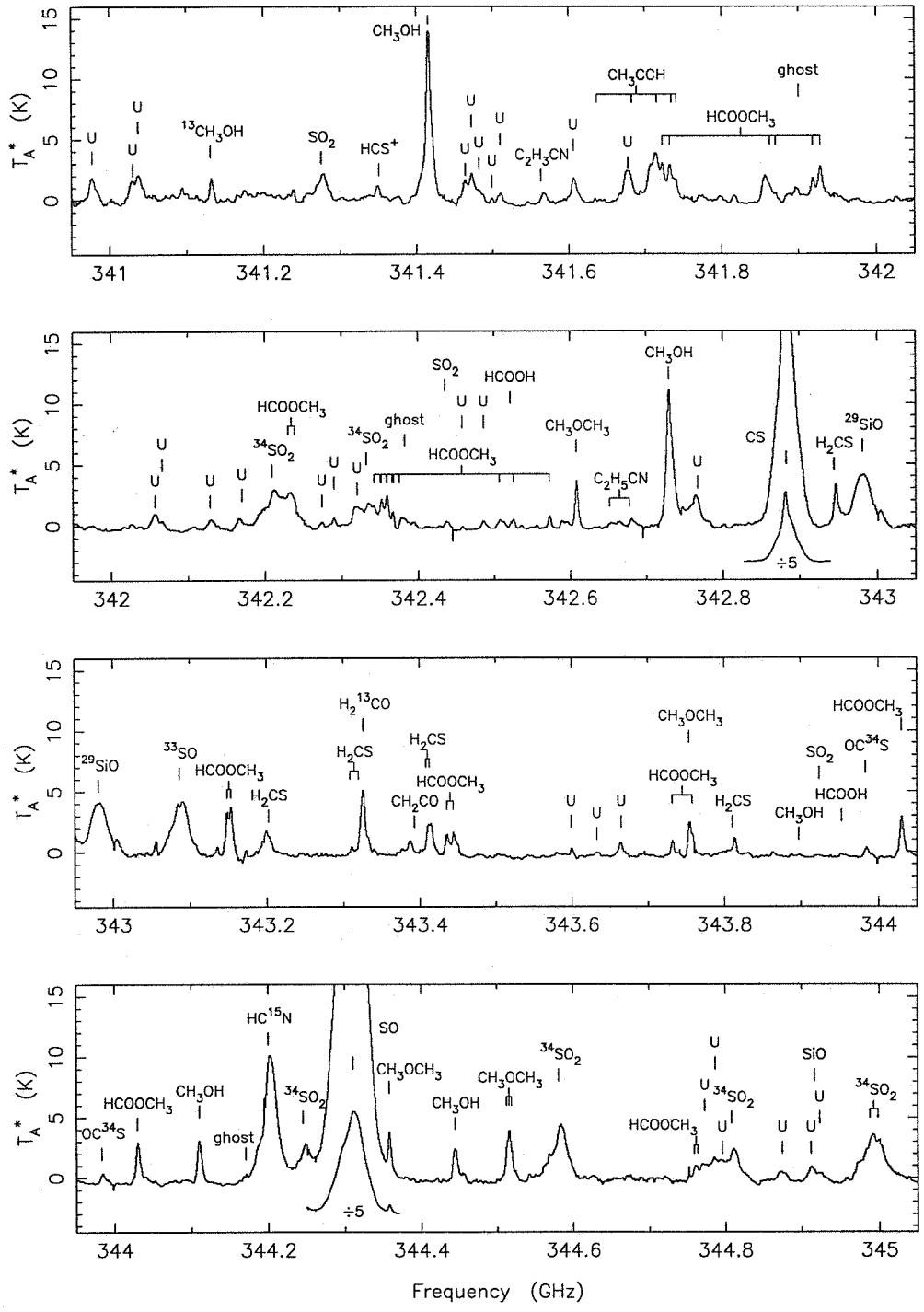

Figure A1.3 — *Continued*

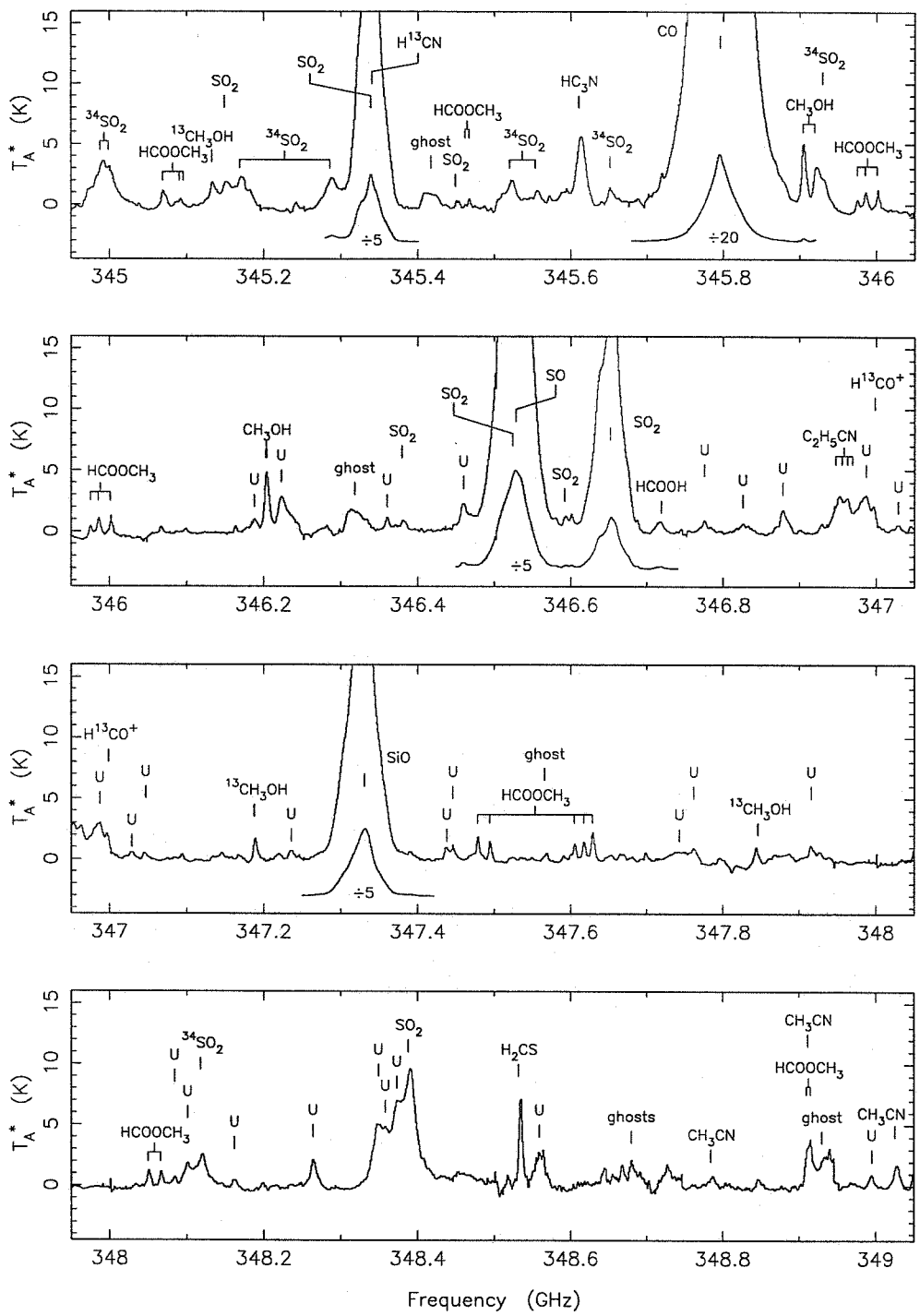

Figure A1.3 — *Continued*

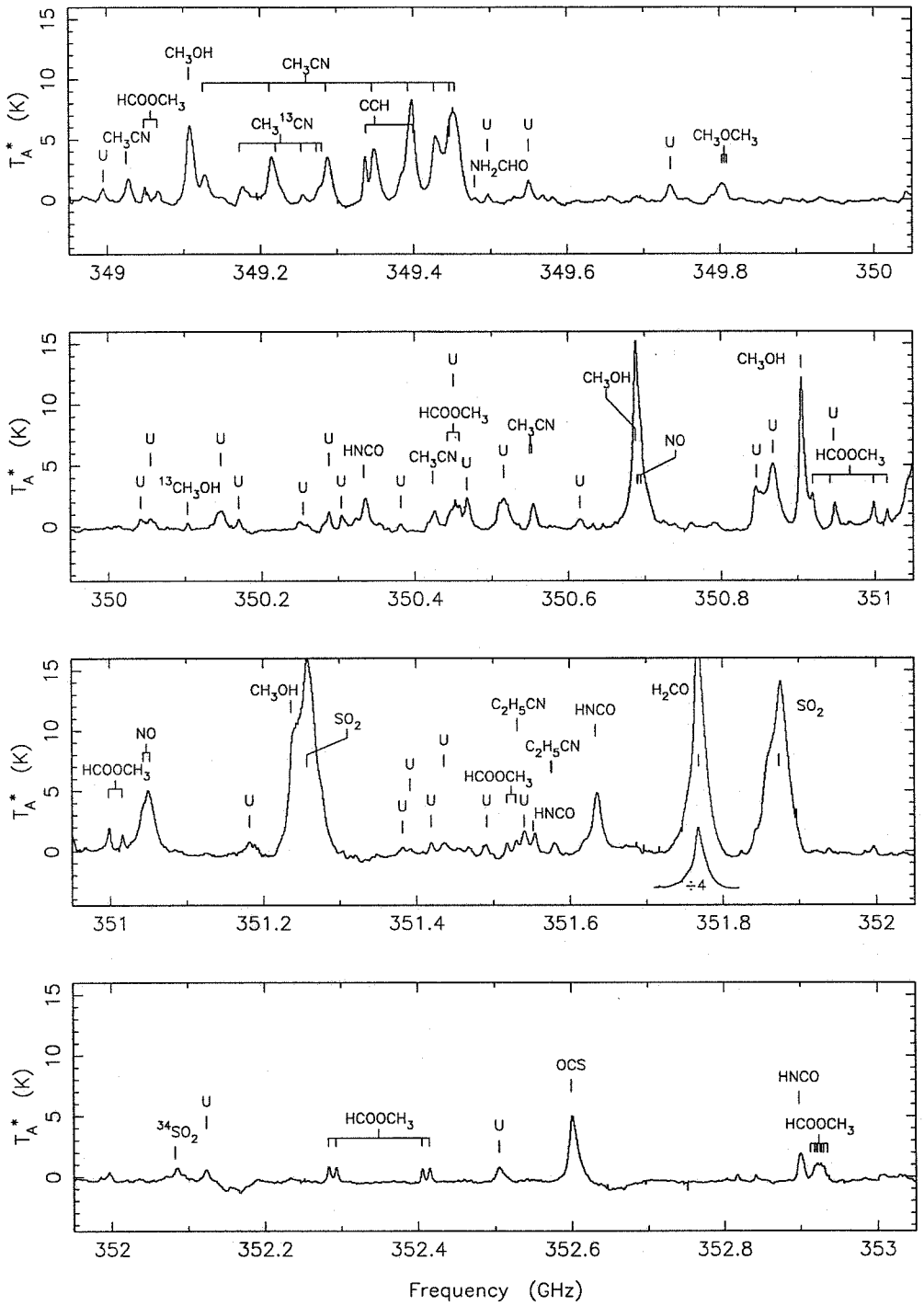

Figure A1.3— *Continued*

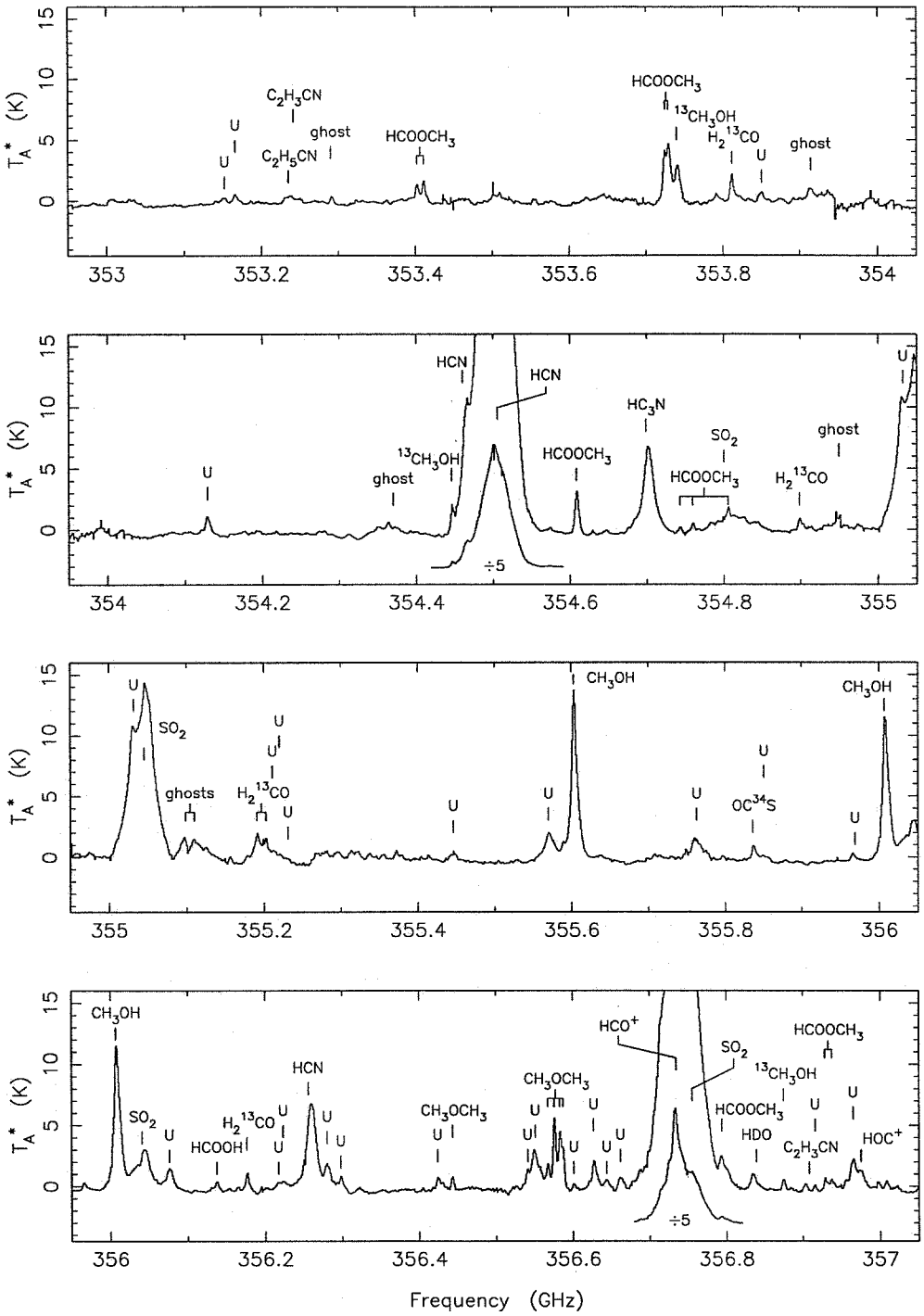

Figure A1.3 — *Continued*

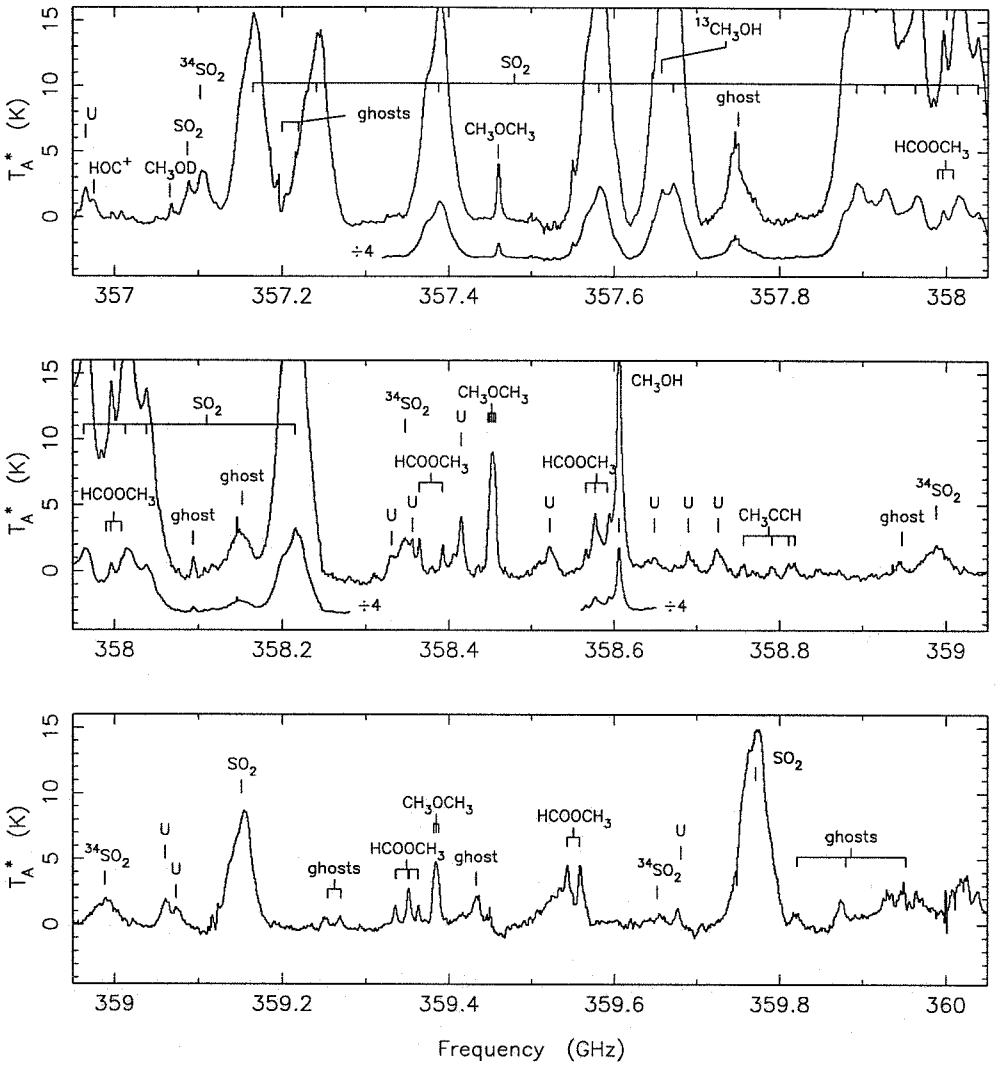

Figure A1.3 — *Continued*

TABLE A1.3

SPECTRAL FEATURES DETECTED IN ORION-KL

ν (MHz)	Molecule	ν (MHz)	Molecule	ν (MHz)	Molecule
325152.920	H_2O	330001.750	$^{13}CH_3OH$	331071.344	CH_3CN
325677.094	$HCOOCH_3$	330191.157	$^{34}SO_2$	331149.344	$HCOOCH_3$
325694.406	$HCOOCH_3$	330194.031	$^{13}CH_3OH$	331159.563	$HCOOCH_3$
326630.625	CH_3OH	330252.813	$^{13}CH_3OH$	331221.594	CH_3OH
326867.514	SO_2	330256.000	$HCOOCH_3$	331443.000	U
326961.188	CH_3OH	330276.400	$HCOOCH_3$	331459.969	$HCOOCH_3$
327001.906	$HCOOCH_3$	330323.906	$HCOOCH_3$	331469.469	$HCOOCH_3$
327163.000	U	330336.906	$^{13}CH_3OH$	331490.000	U
327216.000	U	330342.531	$^{13}CH_3OH$	331502.375	CH_3OH
327317.218	CH_3OH	330350.000	$^{13}CH_3OH$	331523.000	U
327408.156	CH_3OH	330357.000	U	331580.193	SO_2
327431.429	HC_3N	330362.031	$^{13}CH_3OH$	331610.000	U
327487.188	CH_3OH	330371.281	$^{13}CH_3OH$	331666.000	U
327553.000	H_2O-Ghost	330373.438	$^{13}CH_3OH$	331757.000	U
327608.665	CH_3OD	330405.406	CH_3OCH_3	331775.906	$HCOOCH_3$
327614.906	^{13}CO-Ghost	330406.469	CH_3OCH_3	331784.188	$HCOOCH_3$
328004.000	U	330407.563	CH_3OCH_3	331792.094	$HCOOCH_3$
328236.000	U	330408.375	$^{13}CH_3OH$	331795.875	$HCOOCH_3$
328298.107	OCS	330437.424	CH_3CN	331803.750	$HCOOCH_3$
328420.578	U	330442.406	$^{13}CH_3OH$	331809.688	$HCOOCH_3$
328444.300	HNCO	330463.646	$^{13}CH_3OH$	331809.719	$HCOOCH_3$
328468.813	CH_3OH	330464.938	$^{13}CH_3OH$	331812.156	$HCOOCH_3$
328705.000	U	330535.219	$^{13}CH_3OH$	331819.938	$HCOOCH_3$
328761.814	U	330535.875	$^{13}CH_3OH$	331827.719	$HCOOCH_3$
328853.281	CH_3OCH_3	330557.583	CH_3CN	331834.531	$HCOOCH_3$
328853.375	CH_3OCH_3	330588.100	^{13}CO	331995.000	U
328856.656	CH_3OCH_3	330665.222	CH_3CN	332015.780	$CH_3CN(v_8 = 1)$
328859.969	CH_3OCH_3	330667.631	$^{34}SO_2$	332017.770	$CH_3CN(v_8 = 1)$
329198.000	U	330715.000	U	332030.000	U
329239.000	U	330760.184	CH_3CN	332091.409	SO_2
329330.605	$C^{18}O$	330793.906	CH_3OH	332129.700	$OC^{34}S$
329364.188	U	330842.638	CH_3CN	332173.693	$^{34}SO_2$
329385.477	SO	330848.813	HNCO	332329.188	$HCOOCH_3$
329463.000	U	330881.938	$CH_3{}^{13}CN$	332333.969	$HCOOCH_3$
329499.707	$^{34}SO_2$	330900.964	$CH_3{}^{13}CN$	332352.594	$HCOOCH_3$
329573.458	HNCO	330907.306	$CH_3{}^{13}CN$	332391.000	U
329585.088	HNCO	330912.462	CH_3CN	332423.000	U
329632.906	CH_3OH	330969.629	CH_3CN	332431.000	U
329664.537	HNCO	331014.116	CH_3CN	332505.224	SO_2
329861.563	$HCOOCH_3$	331045.905	CH_3CN	332570.906	$HCOOCH_3$
329874.906	$HCOOCH_3$	331064.984	CH_3CN	332571.156	$HCOOCH_3$

TABLE A1.3 - *continued*

ν (MHz)	Molecule	ν (MHz)	Molecule	ν (MHz)	Molecule
332571.375	$HCOOCH_3$	333972.375	$HCOOCH_3$	336456.000	U
332571.656	$HCOOCH_3$	334017.156	$HCOOCH_3$	336520.985	HC_3N
332575.625	$HCOOCH_3$	334031.531	$HCOOCH_3$	336553.346	SO
332575.875	$HCOOCH_3$	334031.844	$HCOOCH_3$	336558.000	U
332576.219	$HCOOCH_3$	334043.969	$HCOOCH_3$	336613.926	CH_3CH_2CN
332576.375	$HCOOCH_3$	334074.000	U	336669.573	SO_2
332604.406	$HCOOCH_3$	334110.000	U	336760.707	$SO_2(v_2 = 1)$
332604.438	$HCOOCH_3$	334140.000	U	336780.000	Ghost
332626.031	$HCOOCH_3$	334264.918	CH_3OD	336865.125	CH_3OH
332687.719	CH_3CH_2CN	334265.827	HCOOH	336889.219	$HCOOCH_3$
332690.000	U	334278.000	U	336918.094	$HCOOCH_3$
332758.272	CH_3OD	334426.594	CH_3OH	337061.061	$C^{17}O$
332780.945	NH_2D	334450.000	Ghost	337135.875	CH_3OH
332781.769	NH_2D	334673.331	SO_2	337180.844	CH_3OCH_3
332782.363	NH_2D	334851.000	$HCOOCH_3$	337186.719	CH_3OCH_3
332789.000	U	334866.969	$HCOOCH_3$	337192.563	CH_3OCH_3
332799.000	U	334872.750	$HCOOCH_3$	337195.000	^{33}SO
332836.289	$^{34}SO_2$	334877.469	$HCOOCH_3$	337275.000	U
332953.313	$HCOOCH_3$	334898.072	U	337285.000	U
332958.250	$HCOOCH_3$	335089.661	CH_3OD	337297.438	CH_3OH
332977.375	$HCOOCH_3$	335096.545	DNCO	337313.000	U
332997.000	U	335133.500	CH_3OH	337350.000	U
333114.781	$^{13}CH_3OH$	335321.375	CH_3CH_2CN	337396.690	$C^{34}S$
333270.000	U	335321.377	CH_3CH_2CN	337420.938	CH_3OCH_3
333278.469	HDS	335335.000	U	337421.344	CH_3OCH_3
333409.375	$HCOOCH_3$	335363.000	U	337421.750	CH_3OCH_3
333419.156	$HCOOCH_3$	335395.500	HDO	337421.750	CH_3OCH_3
333435.156	$HCOOCH_3$	335559.875	$^{13}CH_3OH$	337450.000	U
333449.344	$HCOOCH_3$	335582.000	CH_3OH	337463.656	CH_3OH
333449.375	$HCOOCH_3$	335773.219	SO_2	337489.656	$HCOOCH_3$
333466.000	U	335816.025	$H_2C^{18}O$	337490.531	CH_3OH
333593.156	$HCOOCH_3$	336028.094	$HCOOCH_3$	337503.438	$HCOOCH_3$
333601.969	$HCOOCH_3$	336032.375	$HCOOCH_3$	337519.063	CH_3OH
333625.500	Ghost	336089.222	SO_2	337546.063	CH_3OH
333721.000	U	336136.877	NH_2CHO	337582.227	^{34}SO
333753.446	CH_3CH_2CN	336281.800	Ghost	337605.250	CH_3OH
333767.706	CH_3CH_2CN	336351.469	$HCOOCH_3$	337610.625	CH_3OH
333851.000	U	336354.906	$HCOOCH_3$	337625.688	CH_3OH
333865.000	U	336368.188	$HCOOCH_3$	337635.656	CH_3OH
333902.133	^{34}SO	336373.844	$HCOOCH_3$	337642.375	CH_3OH
333931.914	U	336438.281	CH_3OH	337643.875	CH_3OH

TABLE A1.3 - *continued*

ν (MHz)	Molecule	ν (MHz)	Molecule	ν (MHz)	Molecule
337646.000	CH_3OH	338456.500	CH_3OH	339974.253	U
337648.156	CH_3OH	338475.281	CH_3OH	339992.272	CN
337655.188	CH_3OH	338486.344	CH_3OH	340008.097	CN
337671.188	CH_3OH	338504.099	CH_3OH	340019.602	CN
337685.281	CH_3OH	338512.625	CH_3OH	340031.544	CN
337685.750	CH_3OH	338512.875	CH_3OH	340035.408	CN
337707.563	CH_3OH	338530.250	CH_3OH	340052.695	$C^{33}S$
337712.406	CH_3OCH_3	338540.797	CH_3OH	340118.500	Ghost
337722.344	CH_3OCH_3	338543.188	CH_3OH	340141.219	CH_3OH
337723.000	CH_3OCH_3	338559.938	CH_3OH	340153.000	U
337730.719	CH_3OCH_3	338583.188	CH_3OH	340193.000	U
337731.906	CH_3OCH_3	338611.804	SO_2	340209.667	CH_2CO
337732.188	CH_3OCH_3	338615.000	CH_3OH	340229.048	HCOOH
337744.000	U	338639.938	CH_3OH	340247.770	CN
337748.748	CH_3OH	338721.625	CH_3OH	340248.569	CN
337770.594	CH_3OCH_3	338722.938	CH_3OH	340261.818	CN
337778.000	CH_3OCH_3	338760.396	$^{13}CH_3OH$	340265.025	CN
337779.500	CH_3OCH_3	338773.000	U	340316.384	SO_2
337787.188	CH_3OCH_3	338785.757	$^{34}SO_2$	340394.200	CH_3OH
337787.875	CH_3OCH_3	338888.000	U	340339.000	U
337790.094	CH_3OCH_3	338929.477	^{30}SiO	340449.200	OCS
337829.000	U	339061.000	U	340491.092	NH_2CHO
337839.000	U	339129.313	$HCOOCH_3$	340496.000	U
337880.000	U	339138.000	U	340536.003	NH_2CHO
337892.205	$SO_2(v_2 = 1)$	339152.750	$HCOOCH_3$	340579.000	U
337969.406	CH_3OH	339186.000	$HCOOCH_3$	340609.219	CH_3OCH_3
338080.831	H_2CS	339196.375	$HCOOCH_3$	340609.281	CH_3OCH_3
338124.500	CH_3OH	339310.000	U	340612.594	CH_3OCH_3
338143.700	HCOOH	339341.459	SO	340615.906	CH_3OCH_3
338146.000	U	339468.000	U	340632.978	$HC^{18}O^+$
338201.797	HCOOH	339475.904	CN	340714.155	SO
338248.675	HCOOH	339491.656	CH_3OCH_3	340784.625	Ghost
338306.006	SO_2	339491.719	CH_3OCH_3	340812.000	U
338344.628	CH_3OH	339491.781	CH_3OCH_3	340828.000	U
338355.781	$HCOOCH_3$	339491.781	CH_3OCH_3	340839.000	^{33}SO
338376.272	$SO_2(v_2 = 1)$	339516.658	CN	340872.000	U
338396.375	$HCOOCH_3$	339527.000	U	340977.000	U
338404.580	CH_3OH	339715.795	NH_2CHO	341030.000	U
338408.688	CH_3OH	339780.809	NH_2CHO	341037.000	U
338430.938	CH_3OH	339857.631	^{34}SO	341095.000	U
338442.344	CH_3OH	339904.100	NH_2CHO	341131.219	$^{13}CH_3OH$

TABLE A1.3 - *continued*

ν (MHz)	Molecule	ν (MHz)	Molecule	ν (MHz)	Molecule
341275.521	SO_2	342375.594	$HCOOCH_3$	343731.813	$HCOOCH_3$
341350.826	HCS^+	342382.688	Ghost	343753.313	CH_3OCH_3
341415.625	CH_3OH	342435.884	$SO_2(v_2 = 1)$	343753.313	CH_3OCH_3
341464.000	U	342458.000	U	343754.219	CH_3OCH_3
341472.000	U	342486.000	U	343755.125	CH_3OCH_3
341482.000	U	342506.719	$HCOOCH_3$	343757.938	$HCOOCH_3$
341499.000	U	342521.225	HCOOH	343810.755	H_2CS
341510.000	U	342525.331	$HCOOCH_3$	343897.219	CH_3OH
341563.235	C_2CHCN	342572.410	$HCOOCH_3$	343923.817	$SO_2(v_2 = 1)$
341606.000	U	342608.063	CH_3OCH_3	343952.413	HCOOH
341637.044	CH_3CCH	342608.063	CH_3OCH_3	343983.268	$OC^{34}S$
341678.000	U	342608.125	CH_3OCH_3	344029.600	$HCOOCH_3$
341682.567	CH_3CCH	342608.188	CH_3OCH_3	344110.438	CH_3OH
341715.088	CH_3CCH	342652.045	CH_3CH_2CN	344171.000	Ghost
341722.406	$HCOOCH_3$	342677.720	CH_3CH_2CN	344200.320	$HC^{15}N$
341732.313	$HCOOCH_3$	342729.844	CH_3OH	344245.445	$^{34}SO_2$
341734.606	CH_3CCH	342767.000	U	344310.612	SO
341741.113	CH_3CCH	342883.000	CS	344357.969	CH_3OCH_3
341862.625	$HCOOCH_3$	342944.369	H_2CS	344357.969	CH_3OCH_3
341870.281	$HCOOCH_3$	342981.094	^{29}SiO	344358.063	CH_3OCH_3
341900.125	Ghost	343086.000	^{33}SO	344358.156	CH_3OCH_3
341918.125	$HCOOCH_3$	343148.250	$HCOOCH_3$	344444.656	CH_3OH
341927.500	$HCOOCH_3$	343148.406	$HCOOCH_3$	344512.156	CH_3OCH_3
342057.000	U	343148.531	$HCOOCH_3$	344512.188	CH_3OCH_3
342066.000	U	343148.688	$HCOOCH_3$	344515.375	CH_3OCH_3
342129.000	U	343152.844	$HCOOCH_3$	344518.594	CH_3OCH_3
342170.000	U	343153.000	$HCOOCH_3$	344581.114	$^{34}SO_2$
342208.932	$^{34}SO_2$	343153.125	$HCOOCH_3$	344759.050	$HCOOCH_3$
342230.094	$HCOOCH_3$	343153.281	$HCOOCH_3$	344763.594	$HCOOCH_3$
342238.469	$HCOOCH_3$	343202.331	H_2CS	344773.000	U
342274.000	U	343308.510	H_2CS	344786.600	U
342290.000	U	343319.645	H_2CS	344795.900	U
342320.000	U	343325.669	$H_2{}^{13}CO$	344807.987	$^{34}SO_2$
342332.096	$^{34}SO_2$	343392.887	CH_2CO	344875.000	U
342342.281	$HCOOCH_3$	343408.119	H_2CS	344912.000	U
342350.063	$HCOOCH_3$	343412.325	H_2CS	344923.000	U
342351.688	$HCOOCH_3$	343435.438	$HCOOCH_3$	344916.330	$SiO(v = 1)$
342358.531	$HCOOCH_3$	343443.938	$HCOOCH_3$	344987.647	$^{34}SO_2$
342359.406	$HCOOCH_3$	343599.000	U	344998.248	$^{34}SO_2$
342366.250	$HCOOCH_3$	343633.000	U	345068.600	$HCOOCH_3$
342367.938	$HCOOCH_3$	343665.000	U	345069.000	$HCOOCH_3$

TABLE A1.3 - *continued*

ν (MHz)	Molecule	ν (MHz)	Molecule	ν (MHz)	Molecule
345090.281	$HCOOCH_3$	346955.388	CH_3CH_2CN	348911.420	CH_3CN
345095.313	$HCOOCH_3$	346955.388	CH_3CH_2CN	348914.969	$HCOOCH_3$
345132.594	$^{13}CH_3OH$	346962.819	CH_3CH_2CN	348930.000	Ghost
345148.952	SO_2	346962.819	CH_3CH_2CN	348995.000	U
345168.780	$^{34}SO_2$	346969.239	CH_3CH_2CN	349024.990	CH_3CN
345285.726	$^{34}SO_2$	346969.239	CH_3CH_2CN	349048.531	$HCOOCH_3$
345338.543	SO_2	346987.000	U	349065.656	$HCOOCH_3$
345339.760	$H^{13}CN$	346998.540	$H^{13}CO^+$	349107.031	CH_3OH
345416.875	Ghost	347029.000	U	349125.305	CH_3CN
345448.785	SO_2	347047.000	U	349173.167	$CH_3{}^{13}CN$
345461.563	$HCOOCH_3$	347187.719	$^{13}CH_3OH$	349212.129	CH_3CN
345466.938	$HCOOCH_3$	347236.000	U	349220.028	$CH_3{}^{13}CN$
345519.780	$^{34}SO_2$	347330.631	SiO	349253.500	$CH_3{}^{13}CN$
345553.225	$^{34}SO_2$	347438.000	U	349273.277	$CH_3{}^{13}CN$
345610.076	HC_3N	347446.000	U	349280.277	$CH_3{}^{13}CN$
345651.433	$^{34}SO_2$	347478.406	$HCOOCH_3$	349285.798	CH_3CN
345795.989	CO	347494.000	$HCOOCH_3$	349337.856	CCH
345904.156	CH_3OH	347565.906	Ghost	349338.728	CCH
345919.156	CH_3OH	347604.563	$HCOOCH_3$	349346.112	CH_3CN
345929.351	$^{34}SO_2$	347617.000	$HCOOCH_3$	349393.048	CH_3CN
345975.063	$HCOOCH_3$	347628.375	$HCOOCH_3$	349398.906	CCH
345985.344	$HCOOCH_3$	347743.000	U	349400.292	CCH
346000.906	$HCOOCH_3$	347762.000	U	349426.587	CH_3CN
346188.000	U	347844.000	U	349446.719	CH_3CN
346202.781	CH_3OH	347915.670	U	349453.427	CH_3CN
346204.375	CH_3OH	348050.000	$HCOOCH_3$	349479.547	NH_2CHO
346223.000	U	348065.969	$HCOOCH_3$	349496.000	U
346318.700	Ghost	348084.000	U	349550.000	U
346360.000	U	348101.000	U	349735.000	U
346379.244	$SO_2(v_2 = 1)$	348117.555	$^{34}SO_2$	349803.000	CH_3OCH_3
346460.000	U	348162.000	U	349803.000	CH_3OCH_3
346523.885	SO_2	348264.000	U	349806.094	CH_3OCH_3
346528.481	SO	348349.000	U	349809.188	CH_3OCH_3
346591.758	$SO_2(v_2 = 1)$	348358.000	U	350042.000	U
346652.175	SO_2	348373.000	U	350055.000	U
346718.889	HCOOH	348387.787	SO_2	350103.125	$^{13}CH_3OH$
346776.000	U	348531.873	H_2CS	350147.000	U
346826.000	U	348559.000	U	350170.000	U
346878.000	U	348680.000	Ghosts	350254.000	U
346947.349	CH_3CH_2CN	348784.641	CH_3CN	350288.000	U
346947.349	CH_3CH_2CN	348909.469	$HCOOCH_3$	350304.000	U

TABLE A1.3 - *continued*

ν (MHz)	Molecule	ν (MHz)	Molecule	ν (MHz)	Molecule
350333.345	HNCO	352082.906	$^{34}SO_2$	354759.125	$HCOOCH_3$
350382.000	U	352124.000	U	354799.957	$SO_2(v_2 = 1)$
350423.500	$CH_3CN(v_8 = 1)$	352283.000	$HCOOCH_3$	354805.656	$HCOOCH_3$
350442.250	$HCOOCH_3$	352292.594	$HCOOCH_3$	354805.719	$HCOOCH_3$
350450.000	U	352404.906	$HCOOCH_3$	354898.669	$H_2{}^{13}CO$
350457.594	$HCOOCH_3$	352414.156	$HCOOCH_3$	354949.469	Ghost
350467.000	U	352505.000	U	355032.200	U
350515.000	U	352599.576	OCS	355045.511	SO_2
350549.530	$CH_3CN(v_8 = 1)$	352897.866	HNCO	355098.500	Ghost
350552.230	$CH_3CN(v_8 = 1)$	352912.625	$HCOOCH_3$	355109.781	Ghost
350615.000	U	352918.031	$HCOOCH_3$	355190.918	$H_2{}^{13}CO$
350687.719	CH_3OH	352920.219	$HCOOCH_3$	355202.622	$H_2{}^{13}CO$
350689.500	NO	352922.031	$HCOOCH_3$	355211.000	U
350690.800	NO	352925.598	$HCOOCH_3$	355220.000	U
350694.800	NO	352927.438	$HCOOCH_3$	355231.000	U
350847.000	U	352929.563	$HCOOCH_3$	355446.000	U
350905.125	CH_3OH	352934.969	$HCOOCH_3$	355570.000	U
350919.563	$HCOOCH_3$	353152.000	U	355603.000	CH_3OH
350946.717	U	353166.000	U	355762.457	U
350947.250	$HCOOCH_3$	353234.873	CH_3CH_2CN	355835.971	$OC^{34}S$
350998.094	$HCOOCH_3$	353234.886	CH_3CH_2CN	355851.000	U
351015.844	$HCOOCH_3$	353241.509	C_2H_3CN	355968.500	U
351043.500	NO	353241.526	C_2H_3CN	356006.594	CH_3OH
351051.700	NO	353290.000	Ghost	356040.634	SO_2
351182.000	U	353402.000	$HCOOCH_3$	356076.000	U
351236.719	CH_3OH	353410.563	$HCOOCH_3$	356137.250	HCOOH
351257.206	SO_2	353724.100	$HCOOCH_3$	356176.114	$H_2{}^{13}CO$
351382.000	U	353728.540	$HCOOCH_3$	356217.000	U
351392.000	U	353739.281	$^{13}CH_3OH$	356223.000	U
351419.000	U	353811.873	$H_2{}^{13}CO$	356255.606	$HCN(v_2 = 1)$
351436.000	U	353851.000	U	356280.000	U
351491.406	U	353914.600	Ghost	356298.000	U
351517.250	$HCOOCH_3$	354129.000	U	356424.000	U
351529.125	$HCOOCH_3$	354370.000	Ghost	356442.938	CH_3OCH_3
351531.581	CH_3CH_2CN	354445.938	$^{13}CH_3OH$	356442.938	CH_3OCH_3
351540.000	U	354467.000	U	356443.250	CH_3OCH_3
351551.930	HNCO	354505.476	HCN	356443.563	CH_3OCH_3
351575.923	CH_3CH_2CN	354608.031	$HCOOCH_3$	356541.000	U
351633.457	HNCO	354608.406	$HCOOCH_3$	356551.000	U
351768.652	H_2CO	354698.694	HC_3N	356567.219	CH_3OCH_3
351873.873	SO_2	354742.375	$HCOOCH_3$	356575.250	CH_3OCH_3

TABLE A1.3 - *continued*

ν (MHz)	Molecule	ν (MHz)	Molecule	ν (MHz)	Molecule
356576.000	CH_3OCH_3	358008.188	$HCOOCH_3$	359352.000	$HCOOCH_3$
356582.844	CH_3OCH_3	358013.090	SO_2	359362.313	$HCOOCH_3$
356586.781	CH_3OCH_3	358038.080	SO_2	359381.563	CH_3OCH_3
356586.969	CH_3OCH_3	358093.656	Ghost	359381.563	CH_3OCH_3
356601.000	U	358152.375	Ghost	359384.625	CH_3OCH_3
356627.000	U	358215.640	SO_2	359387.656	CH_3OCH_3
356644.000	U	358331.000	U	359432.688	Ghost
356662.000	U	358347.313	$^{34}SO_2$	359543.031	$HCOOCH_3$
356734.288	HCO^+	358356.000	U	359558.031	$HCOOCH_3$
356755.180	SO_2	358364.250	$HCOOCH_3$	359651.755	$^{34}SO_2$
356793.969	$HCOOCH_3$	358392.344	$HCOOCH_3$	359680.777	U
356839.620	HDO	358415.000	U	359770.689	SO_2
356874.934	$^{13}CH_3OH$	358447.375	CH_3OCH_3	359821.094	Ghost
356908.610	C_2H_3CN	358449.406	CH_3OCH_3	359879.781	Ghost
356916.000	U	358449.406	CH_3OCH_3	359952.063	Ghosts
356928.563	$HCOOCH_3$	358451.406	CH_3OCH_3		
356937.719	$HCOOCH_3$	358451.938	CH_3OCH_3		
356965.000	U	358453.969	CH_3OCH_3		
356975.260	HOC^+	358456.500	CH_3OCH_3		
357066.217	CH_3OD	358456.500	CH_3OCH_3		
357087.045	$SO_2(v_2 = 1)$	358522.000	U		
357102.219	$^{34}SO_2$	358565.813	$HCOOCH_3$		
357165.360	SO_2	358576.600	$HCOOCH_3$		
357200.000	HCN-Ghost	358591.594	$HCOOCH_3$		
357220.000	HCN-Ghost	358605.813	CH_3OH		
357241.190	SO_2	358649.000	U		
357387.570	SO_2	358690.000	U		
357459.438	CH_3OCH_3	358725.906	U		
357459.438	CH_3OCH_3	358756.632	CH_3CCH		
357460.188	CH_3OCH_3	358790.765	CH_3CCH		
357460.969	CH_3OCH_3	358811.248	CH_3CCH		
357581.435	SO_2	358818.077	CH_3CCH		
357657.938	$^{13}CH_3OH$	358947.219	Ghost		
357671.780	SO_2	358988.000	$^{34}SO_2$		
357750.000	Ghost	359060.000	U		
357892.427	SO_2	359073.000	U		
357925.960	SO_2	359151.152	SO_2		
357962.890	SO_2	359254.000	Ghost		
357989.781	$HCOOCH_3$	359270.000	Ghost		
357995.563	$HCOOCH_3$	359335.625	$HCOOCH_3$		
357995.906	$HCOOCH_3$	359350.592	$HCOOCH_3$		

TABLE A1.4

TRANSITIONS OF CO, CS AND SiO

	ν (MHz)	J	T_a^* (K)	$\int T_a^* \, dv$ (K km s^{-1})	notes
CO	345796.0	3–2	109.8	4178.0	
^{13}CO	330588.1	3–2	26.5	316.0	
C^{18}O	329330.6	3–2	8.9	87.5	
C^{17}O	337061.1	3–2	3.4	39.7	
CS	342883.0	7–6	22.0	390.0	
C^{34}S	337396.7	7–6	7.5	71.4	
C^{33}S	340052.7	7–6	4.4	< 35.0	
SiO	347330.6	8–7	26.2	697.0	
^{29}SiO	342981.1	8–7	3.5	89.0	
^{30}SiO	338929.5	8–7	3.1	75.6	

TABLE A1.5

TRANSITIONS OF HCN, HC_3N, OCS, HCO^+ AND HCS^+

	ν (MHz)	J	T_{MB} (K)	$\int T_{MB}\, dv$ (K km s^{-1})	notes
HCN	354505.5	4–3	38.0	1326.0	1
HCN($v_2 = 1$)	356255.6	4–3	5.4	68.9	
$H^{13}CN$	345339.8	4–3	<21.0	< 518.7	2
$HC^{15}N$	344200.3	4–3	8.0	155.8	
HC_3N	327431.4	36–35	< 6.0	< 79.8	
	336521.0	37–36	5.0	< 96.6	
	345610.1	38–37	4.3	64.6	
	354698.7	39–38	5.1	91.4	3
$H^{13}CCCN$	334929.5	38–37	1.9	0.4	
	352544.6	40–39	1.8	0.2	
$HC^{13}CCN$	344142.5	38–37	0.8	0.1	
	353192.4	39–38	2.5	0.2	
OCS	328298.1	27–26	5.6	70.0	
	340449.2	28–27	9.3	< 129.8	4
	352599.6	29–28	4.2	54.0	
$OC^{34}S$	332129.7	28–27	1.6	< 17.6	5
	343983.3	29–28	0.6	3.6	
	355836.0	30–29	0.9	< 8.2	6
HCO^+	356734.3	4–3	35.7	< 780.0	7
$H^{13}CO^+$	346998.5	4–3	< 1.5	< 14.0	8
HOC^+	356975.3	4–3	1.4	12.6	9
$HC^{18}O^+$	340633.0	4–3	1.0	17.0	
HCS^+	341350.8	8–7	0.9	7.5	

[1] Blend with U-line at 354467.
[2] Blend with SO_2 line at 345338.5.
[3] Broad wings, possibly blended with U-line.
[4] Blend with U-line at 340439.
[5] Blend with $HCOOCH_3$ 332122.7 and 322137.8 lines.
[6] Blend with U-line at 355851.
[7] Blend with SO_2 line at 356755.2.
[8] Blend with U-line at 346987 and CH_3CHO (check) at 346995.5.
[9] Blend with U-line at 356965, uncertain identification.

TABLE A1.6

TRANSITIONS OF SO AND NO

	ν (MHz)	$N_J; J, F$	T_a^* (K)	$\int T_a^* \, dv$ (K km s^{-1})	notes
SO	329385.5	$2_1 - 1_0$	4.8	69.3	1
	336553.3	$11_{10} - 10_{10}$			2
	339341.5	$3_3 - 2_3$	4.8	131.2	2
	340714.2	$8_7 - 7_6$	28.7	1051.0	
	344310.6	$8_8 - 7_7$	32.9	1062.5	
	346528.5	$8_9 - 7_8$	30.7	< 1069.8	3
^{34}SO	333902.1	$8_7 - 7_6$	6.4	< 154.6	4
	337582.2	$8_8 - 7_7$	7.8	< 167.3	5
	339857.6	$8_9 - 7_8$	10.9	< 317.7	6
^{33}SO	337195.0	$8_7 - 7_6$	2.8	43.4	7
	340839.0	$8_8 - 7_7$	3.4	< 58.7	8
	343086.0	$8_9 - 7_8$	3.5	80.3	
S^{18}O	355573.6	$9_8 - 8_7$	1.7	23.2	
	358648.8	$9_9 - 8_8$	0.8	9.7	
NO	350689.5	$\frac{7}{2},\frac{9}{2} - \frac{5}{2},\frac{7}{2}$ f			
	350690.8	$\frac{7}{2},\frac{7}{2} - \frac{5}{2},\frac{5}{2}$ f	< 11.1	< 155.6	9
	350694.8	$\frac{7}{2},\frac{5}{2} - \frac{5}{2},\frac{3}{2}$ f			
	351043.5	$\frac{7}{2},\frac{9}{2} - \frac{5}{2},\frac{7}{2}$ e			
	351051.7	$\frac{7}{2},\frac{7}{2} - \frac{5}{2},\frac{5}{2}$ e	4.4	82.6	
	351051.7	$\frac{7}{2},\frac{5}{2} - \frac{5}{2},\frac{3}{2}$ e			

[1] Blend with $HCOOCH_3$ at 329364.2.
[2] Blend with U-line at 336558.
[3] Blend with SO_2 at 346523.9.
[4] Blend with CH_3CHOat 333931.9 (and/or U-line ?).
[5] Blend with $CH_3OH(v_t = 1)$ at 337546.1, 337605.3 and 337610.6.
[6] Blend with strong U-line at 339855.8.
[7] Blend with CH_3OCH_3 lines from 337180 to 337192.
[8] Blend with U-lines at 340812 and 340828.
[9] Blend with CH_3OH at 350687.7 and with the other f components.

TABLE A1.7

TRANSITIONS OF CN AND CCH

	ν (MHz)	N, J, F	T_a^* (K)	$\int T_a^* \, dv$ (K km s^{-1})	notes
CN	339475.9	$4,\frac{5}{2},\frac{5}{2} - 3,\frac{5}{2},\frac{5}{2}$	0.7	< 4.3	1
	339516.7	$4,\frac{5}{2},\frac{7}{2} - 3,\frac{5}{2},\frac{7}{2}$	0.9	6.2	
	339992.3	$4,\frac{5}{2},\frac{3}{2} - 3,\frac{3}{2},\frac{5}{2}$	0.2	0.5	
	340008.1	$4,\frac{5}{2},\frac{5}{2} - 3,\frac{3}{2},\frac{5}{2}$	1.4	10.8	
	340019.6	$4,\frac{5}{2},\frac{3}{2} - 3,\frac{3}{2},\frac{3}{2}$	1.9	11.9	
	340031.5	$4,\frac{5}{2},\frac{7}{2} - 3,\frac{3}{2},\frac{5}{2}$	4.6	27.8	
	340035.4	$4,\frac{5}{2},\frac{3}{2} - 3,\frac{3}{2},\frac{1}{2}$	4.8	21.7	
	340035.4	$4,\frac{5}{2},\frac{5}{2} - 3,\frac{3}{2},\frac{3}{2}$			
	340247.7	$4,\frac{7}{2},\frac{9}{2} - 3,\frac{5}{2},\frac{7}{2}$	8.2	47.5	
	340247.8	$4,\frac{7}{2},\frac{7}{2} - 3,\frac{5}{2},\frac{5}{2}$			
	340248.6	$4,\frac{7}{2},\frac{5}{2} - 3,\frac{5}{2},\frac{3}{2}$			
	340261.8	$4,\frac{7}{2},\frac{5}{2} - 3,\frac{5}{2},\frac{5}{2}$	2.1	16.3	2
	340265.0	$4,\frac{7}{2},\frac{7}{2} - 3,\frac{5}{2},\frac{7}{2}$			
CCH	349337.5	$4,\frac{9}{2},\frac{9}{2} - 3,\frac{7}{2},\frac{7}{2}$	3.0	14.8	
	349338.7	$4,\frac{9}{2},\frac{7}{2} - 3,\frac{7}{2},\frac{5}{2}$			
	349398.9	$4,\frac{7}{2},\frac{7}{2} - 3,\frac{5}{2},\frac{5}{2}$	<6.5	<60.8	3
	349400.3	$4,\frac{7}{2},\frac{5}{2} - 3,\frac{5}{2},\frac{3}{2}$			

[1] Blend with U-line at 339468.

[2] Blend with broad underlying feature.

[3] Blend with $CH_3CN(19_3 - 18_3)$ at 349393.0.

TABLE A1.8

TRANSITIONS OF CH_3CN

	ν (MHz)	J_K	T_a^* (K)	$\int T_a^* dv$ (K km s^{-1})	notes
CH_3CN	330437.4	$18_{10} - 17_{10}$	0.8	<4.3	1
	330557.6	$18_9 - 17_9$	...	...	2
	330665.2	$18_8 - 17_8$	1.1	9.2	3
	330760.2	$18_7 - 17_7$	1.6	11.8	
	330842.6	$18_6 - 17_6$	2.9	41.5	4
	330912.5	$18_5 - 17_5$	2.6	27.0	5
	330969.6	$18_4 - 17_4$	3.1	37.0	
	331014.1	$18_3 - 17_3$	4.6	58.2	
	331045.9	$18_2 - 17_2$	4.1	47.0	
	331065.0	$18_1 - 17_1$	4.8	82.4	
	331071.3	$18_0 - 17_0$	5.2		
	348784.6	$19_{10} - 18_{10}$	0.8	8.6	
	348911.4	$19_9 - 18_9$	...	...	6
	349025.0	$19_8 - 18_8$	1.6	15.0	
	349125.3	$19_7 - 18_7$	1.9	20.8	
	349212.1	$19_6 - 18_6$	2.9	41.5	
	349285.8	$19_5 - 18_5$	3.0	35.1	7
	349346.1	$19_4 - 18_4$	3.5	38.5	
	349393.0	$19_3 - 18_3$	< 6.5	<60.5	8
	349426.6	$19_2 - 18_2$	4.2	58.4	
	349446.7	$19_1 - 18_1$	5.9	51.6	
	349453.4	$19_0 - 18_0$			
$CH_3CN(v_8 = 1)$	332015.8	$17_0 - 16_0$	1.9	19.8	9
	332017.8	$17_{-1} - 16_{-1}$			
	350423.5	$18_{-2} - 17_{-2}$	1.2	9.3	
	350549.5	$18_{-1} - 17_{-1}$	1.7	13.5	
	350552.2	$18_2 - 17_2$			
$CH_3^{13}CN$	330881.9	$18_2 - 17_2$	0.3	1.7	
	330901.0	$18_1 - 17_1$	0.8	4.9	10
	330907.3	$18_0 - 17_0$			
	349220.0	$19_3 - 18_3$	...	...	11
	349253.5	$19_2 - 18_2$	0.6	4.2	
	349273.3	$19_1 - 18_1$	1.0	8.0	12
	349280.3	$19_0 - 18_0$			

[1] Blend with $^{13}CH_3OH$ at 330442.4.
[2] Blend with ^{13}CO(3-2) at 330588.1.
[3] Blend with $^{34}SO_2$ at 330667.6.
[4] Blend with HNCO at 330848.8.
[5] Blend with $CH_3^{13}CN$ at 330901.0 and 330907.3.
[6] Blend with $HCOOCH_3$ at 348909.5 and 348915.0.
[7] Blend with $CH_3^{13}CN$ at 349273.6 and 349280.8.
[8] Blend with CCH at 349398.9 and 349400.3.
[9] Blend with CH_3CH_2CN at 332014.7 and 332020.6 and U-line at 332030.
[10] Blend with $CH_3CN(18_5\text{-}17_5)$.
[11] Blend with $CH_3CN(19_6\text{-}18_6)$.
[12] Blend of with $CH_3CN(19_5\text{-}18_5)$.

TABLE A1.9

TRANSITIONS OF CH_3CCH

	ν (MHz)	J_K	T_a^* (K)	$\int T_a^* \, dv$ (K km s^{-1})	notes
CH_3CCH	341682.6	$20_3 - 19_3$	2.1	14.0	1
	341715.1	$20_2 - 19_2$	3.3	22.5	2
	341734.6	$20_1 - 19_1$	2.5	15.6	3
	341741.1	$20_0 - 19_0$	1.6	10.1	4
	358756.6	$21_3 - 20_3$	0.8	4.9	
	358790.8	$21_2 - 20_2$	0.7	4.8	
	358811.2	$21_1 - 20_1$	0.8	4.1	
	358818.1	$21_0 - 20_0$	0.8	5.2	

[1] Blend with U-line at 341678.

[2] Blend with $HCOOCH_3$ at 341722.4.

[3] Blend with $HCOOCH_3$ at 341732.3 and $CH_3CCH(20_0\text{-}19_0)$

[4] Blend with $CH_3CCH(20_1\text{-}19_1)$.

TABLE A1.10

TRANSITIONS OF SO_2

	ν (MHz)	J_{K_-,K_+}	T_a^* (K)	$\int T_a^* \, dv$ (K km s^{-1})	notes
SO_2	326867.5	$20_{4,16} - 20_{3,17}$	6.3	87.4	1
	331580.2	$11_{6,6} - 12_{5,7}$	1.6	25.2	
	332091.4	$21_{2,20} - 21_{1,21}$	5.8	145.8	
	332505.2	$4_{3,1} - 3_{2,2}$	14.2	366.4	
	334673.3	$8_{2,6} - 7_{1,7}$	8.6	229.7	
	335773.2	$29_{5,25} - 30_{2,28}$	0.4	1.3	
	336089.2	$23_{3,21} - 23_{2,22}$	7.0	168.2	
	336669.6	$16_{7,9} - 17_{6,12}$	3.1	49.6	
	338306.0	$18_{4,14} - 18_{3,15}$	11.3	297.8	
	338611.8	$20_{1,19} - 19_{2,18}$	< 17.4	< 300.6	2
	340316.4	$28_{2,26} - 28_{1,27}$	6.4	128.8	
	341275.5	$21_{8,14} - 22_{7,15}$	2.0	31.6	
	345149.0	$5_{5,1} - 6_{4,2}$	1.9	21.5	3
	345338.5	$13_{2,12} - 12_{1,11}$	<21.0	<518.7	4
	345448.8	$26_{9,17} - 27_{8,20}$	0.6	3.9	
	346523.9	$16_{4,12} - 16_{3,13}$	< 30.7	< 1069.8	5
	346652.2	$19_{1,19} - 18_{0,18}$	15.7	456.8	
	348387.8	$24_{2,22} - 23_{3,21}$	7.6	< 152.0	6
	350862.7	$10_{6,4} - 11_{5,7}$	4.2	8.8	7
	351257.2	$5_{3,3} - 4_{2,2}$	12.5	< 354.5	8
	351873.9	$14_{4,10} - 14_{3,11}$	11.0	282.8	
	355045.5	$12_{4,8} - 12_{3,9}$	11.4	< 333.5	9
	356040.6	$15_{7,9} - 16_{6,10}$	2.6	< 34.8	
	356755.2	$10_{4,6} - 10_{3,7}$	< 16.2	< 96.7	10
	357165.4	$13_{4,10} - 13_{3,11}$	12.2	357.2	
	357241.2	$15_{4,12} - 15_{3,13}$	11.1	326.4	
	357387.6	$11_{4,8} - 11_{3,9}$	13.1	373.0	
	357581.4	$8_{4,4} - 8_{3,5}$	16.6	460.0	
	357671.8	$9_{4,6} - 9_{3,7}$	17.3	< 557.1	11

[1] Lower limits for line intensity and integrated area due to high atmospheric noise and improper sideband cleaning.
[2] Blend with CH_3OH at 338615.0
[3] Blend with $HCOOCH_3$ at 345132.6 and $^{34}SO_2$ at 345168.8.
[4] Blend with $H^{13}CN$(4-3) at 345339.8.
[5] Blend with SO at 346528.5.
[6] Blend with U-line at 348373.
[7] Blend with U-line at 350847.
[8] Blend with CH_3OH at 351236.7.
[9] Blend with U-line at 355030.
[10] Blend with HCO^+ at 356734.3.
[11] Blend with $^{13}CH_3OH$ at 357657.9.

TABLE A1.10 - *continued*

	ν (MHz)	J_{K_-,K_+}	T_a^* (K)	$\int T_a^* \, dv$ (K kms^{-1})	notes
SO_2	357892.4	$7_{4,4} - 7_{3,5}$	17.6	473.5	12
	357926.0	$6_{4,2} - 6_{3,3}$	15.2	355.9	12
	357962.9	$17_{4,14} - 17_{3,15}$	14.8	354.6	12
	358013.1	$5_{4,2} - 5_{3,3}$	14.6	290.1	13,14
	358038.1	$4_{4,0} - 4_{3,1}$	11.0	190.6	14
	358215.6	$20_{0,20} - 19_{1,19}$	19.4	572.5	
	359151.2	$25_{3,23} - 25_{2,24}$	7.1	181.2	
	359770.7	$19_{4,16} - 19_{3,17}$	11.8	381.2	
$SO_2(v_2 = 1)$	336760.7	$20_{1,19} - 19_{2,18}$	0.6	7.9	
	337892.2	$21_{2,20} - 21_{1,21}$	0.8	5.5	15
	338376.3	$8_{2,6} - 7_{1,7}$	0.3	4.2	
	342435.9	$23_{3,21} - 23_{2,22}$	0.5	3.9	
	343923.8	$24_{2,22} - 23_{3,21}$	0.1	0.8	
	346379.2	$19_{1,19} - 18_{0,18}$	0.6	3.8	
	346591.8	$18_{4,14} - 18_{3,15}$	0.9	5.7	
	354800.0	$16_{4,12} - 16_{3,13}$	...	...	16
	357087.0	$5_{3,3} - 4_{2,2}$	2.0	21.8	

[12] Blend of SO_2 lines at 357892.3, 357926.0 and 357962.9.
[13] Blend with $HCOOCH_3$ lines at 357989.8. and 357995.9.
[14] Blend of SO_2 lines at 358013.1 and 358038.1.
[15] Blend with U-line at 337880.
[16] Blended with ghost.

TABLE A1.11

TRANSITIONS OF $^{34}SO_2$

	ν (MHz)	J_{K_-,K_+}	T_a^* (K)	$\int T_a^*\, dv$ (K km s^{-1})	notes
$^{34}SO_2$	329499.7	$5_{5,1} - 6_{4,2}$	0.5	4.9	
	330191.2	$8_{2,6} - 7_{1,7}$	1.4	13.2	1
	330667.6	$21_{2,20} - 21_{1,21}$	1.2	12.3	2
	332173.7	$23_{3,21} - 23_{2,22}$	0.8	9.6	
	332836.3	$16_{4,12} - 16_{3,13}$	2.3	45.0	
	338785.8	$14_{4,10} - 14_{3,1}$	1.9	24.2	
	342208.9	$5_{3,3} - 4_{2,2}$	2.6	38.4	
	342332.1	$12_{4,8} - 12_{3,9}$	1.8	21.4	
	344245.4	$10_{4,6} - 10_{3,7}$	< 2.7	< 40.1	3
	344581.1	$19_{1,19} - 18_{0,18}$	3.9	87.3	
	344808.0	$13_{4,10} - 13_{3,11}$	2.3	39.3	4
	344987.6	$15_{4,12} - 15_{3,13}$	3.2	96.3	
	344998.2	$11_{4,8} - 11_{3,9}$	2.9		
	345168.8	$8_{4,4} - 8_{3,5}$	2.2	46.4	5
	345285.7	$9_{4,6} - 9_{3,7}$	2.1	42.3	6
	345519.7	$7_{4,4} - 7_{3,5}$	1.3	11.0	
	345553.2	$6_{4,2} - 6_{3,3}$	0.6	2.8	
	345651.4	$5_{4,2} - 5_{3,3}$	1.1	9.7	
	345929.4	$17_{4,14} - 17_{3,15}$	2.8	45.1	7
	348117.6	$19_{4,16} - 19_{3,17}$	2.0	27.2	8
	352082.9	$21_{4,18} - 21_{3,19}$	0.7	4.1	
	357102.2	$20_{0,20} - 19_{1,19}$	2.8	39.4	
	358347.3	$23_{4,20} - 23_{3,21}$	2.2	24.1	
	358988.0	$15_{2,14} - 14_{1,13}$	1.7	44.4	
	359651.8	$24_{2,22} - 23_{3,21}$	0.7	5.8	

[1] Blend with $^{13}CH_3OH$ at 330194.0.
[2] Blend with CH_3CN at 330665.2.
[3] Blend with $HC^{15}N$ at 344200.3 and SO at 344310.6
[4] Blend with U-line at 344795.9.
[5] Blend with SO_2 at 345149.0.
[6] Blend with SO_2 at 345338.5 and $H^{13}CN$ at 345339.8.
[7] Blend with wing of CO(3-2) at 345796.0 and CH_3OH at 345919.2.
[8] Blend with U-line at 348100.4.

TABLE A1.12

TRANSITIONS OF H_2O, HDO, HDS AND NH_2D

	ν (MHz)	$J_{K_-,K_+}(,v_F)$	T_a^* (K)	$\int T_a^*\, dv$ (K km s^{-1})	notes
H_2O	325152.9	$5_{1,5} - 4_{2,2}$	24.9	533.1	
HDO	335395.5	$3_{3,1} - 4_{2,2}$	1.4	13.0	
	356839.6	$5_{3,2} - 6_{1,5}$	0.9	6.6	
HDS	333278.5	$2_{0,2} - 1_{1,1}$	1.5	13.0	1
NH_2D	332780.9	$1_{0,1}, 1_0 - 0_{0,0}, 0_1$			
	332781.8	$1_{0,1}, 1_2 - 0_{0,0}, 0_1$	0.5	4.4	2
	332782.4	$1_{0,1}, 1_1 - 0_{0,0}, 0_1$			

[1] Blend with CH_3CH_2CN at 333274.7.

[2] Blend of $F = 0 - 1, 2 - 1$ and $1 - 1$ lines with U-line at 332789.

TABLE A1.13

TRANSITIONS OF CH_3OH

	ν (MHz)	$J_{K-,K+}$	T_a^* (K)	$\int T_a^* \, dv$ (K km s^{-1})	notes
CH_3OH	326630.6	$10_{6,5}A^- - 10_{5,5}A^+$	7.5	39.8	1
	326961.2	$10_{5,6}E - 9_{5,5}E$	4.9	27.7	1
	327317.2	$12_{7,5}A^- - 11_{7,4}A^-$	4.0	36.9	1
	327408.2	$17_{11,6}A^+ - 18_{11,7}A^+$	1.8	8.0	1
	327487.2	$13_{9,5}E - 14_{9,6}E$	1.4	8.5	1
	328468.8	$20_{12,9}A^+ - 19_{12,8}A^+$	1.1	7.5	
	329632.9	$12_{7,5}A^+ - 11_{7,4}A^+$	4.6	28.1	
	330355.3	$20_{12,9}A^- - 19_{12,8}A^-$	0.8	< 5.0	2
	330793.9	$8_{3,6}E - 9_{4,6}E$	3.7	20.8	
	331221.6	$16_{8,9}E - 15_{7,9}E$	2.3	15.3	
	331502.4	$11_{6,5}A^- - 11_{6,6}A^+$	6.9	58.2	3
	335133.5	$2_{2,0}A^- - 3_{2,1}A^+$	4.2	28.6	
	335582.0	$7_{4,3}A^+ - 6_{4,3}A^+$	12.8	100.5	
	336438.3	$14_{11,4}A^\pm - 15_{11,5}A^\pm$	2.1	11.6	
	336865.1	$12_{7,6}A^- - 12_{6,6}A^+$	11.4	93.6	
	337135.9	$3_{3,0}E - 4_{3,1}E$	4.5	22.0	
	338124.5	$7_{4,4}E - 6_{3,3}E$	10.3	77.6	
	338344.6	$3_{4,0}E - 6_{3,4}E$	13.2	< 107.3	4
	338404.6	$7_{7,1}E - 6_{6,0}E$	13.8	< 113.5	5
	338408.7	$7_{4,4}A^+ - 6_{3,3}A^+$			
	338431.0	$7_{1,7}E - 6_{0,6}E$	3.5	22.7	
	338442.3	$7_{7,1}A^\pm - 6_{0,0}A^\pm$	4.7	27.3	
	338456.5	$7_{1,6}E - 6_{1,6}E$	4.7	31.6	
	338475.3	$7_{6,1}E - 6_{6,1}E$	4.6	29.8	
	338486.3	$7_{6,1}A^\pm - 6_{6,1}A^\pm$	5.3	35.2	
	338504.1	$7_{2,6}E - 6_{1,5}E$	7.1	37.8	
	338512.6	$7_{6,2}A^\mp - 6_{5,1}A^\mp$	10.6	80.3	
	338512.9	$7_{5,3}A^- - 6_{4,2}A^-$			
	338530.3	$7_{6,2}E - 6_{5,1}E$	6.9	45.3	
	338540.8	$7_{5,2}A^+ - 6_{5,2}A^+$	12.0	96.5	
	338543.2	$7_{5,2}A^- - 6_{5,2}A^-$			
	338559.9	$7_{2,5}E - 6_{2,5}E$	7.8	52.8	
	338583.2	$7_{5,2}E - 6_{5,2}E$	9.5	< 75.9	6
	338615.0	$7_{4,3}E - 6_{4,3}E$	< 17.1	< 128.7	6
	338639.9	$7_{5,3}A^+ - 6_{4,2}A^+$	9.6	< 76.1	6
	338721.6	$7_{5,3}E - 6_{4,2}E$	13.5	26.8	
	338722.9	$7_{3,5}E - 6_{2,4}E$			

[1] Noisy part of the spectrum, parameters not reliable.
[2] Blend with $^{13}CH_3OH$ at 330350.0 and 330362.0.
[3] Blend with U-line at at 331490.
[4] Blend with wing of SO_2 at 338306.0 and $HCOOCH_3$ at 338355.0.
[5] Blend with $HCOOCH_3$ at 338396.4.
[6] Blend with SO_2 at 338611.8.

TABLE A1.13 - *continued*

	ν (MHz)	J_{K_-,K_+}	T_a^* (K)	$\int T_a^* \, dv$ (K km s^{-1})	notes
CH_3OH	340141.2	$2_{2,0}A^+ - 3_{2,1}A^+$	< 8.2	< 27.1	7
	340394.2	$16_{11,5}A^- - 17_{11,6}A^-$	3.9	21.1	
	340394.3	$16_{11,5}A^+ - 17_{11,6}A^+$			
	341415.6	$7_{4,3}A^- - 6_{4,3}A^-$	10.8	90.5	
	342729.8	$13_{7,6}A^- - 13_{7,7}A^+$	8.7	81.6	
	344110.4	$18_{10,8}E - 17_{10,7}E$	2.7	15.8	
	344444.7	$19_{10,9}A^+ - 18_{10,8}A^+$	2.2	13.9	
	345904.2	$16_{9,8}A^- - 15_{9,7}A^-$	< 4.5	< 35.5	8
	345919.2	$18_{8,11}E - 17_{7,11}E$	...	...	8,9
	346202.8	$5_{5,1}A^- - 6_{5,2}A^-$	3.7	23.3	
	346204.4	$5_{5,1}A^+ - 6_{5,2}A^+$			
	349107.0	$14_{8,7}A^- - 14_{7,7}A^+$	4.5	42.3	
	350687.7	$4_{2,2}E - 3_{1,2}E$	11.2	< 102.7	10
	350905.1	$1_{1,0}A^+ - 0_{0,0}A^+$	9.2	64.2	11
	351236.7	$9_{7,2}E - 10_{7,3}E$	< 7.7	< 44.6	12
	355603.0	$13_{7,7}A^+ - 12_{7,6}A^+$	10.6	86.9	
	356006.6	$15_{8,7}A^- - 15_{8,8}A^+$	8.9	81.0	
	358605.8	$4_{3,2}E - 3_{2,2}E$	< 14.2	< 99.0	13
$CH_3OH(v_t = 1)$	334426.6	$3_{2,2}A^- - 2_{1,1}A^+$	1.9	8.7	
	337297.4	$7_{4,3}A^+ - 6_{4,3}A^+$	4.2	30.7	
	337463.7	$7_{7,1}A^+ - 6_{6,0}A^+$	1.6	10.3	
	337490.5	$7_{1,7}E - 6_{0,6}E$	< 2.0	< 11.1	14
	337519.1	$7_{5,2}A^+ - 6_{5,2}A^+$	2.2	12.6	
	337546.1	$7_{6,1}A^\pm - 6_{6,1}A^\pm$	< 2.4	< 17.0	15
	337605.3	$7_{3,5}E - 6_{2,4}E$	< 3.7	< 16.0	15
	337610.6	$7_{2,5}E - 6_{2,5}E$	< 3.7	<19.6	
	337625.6	$7_{5,3}A^+ - 6_{4,2}A^+$	3.7	< 24.0	
	337635.6	$7_{5,3}A^- - 6_{4,2}A^-$	< 3.9	< 16.2	
	337642.4	$7_{4,3}E - 6_{4,3}E$	< 5.4	< 41.2	15
	337643.8	$7_{4,4}E - 6_{3,3}E$			
	337646.0	$7_{2,6}E - 6_{1,5}E$			
	337648.2	$7_{1,6}E - 6_{1,6}E$			
	337655.2	$7_{5,2}A^\mp - 6_{5,2}A^\mp$	< 3.1	< 61.1	

[7] Blend with ghost at 340118.5 and U-line at 340156.9.
[8] Blend with the wing of CO(3-2) at 345796.0.
[9] Blend with $^{34}SO_2$ at 345929.4.
[10] Blend with NO at 350698.5, 350690.8 and 350694.8.
[11] Blend with $HCOOCH_3$ at 350919.6.
[12] Blend with SO_2 at 351257.2.
[13] Blend with $HCOOCH_3$ at 358606.4.
[14] Blend with $HCOOCH_3$ at 337489.7.
[15] Blend with $^{34}SO_2$ at 337582.2.

TABLE A1.13 - *continued*

	ν (MHz)	J_{K_-,K_+}	T_a^* (K)	$\int T_a^* \, dv$ (K km s^{-1})	notes
$CH_3OH(v_t = 1)$	337671.2	$7_{5,3}E - 6_{4,2}E$	2.1	12.8	
	337685.3	$7_{6,1}E - 6_{6,1}E$	2.3	14.4	
	337685.8	$7_{6,2}A^{\mp} - 6_{5,1}A^{\mp}$			
	337707.6	$7_{3,4}E - 6_{3,4}E$	< 2.5	< 19.7	16
	337748.8	$7_{4,4}A^{+} - 6_{3,3}A^{+}$	2.1	5.9	
	343897.2	$10_{4,6}E - 11_{4,7}E$	0.2	2.0	

[16] Blend with CH_3OCH_3 at 337712.4.

TABLE A1.14

TRANSITIONS OF $^{13}CH_3OH$ AND CH_3OD

	ν (MHz)	J_{K_-,K_+}	T_a^* (K)	$\int T_a^* dv$ (K kms^{-1})	notes
$^{13}CH_3OH$	330001.8	$7_{4,4}E - 6_{3,3}E$	0.8	1.5	
	330194.0	$7_{3,4}E - 6_{3,4}E$	1.4	13.2	1
	330252.8	$7_{4,4}A^+ - 6_{3,3}A^+$	< 0.8	< 2.8	2
	330336.9	$7_{2,6}E - 6_{1,5}E$	0.2	0.8	
	330342.5	$7_{6,2}A^\pm - 6_{5,1}A^\pm$	0.4	3.2	
	330350.0	$7_{5,3}A^- - 6_{4,2}A^-$	0.5	1.1	3
	330362.0	$7_{6,2}E - 6_{5,1}E$	0.3	1.1	3
	330371.3	$7_{5,2}A^+ - 6_{5,2}A^+$	0.8	3.9	
	330373.4	$7_{5,2}A^- - 6_{5,2}A^-$			
	330408.4	$7_{5,2}E - 6_{5,2}E$	< 1.5	< 6.1	4
	330442.4	$7_{4,3}E - 6_{4,3}E$	0.7	2.5	
	330463.7	$11_{6,5}A^- - 11_{6,6}A^+$	1.4	5.0	
	330464.9	$7_{5,3}A^+ - 6_{4,2}A^+$			
	330535.2	$7_{5,3}E - 6_{4,2}E$	1.6	8.5	
	330535.9	$7_{3,5}E - 6_{2,4}E$			
	333114.8	$7_{4,3}A^- - 6_{4,3}A^-$	2.2	20.8	5
	335559.9	$12_{7,6}A^- - 12_{6,6}A^+$	2.1	12.7	
	338760.4	$13_{7,7}A^+ - 12_{7,6}A^+$	1.3	7.2	
	341131.2	$13_{7,6}A^- - 13_{7,7}A^+$	1.7	10.9	
	345132.6	$4_{2,2}E - 3_{1,2}E$	1.8	15.0	6
	347187.7	$14_{8,7}A^- - 14_{7,7}A^-$	1.8	15.1	
	350103.1	$1_{1,0}A^+ - 0_{0,0}A^+$	0.8	1.2	
	353739.3	$15_{8,7}A^- - 15_{8,8}A^+$	2.6	19.8	
	354445.9	$4_{3,2}E - 3_{2,2}E$	< 2.0	< 9.4	7
	356874.9	$13_{8,6}A^- - 12_{8,5}A^-$	0.7	3.2	
	357657.9	$7_{5,3}E - 6_{4,3}E$	...	...	8
CH_3OD	327608.7	$4_2A^- - 4_1A^+$	0.6	2.4	9
	332758.3	$3_2E - 2_1E$	0.5	3.8	
	334264.9	$7_{-1} - 6_0E$	< 1.2	< 6.6	10
	335089.7	$6_2A^- - 6_1A^+$	0.4	1.5	11
	357066.2	$8_1A^+ - 7_1A^+$	< 0.8	< 3.5	

[1] Blend with $^{34}SO_2$ at 330191.2
[2] Blend with $HCOOCH_3$ at 330256.0.
[3] Blend with U-line at 330357.
[4] Blend with CH_3OCH_3 lines at 330405.4, 330406.5 and 330407.6
[5] Blend with CH_3CH_2CN at 333119.5.
[6] Blend with wing of SO_2 at 345149.0.
[7] Blend with wing of HCN(4-3) at 354505.5
[8] Blend with SO_2 at 357671.8.
[9] Blend with ^{13}CO ghost.
[10] Blend with HCOOH line at 334265.8.
[11] Blend with DNCO at 335096.5

TABLE A1.15

TRANSITIONS OF H_2CO, $H_2{}^{13}CO$, $H_2C^{18}O$ AND H_2CS

	ν (MHz)	J_{K_-,K_+}	T_a^* (K)	$\int T_a^* \, dv$ (K km s^{-1})	notes
H_2CO	351768.7	$5_{1,5} - 4_{1,4}$	15.5	276.8	
$H_2{}^{13}CO$	343325.7	$5_{1,5} - 4_{1,4}$	4.3	37.2	
	353811.9	$5_{0,5} - 4_{0,4}$	1.7	9.2	
	354898.7	$5_{2,4} - 4_{2,3}$	0.7	2.5	
	355190.9	$5_{3,3} - 4_{2,2}$	1.8	13.9	1
	355202.6	$5_{3,2} - 4_{3,1}$	1.5	11.3	1
	356176.1	$5_{2,3} - 4_{2,2}$	1.3	8.0	
$H_2C^{18}O$	335816.0	$5_{1,5} - 4_{1,4}$	0.4	1.1	
H_2CS	338080.8	$10_{1,10} - 9_{1,9}$	3.4	17.5	
	342944.4	$10_{0,10} - 9_{0,9}$	2.7	16.8	
	343308.5	$10_{4,7} - 9_{4,6}$	4.2	29.2	
	343308.5	$10_{4,6} - 9_{4,5}$			
	343319.6	$10_{2,9} - 9_{2,8}$	.	.	2
	343408.1	$10_{3,8} - 9_{3,7}$	2.1	17.8	
	343412.3	$10_{3,7} - 9_{3,6}$			
	343810.8	$10_{2,8} - 9_{2,7}$	1.1	5.4	
	348531.9	$10_{1,9} - 9_{1,8}$	5.4	26.8	

[1] Blend of $H_2{}^{13}CO$ lines at 355190.9 and 355202.6.

[2] Blend with $H_2{}^{13}CO$ line at 343325.7.

TABLE A1.16

TRANSITIONS OF HNCO, DNCO, HCOOH, CH_2CO AND NH_2CHO

	ν (MHz)	J_{K_-,K_+}	T_a^* (K)	$\int T_a^* \, dv$ (K kms^{-1})	notes
HNCO	328117.4	$24_{1,24} - 25_{0,25}$	0.4	1.5	
	328444.3	$15_{1,15} - 14_{1,14}$	2.3	12.4	
	329459.9	$15_{3,12} - 14_{3,11}$	1.0	5.5	
	329459.9	$15_{3,13} - 14_{3,13}$			
	329573.5	$15_{2,14} - 14_{2,13}$	1.1	9.9	
	329585.1	$15_{2,13} - 14_{2,12}$	1.1	7.0	
	329664.5	$15_{0,15} - 14_{0,14}$	5.1	60.2	
	330848.8	$15_{1,14} - 14_{1,13}$	<2.7	<34.6	1
	350333.3	$16_{1,16} - 15_{1,15}$	1.9	17.7	
	351417.1	$16_{3,14} - 15_{3,13}$	0.8	5.3	
	351417.2	$16_{3,13} - 15_{3,12}$			
	351551.9	$16_{2,14} - 15_{2,13}$	1.3	9.1	
	351633.5	$16_{0,16} - 15_{0,15}$	3.8	59.1	
	351994.8	$23_{1,23} - 24_{0,24}$	0.6	3.4	
	352897.9	$16_{1,15} - 15_{1,14}$	1.7	13.4	
DNCO	335096.5	$5_{1,4} - 4_{1,3}$	1.4	6.5	2
HCOOH	334265.8	$15_{2,14} - 14_{2,13}$	< 1.2	< 6.6	3
	338143.7	$15_{4,12} - 14_{4,11}$	1.7	13.4	
	338201.8	$15_{3,13} - 14_{3,12}$	0.4	2.5	
	338248.7	$15_{4,11} - 14_{4,10}$	0.3	1.7	
	340229.0	$15_{3,12} - 14_{3,11}$	...	...	4
	342521.2	$16_{1,16} - 15_{1,15}$	0.5	1.1	5
	343952.4	$15_{1,14} - 14_{1,13}$	0.2	0.6	
	346718.8	$15_{2,13} - 14_{2,12}$	0.6	4.8	
	356137.2	$16_{2,15} - 15_{2,14}$	0.7	4.3	
CH_2CO	340209.7	$17_{1,17} - 16_{1,16}$	1.3	5.2	
	343392.9	$17_{2,16} - 16_{2,15}$	1.0	6.9	
NH_2CHO	336136.9	$16_{2,15} - 15_{2,14}$	0.5	3.9	
	339715.8	$16_{8,8} - 15_{8,7}$	0.3	1.4	
	339715.8	$16_{8,9} - 15_{8,8}$			
	339780.8	$16_{7,10} - 15_{7,9}$	0.3	1.1	
	339780.8	$16_{7,9} - 15_{7,8}$			
	339904.1	$16_{6,11} - 15_{6,10}$	2.0	27.6	6
	339904.1	$16_{6,10} - 15_{6,9}$			
	340491.1	$16_{3,14} - 15_{3,13}$	1.8	14.0	7
	340536.0	$16_{4,13} - 15_{4,12}$	0.5	1.6	
	349479.5	$16_{2,14} - 16_{2,13}$	0.4	2.5	

[1] Blend with CH_3CN at 330842.6.
[2] Blend with CH_3OD at 335089.7.
[3] Blend with CH_3OD at 334264.9.
[4] Blend with CN at 340247.8.
[5] Blend with $HCOOCH_3$ at 342525.3.
[6] Posssible blend with U-line.
[7] Blend with U-line at 340496.

TABLE A1.17

TRANSITIONS OF $HCOOCH_3$

	ν (MHz)	J_{K_-,K_+}	T_a^* (K)	$\int T_a^* \, dv$ (K kms^{-1})	notes
$HCOOCH_3$	325677.1	$26_{7,20}E - 25_{7,19}E$	2.1	14.0	1
	325694.4	$26_{7,20}A - 25_{7,19}A$	1.7	13.1	1
	327001.9	$12_{7,4}E - 11_{6,5}E$	1.5	17.0	1
	329364.2	$26_{7,19}E - 25_{7,18}E$	...	...	2
	329861.6	$27_{3,24}E - 26_{3,23}E$	0.5	1.5	
	329874.9	$27_{5,23}A - 26_{5,22}A$	0.4	0.7	
	330256.0	$10_{8,3}E - 9_{7,3}E$	...	...	3
	330276.4	$10_{8,2}E - 9_{7,2}E$	0.2	0.3	
	330323.9	$10_{8,3}A - 9_{7,2}A$	0.8	5.0	
	330323.9	$10_{8,2}A - 9_{7,3}A$			
	331149.3	$28_{6,23}E - 27_{6,22}E$	1.0	4.7	
	331159.6	$28_{4,25}A - 27_{4,24}A$	1.0	6.4	
	331460.0	$28_{5,23}E - 27_{5,22}E$	0.7	4.6	
	331469.5	$28_{3,25}A - 27_{3,24}A$	0.7	3.8	
	331775.9	$29_{2,27}A - 28_{3,26}A$	0.7	5.1	
	331784.2	$29_{5,25}E - 28_{5,24}E$	0.9	5.0	
	331792.1	$29_{3,27}A - 28_{3,26}A$	1.1	10.5	
	331795.9	$29_{4,26}E - 28_{4,25}E$			
	331803.8	$29_{2,27}A - 28_{2,26}A$	1.0	4.1	
	331812.2	$29_{5,25}E - 28_{4,25}E$	0.5	3.4	
	331819.9	$29_{3,27}A - 28_{2,26}A$	0.4	1.9	
	331827.7	$27_{18,9}E - 26_{18,8}E$	0.6	3.9	
	331834.5	$27_{18,10}E - 26_{18,9}E$	0.2	1.1	
	332329.2	$27_{15,12}A - 26_{15,11}A$	0.8	2.9	4
	332329.2	$27_{15,13}A - 26_{15,12}A$			
	332334.0	$27_{15,12}E - 26_{15,11}E$	0.4	3.0	4
	332352.6	$27_{15,13}E - 26_{15,12}E$	0.7	4.8	
	332570.9	$30_{3,28}E - 29_{2,27}E$	3.2	17.9	
	332571.2	$30_{4,27}E - 29_{2,27}E$			
	332571.4	$30_{3,28}E - 29_{3,27}E$			
	332571.7	$30_{4,27}E - 29_{3,27}E$			
	332575.6	$30_{1,29}A - 29_{2,28}E$	3.0	5.2	
	332575.9	$30_{2,29}A - 29_{2,28}E$			
	332576.2	$30_{1,29}A - 29_{1,28}A$			
	332576.4	$30_{2,29}A - 29_{1,28}A$			

[1] Noisy part of spectrum, parameters unreliable.

[2] Blend with SO at 329385.5.

[3] Blend with $^{13}CH_3OH$ at 330252.8.

[4] Blend of $HCOOCH_3$ lines at 332329.2 and 332334.0.

TABLE A1.17 - *continued*

	ν (MHz)	J_{K-},K_+	T_a^* (K)	$\int T_a^* \, dv$ (K km s^{-1})	notes
$HCOOCH_3$	332604.4	$27_{14,13}E - 26_{14,12}E$	1.6	10.7	
	332604.4	$27_{14,13}A - 26_{14,12}A$			
	332604.4	$27_{14,14}A - 26_{14,13}A$			
	332626.0	$27_{14,14}E - 26_{14,13}E$	0.6	3.8	
	332953.3	$27_{13,14}E - 26_{13,13}E$	0.7	2.8	
	332958.3	$27_{13,15}A - 26_{13,14}A$	0.9	5.3	
	332958.3	$27_{13,14}A - 26_{13,13}A$			
	332977.4	$27_{13,15}E - 26_{13,14}E$	0.5	3.2	
	333409.4	$27_{12,15}E - 26_{12,14}E$	0.5	2.6	
	333419.2	$27_{12,16}A - 26_{12,15}A$	1.0	5.5	
	333419.2	$27_{12,15}A - 26_{12,14}A$			
	333435.2	$27_{12,16}E - 26_{12,16}E$	0.7	4.5	
	333449.3	$31_{0,31}A - 30_{1,30}A$	2.4	10.0	
	333449.3	$31_{1,31}A - 30_{1,30}A$			
	333449.3	$31_{0,31}A - 30_{0,30}A$			
	333449.3	$31_{1,31}A - 30_{0,30}A$			
	333449.4	$31_{2,30}E - 30_{1,30}E$			
	333449.4	$31_{1,31}E - 30_{2,29}E$			
	333449.4	$31_{1,31}E - 30_{2,29}E$			
	333449.4	$31_{2,30}E - 30_{1,30}E$			
	333593.2	$27_{6,21}E - 26_{6,20}E$	1.6	7.9	
	333602.0	$27_{4,23}A - 26_{4,22}A$	2.0	16.3	
	333972.4	$15_{6,10}E - 14_{5,9}E$	0.6	3.7	
	334017.2	$27_{11,16}E - 26_{11,15}E$	1.3	9.5	
	334109.2	$15_{6,10}A - 14_{5,9}A$	0.5	2.9	
	334031.5	$27_{11,17}A - 26_{11,16}A$	1.6	9.8	
	334031.8	$27_{11,16}A - 26_{11,15}A$			
	334044.0	$27_{11,17}E - 26_{11,16}E$	0.9	4.7	
	334851.0	$27_{10,17}E - 26_{10,16}E$	0.6	2.3	
	334867.0	$27_{10,18}A - 26_{10,17}A$	0.5	2.1	
	334872.8	$27_{19,17}A - 26_{10,16}A$	0.8	3.2	
	334877.5	$27_{10,18}E - 26_{10,17}E$	0.8	2.5	
	336028.1	$27_{9,19}A - 26_{9,18}A$	1.3	9.6	
	336032.4	$27_{9,19}E - 26_{9,18}E$			
	336351.5	$27_{4,23}E - 26_{4,21}E$	2.2	12.9	
	336354.9	$26_{1,25}E - 25_{1,24}E$			

TABLE A1.17 - *continued*

	ν (MHz)	J_{K_-,K_+}	T_a^* (K)	$\int T_a^* \, dv$ (K km s^{-1})	notes
$HCOOCH_3$	336368.2	$27_{6,22}A - 25_{1,24}A$	1.1	4.3	
	336373.8	$26_{5,21}A - 25_{5,20}A$	1.5	5.9	
	336889.2	$26_{0,26}E - 25_{0,25}E$	1.5	5.4	
	336918.1	$26_{6,20}A - 25_{6,19}A$	1.6	5.4	
	337489.7	$27_{8,20}E - 26_{8,19}E$	<1.6	<8.1	5
	337503.4	$27_{8,20}A - 26_{8,19}A$	1.1	4.7	
	338355.8	$27_{8,19}A - 26_{8,18}A$	...	...	6
	338396.4	$27_{7,21}E - 26_{7,20}E$	...	...	7
	339129.3	$13_{7,7}E - 12_{6,7}E$	0.7	3.7	
	339152.8	$13_{7,6}E - 12_{6,6}E$	0.6	3.4	
	339186.0	$13_{7,7}A - 12_{6,6}A$	0.7	5.0	
	339196.4	$13_{7,6}A - 12_{6,7}A$	0.5	2.5	
	341722.4	$29_{6,24}E - 28_{6,23}E$	< 2.6	< 16.6	8
	341732.3	$29_{4,26}A - 28_{4,25}A$	< 2.5	< 14.1	9
	341862.6	$27_{5,23}A - 26_{4,22}A$	1.7	16.4	
	341870.3	$27_{3,24}E - 26_{6,20}E$	0.8	4.3	
	341918.1	$29_{5,24}E - 28_{5,23}E$	1.7	9.6	
	341927.5	$29_{4,26}A - 28_{3,25}A$	2.4	16.5	
	342162.5	$28_{13,16}E - 28_{12,17}E$	0.6	4.2	
	342166.8	$28_{13,13}E - 28_{12,16}E$			
	342230.1	$29_{6,24}E - 28_{5,23}E$	< 2.4	< 35.6	10
	342238.5	$29_{4,26}A - 28_{3,25}A$			
	342342.3	$30_{4,26}E - 29_{5,25}E$	...	...	11
	342350.1	$30_{2,28}A - 29_{3,27}A$	1.9	11.7	
	342351.7	$30_{5,26}E - 29_{5,25}E$			
	342358.5	$30_{4,26}E - 29_{3,26}E$	2.0	10.1	
	342359.4	$30_{3,28}A - 29_{3,27}A$			
	342366.3	$30_{2,28}A - 29_{2,27}A$	1.2	5.2	
	342367.9	$30_{5,26}E - 29_{4,26}E$			
	342375.6	$30_{3,28}A - 29_{2,27}A$	0.8	4.0	
	342506.7	$11_{8,4}E - 10_{7,4}E$	0.5	2.8	
	342525.3	$11_{8,3}E - 10_{7,3}E$	0.6	2.2	12
	342572.4	$11_{8,4}A - 10_{7,3}A$	0.8	3.2	
	342572.4	$11_{8,3}A - 10_{7,4}A$			

[5] Blend with $CH_3OH(v_t = 1)$ at 337490.5.
[6] Blend with CH_3OH at 338344.6.
[7] Blend with CH_3OH at 338404.6.
[8] Blend with CH_3CCH at 341715.1.
[9] Blend with CH_3CCH at 341734.6.
[10] Blend with $^{34}SO_2$ at 342208.9.
[11] Blend with $^{34}SO_2$ at 342332.1.
[12] Blend with HCOOH at 342521.2.

TABLE A1.17 - *continued*

	ν (MHz)	J_{K_-,K_+}	T_a^* (K)	$\int T_a^* \, dv$ (K km s^{-1})	notes
$HCOOCH_3$	343148.3	$31_{3,29}E - 30_{4,27}E$	2.8	9.9	
	343148.4	$31_{4,28}E - 30_{4,27}E$			
	343148.5	$31_{3,29}E - 30_{3,28}E$			
	343148.7	$31_{4,28}E - 30_{3,28}E$			
	343152.8	$31_{1,30}A - 30_{2,29}A$	3.1	14.5	
	343153.0	$31_{1,30}A - 30_{2,29}A$			
	343153.1	$31_{1,30}A - 30_{1,29}A$			
	343153.3	$31_{1,30}A - 30_{1,29}A$			
	343435.4	$28_{0,28}E - 27_{6,21}E$	1.3	6.8	
	343443.9	$28_{4,24}A - 27_{4,23}A$	1.4	8.7	
	343731.8	$27_{7,20}E - 26_{7,19}E$	0.9	3.2	
	343757.9	$27_{7,20}A - 26_{7,19}A$	< 2.1	< 11.4	13
	344029.6	$32_{0,32}A - 31_{1,31}A$	2.4	12.7	
	344029.6	$32_{1,32}A - 31_{1,31}A$			
	344029.6	$32_{0,32}A - 31_{0,31}A$			
	344029.6	$32_{1,32}A - 31_{0,31}A$			
	344029.6	$32_{2,31}A - 31_{1,31}A$			
	344029.6	$32_{1,32}A - 31_{1,31}A$			
	344029.6	$32_{2,31}A - 31_{2,30}A$			
	344029.6	$32_{1,32}A - 31_{2,30}A$			
	344759.0	$28_{15,13}A - 27_{15,12}A$	...	...	14
	344759.1	$28_{15,14}A - 27_{15,13}A$			
	344763.6	$28_{15,13}E - 27_{15,12}A$			
	344913.3	$20_{13,7}E - 20_{12,8}E$	1.0	8.6	
	344922.2	$20_{13,8}E - 20_{12,9}E$	0.6	5.4	
	345068.8	$28_{14,14}E - 27_{14,13}E$	1.1	7.2	
	345069.0	$28_{14,14}A - 27_{14,13}A$			
	345069.0	$28_{14,15}A - 27_{14,14}A$			
	345090.3	$28_{14,15}E - 27_{14,14}E$	0.5	4.5	
	345461.6	$28_{13,15}E - 27_{13,14}E$	0.2	0.6	
	345466.9	$28_{13,16}A - 27_{13,15}A$	0.6	2.0	
	345466.9	$28_{13,15}A - 27_{13,14}A$			
	345975.1	$28_{12,16}E - 27_{12,15}E$	0.7	3.4	
	345985.3	$28_{12,17}A - 27_{12,16}A$	1.2	7.3	
	345985.4	$28_{12,16}A - 27_{12,15}A$			

[13] Blend with CH_3OCH_3 lines at 343753.3–343755.1.

[14] Blend with U-line at 344773.0.

TABLE A1.17 - *continued*

	ν (MHz)	$J_{K-,K+}$	T_a^* (K)	$\int T_a^* \, dv$ (K km s^{-1})	notes
$HCOOCH_3$	346000.9	$28_{12,17}E - 27_{12,16}E$	1.4	7.1	
	347478.4	$27_{1,26}E - 26_{1,25}E$	1.4	5.9	
	347494.0	$27_{5,22}A - 26_{5,21}A$	1.2	4.2	
	347604.6	$28_{10,18}E - 27_{10,17}E$	1.0	4.2	
	347617.0	$28_{10,19}A - 27_{10,18}A$	1.1	5.0	
	347628.3	$28_{10,19}E - 27_{10,18}E$	1.7	7.6	
	347628.4	$28_{10,18}A - 27_{10,17}A$			
	348050.0	$28_{4,24}E - 27_{4,23}E$	1.0	4.0	
	348066.0	$28_{6,23}A - 27_{6,22}A$	0.9	3.7	
	348909.5	$28_{9,20}E - 27_{9,19}E$	3.0	14.8	15
	348915.0	$28_{9,20}A - 27_{9,19}A$			
	349048.5	$28_{9,19}E - 27_{9,18}E$	0.8	3.4	
	349065.7	$28_{9,19}A - 27_{9,17}A$	0.6	2.5	
	350442.3	$28_{8,20}E - 27_{8,20}E$	1.4	18.1	
	350457.6	$28_{8,21}A - 27_{8,20}A$			
	350919.6	$27_{0,27}E - 26_{0,26}E$	< 2.1	< 19.7	16
	350947.3	$27_{6,21}A - 26_{6,20}A$	1.6	7.7	
	350998.1	$28_{7,22}E - 27_{7,21}E$	1.5	7.8	
	351015.8	$27_{7,22}A - 27_{7,21}A$	1.0	4.9	
	351517.3	$29_{3,26}E - 28_{3,25}E$	0.5	1.2	
	351529.1	$29_{5,25}A - 28_{5,24}A$	0.7	3.6	17
	352283.0	$30_{6,25}E - 29_{6,24}E$	1.0	4.6	
	352292.6	$30_{4,27}A - 29_{4,26}A$	0.9	4.5	
	352404.9	$30_{5,25}E - 29_{5,24}E$	0.8	3.1	
	352414.2	$30_{3,27}A - 29_{3,26}A$	0.8	3.8	
	352912.6	$31_{4,27}E - 30_{5,26}E$	1.1	17.1	
	352918.0	$31_{5,27}E - 30_{5,26}E$			
	352920.2	$31_{2,29}A - 30_{3,28}A$			
	352922.0	$31_{4,27}E - 30_{4,26}E$			
	352925.6	$31_{3,29}A - 30_{3,28}A$			
	352927.4	$31_{5,27}E - 30_{4,26}E$			
	352929.6	$31_{2,29}A - 30_{2,28}A$			
	352935.0	$31_{3,29}A - 30_{2,28}A$			
	353402.0	$29_{0,29}E - 28_{0,28}E$	1.3	6.8	
	353410.6	$29_{4,25}A - 28_{4,24}A$	1.6	8.3	

[15] Blend with $CH_3CN(19_9 - 18_9)$ at 348911.4.

[16] Blend with CH_3OH at 350905.1.

[17] Blend with CH_3CH_2CN at 351531.6.

TABLE A1.17 - *continued*

	ν (MHz)	$J_{K-,K+}$	T_a^* (K)	$\int T_a^* \, dv$ (K km s^{-1})	notes
$HCOOCH_3$	353724.0	$32_{3,30}E - 31_{4,28}E$	3.5	13.4	
	353724.1	$32_{4,29}E - 31_{4,28}E$			
	353724.1	$32_{3,30}E - 31_{3,29}E$			
	353724.2	$32_{4,29}E - 31_{3,29}E$			
	353728.4	$32_{1,31}A - 31_{2,30}A$	3.9	21.1	
	353728.5	$32_{2,31}A - 31_{2,30}A$			
	353728.6	$32_{1,31}A - 31_{1,30}A$			
	353728.7	$32_{2,31}A - 31_{1,30}A$			
	354608.0	$33_{0,33}A - 32_{1,32}A$	2.7	14.9	
	354608.0	$33_{1,33}A - 32_{1,32}A$			
	354608.0	$33_{0,33}A - 32_{0,32}A$			
	354608.0	$33_{1,33}A - 32_{0,32}A$			
	354608.4	$33_{2,32}E - 32_{1,32}E$			
	354608.4	$33_{1,33}E - 32_{1,32}E$			
	354608.4	$33_{2,32}E - 32_{2,31}E$			
	354608.4	$33_{1,33}E - 32_{2,31}E$			
	354742.4	$12_{8,5}E - 11_{7,5}E$	0.5	2.6	
	354759.1	$12_{8,4}E - 11_{7,4}E$	0.7	3.7	
	354805.7	$12_{8,5}A - 11_{7,4}A$	0.7	2.9	
	354805.7	$12_{8,4}E - 11_{7,5}A$			
	356928.6	$29_{16,13}A - 28_{16,12}A$	0.7	4.2	
	356928.6	$29_{16,14}A - 28_{16,13}A$			
	356937.7	$29_{16,13}E - 28_{16,12}E$	0.7	3.8	
	357989.8	$29_{13,16}E - 28_{13,15}E$	...	...	18
	357995.6	$29_{13,17}A - 28_{13,16}A$	...	...	18
	357995.6	$29_{13,16}A - 28_{13,15}A$			
	357995.6	$28_{1,27}A - 27_{1,26}E$			
	358364.3	$28_{7,21}E - 27_{7,20}E$	2.2	9.8	
	358392.3	$28_{7,21}A - 27_{7,20}A$	1.8	8.4	
	358565.8	$29_{12,17}E - 28_{12,16}E$	1.7	5.5	
	358576.6	$29_{12,18}A - 28_{12,17}A$	3.7	21.4	
	358576.6	$29_{12,17}A - 28_{12,16}A$			
	358591.6	$29_{12,18}E - 28_{12,17}E$	3.6	18.4	19
	359335.6	$29_{11,18}E - 28_{11,17}E$	1.4	6.7	
	359350.6	$29_{11,19}A - 28_{11,18}A$	2.4	15.4	
	359352.0	$29_{11,18}A - 28_{11,17}A$			
	359362.3	$29_{11,19}E - 28_{11,18}E$	1.4	6.8	
	359543.0	$29_{4,25}E - 28_{4,24}E$	3.8	23.6	
	359558.0	$29_{6,24}A - 28_{6,23}A$	3.8	25.1	

[18] Blend with SO_2 at 357962.9 and 358013.1.

[19] Blend with CH_3OH at 358605.8.

TABLE A1.18

TRANSITIONS OF CH_3OCH_3

	ν (MHz)	$J_{K-,K+}$	T_a^* (K)	$\int T_a^* \, dv$ (K km s^{-1})	notes
CH_3OCH_3	328853.3	$10_{3,8}EA - 9_{2,7}EA$	1.6	13.5	
	328853.4	$10_{3,8}AE - 9_{2,7}AE$			
	328856.7	$10_{3,8}EE - 9_{2,7}EE$			
	328860.0	$10_{3,8}AA - 9_{2,7}AA$			
	330405.4	$16_{2,15}EA - 15_{1,7}EA$	< 1.5	< 6.1	1
	330405.4	$16_{2,15}AE - 15_{1,7}AE$			
	330406.5	$16_{2,15}EE - 15_{1,7}EE$			
	330407.6	$16_{2,15}AA - 15_{1,7}AA$			
	337180.8	$31_{3,28}AE - 31_{0,31}AE$	...	...	2
	337180.8	$31_{3,29}EA - 31_{0,31}EA$			
	337186.7	$31_{3,29}EE - 31_{0,31}EE$	...	...	2
	337192.6	$31_{3,28}AA - 31_{0,31}AA$			
	337420.9	$21_{2,19}AA - 20_{3,18}AA$	2.1	8.9	
	337421.3	$21_{2,19}EE - 20_{3,18}EE$			
	337421.8	$21_{2,19}AE - 20_{3,18}AE$			
	337421.8	$21_{2,19}EA - 20_{3,18}EA$			
	337712.4	$7_{4,4}EA - 6_{3,3}EA$	< 2.5	< 19.7	3
	337722.3	$7_{4,4}EE - 6_{3,3}EE$	1.8	8.6	
	337723.0	$7_{4,4}AE - 6_{3,3}AE$			
	337730.7	$7_{4,4}AA - 6_{3,3}AA$	2.3	3.5	
	337731.9	$7_{4,3}EA - 6_{3,3}EA$			
	337732.2	$7_{4,3}EE - 6_{3,3}EE$			
	337770.6	$7_{4,4}EA - 6_{3,4}EA$	0.7	1.9	
	337778.0	$7_{4,4}EE - 6_{3,4}EE$	1.9	8.4	
	337779.5	$7_{4,3}AE - 6_{3,4}AE$			
	337787.2	$7_{4,3}AA - 6_{3,4}AA$	2.2	9.1	
	337787.9	$7_{4,3}EE - 6_{3,4}EE$			
	337790.1	$7_{4,3}EA - 6_{3,4}EA$			
	339491.7	$19_{1,18}AA - 18_{2,17}AA$	2.4	11.2	
	339491.7	$19_{1,18}EE - 18_{2,17}EE$			
	339491.8	$19_{1,18}AE - 18_{2,17}AE$			
	339491.8	$19_{1,18}EA - 18_{2,17}EA$			
	340609.2	$10_{3,7}AE - 9_{2.8}AE$	2.7	22.3	
	340609.3	$10_{3,7}EA - 9_{2.8}EA$			
	340612.6	$10_{3,7}EE - 9_{2.8}EE$			
	340615.9	$10_{3,7}AA - 9_{2.8}AA$			
	342608.1	$19_{0,19}AE - 18_{1,18}AE$	3.1	14.7	
	342608.1	$19_{0,19}EA - 18_{1,18}EA$			
	342608.1	$19_{0,19}EE - 18_{1,18}EE$			
	342608.2	$19_{0,19}AA - 18_{1,18}AA$			

[1] Blend with $^{13}CH_3OH$ at 330408.4.

[2] Blend with ^{33}SO at 337195.0.

[3] Blend with $CH_3OH(v_t = 1)$ at 337707.6.

TABLE A1.18 - *continued*

	ν (MHz)	J_{K_-,K_+}	T_a^* (K)	$\int T_a^* \, dv$ (K kms^{-1})	notes
CH_3OCH_3	343753.3	$17_{2,16}EA - 16_{1,15}EA$	< 2.1	< 11.4	4
	343753.3	$17_{2,16}AE - 16_{1,15}AE$			
	343754.2	$17_{2,16}EE - 16_{1,15}EE$			
	343755.1	$17_{2,16}AA - 16_{1,15}AA$			
	344358.0	$19_{1,19}EA - 18_{0,18}EA$	1.9	< 18.5	5
	344358.0	$19_{1,19}AE - 18_{0,18}AE$			
	344358.1	$19_{1,19}EE - 18_{0,18}EE$			
	344358.2	$19_{1,19}AA - 18_{0,18}AA$			
	344512.2	$11_{3,9}EA - 10_{2,8}EA$	3.3	27.6	
	344512.2	$11_{3,9}AE - 10_{2,8}AE$			
	344515.4	$11_{3,9}EE - 10_{2,8}EE$			
	344518.6	$11_{3,9}AA - 10_{2,8}AA$			
	349803.0	$11_{2,9}AE - 10_{1,10}AE$	1.4	22.9	
	349803.0	$11_{2,9}EA - 10_{1,10}EA$			
	349806.1	$11_{2,9}EE - 10_{1,10}EE$			
	349809.2	$11_{2,9}AA - 10_{1,10}AA$			
	356442.9	$25_{1,24}AE - 24_{4,21}AE$	0.9	3.6	
	356442.9	$25_{1,24}EA - 24_{4,21}EA$			
	356443.3	$25_{1,24}EE - 24_{4,21}EE$			
	356443.6	$25_{1,24}AA - 24_{4,21}AA$			
	356567.2	$8_{4,5}EA - 7_{3,4}EA$	1.7	8.8	
	356575.3	$8_{4,5}AE - 7_{3,4}AE$	4.5	18.6	
	356576.0	$8_{4,5}EE - 7_{3,4}EE$			
	356582.8	$8_{4,5}AA - 7_{3,4}AA$	3.7	22.9	
	356586.8	$8_{4,4}EE - 7_{3,4}EE$			
	356587.0	$8_{4,4}EA - 7_{3,4}EA$			
	357459.4	$18_{2,17}EA - 17_{1,16}EA$	3.5	19.1	
	357459.4	$18_{2,17}AE - 17_{1,16}AE$			
	357460.2	$18_{2,17}EA - 17_{1,16}EA$			
	357461.0	$18_{2,17}EA - 17_{1,16}EA$			
	358447.4	$5_{5,0}EA - 4_{4,0}EA$	7.3	63.2	
	358449.4	$5_{5,1}AE - 4_{4,0}AE$			
	358449.4	$5_{5,0}AE - 4_{4,1}AE$			
	358451.4	$5_{5,1}EA - 4_{4,1}EA$			
	358451.9	$5_{5,0}EE - 4_{4,0}EE$			
	358454.0	$5_{5,1}EE - 4_{4,1}EE$			
	358456.5	$5_{5,1}AA - 4_{4,0}AA$			
	358456.5	$5_{5,0}AA - 4_{4,1}AA$			
	359381.6	$12_{3,10}EA - 11_{2,9}EA$	4.0	33.1	
	359381.6	$12_{3,10}AE - 11_{2,9}AE$			
	359384.6	$12_{3,10}EE - 11_{2,9}EE$			
	359387.7	$12_{3,10}AA - 11_{2,9}AA$			

[4] Blend with $HCOOCH_3$ at 343757.9.

[5] Blend with SO at 344310.6.

TABLE A1.19

TRANSITIONS OF CH_2CHCN

	ν (MHz)	$J_{K-,K+}$	T_a^* (K)	$\int T_a^* \, dv$ (K km s^{-1})	notes
CH_2CHCN	327159.7	$34_{3,31} - 33_{3,30}$	1.3	8.2	
	327551.5	$36_{0,36} - 35_{1,35}$	0.9	4.2	
	327881.5	$35_{2,34} - 34_{2,33}$	0.5	...	1
	329190.7	$36_{1,36} - 35_{1,35}$	0.9	3.4	
	329461.5	$36_{0,36} - 35_{0,35}$	< 1.0	< 5.5	2
	331100.6	$36_{1,36} - 35_{0,35}$ 0	1.0	3.	
	332384.2	$35_{8,28} - 34_{8,27}$	1.2	7.7	
	332384.2	$35_{8,27} - 34_{8,26}$			
	332400.7	$35_{9,27} - 34_{9,26}$	0.2	0.8	
	332400.7	$35_{9,26} - 34_{9,25}$			
	332418.3	$35_{7,29} - 34_{7,28}$	0.7	3.2	
	332418.3	$35_{7,28} - 34_{7,27}$			
	332452.5	$35_{10,25} - 34_{10,24}$	0.2	0.8	
	332452.5	$35_{10,26} - 34_{10,25}$			
	332531.0	$35_{11,24} - 34_{11,23}$			
	332531.0	$35_{11,25} - 34_{11,24}$	...	...	3
	332532.5	$35_{6,30} - 34_{6,29}$			
	332534.2	$35_{6,29} - 34_{6,28}$			
	332775.2	$35_{5,31} - 34_{5,30}$	< 0.3	< 0.6	4
	333046.8	$35_{4,32} - 34_{4,31}$	0.4	2.8	
	333764.0	$35_{4,31} - 34_{4,30}$	< 0.7	< 5.3	5

[1] Very broad feature, possible blend with U-lines.
[2] Blend with HNCO at 329459.9.
[3] In the wing of SO_2 at 332505.2.
[4] Blend with NH_2D at 329459.9.
[5] Blend with CH_3CH_2CN at 333767.7.

TABLE A1.19 - *continued*

	ν (MHz)	J_{K_-,K_+}	T_a^* (K)	$\int T_a^* \, dv$ (K km s^{-1})	notes
CH_2CHCN	337039.2	$36_{2,35} - 35_{2,34}$	0.5	3.1	
	338212.4	$37_{1,37} - 36_{1,36}$	0.4	1.3	
	338446.6	$37_{0,37} - 36_{0,36}$	...	...	6
	340047.4	$36_{1,35} - 35_{1,34}$	...	...	7
	341563.0	$36_{3,34} - 35_{3,33}$	0.8	2.4	
	341881.1	$36_{8,29} - 35_{8,28}$	0.6	4.9	8
	341881.1	$36_{8,28} - 35_{8,27}$			
	341893.2	$36_{9,28} - 35_{9,27}$	0.9	6.5	8
	341893.2	$36_{9,27} - 35_{9,26}$			
	342052.2	$36_{6,31} - 35_{6,30}$	1.0	8.2	
	342054.5	$36_{6,30} - 35_{6,29}$			
	342316.9	$36_{5,32} - 35_{5,31}$	1.2	9.2	1
	342374.9	$36_{5,31} - 35_{0,30}$	...	...	9
	342584.9	$36_{4,33} - 35_{4,32}$	0.4	1.7	1
	343445.9	$36_{4,32} - 35_{4,31}$	...	...	10
	346184.3	$37_{2,36} - 36_{2,35}$	1.0	8.5	1
	346942.5	$36_{3,33} - 35_{3,32}$	...	...	11
	347230.7	$38_{1,38} - 37_{1,37}$	0.4	2.3	
	347432.9	$38_{0,38} - 37_{0,37}$	0.7	3.0	
	347758.6	$36_{2,34} - 35_{2,32}$	0.6	4.8	
	348990.8	$37_{1,36} - 36_{1,35}$	0.8	4.9	
	353241.5	$4_{4,1} - 3_{3,0}$	0.5	2.7	
	353241.5	$4_{4,0} - 3_{3,1}$			

[6] Blend with wings of CH_3OH at 338442.3 and 338456.5.
[7] Blend with $C^{33}S$ at 340052.7.
[8] Blend with Ghost.
[9] Blend with $HCOOCH_3$ at 342375.6.
[10] Blend with $HCOOCH_3$ at 343443.9.
[11] Blend with CH_3CH_2CN at 346947.3.

TABLE A1.20

TRANSITIONS OF CH_3CH_2CN

	ν (MHz)	J_{K_-,K_+}	T_a^* (K)	$\int T_a^* \, dv$ (K km s^{-1})	notes
CH_3CH_2CN	328754.8	$37_{3,35} - 36_{3,34}$	0.9	8.3	
	329234.7	$36_{3,33} - 35_{3,32}$	1.7	18.3	
	331439.5	$38_{2,37} - 37_{2,37}$	0.8	7.4	
	331605.6	$37_{9,29} - 36_{9,28}$	1.0	9.5	
	331605.6	$37_{9,28} - 36_{9,27}$			
	331662.3	$37_{2,35} - 36_{2,34}$	0.9	7.8	
	331748.5	$38_{1,37} - 37_{1,36}$	1.7	31.3	
	331756.4	$37_{8,30} - 36_{8,29}$			
	331756.4	$37_{8,29} - 36_{8,28}$			
	332014.7	$37_{7,31} - 36_{7,30}$	< 1.9	< 19.8	1
	332020.6	$37_{7,30} - 36_{7,29}$			
	332428.0	$37_{6,32} - 36_{6,31}$	1.2	9.2	
	332687.7	$19_{4,15} - 18_{3,16}$	0.5	< 2.3	2
	333108.8	$38_{2,37} - 37_{1,36}$	...	...	3
	333265.9	$39_{1,39} - 38_{1,38}$	1.2	9.9	
	333274.7	$39_{0,39} - 38_{0,38}$	...	...	4
	333753.4	$14_{5,10} - 13_{4,9}$	0.5	3.0	
	333767.7	$14_{5,9} - 13_{4,10}$	< 0.7	< 5.3	5
	333921.6	$37_{5,32} - 36_{5,31}$	...	...	6
	335321.4	$9_{6,4} - 8_{5,3}$	...	...	7
	335321.4	$9_{6,3} - 8_{5,4}$			
	336613.9	$20_{4,17} - 19_{3,16}$	1.1	6.3	
	337347.6	$38_{3,36} - 37_{3,35}$	2.7	27.6	
	337445.9	$37_{4,33} - 36_{4,32}$	1.7	13.1	
	339968.2	$38_{3,36} - 37_{2,35}$	1.9	20.6	
	340149.1	$39_{1,38} - 38_{1,37}$	2.4	17.1	
	340151.3	$35_{3,33} - 34_{2,32}$			
	340576.0	$38_{9,30} - 37_{9,29}$	1.7	15.4	
	340576.0	$38_{9,29} - 37_{9,28}$			
	340972.7	$38_{4,35} - 37_{3,34}$	1.5	13.9	
	341025.6	$38_{7,32} - 37_{7,31}$	1.3	8.2	
	341468.7	$38_{6,33} - 37_{6,32}$	1.3	7.0	
	341603.2	$38_{6,32} - 37_{6,31}$	1.5	11.0	

[1] Blend with $CH_3CN(v_8 = 1)$ at 332015.8 and 332017.8.
[2] Blend with U-line at 332694.0.
[3] Blend with $^{13}CH_3OH$ at 333114.8.
[4] Blend with HDS at 333278.5.
[5] Blend with CH_2CHCN at 333764.0.
[6] Blend with wing of ^{34}SO at 333902.1.
[7] Blend with U-line at 335335.0.

TABLE A1.20 - *continued*

	ν (MHz)	J_{K_-,K_+}	T_a^* (K)	$\int T_a^* \, dv$ (K km s^{-1})	notes
CH_3CH_2CN	341678.5	$40_{0,40} - 39_{1,39}$	1.9	22.1	
	341703.7	$40_{1,40} - 39_{1,39}$	2.1	12.3	8
	341710.6	$40_{0,40} - 39_{0,39}$			
	341735.9	$40_{1,40} - 39_{0,39}$	...	...	9
	341852.7	$38_{5,38} - 37_{5,33}$	...	...	10
	342652.0	$15_{5,11} - 14_{4,10}$	0.3	2.5	
	342677.7	$15_{5,10} - 14_{4,11}$	0.4	2.5	
	343194.6	$38_{5,33} - 37_{5,32}$	...	...	11
	346947.3	$9_{8,1} - 9_{7,2}$	2.4	25.7	
	346947.3	$9_{8,2} - 9_{7,3}$			
	346955.4	$10_{8,2} - 10_{7,3}$			
	346955.4	$10_{8,3} - 10_{7,4}$			
	346962.8	$11_{8,3} - 11_{7,4}$			
	346962.8	$11_{8,4} - 11_{7,5}$			
	346969.2	$12_{8,4} - 12_{7,5}$			
	346969.2	$12_{8,5} - 12_{7,4}$			
	351531.6	$16_{5,12} - 15_{4,11}$	...	...	12
	351575.9	$16_{5,11} - 15_{4,12}$	1.0	9.4	
	353234.9	$11_{6,6} - 10_{5,5}$	0.3	2.0	
	353234.9	$11_{6,5} - 10_{5,6}$			

[8] Blend with CH_3CCH at 341715.1 and $HCOOCH_3$ at 341722.4.
[9] Blend with $HCOOCH_3$ at 341732.3 and CH_3CCH at 341734.6.
[10] Blend with $HCOOCH_3$ at 341862.6.
[11] Blend with U-line at 343202.
[12] Blend with $HCOOCH_3$ at 351529.1.

TABLE A1.21

UNIDENTIFIED LINES

ν (MHz)	T_a^* (K)	$\int T_a^* \, dv$ (K km s^{-1})	notes
327216	1.7	15.4	1
328004	1.0	3.4	
328415	1.0	4.0	
330357	0.7	2.8	3
330715	0.5	1.3	
331490	...	...	4
331995	1.0	6.5	
332030	1.6	13.2	5
332789	0.5	2.9	
332799	0.5	3.1	
332997	0.9	4.4	
333466	0.4	1.2	
333721	0.4	4.8	?
333851	0.6	3.2	?
333865	1.1	6.8	
334074	0.7	2.9	
334140	0.4	1.2	
334278	0.4	1.4	
334895	0.9	8.9	

? Tentatively identified as a real spectral feature.

[1] Double or multiple peaked structure.

[2] Triangular lineshape.

[3] Blend with $^{13}CH_3OH$ at 330350.0 and 330362.0.

[4] Blend with CH_3OH at 331502.4.

[5] Blend with CH_3CN-$v_8 = 1$ at 332017.8.

TABLE A1.21 - *continued*

ν (MHz)	T_a^* (K)	$\int T_a^* \, dv$ (K km s^{-1})	notes
335335	0.4	4.7	
335363	0.3	2.3	
335703	0.5	3.5	
335742	0.5	4.7	1
336456	0.4	1.8	
337275	0.8	3.6	
337285	1.5	6.7	
337313	1.2	5.6	
337744	0.7	2.7	
337839	0.6	1.9	
337880	1.1	6.1	
338773	1.5	9.6	
338888	0.3	1.3	
339061	0.5	3.2	
339138	0.3	2.5	?
339313	...	...	6
339468	0.4	2.2	1,7
339527	0.7	6.5	
340193	1.4	8.7	
340812	...	...	1,8,?
340828	...	...	1,8
340872	0.7	3.5	
341037	1.6	14.4	
341095	0.9	5.0	?
341472	1.7	8.3	?
341482	0.7	8.9	?
341499	0.2	0.3	
341510	0.5	2.3	
341800	0.4	5.9	
341818	0.4	6.5	

[6] Blend with wing of SO at 339341.5.
[7] Blend with CN at 339475.9.
[8] Blend with wing of ^{33}SO at 340839.0.

TABLE A1.21 - *continued*

ν (MHz)	T_a^* (K)	$\int T_a^* \, dv$ (K kms^{-1})	notes
341800	0.4	5.9	
341818	0.4	6.5	
342066	0.4	1.7	
342129	0.5	3.1	
342274	0.3	1.2	
342290	0.6	3.0	1
342458	0.2	0.5	
342486	0.5	3.6	?
342767	2.1	31.9	9
343202	1.5	16.6	
343599	0.5	1.9	?
343633	0.3	1.6	?
343665	0.9	5.9	?
344773	...	...	10
344788	...	...	10
344796	...	...	10
344875	0.6	7.3	1
346223	2.4	35.8	
346360	0.8	4.0	
346776	0.6	3.8	1
346826	0.4	3.2	1
346878	1.2	10.9	2
346987	2.1	26.5	11
347029	0.6	2.3	
347047	0.3	0.8	?
347446	0.8	3.6	
347743	0.4	6.4	?
347844	0.8	3.4	
347915	0.9	4.7	
348084	0.4	1.8	
348101	1.3	11.2	12,?

[9] Blend with wing of CH_3OH at 342729.8.

[10] Blend with each other, $^{34}SO_2$ at 344808.0 and $HCOOCH_3$ at 344759.1.

[11] Blend with $H^{13}CO^+$(4-3) at 346998.50.

[12] Blend with $^{34}SO_2$ at 348117.5.

TABLE A1.21 - *continued*

ν (MHz)	T_a^* (K)	$\int T_a^* \, dv$ (K km s^{-1})	notes
348162	0.6	5.3	?
348264	1.9	20.0	?
348349	4.1	27.1	13
348358	4.0	66.6	13
348373	...	...	13
348559	2.3	15.0	?
348995	0.8	4.9	
349496	0.4	0.8	
349550	1.3	10.3	
349735	1.0	8.4	
350042	0.5	3.6	
350055	0.6	4.4	
350147	1.1	12.1	
350170	0.5	2.1	
350254	0.3	2.5	1
350288	1.0	6.2	
350304	0.8	5.0	
350382	0.4	2.5	
350450	1.6	17.1	1
350467	2.1	17.2	
350515	2.1	34.5	
350615	0.6	5.4	
350847	2.6	30.5	14
351182	0.9	13.0	1
351382	0.5	4.0	?
351392	0.4	3.7	?
351436	0.8	10.1	
351490	0.7	5.5	?
351540	1.2	8.2	
352124	0.7	4.7	
352505	0.9	3.2	2
353152	0.3	2.5	?
353166	0.6	3.8	?
353851	0.7	5.3	

[13] Blend with each other and SO_2 at 348387.8.
[14] Blend with SO_2 at 350862.7.

TABLE A1.21 - *continued*

ν (MHz)	T_a^* (K)	$\int T_a^* \, dv$ (K km s^{-1})	notes
354129	1.0	5.9	
354467	...	...	15
355030	...	...	16
355211	0.9	...	17
355220	0.6	...	17
355231	0.4	...	17
355446	0.6	3.5	
355760	1.4	18.7	2
355851	0.3	2.4	1,18?
355966	0.5	2.3	2
356223	0.5	2.9	
356280	1.6	12.9	
356298	0.8	3.5	
356424	0.8	5.5	
356541	1.2	6.1	
356551	2.5	23.7	1
356601	0.3	1.0	
356627	1.8	12.0	
356644	0.6	4.0	
356662	0.7	4.9	
356916	0.3	0.4	?
356965	1.9	15.2	
358331	1.2	8.6	
358356	2.2	10.7	
358415	3.4	23.0	
358522	1.7	15.8	
358690	1.1	8.1	
358725	1.3	12.3	
359060	1.7	17.0	
359073	1.2	11.4	
359677	1.0	6.0	

[15] Blend with wing of HCN(4-3) at 354505.5.
[16] Blend with wing of SO_2 at 355045.5.
[17] Blend of three U-lines.
[18] Blend with wing of $OC^{34}S$ at 355836.0.

A2. The CSO Orion-S Spectral Line Survey

A2.1. Overview

Orion-S is a second condensation in the Orion molecular cloud located 1.′5 south of the hot core region. First identified as a star formation region through NH_3 line observations (Ziurys *et al.* 1981) and 400 μm continuum maps (Keene *et al.* 1982), Orion-S should provide a useful comparison source which likely had pre-existing physical conditions and chemical abundances similar to those of Orion-KL. For a recent discussion of the structure and chemistry of Orion-S, see McMullin, Mundy & Blake (1993), where it is suggested that Orion-S is at an early stage of chemical evolution.

Our original intent was to obtain a spectral line survey of Orion-S with the same frequency coverage and sensitivity as the survey of Orion-KL. However, as the initial observations progressed, we concluded that an unbiased complete survey would only be meaningful if a much greater sensitivity was achieved and that the observations required were simply impractical. Given the limited telescope time available, we decided to concentrate on obtaining complete frequency coverage for Orion-KL, and to selectively observe Orion-S. We therefore chose frequencies at which the Orion-KL survey displayed strong line emission, or emission from particular species, and made observations of Orion-S at those same frequencies. The final spectrum we obtained gives continuous spectral coverage of Orion-S from approximately 342 to 355 GHz and approximately 63% coverage of the range between 330 and 360 GHz. In addition, we made one observation at the frequency of the 325 GHz H_2O line, which was not detected. Because of the much higher noise level of that scan, we have not included the data in our calculations of line flux. A total of 43 DSB observations have been combined to form our data set. In some cases, where the lines could be unambiguously identified, we did not obtain scans at shifted frequencies. In these instances, the data can not be deconvolved and the original DSB observations are presented.

The Orion-S survey parameters (apart from the actual frequency coverage) are identical to the Orion-KL survey. All of the observations were made during the same observing runs using the same receiver settings. The pointing, beam efficiency, system temperatures and atmospheric transmission were essentially the same for the two sources, but of course the coupling of the source to the beam is likely to be

TABLE A2.1

CENTER FREQUENCIES OF OBSERVATIONS FOR THE CSO ORION-S SPECTRAL LINE SURVEY

USB Center (GHz)	LSB Center (GHz)	Date Observed	USB Center (GHz)	LSB Center (GHz)	Date Observed
328.000	325.200	12 January 1991	348.000	345.200	14 January 1990
333.500	330.700	15 March 1990	348.250	345.450	15 January 1990
333.750	330.950	15 March 1990	348.500	345.700	15 January 1990
337.000	334.200	16 March 1990	348.540	345.740	17 January 1990
341.310	338.510	14 March 1990	348.550	345.750	17 January 1990
342.750	339.950	14 March 1990	348.750	345.950	18 January 1990
343.000	340.200	14 March 1990	349.000	346.200	18 January 1990
345.000	342.200	12 January 1990	349.250	346.450	18 January 1990
345.250	342.450	12 January 1990	351.750	348.950	16 February 1990
345.500	342.700	12 January 1990	352.000	349.200	16 February 1990
345.650	342.850	13 January 1990	352.250	349.450	16 February 1990
345.796	342.996	12 January 1990	352.750	349.950	16 February 1990
345.850	343.050	13 January 1990	353.250	350.450	15 February 1990
346.000	343.200	13 January 1990	353.500	350.700	15 February 1990
346.250	343.450	13 January 1990	353.750	350.950	15 February 1990
346.500	343.700	13 January 1990	354.000	351.200	14 February 1990
346.750	343.950	14 January 1990	354.250	351.450	14 February 1990
347.000	344.200	14 January 1990	354.500	351.700	14 February 1990
347.250	344.450	14 January 1990	356.510	353.710	13 March 1990
347.250	344.450	15 January 1991	357.250	354.450	13 March 1990
347.500	344.700	14 January 1990	357.810	355.010	18 January 1991
347.750	344.950	14 January 1990			

different. We have used the same correction for extended efficiency (η_{ext} = 0.76) as in the Orion-KL survey to facilitate direct comparisons between the emission from the two sources, but note that the emission from Orion-S is in general more spatially compact. Low-order polynomial baselines were again removed from the DSB observations and used to evaluate the continuum emission seen. Because of the reduced number of lines and smaller line widths, the appropriate baselines were more easily determined for this source.

Table A2.1 lists the actual center frequencies observed towards Orion-S, with Table A2.2 summarizing the approximate frequency ranges covered and dates for each of the observing sessions. In Figure A2.1 we plot the frequency coverage thus obtained.

TABLE A2.2

CSO ORION-S SPECTRAL LINE SURVEY
SUMMARY OF OBSERVING DATES AND FREQUENCIES

Dates	Frequencies [a] (GHz)
1990 January 12–18	342–349.5
1990 February 14–16	349–355
1990 March 13–19	330–343, 353.5–357.5 [b]
1991 January 11–18	325, 328, 344, 347, 355, 358 [c]

[a] Approximate frequency ranges covered during each observing session.
[b] Only selected frequencies within these ranges were observed.
[c] Three scans were observed, with the approximate LSB and USB frequencies shown.

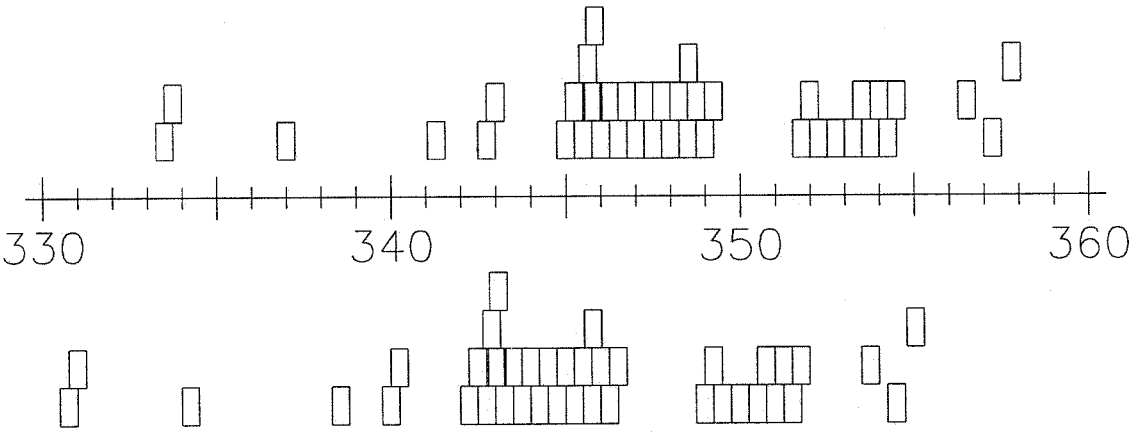

Figure A2.1 Frequency coverage of the Orion-S observations. Each DSB observation is represented by a pair of boxes: one showing the frequency range in the upper sideband and one showing the range of the lower sideband.

A2.2. Results

We present here a summary of the results of our observations of Orion-S, again concentrating on the question of the integrated line flux. A more detailed description of this survey including comparisons with the Orion-KL data will be published separately (Groesbeck *et al.* 1994).

A compressed view of the single sideband spectrum obtained from our survey is shown in Figure A2.2, with the expanded view shown in Figure A2.3. Where the observations do not permit the deconvolution to be performed, we have assigned the observed lines to a given sideband. For such lines

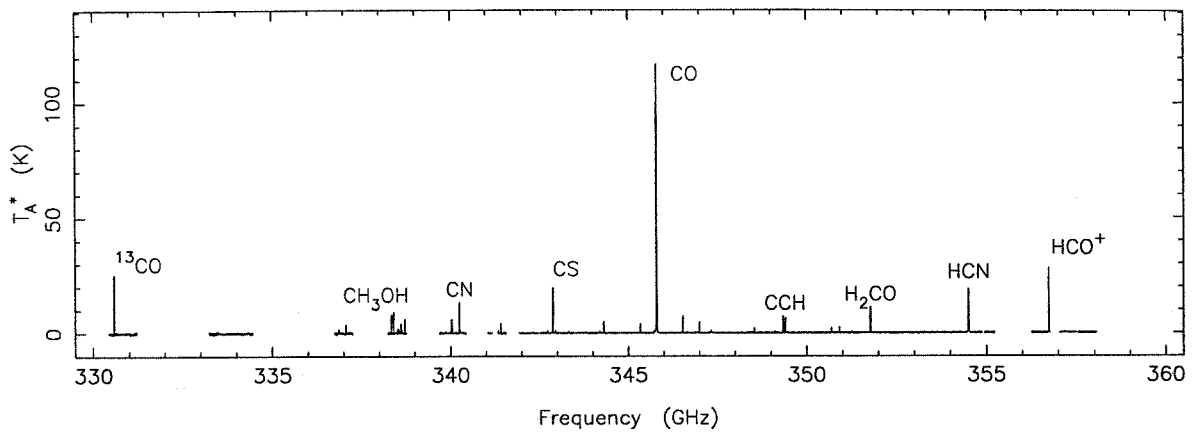

Figure A2.2 A compressed view of the CSO spectral line survey of Orion-S.

we plot the original DSB data at the assigned frequency only, leaving the corresponding image frequency blank. Where no lines were seen in such scans, we plot the observed spectrum (consisting essentially of noise) at both of the sideband frequencies. Thus there exist short gaps in the plotted spectrum at frequencies which were nevertheless included in the observations and in the calculations of the average line flux. In a very few places, we have also omitted a narrow section where a processing artifact or ghost was prominent. The resulting spectral coverage is continuous between 342 and 355 GHz, and the total frequency range observed totals 63% of the 330–360 GHz atmospheric window.

Comparison of Figures A1.2 and A2.2 shows several striking differences between the spectra of the two sources. Many fewer lines are detected in the southern source, even allowing for the reduced frequency coverage, and those detected are weaker and generally much narrower. The SO_2 lines so visible in the Orion-KL spectrum are nearly absent in Orion-S, while the CO J = 3–2 line is nearly as bright (though much narrower). Table A2.3 presents a list of the detected lines sorted by frequency, while Table A2.4 presents the lines and intensities sorted by species.

We detected 78 distinct spectral features, identified with 108 molecular transitions (including blends) from 16 species. Only 2 of the spectral lines detected in this survey remain unidentified. We believe that the reduced number of unidentified lines relative to the Orion-KL survey results largely from the limited sensitivity of this survey. It seems likely that additional unidentified lines at or just below the noise level may be present within our data set. We also note that all of the species detected in Orion-S were also seen

in Orion-KL.

As a result of the weaker, narrower lines, the line contribution to the total flux is much less significant in Orion-S. The continuum emission towards Orion-S was nearly as strong as towards Orion-KL, 0.8 K on the uncorrected T_A^* scale as determined from the baseline offsets. However, the average integrated line flux over the range of observed frequencies was only 0.07 K, yielding a line contribution of 8% of the total flux observed. The CO line by itself contributes 24% of the line flux in this case, with other significant amounts coming from HCN, HCO^+, CH_3OH, and ^{13}CO. Again the bulk of the line flux is carried in a rather small number of lines from relatively few species, suggesting the possibility of obtaining reasonably accurate results from simulations. As our observing frequencies were deliberately chosen to include strong lines, this contribution is likely to represent an upper limit for the average within the entire 330–360 GHz band. A lower limit to the line contribution of 5% of the total flux is obtained by assuming that no additional lines would be detected if the entire 30 GHz band were observed. Again, further discussions and comparisons of the integrated line flux and the total flux may be found in Chapter 5.

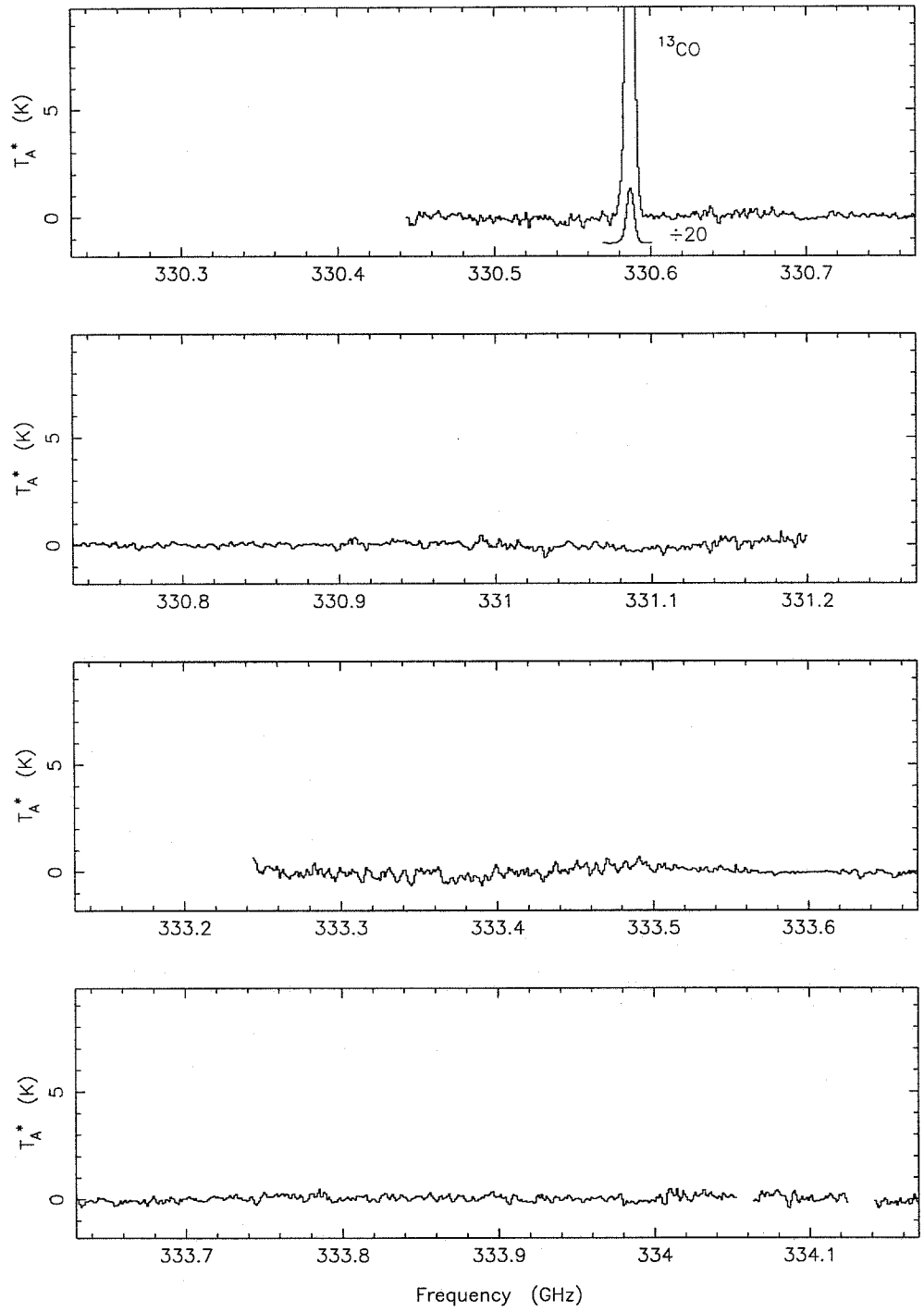

Figure A2.3 Spectrum of Orion-S from 330 to 360 GHz. The data have been corrected by the extended beam efficiency of 0.76. The rest frequency scale has been established using a v_{LSR} of 9 km s^{-1}. Tick marks show the rest frequencies of identified transitions.

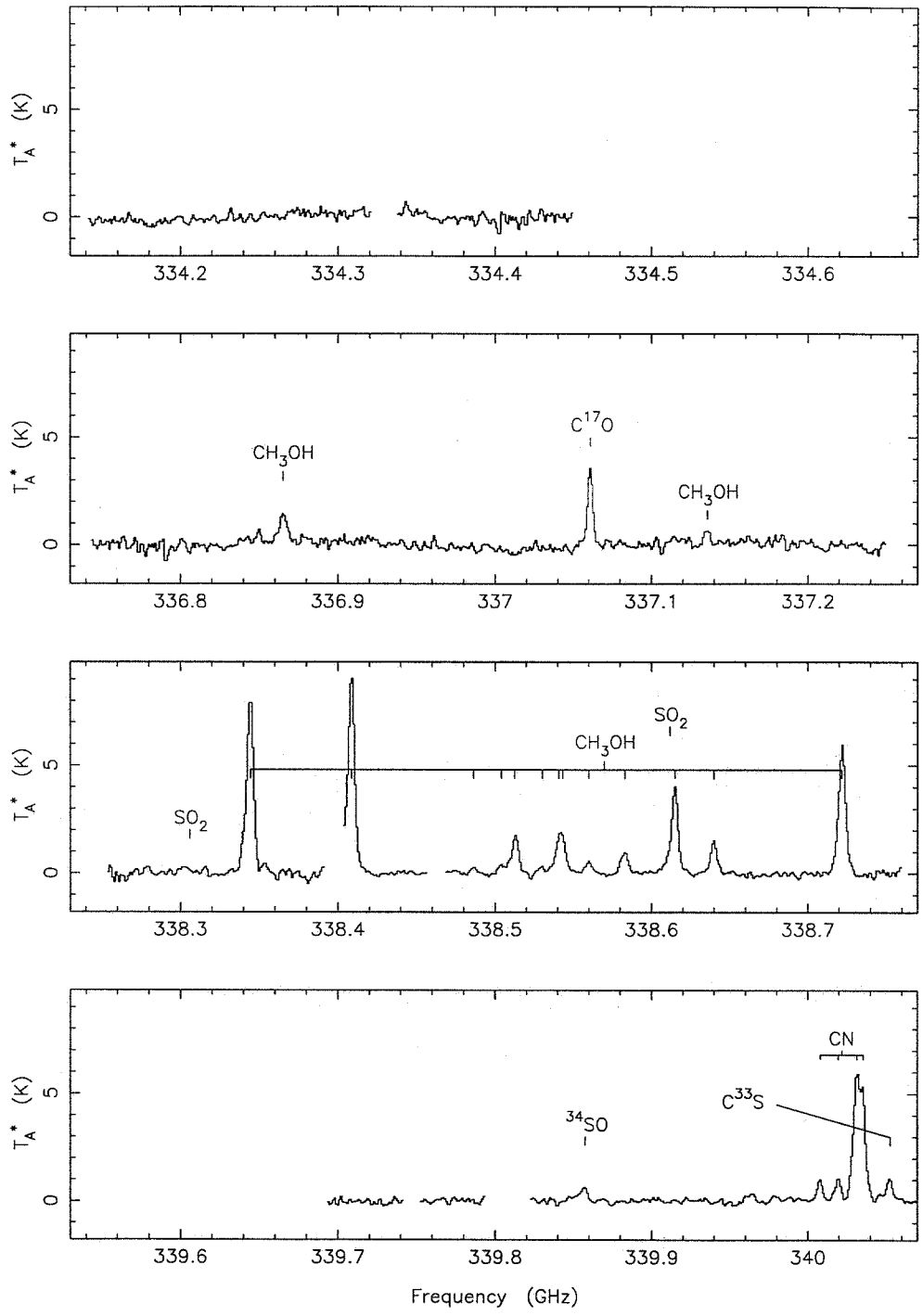

Figure A2.3 — *Continued*

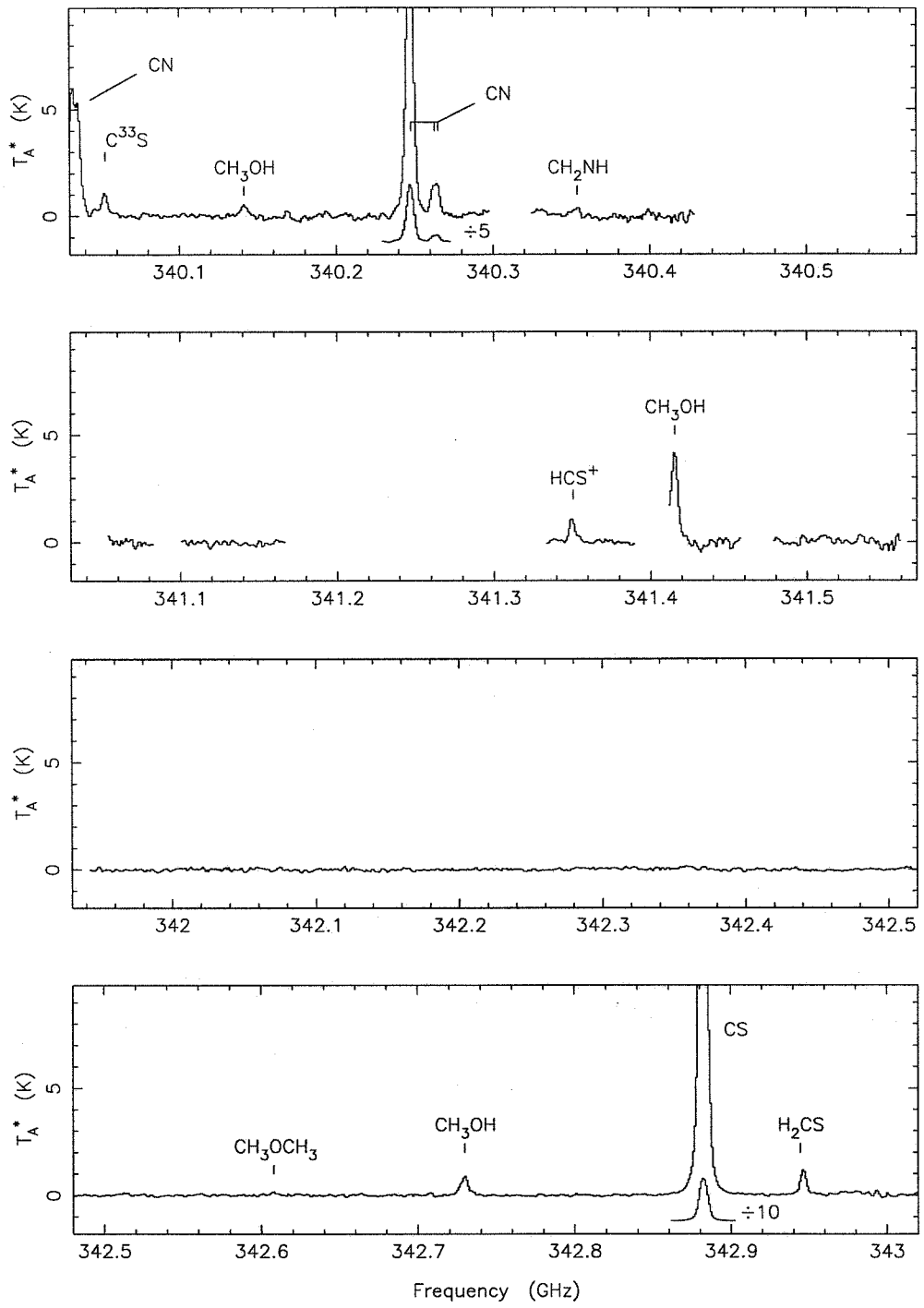

Figure A2.3 — *Continued*

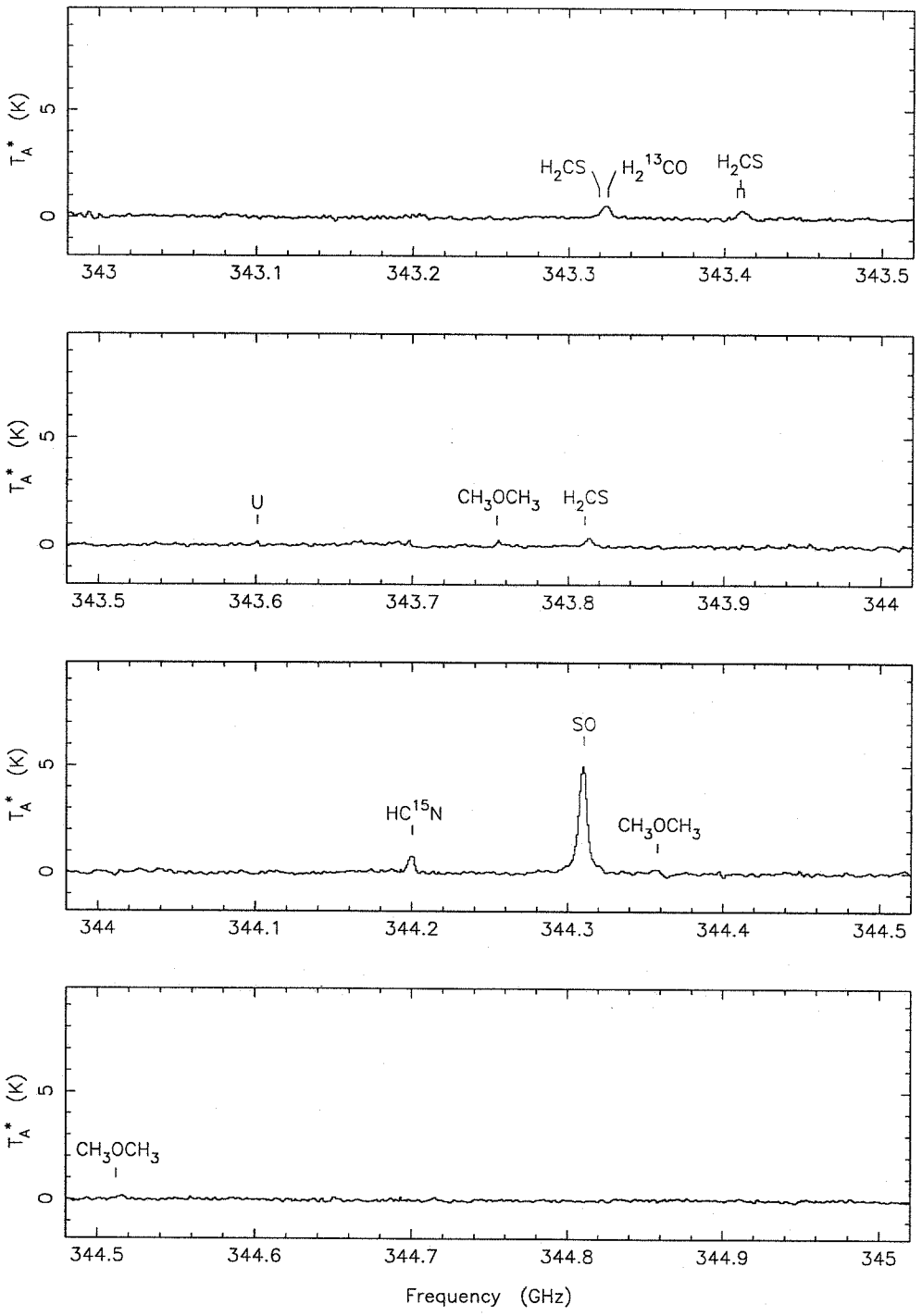

Figure A2.3 — *Continued*

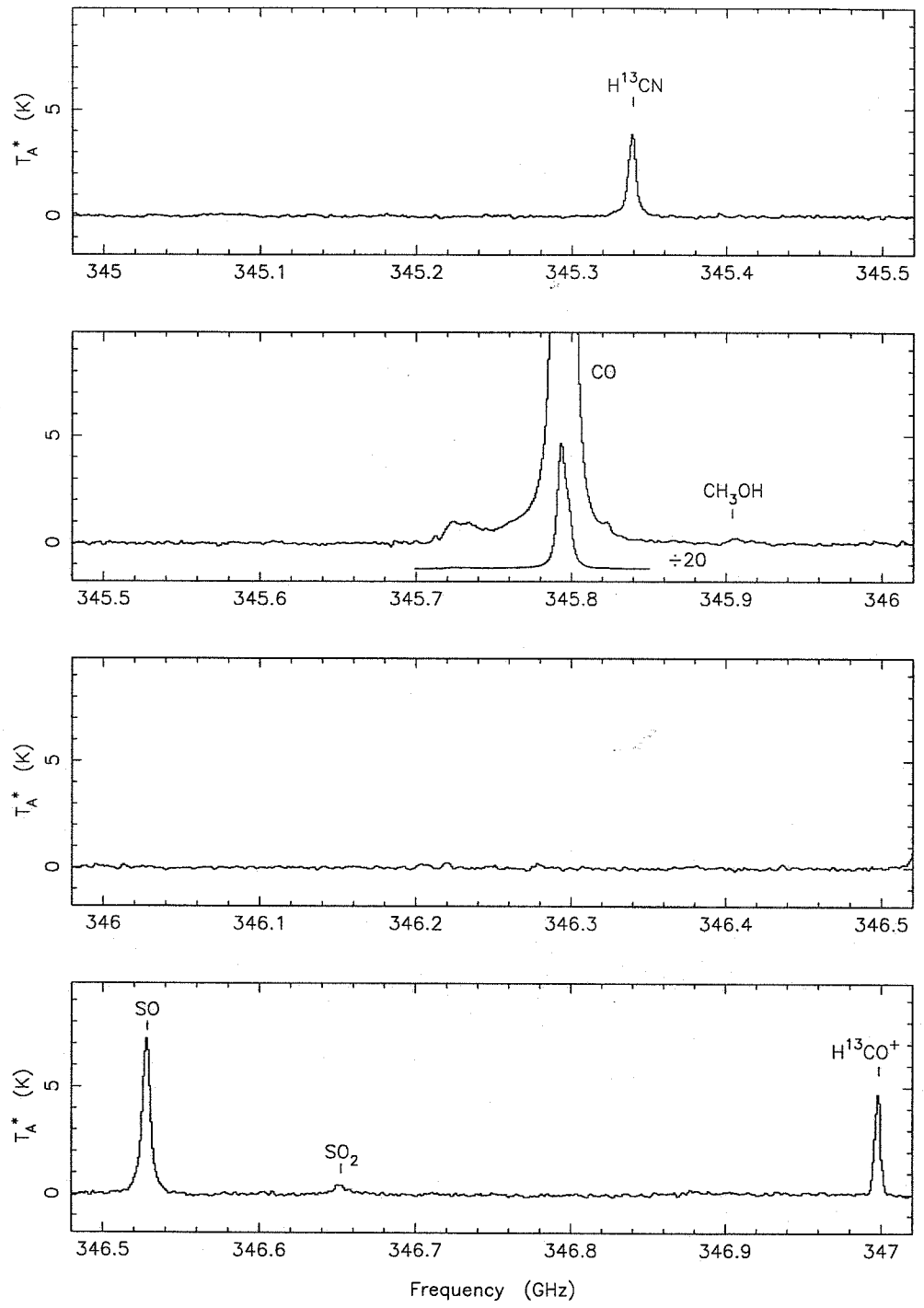

Figure A2.3 — *Continued*

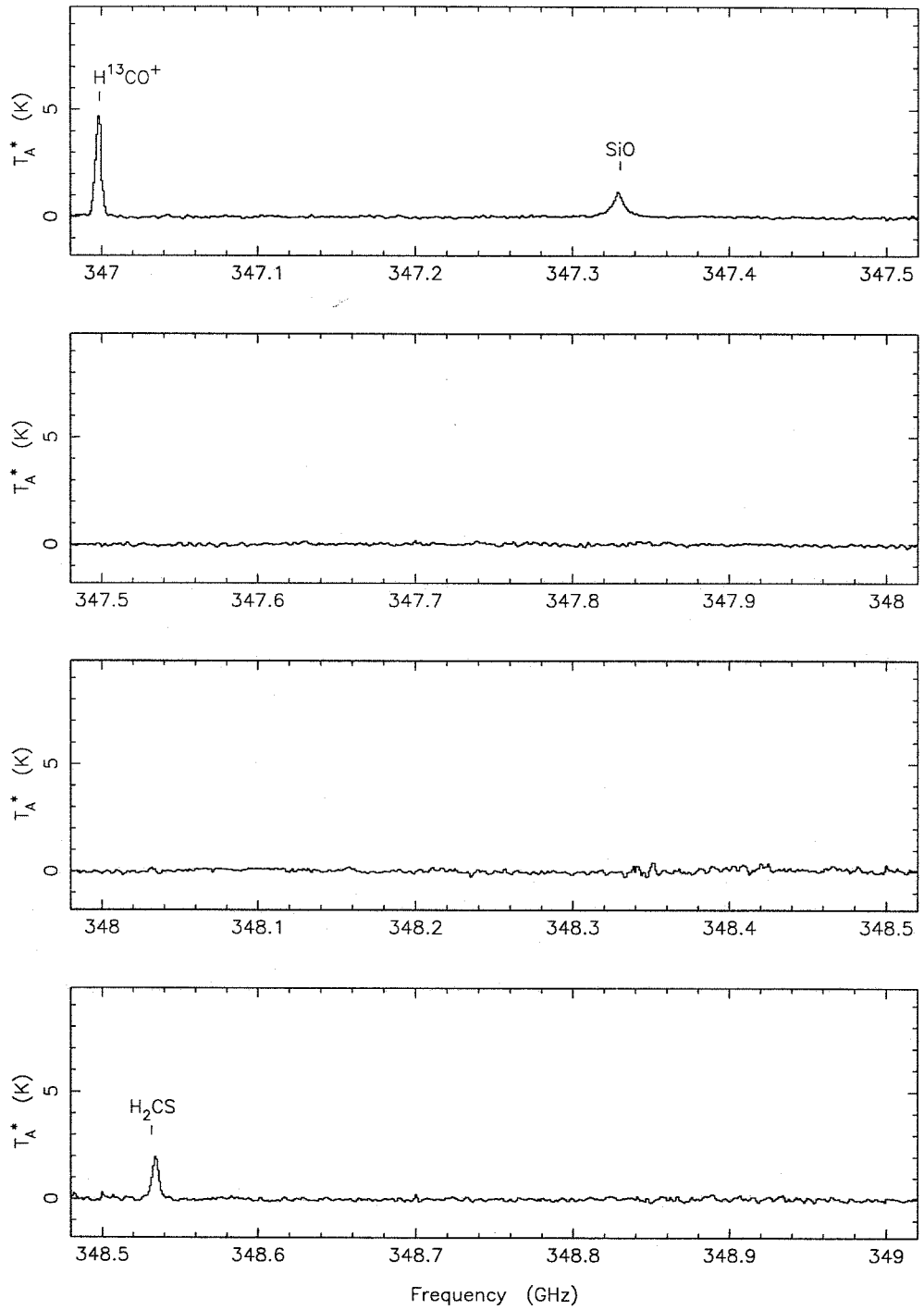

Figure A2.3 — *Continued*

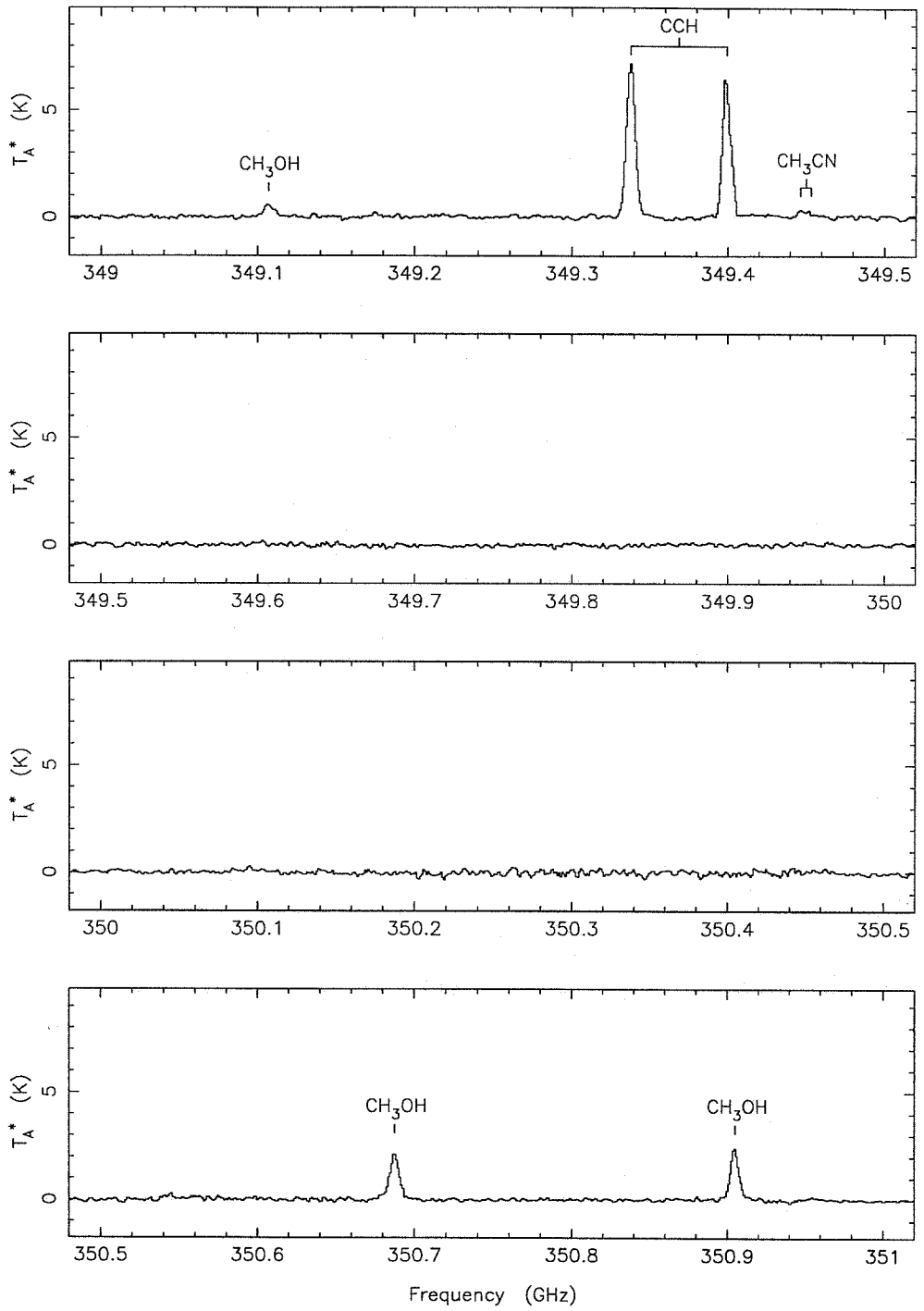

Figure A2.3 — *Continued*

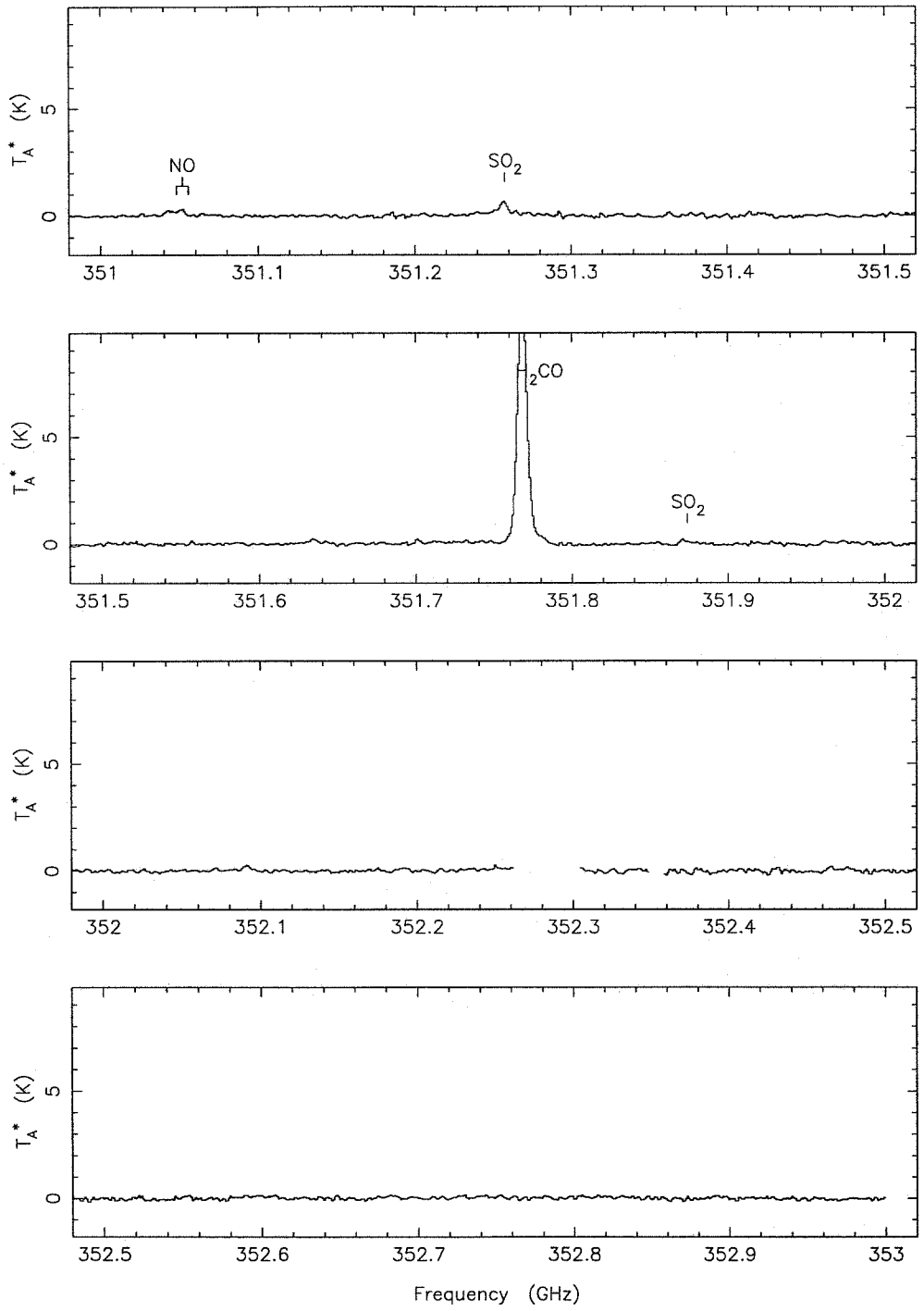

Figure A2.3 — *Continued*

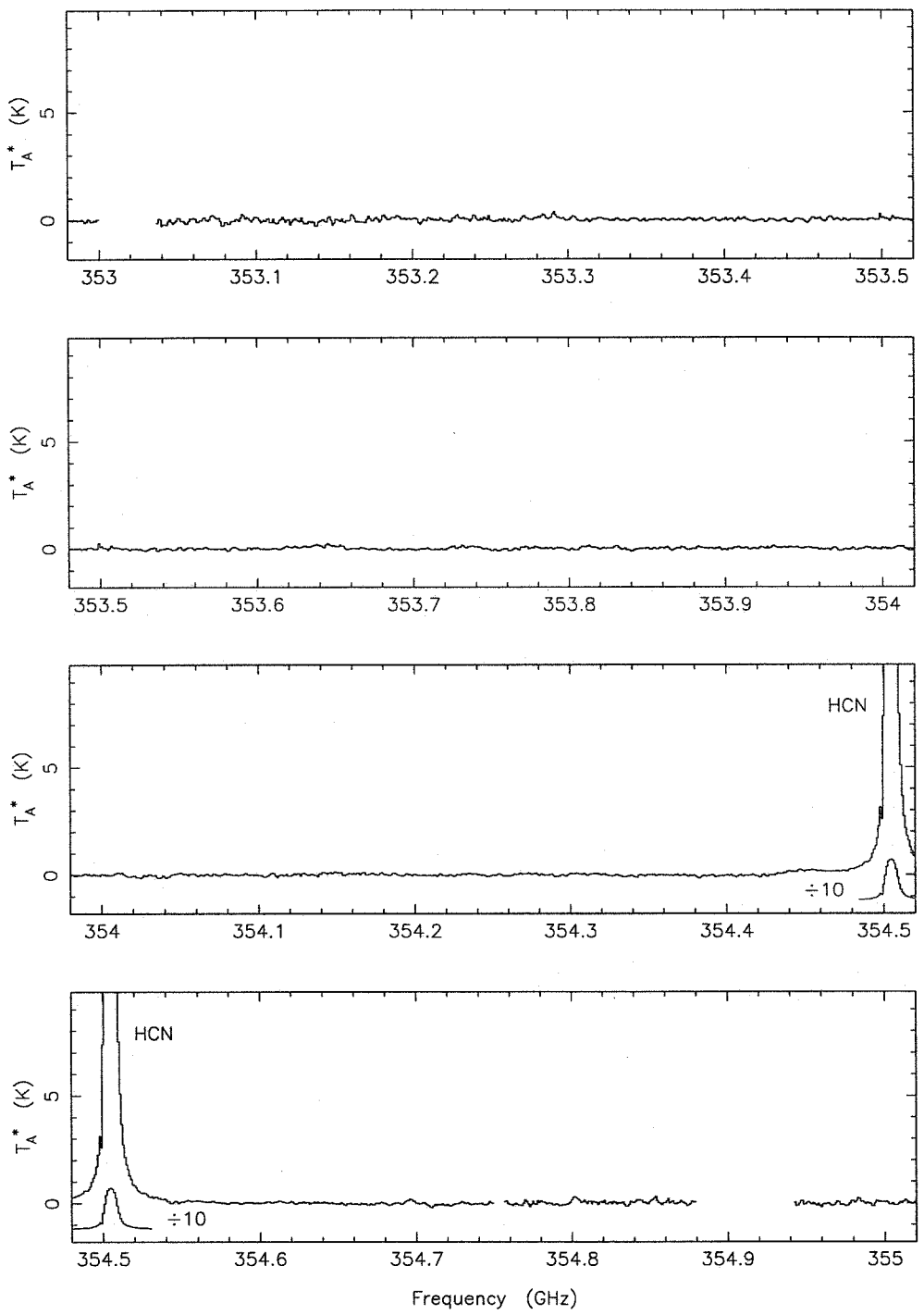

Figure A2.3 — *Continued*

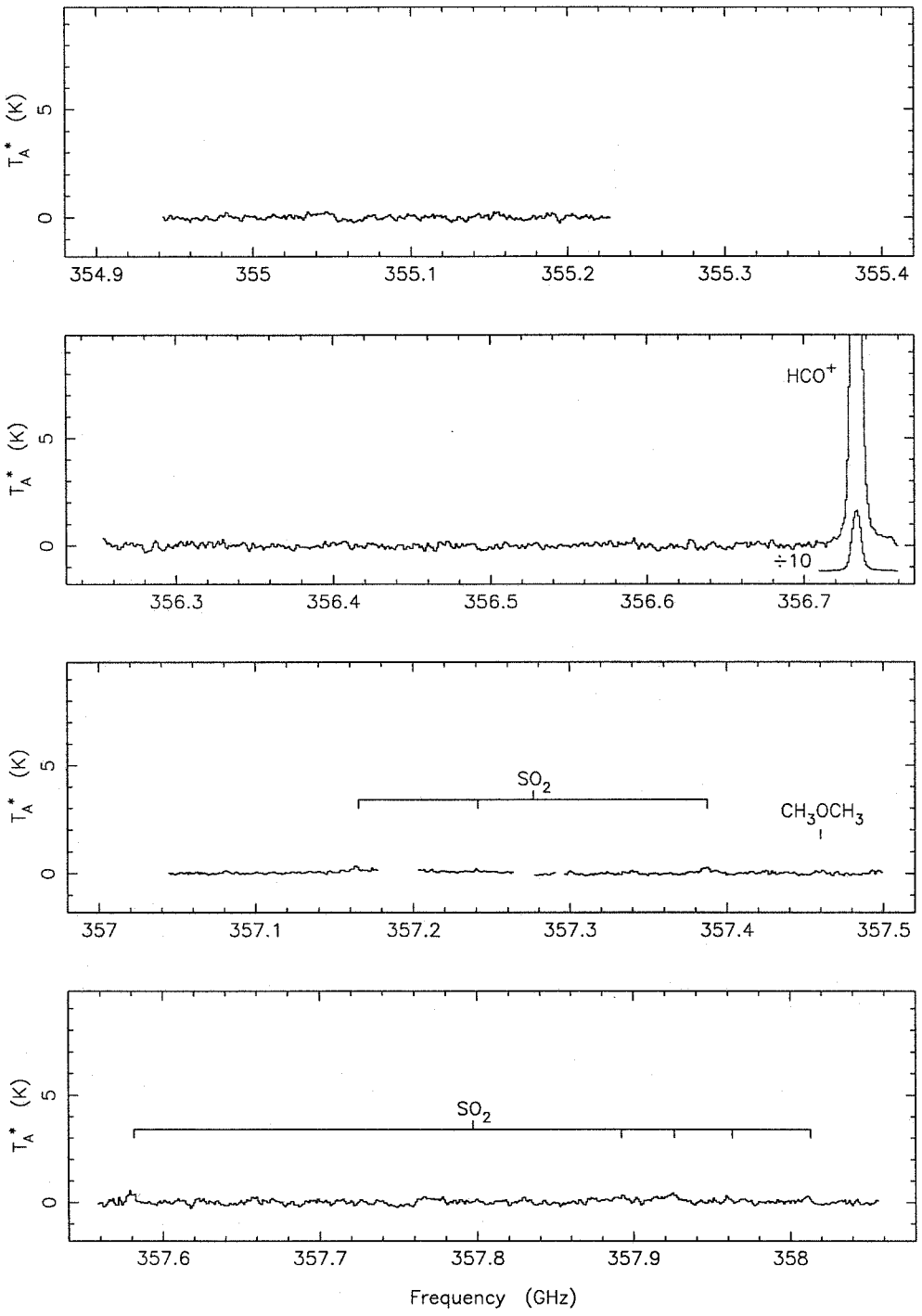

Figure A2.3 — *Continued*

TABLE A2.3

LINES DETECTED IN ORION-S

Frequency (MHz)	Species	Frequency (MHz)	Species	Frequency (MHz)	Species
330588.1	^{13}CO	342608.1	CH_3OCH_3	349338.7	CCH
336865.2	CH_3OH	342729.8	CH_3OH	349446.7	CH_3CN
337061.1	$C^{17}O$	342883.0	CS	349453.4	CH_3CN
337135.9	CH_3OH	342944.4	H_2CS	349398.9	CCH
338306.0	SO_2	343319.6	H_2CS	349400.3	CCH
338344.6	CH_3OH	343325.5	$H_2{}^{13}CO$	349803.0	CH_3OCH_3
338404.6	CH_3OH	343408.1	H_2CS	349806.1	CH_3OCH_3
338408.7	CH_3OH	343412.3	H_2CS	349809.2	CH_3OCH_3
338486.3	CH_3OH	343601	U	350687.7	CH_3OH
338504.1	CH_3OH	343753.3	CH_3OCH_3	350689.5	NO
338512.6	CH_3OH	343754.2	CH_3OCH_3	350690.8	NO
338512.9	CH_3OH	343755.1	CH_3OCH_3	350694.8	NO
338530.3	CH_3OH	343810.8	H_2CS	350905.1	CH_3OH
338540.8	CH_3OH	344200.3	$HC^{15}N$	351043.5	NO
338543.2	CH_3OH	344310.6	SO	351051.7	NO
338559.9	CH_3OH	344358.0	CH_3OCH_3	351257.2	SO_2
338583.2	CH_3OH	344358.1	CH_3OCH_3	351768.7	H_2CO
338611.8	SO_2	344358.2	CH_3OCH_3	351873.9	SO_2
338615.0	CH_3OH	344515.0	CH_3OCH_3	354505.5	HCN
338639.9	CH_3OH	344515.0	CH_3OCH_3	355045.5	SO_2
338721.6	CH_3OH	344515.0	CH_3OCH_3	356734.3	HCO^+
338722.9	CH_3OH	345338.5	SO_2	356755.2	SO_2
339857.6	^{34}SO	345339.8	$H^{13}CN$	357165.4	SO_2
340008.1	CN	345796.0	CO	357241.2	SO_2
340019.6	CN	345904.2	CH_3OH	357387.6	SO_2
340031.5	CN	346220	U	357459.4	CH_3OCH_3
340035.4	CN	346523.9	SO	357460.2	CH_3OCH_3
340052.7	$C^{33}S$	346528.5	SO_2	357461.0	CH_3OCH_3
340141.2	CH_3OH	346652.2	SO_2	357581.4	SO_2
340247.8	CN	346998.5	$H^{13}CO^+$	357892.4	SO_2
340261.8	CN	347330.6	SiO	357926.0	SO_2
340265.0	CN	348531.9	H_2CS	357962.9	SO_2
341350.8	HCS^+	349107.0	CH_3OH	358013.1	SO_2
341415.6	CH_3OH	349337.5	CCH		

TABLE A2.4

OBSERVED LINES AND INTENSITIES IN ORION-S

Species	Frequency (MHz)	Transition	E_{lower} (K)	T_A^* (peak) [a] (K)	$\int T_A^* dv$ [a] (K km s^{-1})
CO	345796.0	3 – 2	16.6	118.4	995.8
^{13}CO	330588.1	3 – 2	15.9	26.2	136.0
C^{17}O	337061.1	3 – 2	16.2	3.8	13.0
CS	342883.0	7 – 6	49.4	20.0	119.6
C^{33}S	340052.7	7 – 6	49.0	1.2	4.5
SiO	347330.6	8 – 7	58.3	1.1	10.1
SO	344310.6	$8_8 - 7_7$	71.0	5.0	32.1
	346528.5	$8_9 - 7_8$	62.1	7.2	52.7 [b]
^{34}SO	339857.6	$8_9 - 7_8$	61.0	0.8	3.8
CN	340008.1	$3,\frac{5}{2},\frac{5}{2} - 2,\frac{3}{2},\frac{5}{2}$	16.3	1.1	4.1
	340019.6	$3,\frac{5}{2},\frac{3}{2} - 2,\frac{3}{2},\frac{3}{2}$	16.3	1.1	4.1
	340031.5	$3,\frac{5}{2},\frac{7}{2} - 2,\frac{3}{2},\frac{5}{2}$	16.3	6.1	23.1 [c]
	340035.4	$3,\frac{5}{2},\frac{3}{2} - 2,\frac{3}{2},\frac{1}{2}$	16.3	4.6 *	21.8 *[c]
	340035.4	$3,\frac{5}{2},\frac{5}{2} - 2,\frac{3}{2},\frac{3}{2}$	16.3	...	...
	340247.8	$3,\frac{7}{2},\frac{7}{2} - 2,\frac{5}{2},\frac{5}{2}$	16.3	11.8 *	52.8 *
	340247.8	$3,\frac{7}{2},\frac{9}{2} - 2,\frac{5}{2},\frac{7}{2}$	16.3	...	...
	340248.6	$3,\frac{7}{2},\frac{5}{2} - 2,\frac{5}{2},\frac{3}{2}$	16.3	...	...
	340261.8	$3,\frac{7}{2},\frac{5}{2} - 2,\frac{5}{2},\frac{5}{2}$	16.3	1.1	3.8 [d]
	340265.0	$3,\frac{7}{2},\frac{7}{2} - 2,\frac{5}{2},\frac{3}{2}$	16.3	1.1	3.8 [d]
NO	350689.5	$\frac{7}{2},\frac{9}{2} - \frac{5}{2},\frac{7}{2}$ f	19.2	2.1 *	13.4 *[e]
	350690.8	$\frac{7}{2},\frac{7}{2} - \frac{5}{2},\frac{5}{2}$ f	19.2	...	...
	350694.8	$\frac{7}{2},\frac{5}{2} - \frac{5}{2},\frac{3}{2}$ f	19.2	...	...
	351043.5	$\frac{7}{2},\frac{9}{2} - \frac{5}{2},\frac{7}{2}$ e	19.3	0.3	1.5
	351051.7	$\frac{7}{2},\frac{7}{2} - \frac{5}{2},\frac{5}{2}$ e	19.3	0.3 *	1.1 *
	351051.7	$\frac{7}{2},\frac{5}{2} - \frac{5}{2},\frac{3}{2}$ e	19.3	...	...
HCN	354505.5	4 – 3	25.5	20.1	160.0
H^{13}CN	345339.8	4 – 3	24.9	3.8	24.3 [f]
HC^{15}N	344200.3	4 – 3	24.8	0.8	3.2
HCO$^+$	356734.3	4 – 3	25.7	29.1	172.5
H^{13}CO$^+$	346998.5	4 – 3	25.0	4.6	18.1
HCS$^+$	341350.8	8 – 7	57.3	1.2	4.4
C_2H	349337.5	$4,\frac{9}{2},5 - 3,\frac{7}{2},4$	25.1	7.2 *	42.1 *
	349338.7	$4,\frac{9}{2},4 - 3,\frac{7}{2},3$	25.1	...	...
	349398.9	$4,\frac{7}{2},4 - 3,\frac{5}{2},3$	25.2	6.2 *	34.1 *
	349400.3	$4,\frac{7}{2},3 - 3,\frac{5}{2},2$	25.2	...	...
H_2CO	351768.7	$5_{1,5} - 4_{1,4}$	45.6	11.3	74.6
H_2^{13}CO	343325.5	$5_{1,5} - 4_{1,4}$	44.8	0.5	3.6 [g]
H_2CS	342944.4	$10_{0,10} - 9_{0,9}$	74.1	1.2	4.8
	343319.6	$10_{2,9} - 9_{2,8}$	126.9	0.5	3.6 [g]
	343408.1	$10_{3,8} - 9_{3,7}$	192.5	0.4 *	2.3 *
	343412.3	$10_{3,7} - 9_{3,6}$	192.5	...	...
	343810.8	$10_{2,8} - 9_{2,7}$	126.9	0.4	2.0
	348531.9	$10_{1,9} - 9_{1,8}$	88.5	1.8	8.7

[a] Values indicated by * refer to blended lines of the same species and include the contribution of the additional lines, for which no value is shown.

[b] Blended with SO_2 $16_{4,12} - 16_{3,13}$ line; the blended intensity is shown.

[c] Separate estimates at the different frequencies were made for these blended transitions

[d] Separate estimates at the different frequencies were made for these blended transitions

[e] Blended with CH_3OH $4_{2,2}$ E – $3_{1,2}$ E line; the blended intensity is shown.

[f] Blended with SO_2 $13_{2,12} - 12_{1,13}$ line; the blended intensity is shown.

[g] Blend of H_2^{13}CO and H_2CS transitions; the blended intensity is shown

TABLE A2.4 - *Continued*

Species	Frequency (MHz)	Transition	E_{lower} (K)	T_{MB} (peak) [a] (K)	$\int T_{MB}\,dv$ [a] (K km s^{-1})
SO_2	338306.0	$18_{4,14} - 18_{3,15}$	180.6	0.3	1.9
	338611.8	$20_{1,19} - 19_{2,18}$	182.6	0.3	1.4 [h]
	345338.5	$13_{2,12} - 12_{1,11}$	76.4	3.8	24.3 [i]
	346523.9	$16_{4,12} - 16_{3,13}$	147.8	7.2	52.7 [j]
	346652.2	$19_{1,19} - 18_{0,18}$	151.5	0.4	3.6
	351257.2	$5_{3,3} - 4_{2,2}$	19.0	0.5	3.5
	351873.9	$14_{4,10} - 14_{3,11}$	119.0	0.1	1.0
	355045.5	$12_{4,8} - 12_{3,9}$	94.0	0.3	2.6
	356755.2	$10_{4,6} - 10_{3,7}$	72.7	0.4	3.0 [k]
	357165.4	$13_{4,10} - 13_{3,11}$	105.8	0.4	2.8 [l]
	357241.2	$15_{4,12} - 15_{3,13}$	132.5	0.3	4.7 [l]
	357387.6	$11_{4,8} - 11_{3,9}$	82.8	0.3	2.2
	357581.4	$8_{4,4} - 8_{3,5}$	55.2	0.5	2.2
	357671.8	$9_{4,6} - 9_{3,7}$	63.5	0.1	0.9 [m]
	357892.4	$7_{4,4} - 7_{3,5}$	47.8	0.3	2.4
	357926.0	$6_{4,2} - 6_{3,3}$	41.4	0.4	3.4
	357962.9	$17_{4,14} - 17_{3,15}$	162.9	0.3	0.9
	358013.1	$5_{4,2} - 11_{3,3}$	35.9	0.3	1.2
	358038.1	$4_{4,0} - 11_{3,1}$	31.3	0.1	0.9 [m]
CH_3OH	336865.2	$12_{7,6}$ A$^-$ – $12_{6,6}$ A$^+$	180.9	1.3	8.5
	337135.9	$3_{3,0}$ E – $4_{3,1}$ E	44.3	0.8	2.9
	338344.6	$7_{3,4}$ E – $6_{3,4}$ E	53.1	8.2	38.7
	338404.6	$7_{7,1}$ E – $6_{6,0}$ E	226.4	9.1 *	43.7 *
	338408.7	$7_{4,4}$ A$^+$ – $6_{3,3}$ A$^+$	48.8	...	...
	338486.3	$7_{6,1}$ A$^\pm$ – $6_{6,1}$ A$\pm$	186.6	0.3	1.0
	338504.1	$7_{2,6}$ E – $6_{1,5}$ E	135.5	0.4	2.0
	338512.6	$7_{6,2}$ A$^\pm$ – $6_{5,1}$ A$^\pm$	129.1	1.7 *	8.6 *
	338512.9	$7_{5,3}$ A$^-$ – $6_{4,2}$ A$^-$	86.5	...	...
	338530.3	$7_{6,2}$ E – $6_{5,1}$ E	143.6	0.3	1.3
	338540.8	$7_{5,2}$ A$^+$ – $6_{5,2}$ A$^+$	98.5	1.1 *	6.1 *
	338543.2	$7_{5,2}$ A$^-$ – $6_{5,2}$ A$^-$	98.5	...	...
	338559.9	$7_{2,5}$ E – $6_{2,5}$ E	110.3	0.5	2.8
	338583.2	$7_{5,2}$ E – $6_{5,2}$ E	95.3	1.1	5.1
	338615.0	$7_{4,3}$ E – $6_{4,3}$ E	68.6	3.7	14.0
	338639.9	$7_{5,3}$ A$^+$ – $6_{4,2}$ A$^+$	86.5	1.6	6.5
	338721.6	$7_{5,3}$ E – $6_{4,2}$ E	69.8	5.9 *	28.2 *
	338722.9	$7_{3,5}$ E – $6_{2,4}$ E	73.5	...	...
	340141.2	$2_{2,0}$ A$^+$ – $3_{2,1}$ A$^+$	28.3	0.5	2.6
	341415.6	$7_{4,3}$ A$^-$ – $6_{4,3}$ A$^-$	63.7	4.3	18.0
	342729.8	$13_{7,6}$ A$^-$ – $13_{7,7}$ A$^+$	211.0	0.8	4.7
	345904.2	$16_{9,8}$ A$^-$ – $15_{9,7}$ A$^-$	316.0	0.3	1.9
	349107.0	$14_{7,6}$ A$^-$ – $14_{7,7}$ A$^+$	243.5	0.5	4.0
	350687.7	$4_{2,2}$ E – $3_{1,2}$ E	18.3	2.1	13.4 [n]
	350905.1	$1_{1,0}$ A$^+$ – $0_{0,0}$ A$^+$	0.0	2.4	13.4

[h] Blended with CH_3OH $7_{4,3}$ E – $6_{4,3}$ E line; the blended intensity is shown.

[i] Blended with $H^{13}CN$ 4 – 3 line; the blended intensity is shown.

[j] Blended with SO $8_9 - 7_8$ line; the blended intensity is shown.

[k] Blended with wing of HCO^+ 4 – 3 line; an estimated intensity is given

[l] Blended in DSB observations with wing of HCN 4 – 3 line; an estimated intensity is given

[m] Transition not clearly detected; an upper limit is given

[n] Blended with NO $\frac{7}{2} - \frac{5}{2}$ f line; the blended intensity is shown.

TABLE A2.4 - *Continued*

Species	Frequency (MHz)	Transition	E_{lower} (K)	T_{MB} (peak) [a] (K)	$\int T_{MB}\,dv$ [a] (K km s^{-1})
CH_3CN	349446.7	$19_4 - 18_4$	158.12	0.3 *	2.3 *
	349453.4	$19_0 - 18_0$	151.0	...	...
CH_3OCH_3	342608.1	$19_{0,19}$ AE – $18_{1,18}$ AE	150.7	0.1 *	0.7 *
	342608.1	$19_{0,19}$ EA – $18_{1,18}$ EA	150.7	...	...
	342608.1	$19_{0,19}$ EE – $18_{1,18}$ EE	150.7	...	...
	342608.1	$19_{0,19}$ AA – $18_{1,18}$ AA	150.7	...	...
	343753.3	$17_{2,16}$ EA – $16_{1,15}$ EA	127.2	0.3 *	0.8 *
	343753.3	$17_{2,16}$ AE – $16_{1,15}$ AE	127.2	...	...
	343754.2	$17_{2,16}$ EE – $16_{1,15}$ EE	127.2	...	...
	343755.1	$17_{2,16}$ AA – $16_{1,15}$ AA	127.2	...	...
	344358.0	$19_{1,19}$ EA – $18_{0,18}$ EA	150.7	0.3 *	1.1 *
	344358.0	$19_{1,19}$ AE – $18_{0,18}$ AE	150.7	...	...
	344358.1	$19_{1,19}$ EE – $18_{0,18}$ EE	150.7	...	...
	344358.2	$19_{1,19}$ AA – $18_{0,18}$ AA	150.7	...	...
	344512.2	$11_{3,9}$ EA – $10_{2,8}$ EA	56.3	0.1 *	0.9 *
	344512.2	$11_{3,9}$ AE – $10_{2,8}$ AE	56.3	...	...
	344515.4	$11_{3,9}$ EE – $10_{2,8}$ EE	56.3	...	...
	344518.6	$11_{3,9}$ AA – $10_{2,8}$ AA	56.3	...	...
	349803.0	$11_{2,9}$ EA – $10_{1,10}$ EA	49.7	0.1 *	0.8 *
	349803.0	$11_{2,9}$ AE – $10_{1,10}$ AE	49.7	...	...
	349806.1	$11_{2,9}$ EE – $10_{1,10}$ EE	49.7	...	...
	349809.2	$11_{2,9}$ AA – $10_{1,10}$ AA	49.7	...	...
	357459.4	$18_{2,17}$ EA – $17_{1,16}$ EA	142.7	0.1 *	0.7 *
	357459.4	$18_{2,17}$ AE – $17_{1,16}$ AE	142.7	...	...
	357460.2	$18_{2,17}$ EE – $17_{1,16}$ EE	142.7	...	...
	357461.0	$18_{2,17}$ AA – $17_{1,16}$ AA	142.7	...	...
U	343601			0.1	0.3
U	346220			0.3	1.1

References for Appendix A

Avery, L. W., *et al.* 1992, *Astrophys. J. (Suppl.)*, **83**, 363.

Blake, G. A., Sutton, E. C., Masson, C. R., & Phillips, T. G. 1986, *Astrophys. J. (Suppl.)*, **60**, 357.

Cernicharo, J., Guélin, M., Kahane, C., Bogey, M., Demuynck, C., & Destombes, J. L. 1991, *Astron. Astrophys.*, **246**, 213.

Cummins, S. E., Linke, R. A., & Thaddeus, P. 1986, *Astrophys. J. (Suppl.)*, **60**, 819.

Ellison, B. N., Schaffer, P. L., Schaal, W., Vail, D., & Miller, R. E. 1989, *Int'l. J. IR & MM Waves*, **10**, 937.

Genzel, R., & Stutzki, J. 1989, *Ann. Rev. Astron. Astrophys.*, **27**, 41.

Greaves, J. S., & White, G. J. 1991, *Astron. Astrophys. Suppl.*, **91**, 237.

Groesbeck, T. D., Phillips, T. G., & Blake, G. A. 1994, in preparation.

Hjalmarson, Å 1989, in *The Physics and Chemistry of Interstellar Molecular Clouds*, eds. G. Winnewisser & J. T. Armstrong (Springer-Verlag:Berlin), p. 73.

Irvine, W. M., *et al.* 1988, *Astrophys. J. (Letters)*, **334**, L107.

Jewell, P. R., Hollis, J. M., Lovas, F. J., & Snyder, L. E. 1989, *Astrophys. J. (Suppl.)*, **70**, 833.

Johansson, L. E. B. *et al.* 1984, *Astron. Astrophys.*, **130**, 227.

Kaifu, N., Suzuki, H., Ohishi, M., Miyajai, T., Ishikawa, S., Kasuga, T., Morimoto, M., & Saito, S. 1987, *Astrophys. J. (Letters)*, **317**, L111.

Keene, J., Hildebrand, R. H., & Whitcomb, S. E. 1982, *Astrophys. J. (Letters)*, **252**, L11.

McMullin, J. P., Mundy, L. G., & Blake, G. A. 1993, *Astrophys. J.*, **405**, 599.

Schilke, P., Groesbeck, T. D., Phillips, T. G., & Blake, G. A. 1994, in preparation.

Sutton, E. C., Blake, G. A., Masson, C. R., & Phillips, T. G. 1984, *Astrophys. J. (Letters)*, **283**, L41.

Sutton, E. C., Blake, G. A., Masson, C. R., & Phillips, T. G. 1985, *Astrophys. J. (Suppl.)*, **58**, 341.

Sutton, E. C., Jaminet, P. A., Danchi, W. C., & Blake, G. A. 1991, *Astrophys. J. (Suppl.)*, **77**, 255.

Turner, B. E. 1989, *Astrophys. J. (Suppl.)*, **70**, 539.

Ziurys, L. M., Martin, R. N., Pauls, T. A., & Wilson, T. L. 1981, *Astron. Astrophys.*, **104**, 288.

Ziurys, L. M., & McGonagle, D. 1993, *Astrophys. J. (Suppl.)*, **89**, 155.

Appendix B

Spectral Line Survey of IRC +10216

In addition to the surveys of Orion-KL and Orion-S presented in Appendix A, we initially concentrated on the carbon star IRC +10216 which had been the subject of previous spectral line surveys between 72 and 91 GHz (Johansson *et al.* 1984) and between 340 and 365 GHz (Avery *et al.* 1992), and an unpublished survey covering large sections of the spectrum between 80 and 250 GHz which has served as the basis for several papers describing particular molecules (*cf.* Cernicharo *et al.* 1991, Kahane *et al.* 1988). A rich molecular spectrum has been observed towards IRC +10216, which serves in many respects as a reference source for other evolved stars just as Orion does for hot cores. The molecular transitions seen towards IRC +10216 arise from the circumstellar shell of gas and dust which consists of material being expelled from the star. The roughly spherical geometry and constant outflow velocity of 14.5 km s^{-1} lead to a set of well known line shapes which depend upon the optical depth of the transitions and the radial extent of the emitting region (Morris 1975, Olofsson *et al.* 1982). Previous authors had suggested that the integrated line emission from this source might be responsible for a substantial fraction of the total observed flux (Walmsley *et al.* 1991, Avery *et al.* 1992). In this appendix we present the deconvolved SSB spectrum from the CSO spectral line survey of IRC +10216 covering the 330–358 GHz range. A detailed analysis of the survey, including consideration of the individual species and transitions detected has been published separately (Groesbeck, Phillips, & Blake 1994).

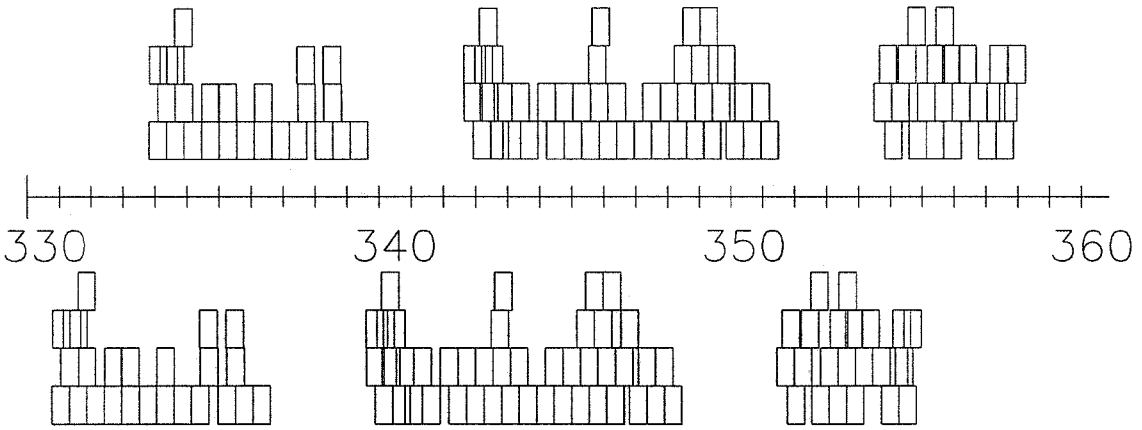

Figure B1.1 Frequency coverage of the IRC +10216 observations. Each DSB observation is represented by a pair of boxes: one showing the frequency range in the upper sideband and one showing the range of the lower sideband.

B1. The CSO IRC +10216 Spectral Line Survey

B1.1. Overview

Our initial observations for the CSO 330-360 GHz line survey project were made in December 1988, and included observations of both the Orion region and IRC +10216. The observing procedures and calibration methods used are presented in Chapter 3 of this thesis with a description of the deconvolution method used to obtain a single sideband form of the spectrum given in Chapter 4. As described therein, observations were usually made at intervals of 250 MHz, or half the backend width. However, time constraints prevented us from obtaining a complete set of such observations; the actual data set includes both more sparsely sampled regions as well as regions where additional smaller LO shifts were made. We list the observing frequencies used in our data set in Table B1.1, showing both the upper and lower sideband center frequencies for the 107 scans included in the survey. Figure B1.1 shows the frequency coverage which resulted from our observations. There is a significant amount of overlap between the present survey and the DSB data presented by Avery *et al.* from their survey conducted using the 15m JCMT. In general there is good agreement between the two surveys, although the present data set offers significantly greater sensitivity.

TABLE B1.1

CENTER FREQUENCIES OF OBSERVATIONS
FOR THE CSO SPECTRAL LINE SURVEY OF IRC+10216

USB Center (GHz)	LSB Center (GHz)	Date Observed	USB Center (GHz)	LSB Center (GHz)	Date Observed
333.250	330.450	16 March 1990	347.350	344.550	03 May 1989
333.270	330.470	16 March 1990	347.600	344.800	03 May 1989
333.500	330.700	16 March 1990	347.850	345.050	03 May 1989
333.570	330.770	16 March 1990	348.100	345.300	03 May 1989
333.750	330.950	11 January 1991	348.250	345.450	14 January 1990
333.760	330.960	11 January 1991	348.350	345.550	03 May 1989
333.990	331.190	11 January 1991	348.500	345.700	08 January 1991
334.000	331.200	11 January 1991	348.500	345.700	14 January 1990
334.250	331.450	12 January 1991	348.600	345.800	03 May 1989
334.750	331.950	12 January 1991	348.750	345.950	14 January 1990
334.760	331.960	12 January 1991	348.850	346.050	03 May 1989
335.240	332.440	12 January 1991	349.000	346.200	14 January 1990
335.250	332.450	12 January 1991	349.090	346.290	07 January 1991
335.750	332.950	12 January 1991	349.100	346.300	07 January 1991
336.250	333.450	13 January 1991	349.110	346.310	07 January 1991
336.260	333.460	13 January 1991	349.350	346.550	07 January 1991
336.750	333.950	13 January 1991	349.360	346.560	07 January 1991
337.250	334.450	13 January 1991	349.500	346.700	08 January 1991
337.480	334.680	16 March 1990	349.510	346.710	08 January 1991
337.500	334.700	16 March 1990	349.750	346.950	08 January 1991
338.000	335.200	19 March 1990	349.750	346.950	17 January 1990
338.230	335.430	19 March 1990	350.000	347.200	08 January 1991
338.250	335.450	19 March 1990	350.000	347.200	17 January 1990
338.500	335.700	19 March 1990	350.010	347.210	08 January 1991
339.000	336.200	13 January 1991	350.010	347.210	17 January 1990
342.240	339.440	10 January 1991	350.250	347.450	09 January 1991
342.250	339.450	10 January 1991	350.260	347.460	17 January 1990
342.250	339.450	14 March 1990	350.500	347.700	09 January 1991
342.500	339.700	10 January 1991	350.750	347.950	09 January 1991
342.550	339.750	10 January 1991	350.760	347.960	09 January 1991
342.680	339.880	17 March 1990	354.000	351.200	14 March 1990
342.700	339.900	17 March 1990	354.150	351.350	14 March 1990
342.850	340.050	27 April 1989	354.300	351.500	14 March 1990
343.000	340.200	14 March 1990	354.500	351.700	14 March 1990
343.100	340.300	27 April 1989	354.700	351.900	14 March 1990
343.350	340.550	27 April 1989	354.970	352.170	11 January 1992
343.600	340.800	27 April 1989	355.000	352.200	11 January 1992
343.850	341.050	25 April 1989	355.250	352.450	11 January 1992
344.350	341.550	21 January 1989	355.500	352.700	11 January 1992
344.600	341.800	20 January 1989	355.530	352.730	11 January 1992
344.850	342.050	20 January 1989	355.750	352.950	18 March 1990
345.100	342.300	20 January 1989	355.780	352.980	18 March 1990
345.350	342.550	19 January 1989	355.970	353.170	11 January 1992
345.600	342.800	18 January 1989	356.000	353.200	11 January 1992
345.796	342.996	25 April 1989	356.250	353.450	11 January 1992
345.796	342.996	27 April 1989	356.440	353.640	18 March 1990
345.850	343.050	18 January 1989	356.750	353.950	13 March 1990
345.895	343.095	07 January 1991	357.000	354.200	13 March 1990
345.900	343.100	07 January 1991	357.250	354.450	13 March 1990
345.905	343.105	07 January 1991	357.330	354.530	18 March 1990
346.100	343.300	19 January 1989	357.500	354.700	13 March 1990
346.350	343.550	01 May 1989	357.600	354.600	13 January 1992
346.600	343.800	01 May 1989	357.850	354.850	13 January 1992
347.100	344.300	03 May 1989			

TABLE B1.2
CSO IRC+10216 SPECTRAL LINE SURVEY
SUMMARY OF OBSERVING DATES AND FREQUENCIES

Dates	Frequencies [a] (GHz)
1989 January 18–21	341–346
1989 April 25–May 3	340–341,343-349
1990 January 14–17	345–350
1990 March 13–19	330–331,333–336,337–340,351–358
1991 January 7–13	331–340,342–343,346–351
1992 January 11–13	352–358 [b]

[a] Approximate frequency ranges covered during each observing session.
[b] Several small regions within this range were observed to complete the continuous spectrum.

During the initial phases of the line survey observations we concentrated on the Orion region and IRC +10216. All of the frequencies observed during the initial 1988 December period were later re-observed, so that all of the data included in the final results date from 1989 January and later. The bulk of the observations were completed in 1991 January, with several LO settings observed in 1992 January in order to make the spectral range covered by the survey continuous. Table B1.2 summarizes the observing dates and the approximate frequency ranges covered during each period. IRC +10216 is known to exhibit variations in its infrared intensity with a period of some 644 days (Witteborn *et al.* 1980). The overlapping nature of the observations resulted in many frequencies being observed at more than one epoch. No evidence was seen for systematic variations in the line intensities; the variations seen between different sessions were comparable to the variations seen during a single session. For the deconvolution process, it was assumed that the line intensities were constant throughout the survey observations.

The remaining details of the observations are essentially identical to those of the Orion surveys. The telescope had a FWHM beamwidth of 20″ averaged over the range of frequencies in the survey. Pointing was checked frequently by observing planets and strong lines of species with compact emission from IRC +10216 itself. Throughout the observations, the pointing was found to be accurate to $\lesssim 5''$. The facility SIS receiver (Ellison *et al.* 1989) was used for all observations, giving receiver temperatures of typically 200 - 250 K (SSB) and system temperatures ranging from 700 to 2000 K (SSB). The atmospheric opacity was usually less than 0.25, reaching 0.8 on occasion. The facility backend (an acousto-optic

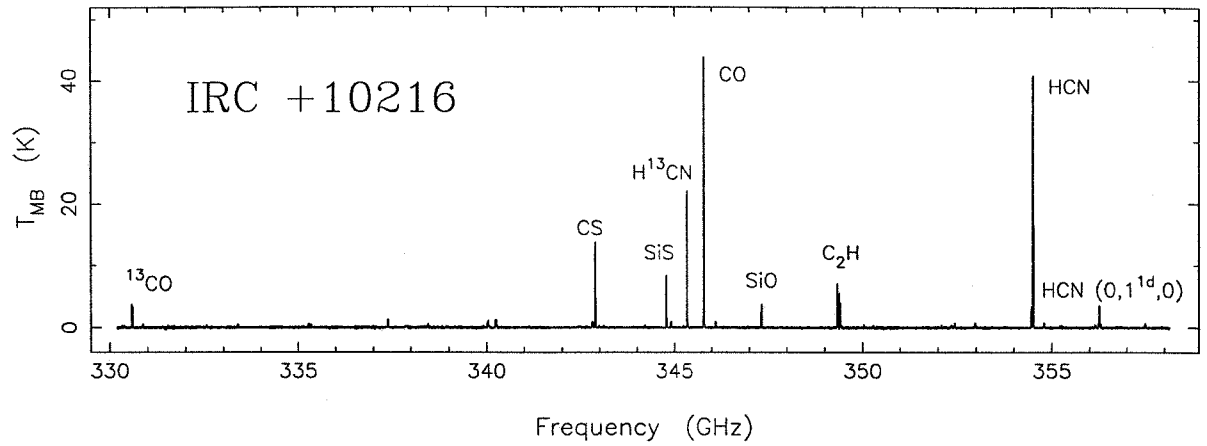

Figure B1.2 A compressed view of the CSO spectral line survey of IRC +10216.

spectrometer) was used which had a bandwidth of 500 MHz and a nominal channel width of 0.49 MHz. A channel width of 1.0 MHz is used to reconstruct the SSB spectrum; this corresponds more closely to the actual resolution of the backend as determined from frequency calibration measurements. The chopper wheel method as described in Chapter 3 was used to calibrate the data as the observations were made, and low order polynomial baselines were removed from the DSB spectra. The data presented here have been corrected for a main beam efficiency of $\eta_{MB} = 0.60$ as found from observations of planets. As the different species exhibit emission from regions of varying angular extent, the use of a single efficiency correction will result in some errors in the brightness temperatures obtained, particularly for emission from very extended or very compact regions. For reference, the extended efficiency was found to be $\eta_{ext} = 0.76$ from observations of the moon.

B1.2. Results

Figure B1.2 shows a compressed view of the reduced single sideband spectrum obtained from our observations. The resulting spectrum extends continuously from 330 to 358 GHz, with a noise level of ~90 mK in main beam brightness temperature units over most of the band. Figure B1.3 presents an expanded view of the spectrum, with the individual strong lines shown in Figure B1.4. The frequency scale has been established assuming a source velocity of $-26\,\mathrm{km\ s^{-1}}$. In comparison to the Orion-KL survey, the overall line density is quite low, and is in fact even less than for the Orion-S survey. A total of 56 spectral lines are detected, with only 2 remaining unidentified. The remaining features have been identified

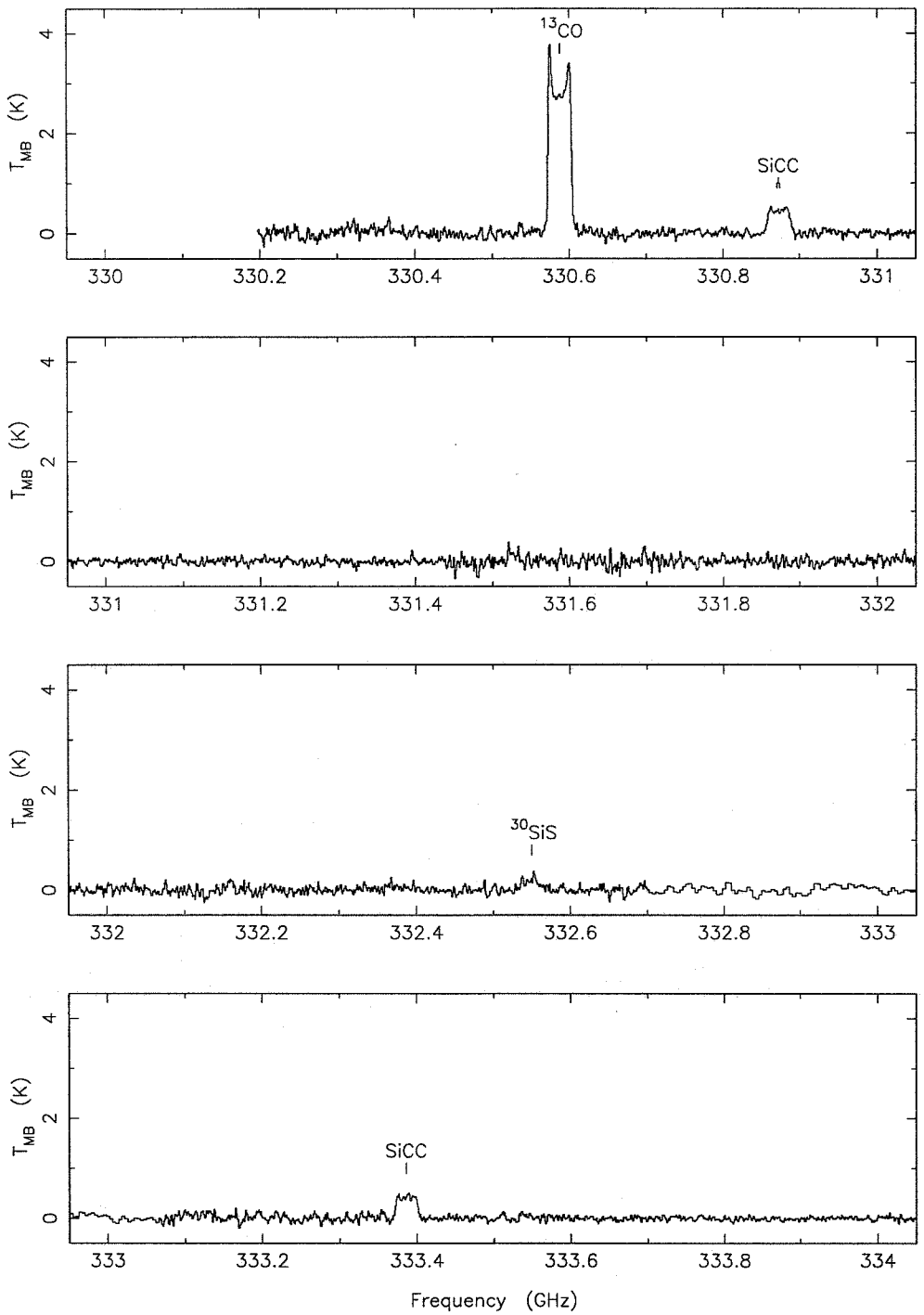

Figure B1.3 Spectrum of IRC +10216 from 330 to 358 GHz. The data have been corrected by the main beam efficiency of 0.60. The rest frequency scale has been established using a v_{LSR} of -26 km s^{-1}. Tick marks show the rest frequencies of identified transitions.

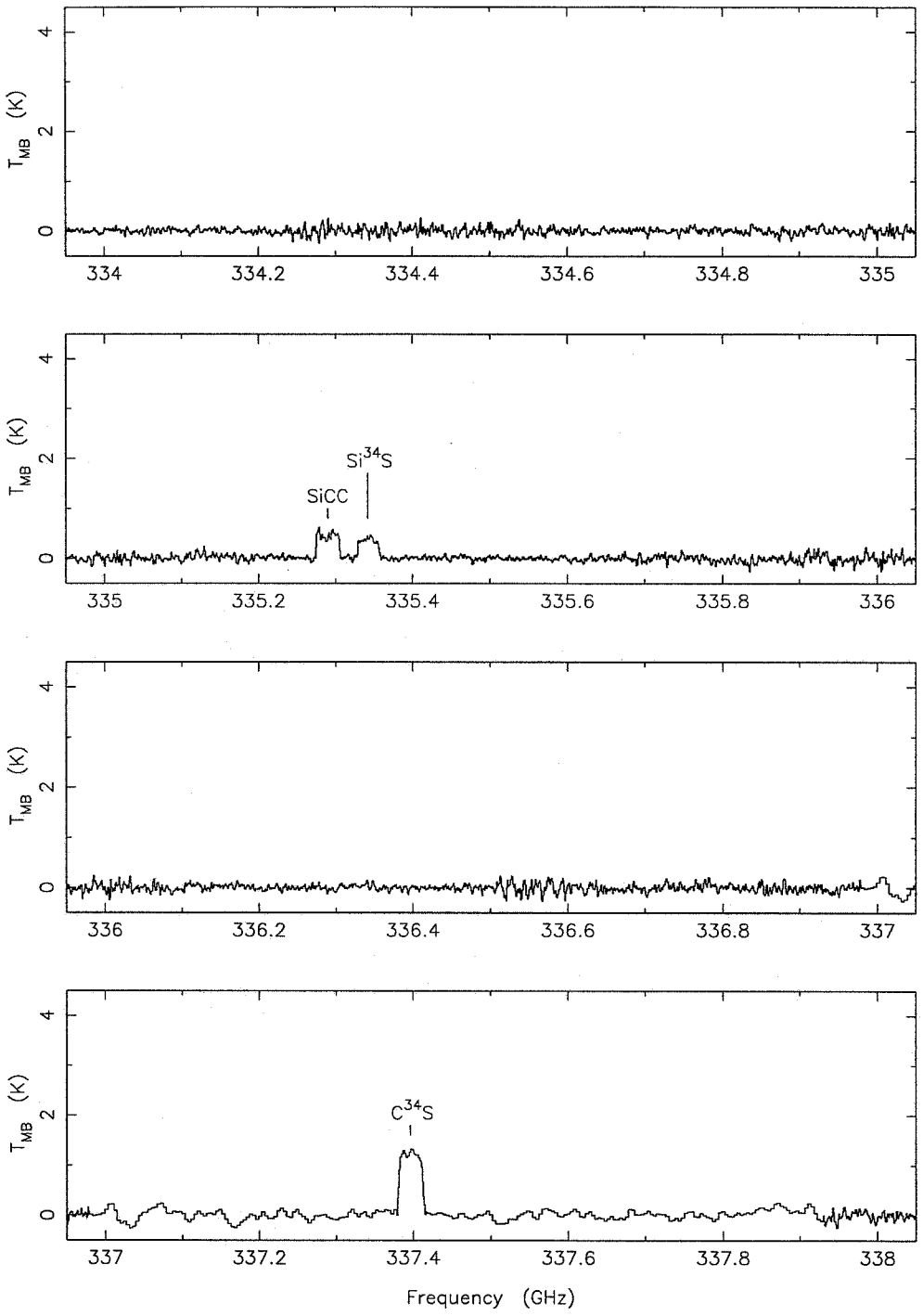

Figure B1.3 — *Continued*

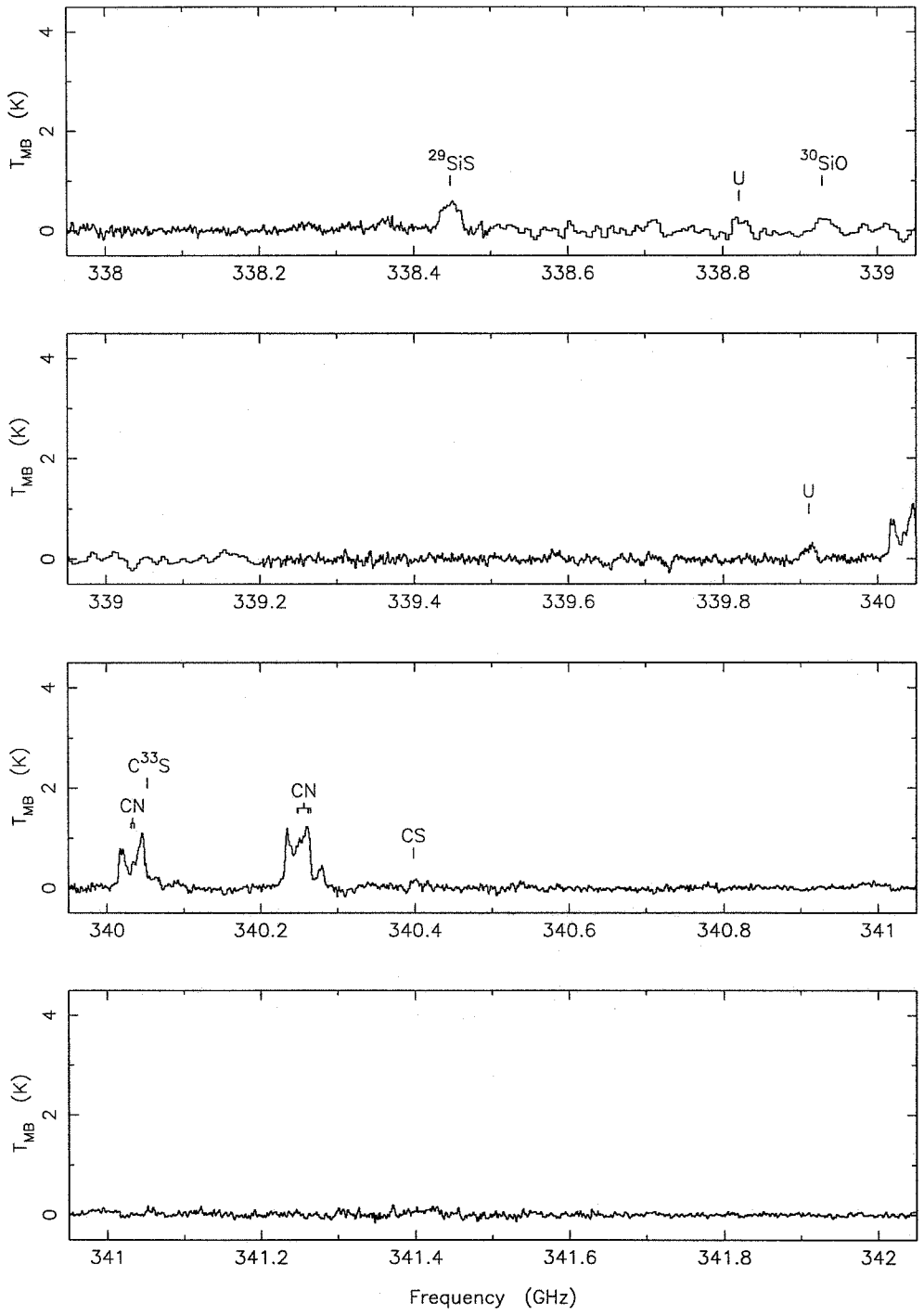

Figure B1.3 — *Continued*

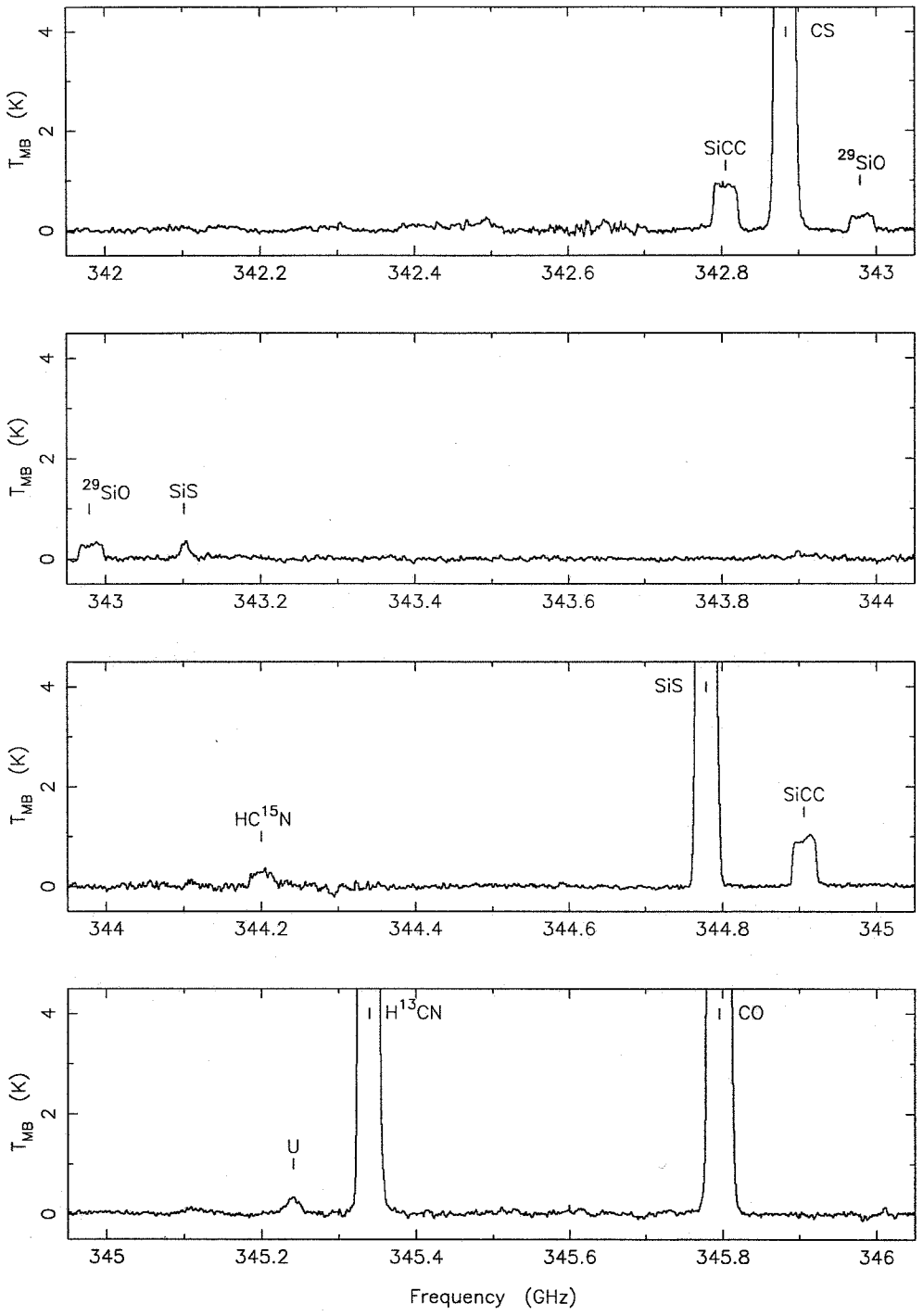

Figure B1.3 — *Continued*

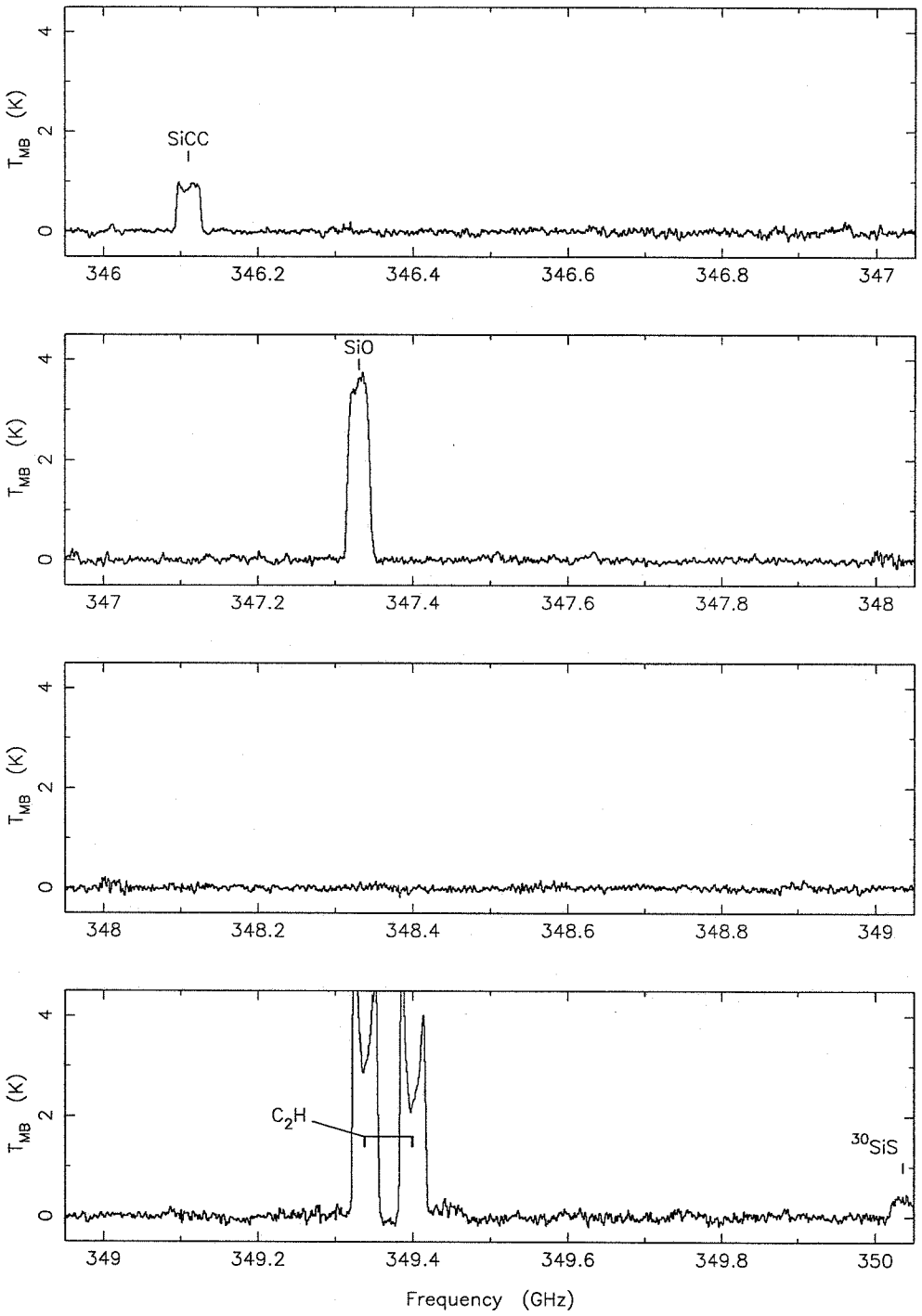

Figure B1.3 — *Continued*

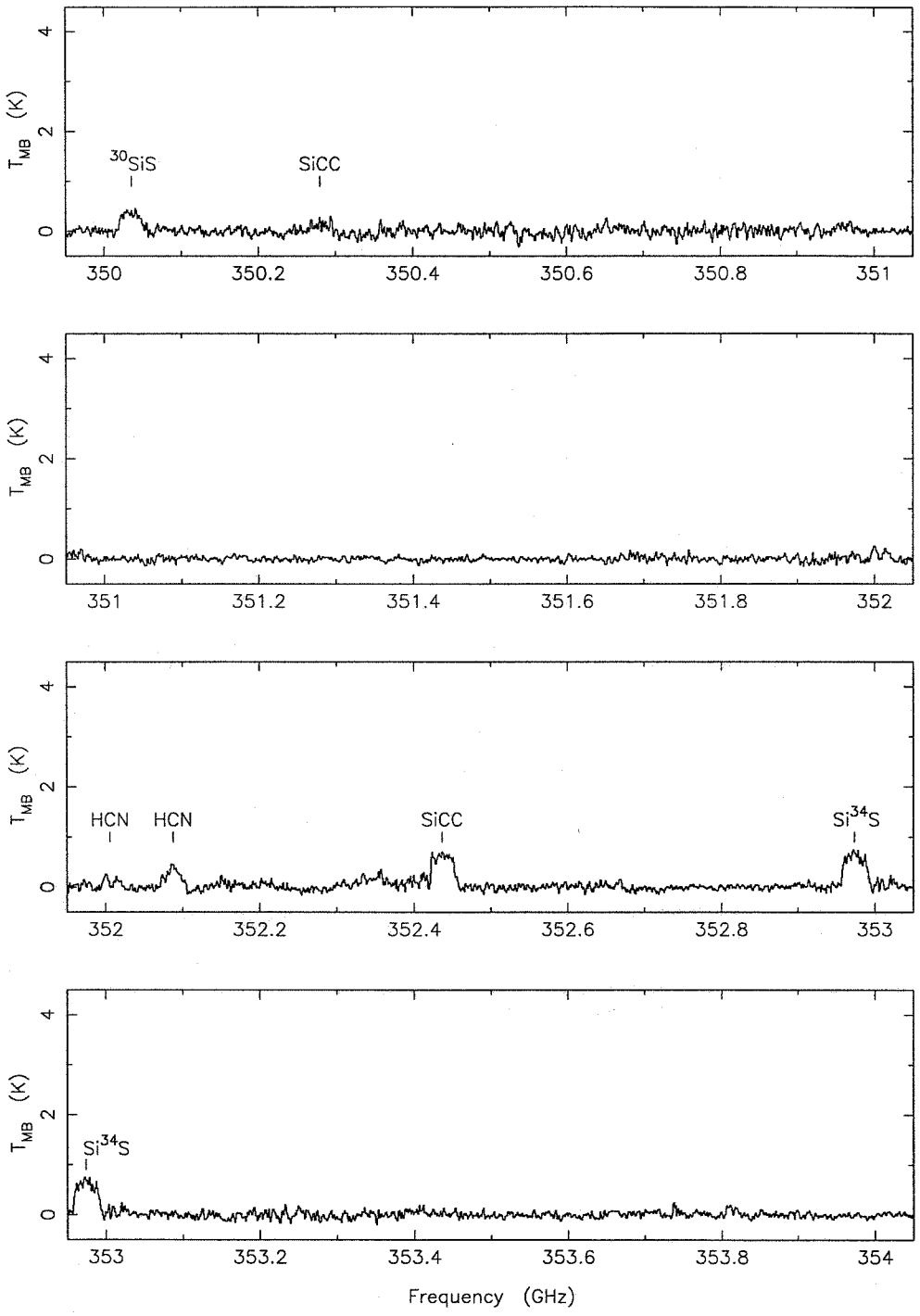

Figure B1.3 — *Continued*

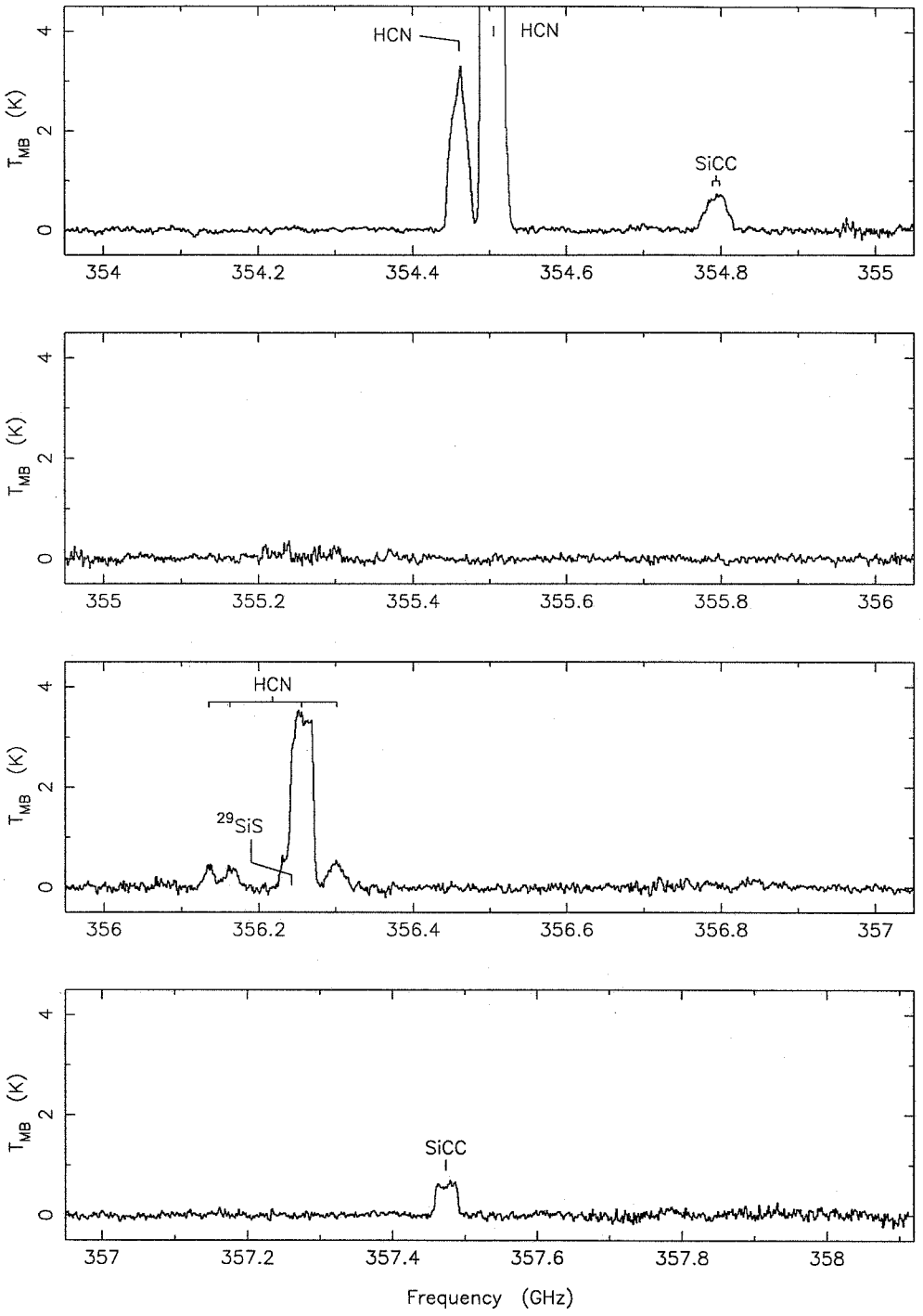

Figure B1.3— *Continued*

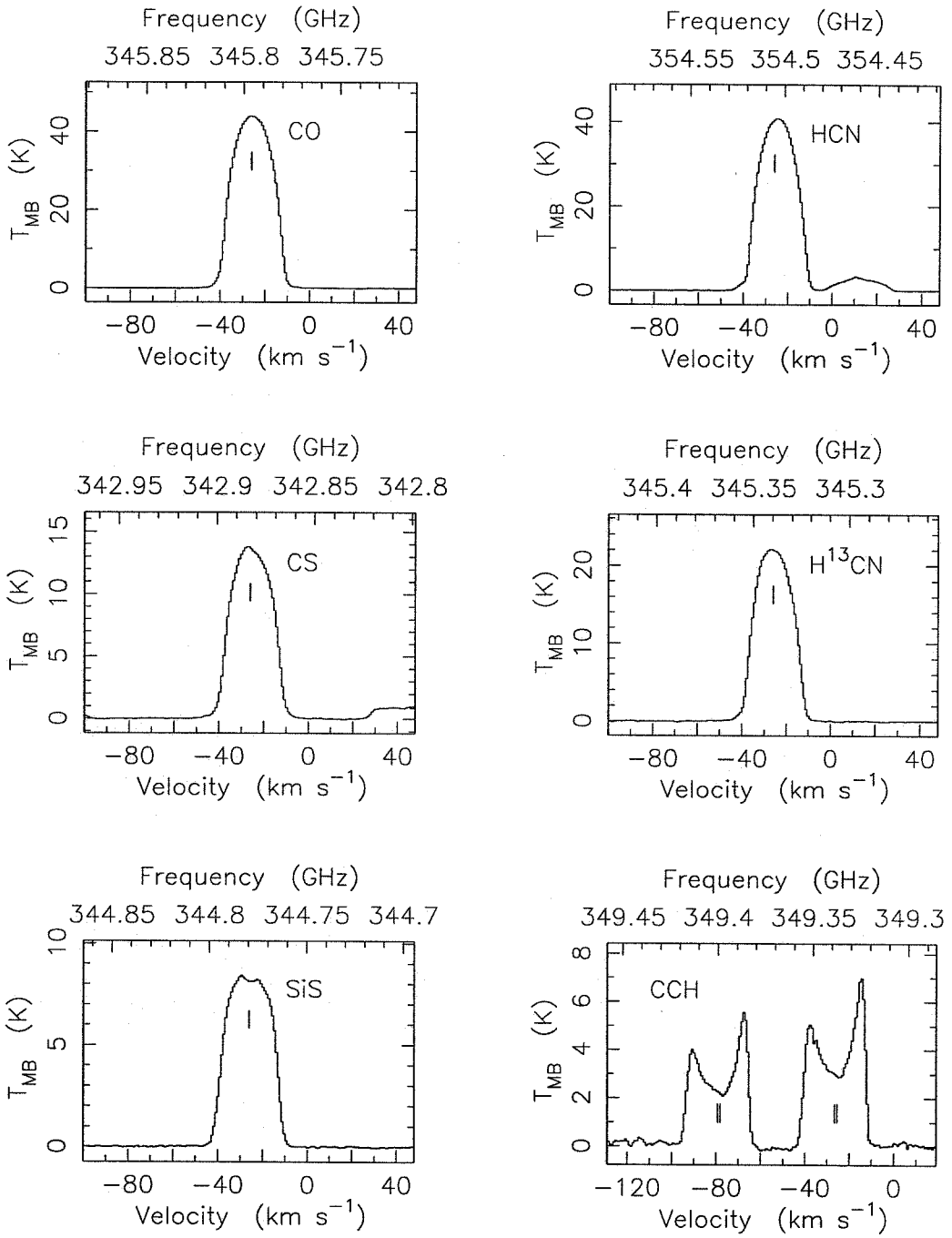

Figure B1.4 Strong lines observed within the frequency range covered by the survey. Tick marks indicate the rest frequencies of the lines and are shown at −26 km s^{-1} for all lines except the CCH blends. For these, the reference velocity of −26 km s^{-1} occurs midway between the lower frequency pair of lines. The unlabeled weaker lines which are visible are from SiCC at 342.805 GHz and from the vibrationally excited HCN (0, 1^{1c}, 0) state at 354.460 GHz.

TABLE B1.3

LINES DETECTED IN THE CSO SPECTRAL LINE SURVEY OF IRC +10216

Frequency (MHz)	Species	Transition	Frequency (MHz)	Species	Transition
330588.1	^{13}CO	3 – 2	344906.0	SiCC	$16_{0,16} - 15_{0,15}$
330870.5	SiCC	$14_{6,9} - 13_{6,8}$	345238.7	$H^{13}CN$ (0,1^{1c},0) [a]	4 – 3
330874.5	SiCC	$14_{6,8} - 13_{6,7}$	345339.8	$H^{13}CN$	4 – 3
332550.3	^{30}SiS	19 – 18	345796.0	CO	3 – 2
333386.1	SiCC	$14_{4,11} - 13_{4,10}$	346110.0	SiCC	$14_{2,12} - 13_{2,11}$
335289.7	SiCC	$14_{4,10} - 13_{4,9}$	347330.6	SiO	8 – 7
335342.0	Si^{34}S	19 – 18	349337.5	C_2H	$4,\frac{9}{2},5 - 3,\frac{7}{2},4$
337396.7	C^{34}S	7 – 6	349338.7	C_2H	$4,\frac{9}{2},4 - 3,\frac{7}{2},3$
338447.3	^{29}SiS	19 – 18	349398.9	C_2H	$4,\frac{7}{2},4 - 3,\frac{5}{2},3$
338821	U		349400.3	C_2H	$4,\frac{7}{2},3 - 3,\frac{5}{2},2$
338929.0	^{30}SiO	8 – 7	350035.7	^{30}SiS	20 – 19
339911	U		350280.0	SiCC	$15_{10,5} - 14_{10,4}$
340031.5	CN	$3,\frac{5}{2},\frac{7}{2} - 2,\frac{3}{2},\frac{5}{2}$	350280.0	SiCC	$15_{10,6} - 14_{10,5}$
340035.4	CN	$3,\frac{5}{2},\frac{3}{2} - 2,\frac{3}{2},\frac{1}{2}$	352005.7	HCN (0,0^0,1)	4 – 3
340035.4	CN	$3,\frac{5}{2},\frac{5}{2} - 2,\frac{3}{2},\frac{3}{2}$	352087.9	HCN (1,0^0,0)	4 – 3
340052.7	C^{33}S	7 – 6	352436.5	SiCC	$15_{8,8} - 14_{8,7}$
340247.8	CN	$3,\frac{7}{2},\frac{7}{2} - 2,\frac{5}{2},\frac{5}{2}$	352436.5	SiCC	$15_{8,7} - 14_{8,6}$
340247.8	CN	$3,\frac{7}{2},\frac{9}{2} - 2,\frac{5}{2},\frac{7}{2}$	352974.0	Si^{34}S	20 – 19
340248.6	CN	$3,\frac{7}{2},\frac{5}{2} - 2,\frac{5}{2},\frac{3}{2}$	354460.3	HCN (0,1^{1c},0)	4 – 3
340261.8	CN [a]	$3,\frac{7}{2},\frac{5}{2} - 2,\frac{5}{2},\frac{5}{2}$	354505.5	HCN	4 – 3
340265.0	CN [a]	$3,\frac{7}{2},\frac{7}{2} - 2,\frac{5}{2},\frac{7}{2}$	354789.5	SiCC	$15_{6,10} - 14_{6,9}$
340398.1	CS (v=1)	7 – 6	354798.4	SiCC	$15_{6,9} - 14_{6,8}$
342805.0	SiCC	$15_{2,14} - 14_{2,13}$	356135.4	HCN (0,2^{2d},0)	4 – 3
342883.0	CS	7 – 6	356162.7	HCN (0,2^{2c},0)	4 – 3
342979.1	^{29}SiO	8 – 7	356242.4	^{29}SiS	20 – 19
343101.0	SiS (v=1)	19 – 18	356255.7	HCN (0,1^{1d},0)	4 – 3
344200.3	HC^{15}N	4 – 3	356301.3	HCN (0,2^0,0)	4 – 3
344779.5	SiS	19 – 18	357473.4	SiCC	$15_{4,12} - 14_{4,11}$

[a] Tentative identification.

with 8 molecules and their isotopomers which have previously been observed towards IRC +10216. The small number of unidentified lines when compared to the Orion-KL survey seems to reflect a real difference in the complexity of the observed chemistry, with fewer species seen toward IRC +10216, although heavier species (*e.g.*, HC_3N, HC_5N) which have been observed at lower frequencies are absent from our survey because of partition function and level population considerations. Table B1.3 lists the detected spectral lines sorted by frequency. More detailed information about the lines, including quantum numbers and intensities, is given in Table B1.4.

Unlike the Orion surveys, we were unable to use our observations to measure the weaker continuum emission from IRC +10216. We therefore compare our integrated line flux to published broadband

TABLE B1.4

TRANSITION ENERGIES AND INTEGRATED INTENSITIES FOR CSO LINE SURVEY OF IRC+10216

Species	Frequency (MHz)	Transition	E_{lower} (K)	$\int T_{MB}\,dv$ (K km s^{-1})
CO	345796.0	3 – 2	16.6	955.6
^{13}CO	330588.1	3 – 2	15.9	86.4
CS	342883.0	7 – 6	49.4	301.5
CS (v=1)	340398.1	7 – 6	1879.4	2.0
C^{34}S	337396.7	7 – 6	48.6	34.2
C^{33}S	340052.7	7 – 6	49.0	~3 [a]
SiO	347330.6	8 – 7	58.3	87.8
^{29}SiO	342979.1	8 – 7	57.6	8.0
^{30}SiO	338929.0	8 – 7	56.9	4.5
SiS	344779.5	19 – 18	149.0	201.7
SiS (v=1)	343101.0	19 – 18	1219.4	4.3
^{29}SiS	338447.3	19 – 18	146.2	13.5
	356242.4	20 – 19	162.5	~20 [b]
^{30}SiS	332550.3	19 – 18	143.7	5.1
	350035.7	20 – 19	159.6	8.4
Si^{34}S	335342.0	19 – 18	144.9	9.6
	352974.0	20 – 19	161.0	17.2
CN	340031.5	$3,\frac{5}{2},\frac{7}{2} - 2,\frac{3}{2},\frac{5}{2}$	16.3	~21 [c]
	340035.4	$3,\frac{5}{2},\frac{3}{2} - 2,\frac{3}{2},\frac{1}{2}$	16.3	...
	340035.4	$3,\frac{5}{2},\frac{5}{2} - 2,\frac{3}{2},\frac{3}{2}$	16.3	...
	340247.8	$3,\frac{7}{2},\frac{7}{2} - 2,\frac{5}{2},\frac{5}{2}$	16.3	34.5 [d]
	340247.8	$3,\frac{7}{2},\frac{9}{2} - 2,\frac{5}{2},\frac{7}{2}$	16.3	...
	340248.6	$3,\frac{7}{2},\frac{5}{2} - 2,\frac{5}{2},\frac{3}{2}$	16.3	...
	340261.8	$3,\frac{7}{2},\frac{5}{2} - 2,\frac{5}{2},\frac{5}{2}$	16.3	...
	340265.0	$3,\frac{7}{2},\frac{7}{2} - 2,\frac{5}{2},\frac{7}{2}$	16.3	...
HCN	354505.5	4 – 3	25.5	831.7
HCN (0,1^{1c},0)	354460.3	4 – 3	1050 [e]	62.5
HCN (0,1^{1d},0)	356255.7	4 – 3	1050 [e]	~72 [f]
HCN (0,2^{0},0)	356301.3	4 – 3	2056 [e]	9.4
HCN (0,2^{2c},0)	356162.7	4 – 3	2078 [e]	6.3 [g]
HCN (0,2^{2d},0)	356135.4	4 – 3	2078 [e]	5.2 [g]
HCN (0,0^{0},1)	352005.7	4 – 3	3042 [e]	2.6
HCN (1,0^{0},0)	352087.9	4 – 3	4789 [e]	6.8
HC^{15}N	344200.3	4 – 3	24.8	7.7
H^{13}CN	345339.8	4 – 3	24.9	450.4
H^{13}CN (0,1^{1c},0)	345238.7	4 – 3	1041 [h]	6.0
C_2H	349337.5	$4,\frac{9}{2},5 - 3,\frac{7}{2},4$	25.1	121.3 [i]
	349338.7	$4,\frac{9}{2},4 - 3,\frac{7}{2},3$	25.1	...
	349398.9	$4,\frac{7}{2},4 - 3,\frac{5}{2},3$	25.2	93.3 [i]
	349400.3	$4,\frac{7}{2},3 - 3,\frac{5}{2},2$	25.2	...
SiCC	330870.5	$14_{6,9} - 13_{6,8}$	173.2	6.4 [j]
	330874.5	$14_{6,8} - 13_{6,7}$	173.2	6.4 [j]
	333386.1	$14_{4,11} - 13_{4,10}$	134.7	11.0
	335289.7	$14_{4,10} - 13_{4,9}$	134.8	13.0
	342805.0	$15_{2,14} - 14_{2,13}$	124.9	26.3
	344906.0	$16_{0,16} - 15_{0,15}$	127.6	27.1
	346110.0	$14_{2,12} - 13_{2,11}$	115.0	24.6
	350280.0	$15_{10,5} - 14_{10,4}$	311.5	1.6 [j]
	350280.0	$15_{10,6} - 14_{10,5}$	311.5	1.6 [j]
	352436.5	$15_{8,8} - 14_{8,7}$	242.9	9.1 [j]
	352436.5	$15_{8,7} - 14_{8,6}$	242.9	9.1 [j]
	354789.5	$15_{6,10} - 14_{6,9}$	189.1	9.5 [j]
	354798.4	$15_{6,9} - 14_{6,8}$	189.1	9.5 [j]
	357473.4	$15_{4,12} - 14_{4,11}$	150.7	16.6
U	338821			3.3
U	339911			3.0

[a] Blended with CN $3_{\frac{5}{2}} - 2_{\frac{3}{2}}$ lines; intensity is estimated.

[b] Blended with HCN (0,1^{1d}, 0) line; intensity is estimated.

[c] Blend of CN $3_{\frac{5}{2}} - 2_{\frac{3}{2}}$ lines and C^{33}S lines; a single intensity is estimated for the blended CN lines.

[d] Blend of CN $3_{\frac{7}{2}} - 2_{\frac{5}{2}}$ lines; a single integrated intensity is given for the blended lines.

[e] Taken from Carter, Mills, & Handy 1993.

[f] Blended with ^{29}SiS line; intensity is estimated.

[g] Blended HCN lines; intensity of each is estimated.

[h] Taken from Wang & Overend 1973.

[i] Blends of C_2H lines; a single integrated intensity is given for each blend.

[j] SiCC lines with equal energies and line strengths which are blended together; equal intensities are assigned to each line.

measurements (Sopka *et al.* 1985, Walmsley *et al.* 1991, Sandell 1994), finding that line emission contributes approximately 5 Jy, or $\gtrsim$65% of the observed total flux from IRC +10216 in this window (see Chapter 5 for details of the comparison method including error estimates). The greatest contribution of any single line comes from the CO J = 3–2 transition, representing some 26% of the detected line flux. Nearly as great is the 23% contribution of the HCN J = 4–3 line; in addition, the $H^{13}CN$ J = 4–3 line contributes 12% of the integrated line emission. SiCC has the largest number of detected lines for any species, but contributes less than 5% of the line flux. The dominant contributions to the flux thus come from relatively few lines. This has two important consequences when considering the line to continuum flux ratio: 1) reasonably accurate simulations of the integrated line emission may be performed using relatively few parameters and concentrating on the brightest lines; and 2) the line flux contribution will be strongly dependent on the precise frequency response of broadband measurements, as the inclusion or exclusion of particular lines will greatly affect the integrated line emission seen.

References for Appendix B

Avery, L. W., *et al.* 1992, *Astrophys. J. (Suppl.)*, **83**, 363.

Carter, S., Mills, I. M., & Handy, N. C. 1993, *J. Chem. Phys.*, **99**, 4379.

Cernicharo, J., Guélin, M., Kahane, C., Bogey, M., Demuynck, C., & Destombes, J. L. 1991, *Astron. Astrophys.*, **246**, 213.

Ellison, B. N., Schaffer, P. L., Schaal, W., Vail, D., & Miller, R. E. 1989, *Int'l. J. IR & MM Waves*, **10**, 937.

Groesbeck, T. D., Phillips, T. G., & Blake, G. A. 1994, *Astrophys. J. (Suppl.)*, **94**, 147.

Johansson, L. E. B. *et al.* 1984, *Astron. Astrophys.*, **130**, 227.

Kahane, C., Gomez-Gonzalez, J., Cernicharo, J., & Guélin, M 1988, *Astron. Astrophys.*, **190**, 167.

Morris, M. 1975, *Astrophys. J.*, **197**, 603.

Olofsson, H., Johansson, L. E. B., Hjalmarson, Å., & Nguyen-Q-Rieu. 1982, *Astron. Astrophys.*, **107**, 128.

Sandell, G. 1994, private communication.

Sopka, R. J., Hildebrand, R., Jaffe, D. T., Gatley, I., Roellig, T., Werner, M., Jura, M., & Zuckerman, B. 1985, *Astrophys. J.*, **294**, 242.

Walmsley, C. M., Chini, R., Keysa, E., Steppe, H., Forveille, T., & Omont, A. 1991, *Astron. Astrophys.*, **248**, 555.

Wang, V. K., & Overend, J. 1973, *Spectrochim. Acta*, **29A**, 687.

Witteborn, F. C., Strecker, D. W., Erickson, E. F., Smith, S. M., Goebel, J. H., & Taylor, B. J. 1980, *Astrophys. J.*, **238**, 577.

Appendix C

Spectral Line Surveys of IRAS 16293–2422, VY CMa, and OH 231.8+4.2

Spectral line surveys have in general been performed for sources which display strong line emission and which possess large line densities, e.g. Orion-KL, Sgr B2, and IRC +10216 (Johansson *et al.* 1984, Sutton *et al.* 1985, Blake *et al.* 1986, Cummins, Linke, & Thaddeus 1986, Turner 1989, Greaves & White 1991, Jewell *et al.* 1989, Sutton *et al.* 1991, Avery *et al.* 1992). Because surveys extend over large frequency ranges, they can achieve only a limited sensitivity when compared to targeted observations of individual lines, and are more suited to the brightest sources. The usual goals of line surveys are to understand the physical and chemical conditions in the source, possibly to detect new species, and in general to collect information about the transitions which may be astronomically observed. Hence the large number of lines in bright and chemically complex sources such as those listed above also makes them attractive candidates for line surveys.

For the purposes of this thesis, we wished to compare the integrated line flux with the total flux in several types of sources. We were therefore interested in collecting spectral line information for additional sources, where the line density and the brightness of the lines was lower than that of Orion-KL or IRC +10216 but the total flux was also less, in order to determine the integrated line flux. We chose an example of a low-mass star-forming region, IRAS 16293–2422, and two oxygen-rich stars, VY CMa and OH 231.8+4.2, to include in our study of the integrated line flux (see Chapter 5 of this thesis for

descriptions of the individual sources).

To obtain complete spectral coverage of the 330–360 GHz atmospheric window with the appropriate sensitivity for these sources would have required prohibitive amounts of telescope time (particularly since the complete surveys of Appendix A and Appendix B were already being performed). Instead, we made observations at frequencies chosen to include specific lines, obtaining approximately 50% coverage of the window for IRAS 16293–2422 and 30% coverage for the two stars. The data which had been collected for the Orion and IRC +10216 line surveys were used together with the line catalogs to select the actual frequencies observed, with the LO settings chosen to include as many potentially strong lines as possible.

Apart from the selection of observing frequencies, the methods used for these surveys are essentially identical to those employed for the complete surveys. The observing procedures and calibration techniques are described in Chapter 3 of this thesis, and the deconvolution method used to obtain the spectra in single sideband form is presented in Chapter 4. We note that of the sources considered in this appendix, only for the survey of IRAS 16293–2422 is the spectral coverage and observed line density sufficient to make it desirable to perform the deconvolution. For VY CMa and OH 231.8+4.2, we instead present averages of the DSB spectra obtained for the relatively few lines detected. With the exception of SO_2 lines occurring in the same sideband, no blending of lines is observed for these sources so that the use of DSB observations does not pose an undue problem.

All of the data were obtained using the facility 345 GHz receiver (Ellison *et al.* 1989) at the CSO 10.4 m telescope on Mauna Kea, Hawaii, with a FWHM beamwidth of 20″ averaged over the range of observed frequencies. The pointing was found to be accurate to $\lesssim 5''$ based on observations of planets; we also optimized our pointing on the sources using the relatively bright CO J = 3–2 line. All of the observations presented here have been corrected for a main beam efficiency of 0.60. Frequency calibrations were performed often to determine the precise spectral range and resolution of the facility backend used (an AOS spectrometer). The nominal channel resolution measured was 0.49 MHz per channel; the actual resolution was observed to be ~1.0 MHz per channel. The SSB reconstruction of the IRAS 16293–2422 survey therefore has channels which are 1 MHz wide, while the DSB observations have been smoothed to have similar channel widths.

TABLE C1.1

CENTER FREQUENCIES OF OBSERVATIONS
FOR THE CSO IRAS 16293-2422 SPECTRAL LINE SURVEY

USB Center (GHz)	LSB Center (GHz)	Date Observed	USB Center (GHz)	LSB Center (GHz)	Date Observed
332.650	329.850	19 March 1990	344.571	341.771	15 July 1990
332.945	330.145	15 July 1990	344.581	341.781	15 July 1990
332.950	330.150	15 July 1990	345.440	342.640	13 July 1990
332.955	330.155	15 July 1990	345.480	342.680	13 July 1990
333.388	330.588	15 July 1990	345.600	342.800	02 May 1989
333.393	330.593	15 July 1990	345.673	342.873	15 July 1990
334.740	331.940	19 March 1990	345.683	342.883	13 July 1990
334.750	331.950	19 March 1990	345.796	342.996	11 July 1990
340.197	337.397	14 July 1990	345.800	343.000	18 March 1990
340.740	337.940	16 March 1990	345.800	343.000	25 April 1989
340.750	337.950	16 March 1990	345.850	343.050	27 April 1989
341.295	338.495	14 March 1990	346.100	343.300	02 May 1989
341.300	338.500	14 March 1990	346.760	343.960	18 March 1990
342.658	339.858	13 July 1990	346.763	343.963	18 March 1990
342.668	339.868	13 July 1990	347.225	344.425	18 March 1990
342.850	340.050	02 May 1989	347.300	344.500	18 March 1990
342.883	340.083	14 July 1990	354.505	351.705	13 July 1990
343.070	340.270	16 July 1990	354.569	351.769	13 July 1990
343.100	340.300	16 July 1990	356.530	353.730	13 March 1990
343.105	340.305	16 July 1990	356.734	353.934	13 July 1990
343.193	340.393	11 July 1990	357.250	354.450	13 March 1990
343.198	340.398	11 July 1990	357.260	354.460	13 March 1990

As in Appendices A and B, we present the spectra here together with some comments on the integrated line flux for each source. A more detailed analysis of the integrated line flux, together with comparisons to continuum observations, is given in Chapter 5.

C1. The CSO IRAS 16293–2422 Spectral Line Survey

All of the observations of IRAS 16293–2422 were made during 3 sessions beginning in April 1989, with the majority of the observations made in March 1990 and July 1990. As for Orion-S, practical considerations caused us to abandon the idea of performing a complete survey over the entire 330-360 GHz range, and to make observations at selected frequencies instead. Since we were not assembling a complete survey, a variety of frequencies were observed during each session. Table C1.1 lists the frequencies and dates of the observations, showing the center frequency for both the upper and lower sidebands. Figure C1.1 shows a graphical representation of the resulting frequency coverage. We attempted to include the

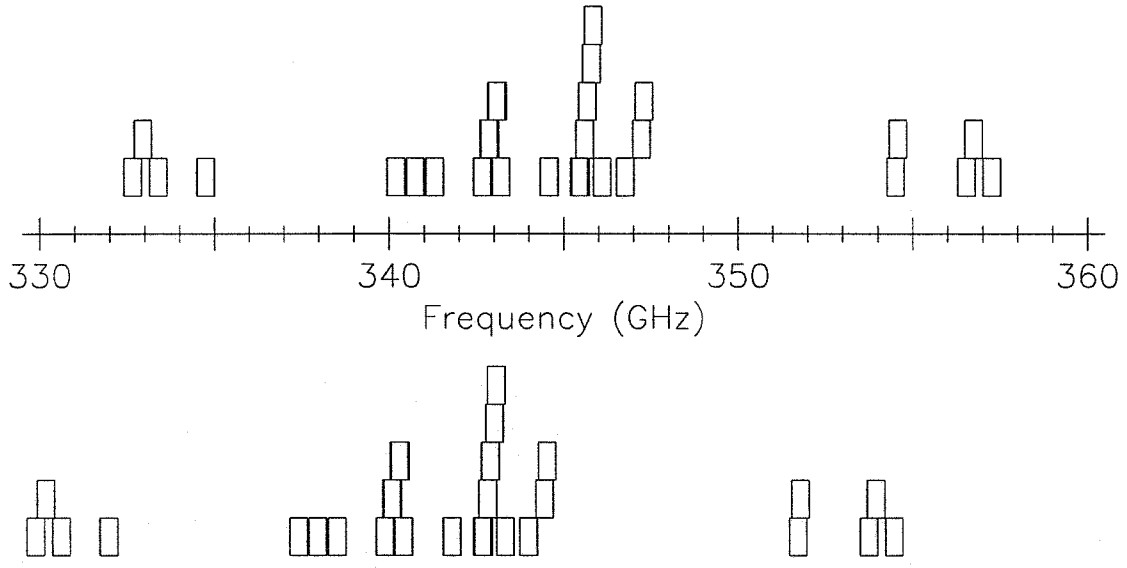

Figure C1.1 Frequency coverage of the IRAS 16293–2422 observations. Each DSB observation is represented by a pair of boxes: one showing the frequency range in the upper sideband and one showing the range of the lower sideband.

frequencies of potential strong lines in our observations rather than to achieve complete spectral coverage. As a result, the frequency coverage is much less uniform than for the complete surveys and does not include any lengthy (>3 GHz) continuous sections. When all of the scans are combined, approximately 50% of the frequency range between 330 and 360 GHz is included in our survey. The results of our line survey have been combined with lower frequency observations and presented in analyses of the chemistry of IRAS 16293–2422 (Blake *et al.* 1994, van Dishoeck *et al.* 1994).

The rich spectrum of molecular line emission from IRAS 16293–2422 is readily observable because of its proximity. As a result, it has been thoroughly studied (*e.g.*, Mundy *et al.* 1992; Mundy, Wootten & Wilking 1990; Walker *et al.* 1988, 1990) and has been used as a representative example of a low-mass star-forming region. Indeed, Blake *et al.* identify IRAS 16293–2422 as "the low mass counterpart to Orion-KL," both because of its use as a standard source for comparison and because of its tremendously rich spectrum.

C1.1. Results

A compressed view of the single sideband spectrum obtained from our survey is shown in Fig-

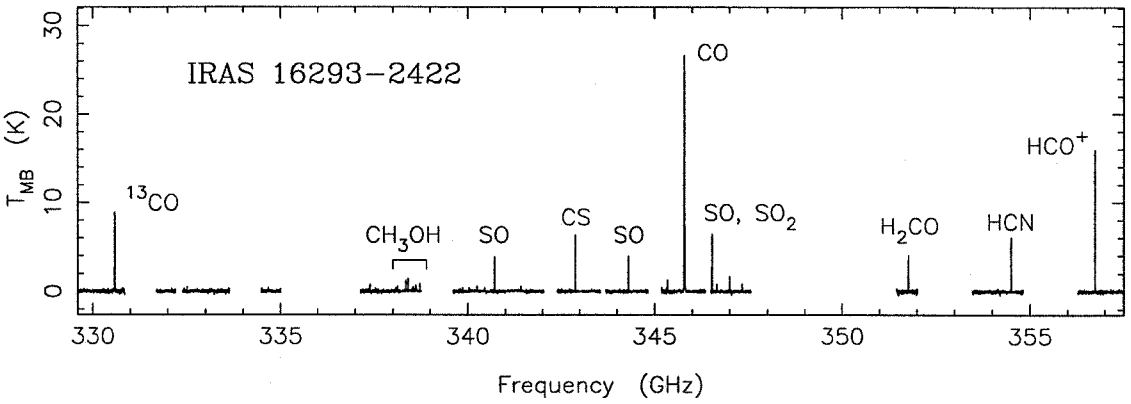

Figure C1.2 A compressed view of the CSO spectral line survey of IRAS 16293–2422.

ure C1.2, with an expanded view shown in Figure C1.3. Where the observations do not permit the deconvolution to be performed, we have assigned the observed lines to a given sideband. For such lines we plot the original DSB data at the assigned frequency only, leaving the corresponding image frequency blank. Where no lines were seen in such scans, we plot the observed spectrum (consisting essentially of noise) at both the upper and lower sideband frequencies.

A total of 65 lines were detected within the frequency range of our observations; Table C1.2 lists the frequencies and species of the detected lines, while information about the specific transitions is shown in Table C1.3. A total of 15 distinct chemical species have been identified in our survey, with 3 of the observed lines remaining unidentified. The relatively low number of unidentified lines seems likely to result from inadequate sensitivity and an inability to distinguish between lines and noise at the level of the noise. The difficulty of identifying weak lines in this source is exacerbated by the narrowness of the emission lines which gives them an appearance similar to noise spikes.

We note that despite the reduced frequency coverage, relative to IRC +10216 we detect a greater number of lines which are identified with a greater number of species. The line density thus appears to be intermediate between that of Orion-KL and IRC +10216, with the general appearance of the spectrum most similar to that of Orion-S. Blake *et al.* (1994) note that the chemical complexity appears to be intermediate between that of hot cores such as Orion-KL and cold dark clouds such as L134N. Van Dishoeck *et al.* (1994) conclude that qualitatively the physical and chemical regimes in IRAS 16293–2422 are similar to

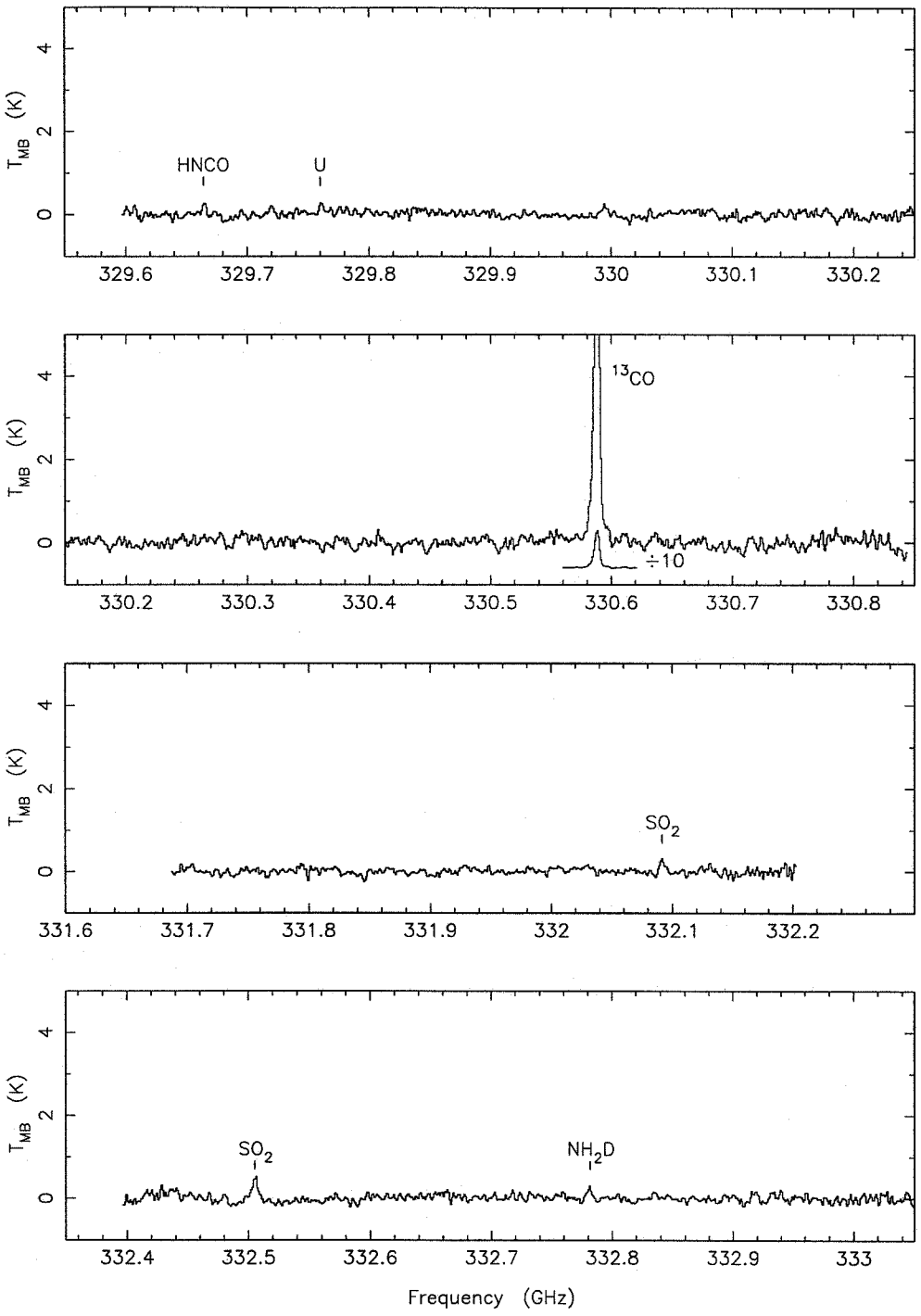

Figure C1.3 Spectrum of IRAS 16293–2422 from the CSO line survey between 330 and 360 GHz. The data have been corrected by the main beam efficiency of 0.60. The rest frequency scale has been established using a v_{LSR} of 4 km s^{-1}. Tick marks show the rest frequencies of identified transitions.

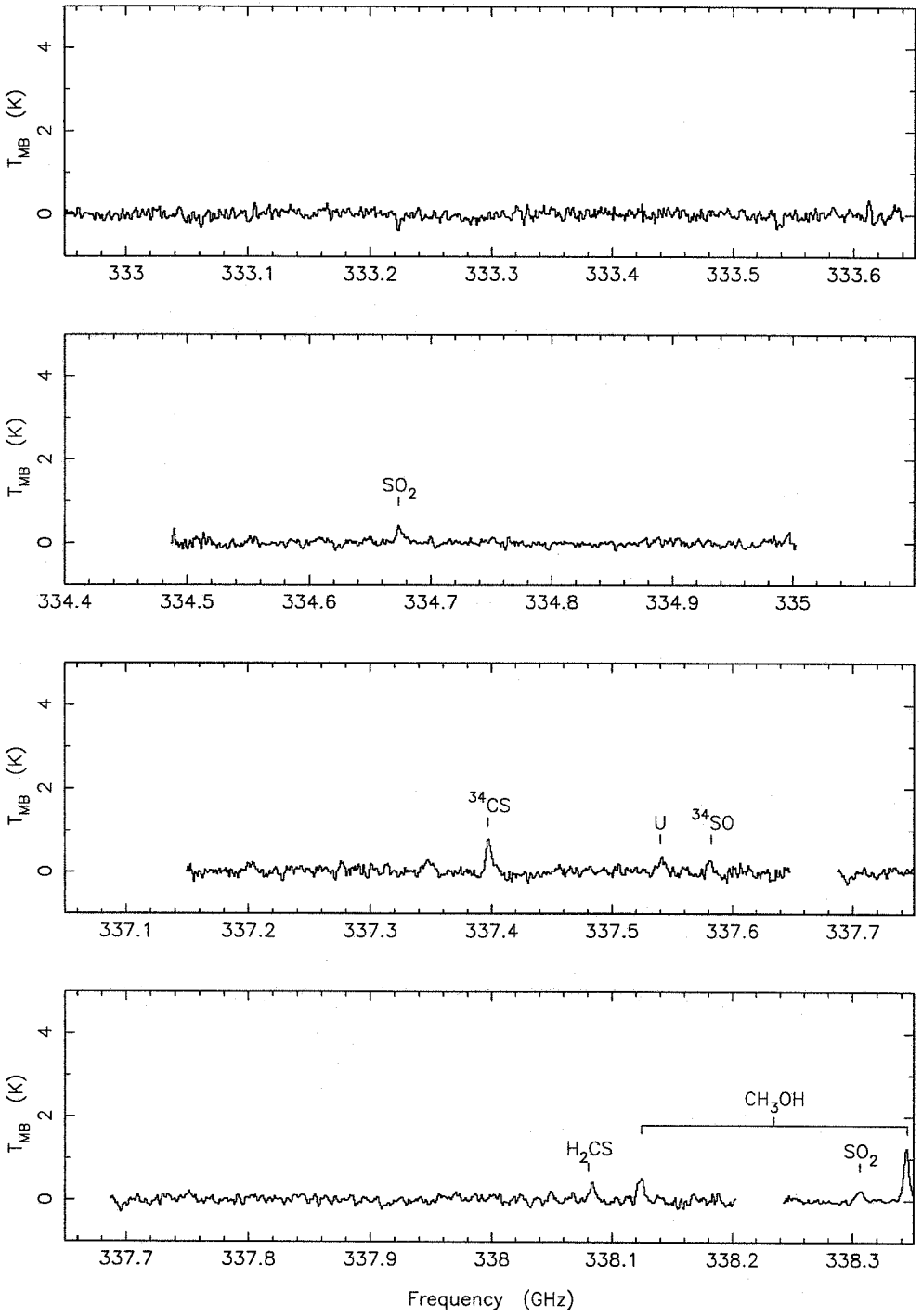

Figure C1.3 — *Continued*

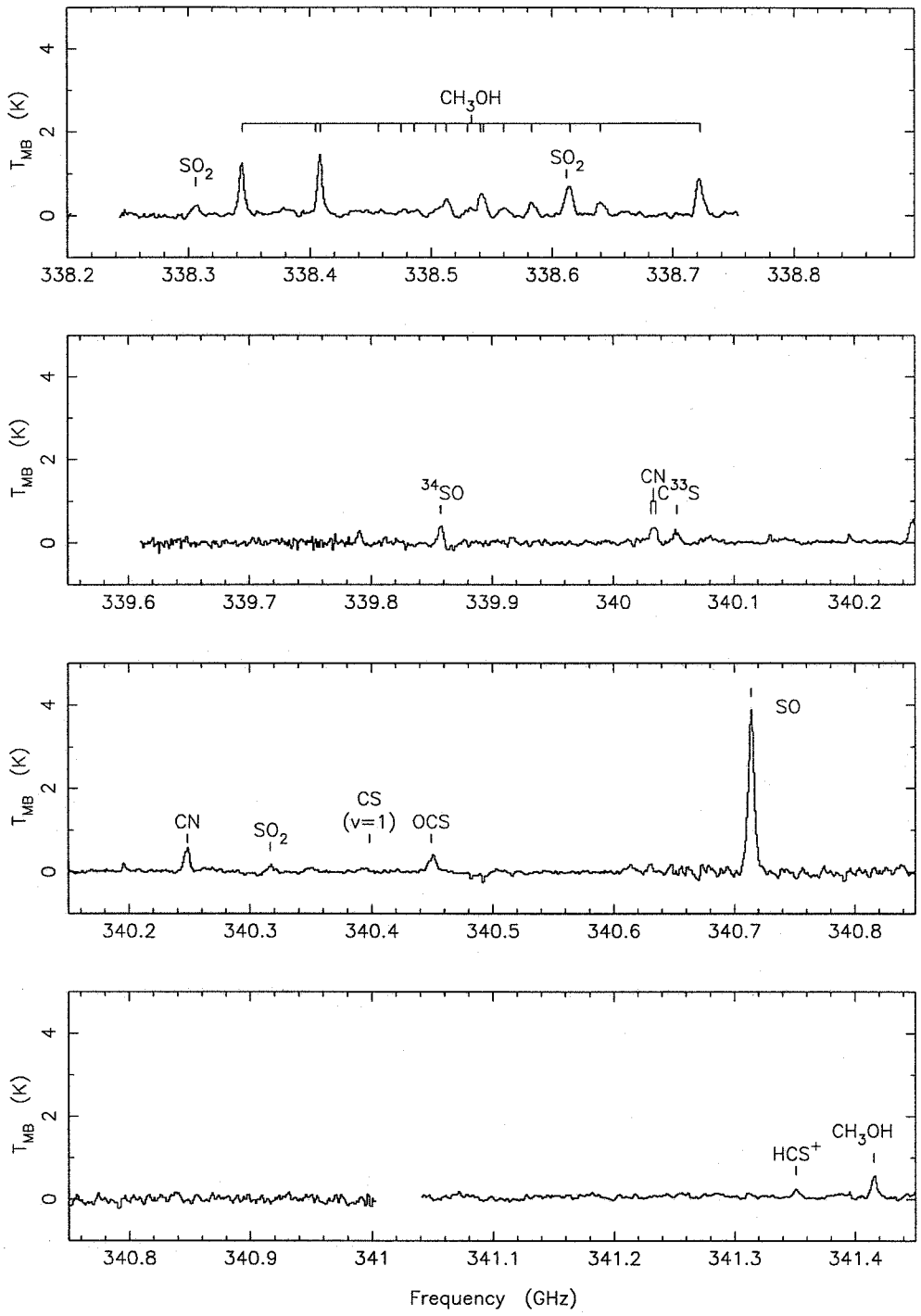

Figure C1.3 — *Continued*

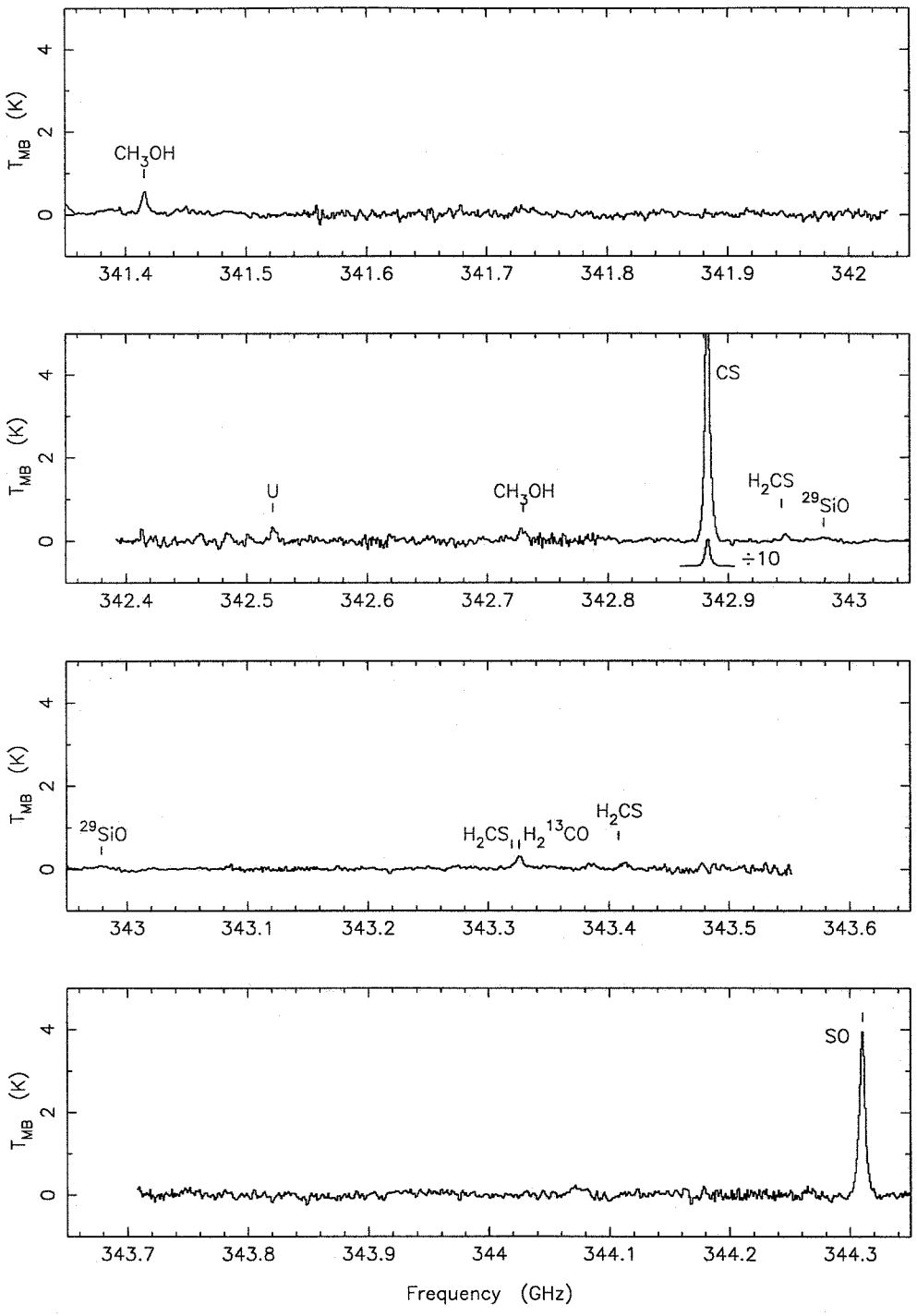

Figure C1.3 — *Continued*

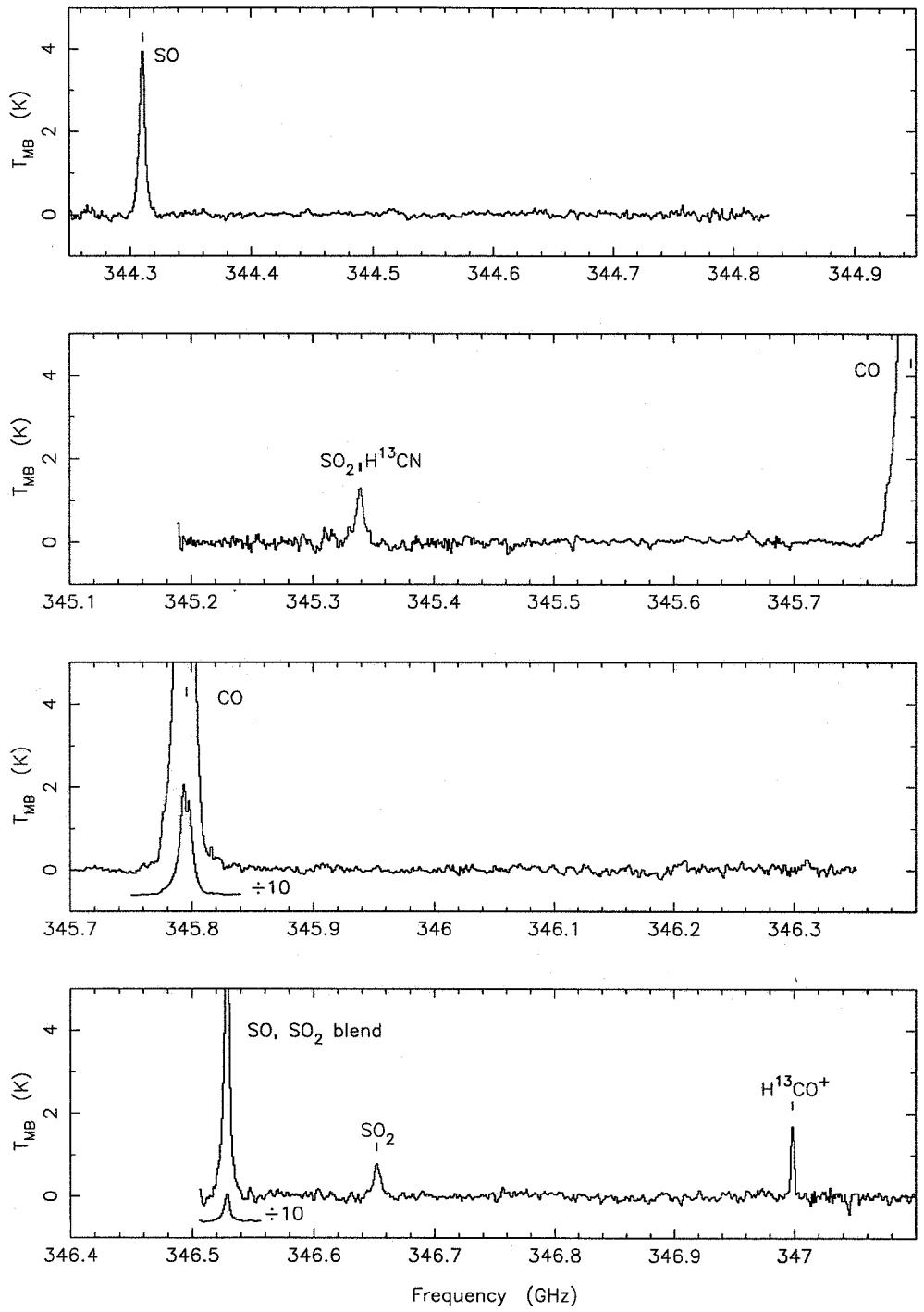

Figure C1.3 — *Continued*

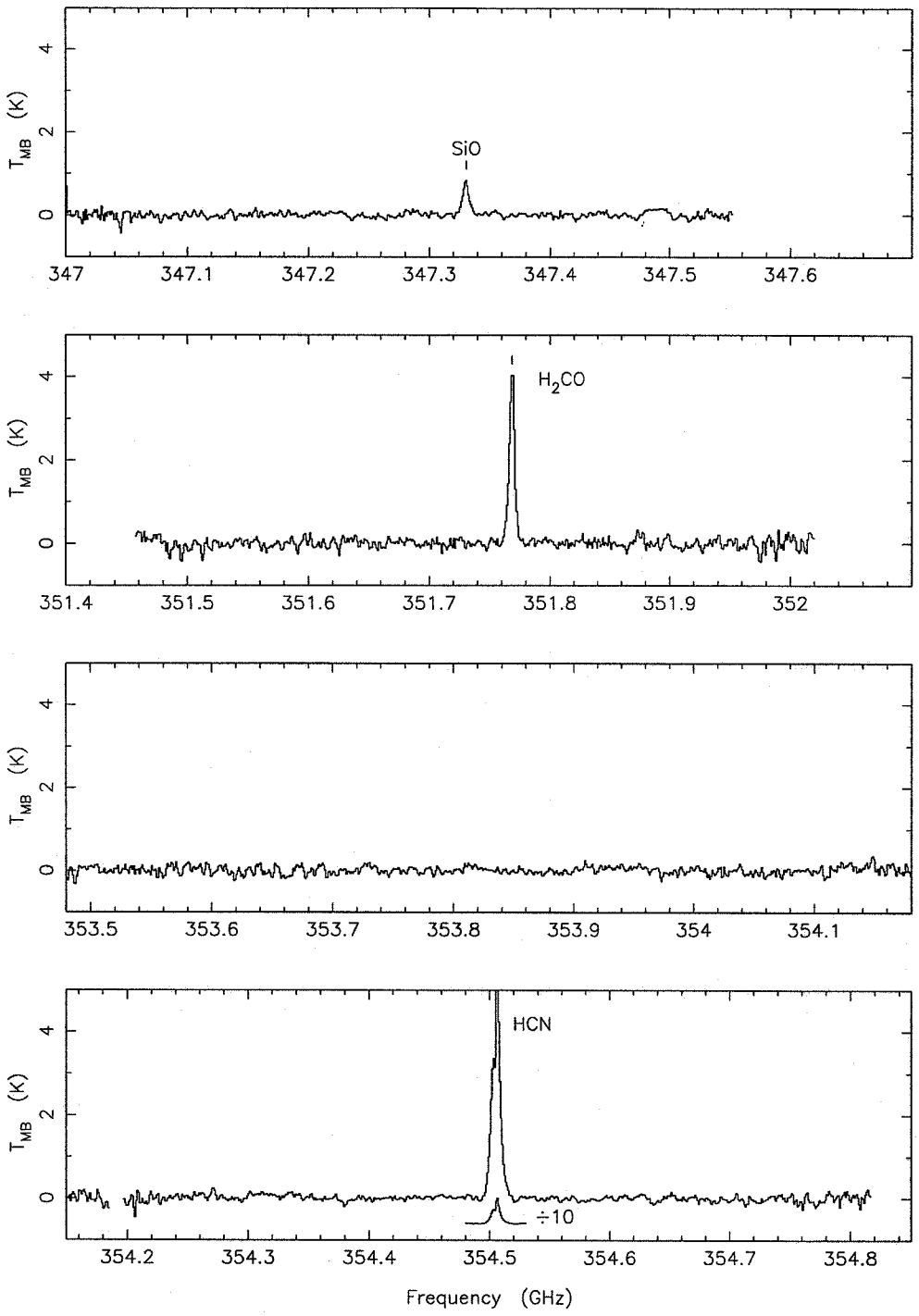

Figure C1.3—*Continued*

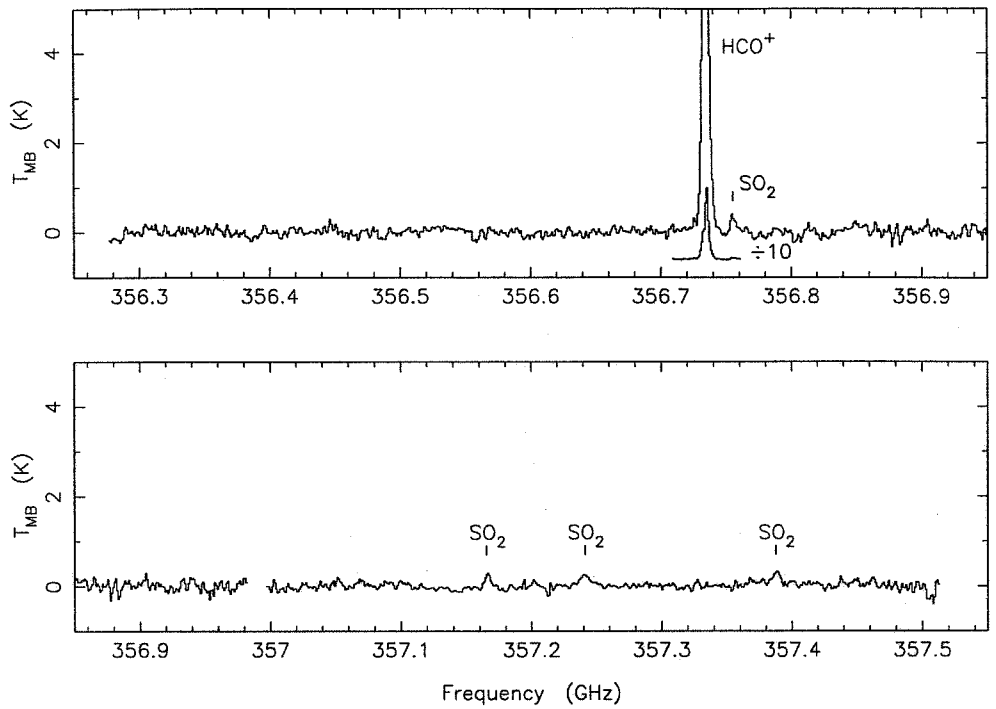

Figure C1.3 — *Continued*

TABLE C1.2

LINES DETECTED IN IRAS 16293-2422

Frequency (MHz)	Species	Frequency (MHz)	Species	Frequency (MHz)	Species
329664.0	HCNO	338540.8	CH_3OH	342944.0	H_2CS
329760	U	338543.2	CH_3OH	342979.1	^{29}SiO
330588.1	^{13}CO	338559.9	CH_3OH	343319.6	H_2CS
332091.4	SO_2	338583.2	CH_3OH	343325.7	$H_2{}^{13}CO$
332505.2	SO_2	338611.8	SO_2	343408.1	H_2CS
332781.8	NH_2D	338615.0	CH_3OH	344310.6	SO
334673.3	SO_2	338639.9	CH_3OH	345338.5	SO_2
337396.7	^{34}CS	338722.3	CH_3OH	345339.8	$H^{13}CN$
337540	U	339857.6	^{34}SO	345796.0	CO
337582.2	^{34}SO	340031.5	CN	346523.9	SO_2
338080.8	H_2CS	340035.4	CN	346528.5	SO
338124.5	CH_3OH	340052.7	$C^{33}S$	346652.2	SO_2
338306.0	SO_2	340248.2	CN	346998.5	$H^{13}CO^+$
338344.6	CH_3OH	340316.4	SO_2	347330.6	SiO
338404.6	CH_3OH	340398.1	CS (v=1)	351768.7	H_2CO
338408.7	CH_3OH	340449.2	OCS	354505.5	HCN
338456.5	CH_3OH	340714.2	SO	356734.3	HCO+
338475.3	CH_3OH	341350.8	HCS^+	356755.2	SO_2
338486.3	CH_3OH	341415.6	CH_3OH	357165.4	SO_2
338504.1	CH_3OH	342522	U	357241.2	SO_2
338512.8	CH_3OH	342729.8	CH_3OH	357387.6	SO_2
338530.3	CH_3OH	342883.0	CS		

those found in high-mass star-forming regions, and that the chemical composition in a star-forming region depends more on the age of the object than its mass.

The steps used to determine the total integrated line flux are outlined in Chapter 5, where the errors associated with our measurements and comparisons of the line and continuum flux are also discussed. A direct summation of the observed lines provides the first estimate of the line flux; however, this value may require adjusting to account for the incomplete frequency coverage. This summation yields a line flux of 1.7 Jy averaged over the actual range of the survey (corrected for the main beam efficiency). Since we have attempted to include the regions where the line emission is likely to be the strongest, this represents a probable upper limit to the line flux. A lower limit of 0.8 Jy is found by assuming no additional line emission occurs within the 330-360 GHz range but outside the specific frequencies of our survey. If the aperture efficiency were used instead of the main beam efficiency, the maximum possible value for the line flux would be 2.5 Jy. The total flux as determined by Sandell (1994) is $\sim$16 Jy at 870 μm; thus the lines represent at most 15% of the total flux, and a value of $\lesssim$10% seems more likely in light of our attempts to include all of the strong lines in our observations. A more complete discussion of the line flux estimate is given in Chapter 5.

Of the individual lines and species, by far the most important for the line flux is the CO J = 3–2 line, which represents some 42% of the total detected line flux. Including the corresponding ^{13}CO line raises the contribution to 48%, so that nearly half the total integrated line emission arises from CO. Other important molecules are SO, HCO^+, CH_3OH, and HCN, which together contribute 36% of the total line flux (including the emission from all isotopomers). Less important, but still significant, is the emission from CS, SO_2, and H_2CO. We note that only CH_3OH, with 21 transitions detected, and SO_2, with 13 transitions detected, display emission in a number of lines identified with a single species.

The proportion of the total flux contributed by the lines appears similar to that in Orion-S, and significantly less than that found for Orion-KL and IRC +10216. It also appears true that, again for this source, simulations using a relatively few molecules and simple calculations can yield approximately correct results for the line flux at unobserved frequencies, and that the contribution of the lines will depend strongly on the particular frequencies observed and the inclusion or exclusion of particular strong lines.

TABLE C1.3

OBSERVED LINES AND INTENSITIES IN IRAS 16293-2422

Species	Frequency (MHz)	Transition	E_{lower} (K)	T_{MB} (peak) (K)	$\int T_{MB}\,dv$ (K km s^{-1})
CO	345796.0	3 – 2	16.6	26.7	285.0
^{13}CO	330588.1	3 – 2	15.9	9.1	43.3
CS	342883.0	7 – 6	49.4	6.6	26.2
CS (v=1)	340398.1	7 – 6	1879.4	0.2	0.7
$C^{34}S$	337296.7	7 – 6	48.6	0.9	3.7
$C^{33}S$	340052.7	7 – 6	49.0	0.9	3.7
SiO	347330.6	8 – 7	58.3	0.8	4.5
^{29}SiO	342979.1	8 – 7	57.6	0.2	1.0
SO	340714.2	$8_7 - 7_6$	64.9	3.8	20.7
	344310.6	$8_8 - 7_7$	71.0	3.9	22.8
	346528.5	$8_9 - 7_8$	62.1	6.4	36.5 [a]
^{34}SO	337582.2	$8_8 - 7_7$	69.9	0.4	1.6
	339857.6	$8_9 - 7_8$	61.0	0.6	3.2
SO_2	332091.4	$21_{2,20} - 21_{1,21}$	203.6	0.3	3.2
	332505.2	$4_{3,1} - 3_{2,2}$	15.3	0.6	1.9
	334673.3	$8_{2,6} - 7_{1,7}$	27.1	0.3	1.3
	338306.0	$18_{4,14} - 18_{3,15}$	180.6	0.3	1.6
	338611.8	$20_{1,19} - 19_{2,18}$	182.6	0.7	5.4 [b]
	340316.4	$28_{2,26} - 28_{1,27}$	375.5	0.5	2.2
	345338.5	$13_{2,12} - 12_{1,11}$	76.4	1.2	8.1 [c]
	346523.9	$16_{4,12} - 16_{3,13}$	147.8	6.4	36.5 [d]
	346652.2	$19_{1,19} - 18_{0,18}$	151.5	0.8	5.0
	356755.2	$10_{4,6} - 10_{3,7}$	72.7	0.3	1.6
	357165.4	$13_{4,10} - 13_{3,11}$	105.8	0.3	1.6
	357241.2	$15_{4,12} - 15_{3,13}$	132.5	0.3	2.0
	357387.6	$11_{4,8} - 11_{3,9}$	82.8	0.3	2.2
CN	340031.5	$3,\frac{5}{2},\frac{7}{2} - 2,\frac{3}{2},\frac{5}{2}$	16.3	0.5	2.8 [e]
	340035.4	$3,\frac{5}{2},\frac{3}{2} - 2,\frac{3}{2},\frac{1}{2}$	16.3	...	...
	340035.4	$3,\frac{5}{2},\frac{5}{2} - 2,\frac{3}{2},\frac{3}{2}$	16.3	...	...
	340247.8	$3,\frac{7}{2},\frac{7}{2} - 2,\frac{5}{2},\frac{5}{2}$	16.3	0.7	3.0 [f]
	340247.8	$3,\frac{7}{2},\frac{9}{2} - 2,\frac{5}{2},\frac{7}{2}$	16.3	...	...
	340248.6	$3,\frac{7}{2},\frac{5}{2} - 2,\frac{5}{2},\frac{3}{2}$	16.3	...	...
HCN	354505.5	4 – 3	25.5	0.6	11.3
$H^{13}CN$	345339.8	4 – 3	25.5	1.2	8.1 [g]
HNCO	329664.5	$15_{0,15} - 14_{0,14}$	110.8	0.3	0.9

[a] Blended with SO_2 $16_{4,12} - 16_{3,13}$ line; the blended intensity is shown.

[b] Blended with CH_3OH $7_{4,3}$ E – $6_{4,3}$ E line; the blended intensity is shown.

[c] Blended with $H^{13}CN$ 4 – 3 line; the blended intensity is shown.

[d] Blended with SO $8_9 - 7_8$ line; the blended intensity is shown.

[e] Blend of CN $3_{\frac{7}{2}} - 2_{\frac{5}{2}}$ lines; the blended intensity is shown.

[f] Blend of CN $3_{\frac{5}{2}} - 2_{\frac{3}{2}}$ lines; the blended intensity is shown.

[g] Blended with SO_2 $13_{2,12} - 12_{1,11}$ line; the blended intensity is shown.

TABLE C1.3 - *Continued*

Species	Frequency (MHz)	Transition	E_{lower} (K)	T_{MB} (peak) (K)	$\int T_{MB}\,dv$ (K km s^{-1})
H_2CO	351768.7	$5_{1,5} - 4_{1,4}$	45.6	4.2	19.2
$H_2{}^{13}CO$	343325.5	$5_{1,5} - 4_{1,4}$	44.8	0.3	2.6 [h]
H_2CS	338080.8	$10_{1,10} - 9_{1,9}$	86.2	0.4	3.0
H_2CS	342944.4	$10_{0,10} - 9_{0,9}$	74.1	0.2	0.9
H_2CS	343319.6	$10_{2,9} - 9_{2,8}$	126.9	0.3	2.6 [i]
H_2CS	343408.1	$10_{3,8} - 9_{3,7}$	192.5	0.2	0.9
HCO^+	356734.3	4 – 3	25.7	15.9	63.1
$H^{13}CO^+$	346998.5	4 – 3	25.0	2.0	6.1
HCS^+	341350.8	8 – 7	57.3	0.2	1.7
NH_2D	332781.8	$1_{0,1} - 0_{0,0}$	0.6	0.4	1.4
OCS	340449.2	28 – 27	220.6	0.4	2.5
CH_3OH	338124.5	$7_{4,4}$ E – $6_{3,3}$ E	60.7	0.6	3.0
CH_3OH	338344.6	$7_{3,4}$ E – $6_{3,4}$ E	53.1	1.2	6.4
CH_3OH	338404.6	$7_{7,1}$ E – $6_{6,0}$ E	226.4	1.5	7.4 [j]
CH_3OH	338408.7	$7_{4,4}$ A^+ – $6_{3,3}$ A^+	48.8	...	...
CH_3OH	338456.5	$7_{1,6}$ E – $6_{1,6}$ E	171.6	0.1	0.7
CH_3OH	338475.3	$7_{6,1}$ E – $6_{6,1}$ E	183.6	0.1	0.7
CH_3OH	338486.3	$7_{6,1}$ $A^\pm$ – $6_{6,1}$ A±	186.6	0.1	0.6
CH_3OH	338504.1	$7_{2,6}$ E – $6_{1,5}$ E	135.5	0.2	1.0
CH_3OH	338512.6	$7_{6,2}$ $A^\pm$ – $6_{5,1}$ $A^\pm$	129.1	0.4	2.5 [j]
CH_3OH	338512.9	$7_{5,3}$ A^- – $6_{4,2}$ A^-	86.5	...	...
CH_3OH	338530.3	$7_{6,2}$ E – $6_{5,1}$ E	143.6	0.2	1.2
CH_3OH	338540.8	$7_{5,2}$ A^+ – $6_{5,2}$ A^+	98.5	0.5	3.4 [j]
CH_3OH	338543.2	$7_{5,2}$ A^- – $6_{5,2}$ A^-	98.5	...	...
CH_3OH	338559.9	$7_{2,5}$ E – $6_{2,5}$ E	110.3	0.2	1.4
CH_3OH	338583.2	$7_{5,2}$ E – $6_{5,2}$ E	95.3	0.3	1.8
CH_3OH	338615.0	$7_{4,3}$ E – $6_{4,3}$ E	68.6	0.7	5.4
CH_3OH	338639.9	$7_{5,3}$ A^+ – $6_{4,2}$ A^+	86.5	0.3	2.3
CH_3OH	338721.6	$7_{5,3}$ E – $6_{4,2}$ E	69.8	0.9	5.5 [j]
CH_3OH	338722.9	$7_{3,5}$ E – $6_{2,4}$ E	73.5	...	...
CH_3OH	341415.6	$7_{4,3}$ A^- – $6_{4,3}$ A^-	63.7	0.6	3.4
CH_3OH	342729.8	$13_{7,6}$ A^- – $13_{7,7}$ A^+	211.0	0.3	1.8
U	329760			0.3	1.1
U	337540			0.4	2.1
U	342522			0.4	1.5

[h] Blended with H_2CS $10_{2,9} - 9_{2,8}$ line; the blended intensity is shown.

[i] Blended with $H_2{}^{13}CO$ $5_{1,5} - 4_{1,4}$ line; the blended intensity is shown.

[j] Blend of CH_3OH lines; the blended intensity is shown.

[k] Blended with SO_2 $20_{1,19} - 19_{2,18}$ line; the blended intensity is shown.

TABLE C2.1

CENTER FREQUENCIES OF OBSERVATIONS FOR THE CSO VY CMA SPECTRAL LINE SURVEY

USB Center (GHz)	LSB Center (GHz)	Date Observed	USB Center (GHz)	LSB Center (GHz)	Date Observed
330.500	327.700	12 January 1991	347.170	344.370	07 January 1991
333.388	330.588	11 January 1991	351.350	348.550	09 January 1991
341.730	338.930	09 January 1991	351.355	348.555	09 January 1991
341.740	338.940	09 January 1991	351.360	348.560	09 January 1991
345.850	343.050	07 January 1991	354.460	351.660	09 January 1991
345.851	343.051	07 January 1991	354.465	351.665	09 January 1991
345.855	343.055	07 January 1991	354.470	351.670	09 January 1991
346.520	343.720	08 January 1991	356.731	353.931	08 January 1991
346.525	343.725	08 January 1991	356.734	353.934	08 January 1991
346.530	343.730	08 January 1991	356.737	353.937	08 January 1991
347.165	344.365	07 January 1991	358.080	355.080	13 January 1992

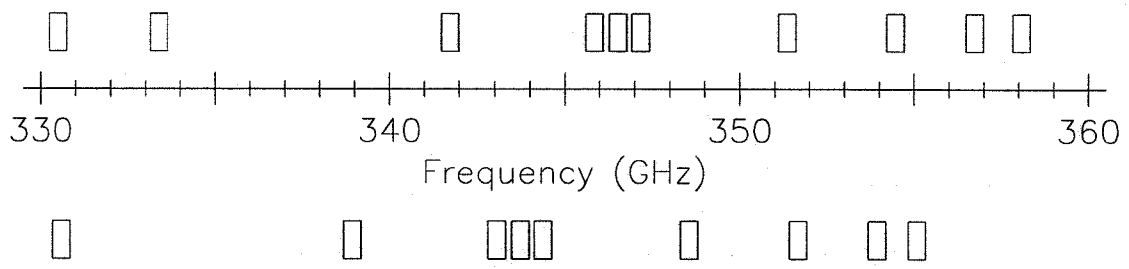

Figure C2.1 Frequency coverage of the VY CMa observations. Each DSB observation is represented by a pair of boxes: one showing the frequency range in the upper sideband and one showing the range of the lower sideband.

C2. The CSO VY CMa Spectral Line Survey

All of the observations of VY CMa were made during a single session in January 1991, with the exception of a single scan (chosen to include several potentially strong SO_2 lines) taken in January 1992. A list of the observed frequencies is given in Table C2.1, with a graphical display of the resulting frequency coverage shown in Figure C2.1. As for the IRAS 16293–2422 survey, but to an even greater extent, we selected a relatively low number of frequencies for observation, achieving approximately 30% coverage of the 330-360 GHz band. The frequencies were selected so as to include potentially strong lines; we attempted to include more than one such line in each scan through a judicious choice of the LO frequency

when possible. For many of the selected LO frequencies, we made DSB observations with 5 or 10 MHz shifts to confirm the identification of the lines with a particular sideband. Apart from these small shifts, we did not attempt to have the different DSB scans overlap. Hence the observed frequencies occur in many relatively short sections, with no lengthy continuous section as was the case for other sources. Particularly in light of the relatively weak emission from this source when compared to other sources surveyed, a much greater sensitivity than practical would have been required to make a complete survey meaningful.

C2.1. Results

Because we detected relatively few lines towards VY CMa, and given the discontinuous nature of the observed frequencies, we have chosen to plot only the detected lines for this source rather than the entire frequency range observed. These lines, as well as the frequency ranges around a few transitions which we did not detect, are shown in Figure C2.2. Excitation information about the specific transitions and the observed intensities are given in Table C2.2. A total of 10 transitions from 6 molecules are detected. We detect isotopomers only of SiO (^{29}SiO and ^{30}SiO are both seen, with 23% and 12% respectively of the integrated intensity of ^{28}SiO), while SO and SO_2 are the only molecules for which multiple lines are observed. No unidentified lines were observed; this probably reflects both the limited frequency range sampled and the relatively weak emission from only simple molecules that we do observe. The line density appears to be similar to that of IRC +10216, and rather lower than that of any of the star-forming regions (Orion-KL, Orion-S, IRAS 16293–2422) observed.

In terms of the individual lines, the CO J = 3–2 transition is still the largest single contributor to the line flux, but the SiO J = 8–7 line has an integrated intensity which is nearly as large, and is in fact has a larger peak intensity. Each of these lines contributes approximately 30% of the line flux, while the amount contributed by the HCN J = 4–3 line is approximately half as great. Transitions of SO and the isotopomers ^{29}SiO and ^{30}SiO contain nearly all of the remaining detected line flux.

Given the rather limited frequency coverage of the survey, the comparison of the line flux and the total flux is necessarily rather uncertain. Averaging the detected line flux over the actual range of frequencies observed should give an upper limit for the average line flux, since the observed frequencies

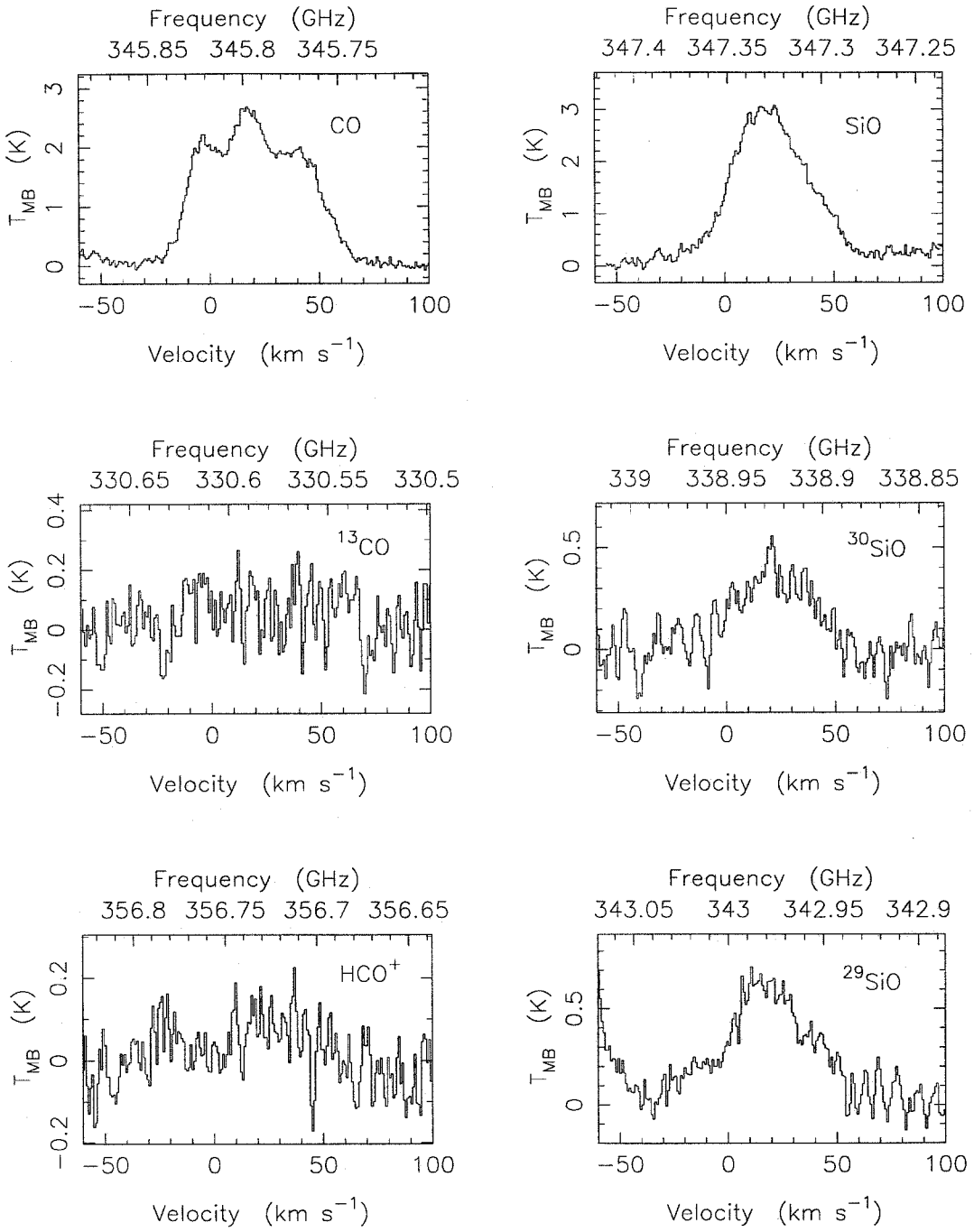

Figure C2.2 Lines observed in the CSO minisurvey of VY Canis Majoris. The observations have been corrected for the main beam efficiency of 0.6 and the indicated frequency scale has been determined for a source velocity of 18.7 km s^{-1}.

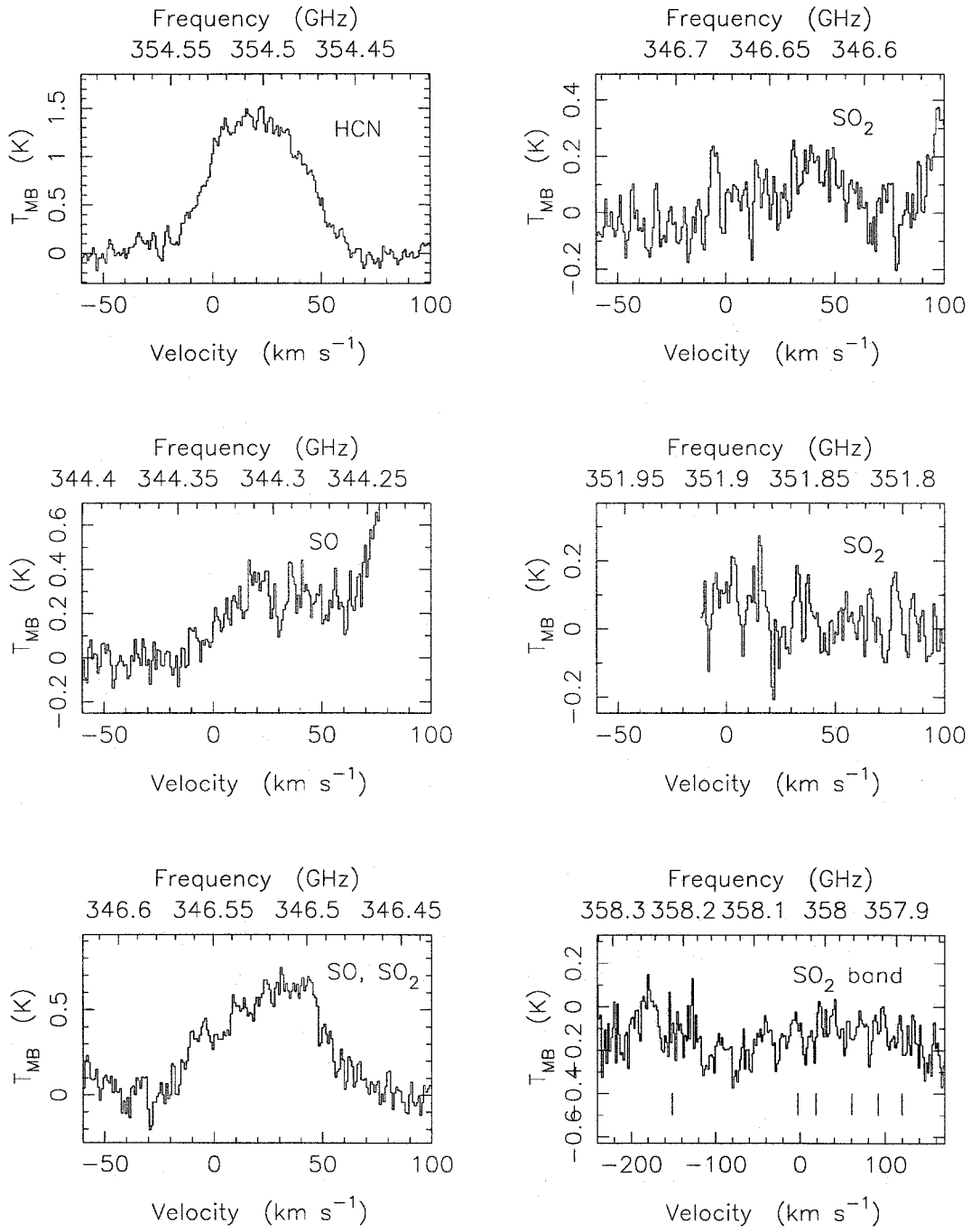

Figure C2.2—*Continued*

TABLE C2.2

OBSERVED LINES AND INTENSITIES IN VY CANIS MAJORIS

Species	Frequency (MHz)	Transition	E_{lower} (K)	T_{MB} (peak) (K)	$\int T_{MB}\,dv$ (K km s^{-1})
CO	345796.0	3 – 2	16.6	2.5	141.5
^{13}CO	330588.1	3 – 2	15.9	< 0.1	< 0.7
SiO	347330.6	8 – 7	58.3	3.0	134.3
^{29}SiO	342979.1	8 – 7	57.6	0.7	31.2
^{30}SiO	338929.0	8 – 7	56.9	0.3	15.5
HCN	354505.5	4 – 3	25.5	1.2	71.7
HCO$^+$	356734.3	4 – 3	25.7	0.1	4.2
SO	344310.6	$8_8 - 7_7$	80.0	0.3	25.0
SO	346528.5	$8_9 - 7_8$	62.1	0.6	36.0 [a]
SO_2	346523.9	$16_{4,12} - 16_{3,13}$	147.8	—	— [b]
SO_2	346652.2	$19_{1,19} - 18_{0,18}$	151.5	0.2	5.2
SO_2	351873.8	$14_{4,10} - 14_{3,11}$	119.0	$\lesssim 0.2$	$\lesssim 4.3$

[a] Blended with SO_2 $16_{4,12} - 16_{3,13}$ line; intensity is given for the blend.

[b] Blended with SO $8_9 - 7_8$ line.

were selected for their bright line emission. Averaging over the entire 330–360 GHz range, on the other hand, gives a lower limit obtained by assuming that no additional line flux is present in the unobserved regions. In the case of VY CMa, the resulting upper and lower limits for the average integrated line flux are 2.1 Jy and 0.6 Jy, respectively. (The factor of 3 difference between the limits results directly from the 28% frequency coverage achieved by our survey.) Based upon the weak emission detected, and the apparent lack of emission from additional species, it seems likely that the actual line flux is closer to the lower limit found by us. Even so, a value of 0.6 Jy represents $\gtrsim$30% of the total flux seen by Sandell (1994) towards this source at 850 μm (*cf.* also Knapp, Sandell, & Robson 1993). Note that Knapp *et al.* quote a value of 0.32 Jy for the CO J = 3–2 line alone; since the SiO J = 8–7 line contributes very nearly the same integrated intensity, these two lines alone correspond to a flux of 0.6 Jy in the range of their 850 μm filter, thus confirming our lower limit value.

TABLE C3.1

CENTER FREQUENCIES OF OBSERVATIONS FOR THE CSO OH 231.8 +4.2 SPECTRAL LINE SURVEY

USB Center (GHz)	LSB Center (GHz)	Date Observed	USB Center (GHz)	LSB Center (GHz)	Date Observed
333.388	330.588	11 January 1991	351.336	348.536	10 January 1991
333.395	330.595	11 January 1991	351.350	348.550	10 January 1991
341.740	338.940	09 January 1991	351.355	348.555	10 January 1991
345.850	343.050	10 January 1991	354.460	351.660	07 January 1991
345.855	343.055	10 January 1991	354.470	351.670	07 January 1991
345.860	343.060	10 January 1991	354.500	351.700	06 January 1991
346.525	343.725	08 January 1991	354.510	351.710	06 January 1991
346.530	343.730	08 January 1991	356.734	353.934	13 January 1991
347.165	344.365	08 January 1991	357.200	354.200	13 January 1992
347.170	344.370	08 January 1991	357.550	354.550	13 January 1992
351.330	348.530	10 January 1991	358.080	355.080	13 January 1992
351.333	348.533	10 January 1991			

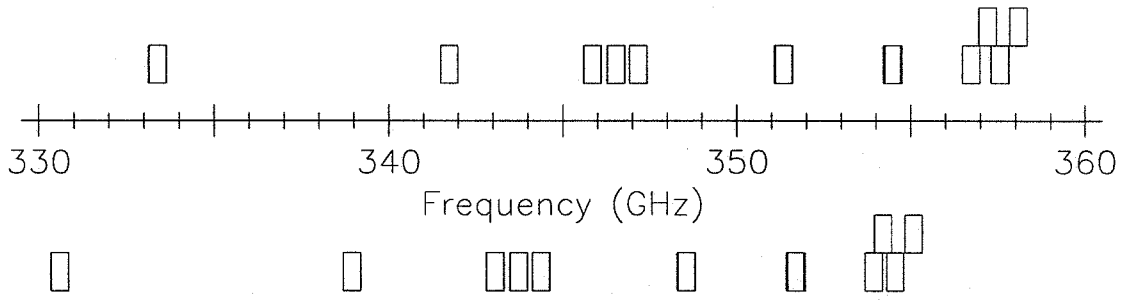

Figure C3.1 Frequency coverage of the VY CMa observations. Each DSB observation is represented by a pair of boxes: one showing the frequency range in the upper sideband and one showing the range of the lower sideband.

C3. The CSO OH 231.8+4.2 Spectral Line Survey

The observations of OH 231.8+4.2 were made during the same sessions as the observations of VY CMa. In general, we used the same frequency settings and tunings for the two sources, observing first one and then the other at a particular LO setting, so the frequency coverage is nearly identical for both. In a few cases, the exact sets of frequencies with LO shifts are different for the two sources; essentially the same set of potentially strong lines were observed, however. A list of the frequencies observed towards OH 231.8+4.2 is given in Table C3.1, with a graphical display of the resulting frequency coverage shown in Figure C3.1. As for VY CMa, we achieved approximately 30% coverage of the 330-360 GHz frequency

band in the combined scans, with the observations covering many short sections of the band rather than a long continuous section. We again note the comparatively weak emission from these two sources which led us to search for individual lines in this manner instead of conducting a complete survey.

C3.1. Results

In Figure C3.2 we have plotted the observed transitions as we did for VY CMa, *i.e.*, the transitions are shown individually rather than as a part of a plot of the entire surveyed region. Specific information about the transitions observed is given in Table C3.2. A number of differences are evident between the spectra of VY CMa and OH 231.8+4.2. The most striking of these is the clear detection of emission from the SO_2 lines in the branch near 358 GHz in OH 231.8 as compared with the weak emission seen towards VY CMa. In addition, the strong emission from SiO seen in VY CMa is nearly absent here, whereas ^{13}CO emission was absent in VY CMa but is quite strong here. The number of detected speces is similar for the two sources, and the line density (apart from the large number of SO_2 lines occuring close together) is also similar, again more like that seen for IRC +10216 than for the star-forming regions. Again, no unidentified lines were seen, with the same factors of limited frequency coverage and weak emission from only simple molecules the likely causes.

The differences in the spectra between VY CMa and OH 231.8+4.2 are reflected in considerations of the integrated line flux, of course. For this source, the CO J = 3–2 line is clearly the single most important line, with an integrated intensity more than twice as great as that of the corresponding ^{13}CO line and four times greater than that of any other transition observed. The relative contribution of CO to the integrated line flux is about the same in the two sources, representing 30% and 29% of the total observed line flux in VY CMa and in OH 231.8+4.2, respectively. However, the ^{13}CO J = 3–2 line contributes another 11% of the line flux in this source, but is not detected in VY CMa. None of the individual SO_2 transitions contributes more than 6% of the total line flux, but together they are responsible for nearly half (48%) of the total line flux, or more than CO and ^{13}CO combined. The remainder of the line flux is contained in transitions of SO (7% of the total line flux), HCN (3%), CS (1%), and SiO (1%). These are in sharp contrast to the corresponding percentages in VY CMa, where SiO is nearly as important as CO,

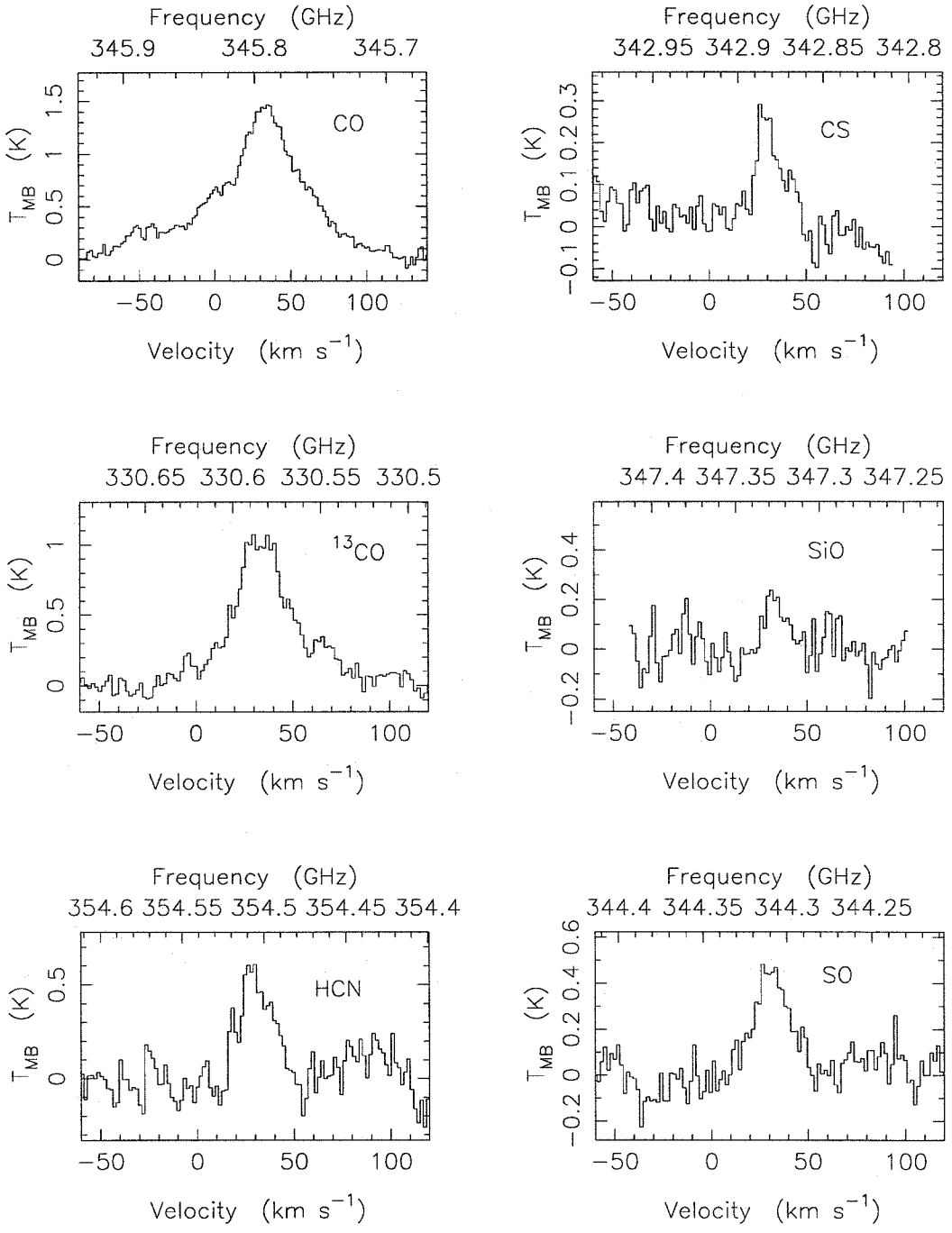

Figure C3.2 Lines observed in the CSO minisurvey of OH 231.8+4.2. The observations have been corrected for the main beam efficiency of 0.6 and the indicated frequency scale has been determined for a source velocity of 30.0 km s^{-1}.

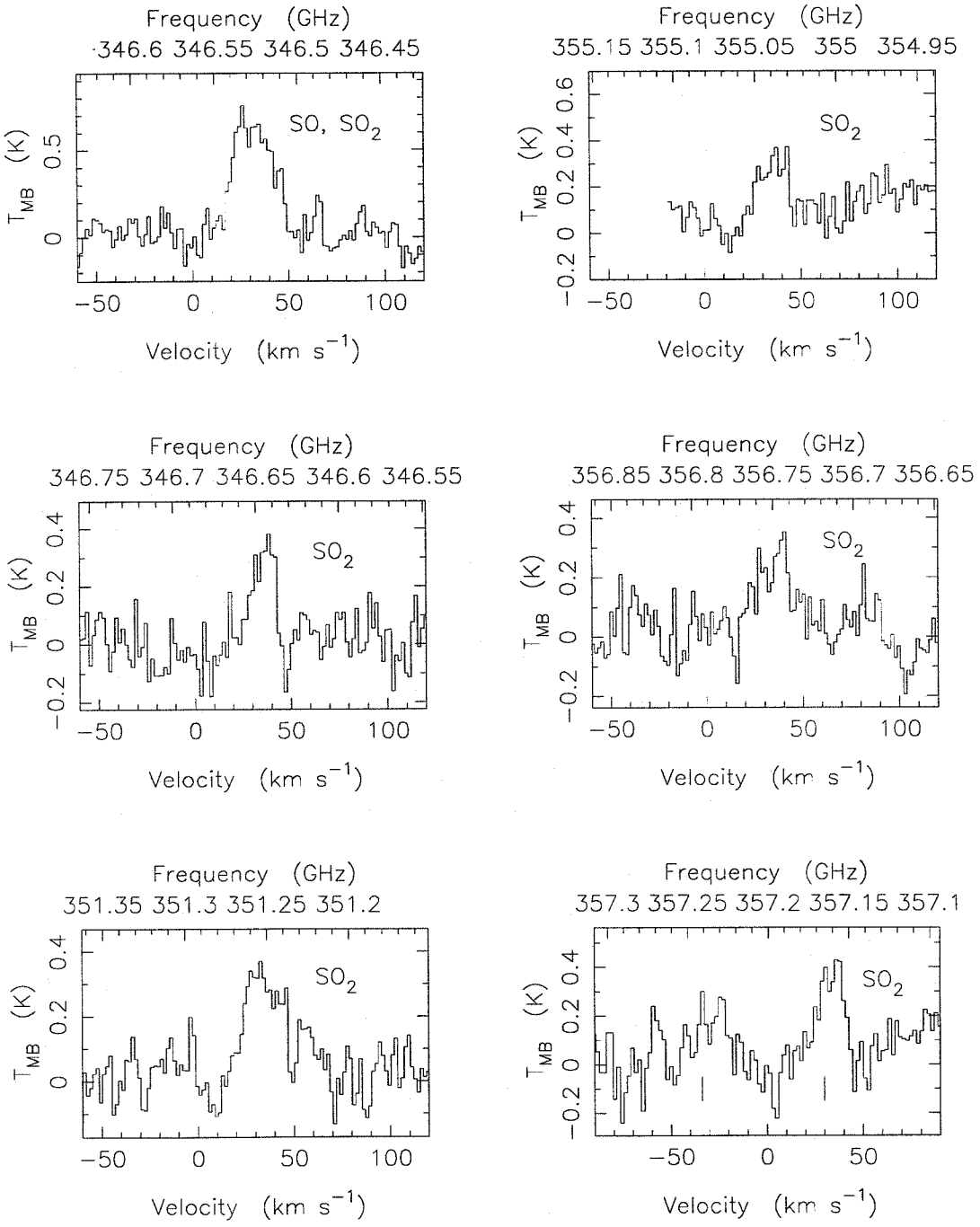

Figure C3.2 — *Continued*

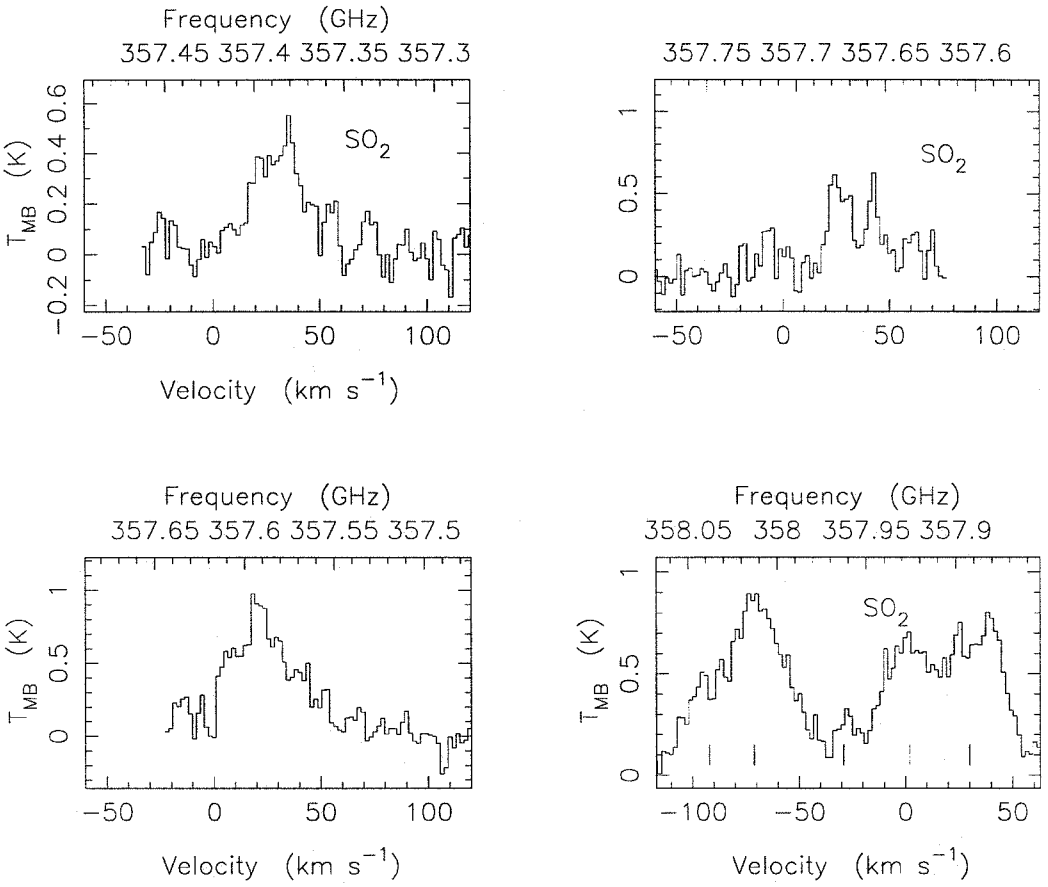

Figure C3.2 — *Continued*

TABLE C3.2

OBSERVED LINES AND INTENSITIES IN OH 231.8+4.2

Species	Frequency (MHz)	Transition	E_{lower} (K)	T_{MB} (peak) (K)	$\int T_{MB}\,dv$ (K km s^{-1})
CO	345796.0	3 – 2	16.6	1.5	99.5
^{13}CO	330588.1	3 – 2	15.9	1.1	40.7
SiO	347330.6	8 – 7	58.3	0.2	2.6
CS	342883.0	7 – 6	49.4	0.3	4.2
HCN	354505.5	4 – 3	25.5	0.6	11.3
SO	344310.6	$8_8 - 7_7$	80.0	0.5	10.2
	346528.5	$8_9 - 7_8$	62.1	0.6	13.8 [a]
SO_2	346523.9	$16_{4,12} - 16_{3,13}$	147.8	0.3	3.0 [b]
	346652.2	$19_{1,19} - 18_{0,18}$	151.5	0.3	4.4
	351257.2	$5_{3,3} - 4_{2,2}$	19.0	0.3	9.4
	355045.5	$12_{4,8} - 12_{3,9}$	94.0	0.3	6.6
	356755.2	$10_{4,6} - 10_{3,7}$	72.7	0.3	6.2
	357165.4	$13_{4,10} - 13_{3,11}$	105.8	0.4	6.7
	357241.2	$15_{4,12} - 15_{3,13}$	132.5	0.2	4.5
	357387.6	$11_{4,8} - 11_{3,9}$	82.8	0.5	13.4
	357581.4	$8_{4,4} - 8_{3,5}$	55.2	0.5	17.5
	357671.8	$9_{4,6} - 9_{3,7}$	63.5	0.5	12.3
	357892.4	$7_{4,4} - 7_{3,5}$	47.8	0.8	20.1 [c]
	357926.0	$6_{4,2} - 6_{3,3}$	41.4	0.7	19.7 [c]
	357962.9	$17_{4,14} - 17_{3,15}$	162.9	<0.2	<3.5 [d]
	358013.1	$5_{4,2} - 5_{3,3}$	35.9	0.8	21.0 [c]
	358038.1	$4_{4,0} - 4_{3,1}$	31.3	0.5	14.7 [c]

[a] Blended with SO_2 $16_{4,12} - 16_{3,13}$ line; estimated intensity for the SO line only.

[b] Blended with SO $8_9 - 7_8$ line; estimated intensity for the SO_2 line only.

[c] Estimated as part of several partially blended SO_2 lines.

[d] Upper limit; hidden by other SO_2 lines.

and HCN and SO are also significant contributors.

Just as for VY CMa, we compute upper and lower limits for the average integrated line flux at these frequencies, obtaining somewhat lower flux values of 1.3 Jy and 0.4 Jy, respectively. It again seems probable that the actual line flux is closer to the lower limit, since the transitions most likely to exhibit strong emission were included in our observations. The total flux observed for OH 231.8+4.2 at these frequencies is nearly the same as that for VY CMa (Sandell 1994, Knapp *et al.* 1993). Hence the lower line flux detected for OH 231.8+4.2 corresponds to a somewhat smaller contribution to the total flux of $\gtrsim$20% by the integrated line emission.

References for Appendix C

Avery, L. W., *et al.* 1992, *Astrophys. J. (Suppl.)*, **83**, 363.

Blake, G. A., Sutton, E. C., Masson, C. R., & Phillips, T. G. 1986, *Astrophys. J. (Suppl.)*, **60**, 357.

Blake, G. A., van Dishoeck, E. F., Jansen, D. J., Groesbeck, T. D., & Mundy, L. G. 1994, *Astrophys. J.*, **428**, 680.

Cummins, S. E., Linke, R. A., & Thaddeus, P. 1986, *Astrophys. J. (Suppl.)*, **60**, 819.

Ellison, B. N., Schaffer, P. L., Schaal, W., Vail, D., & Miller, R. E. 1989, *Int'l. J. IR & MM Waves*, **10**, 937.

Greaves, J. S., & White, G. J. 1991, *Astron. Astrophys. Suppl.*, **91**, 237.

Jewell, P. R., Hollis, J. M., Lovas, F. J., & Snyder, L. E. 1989, *Astrophys. J. (Suppl.)*, **70**, 833.

Johansson, L. E. B. *et al.* 1984, *Astron. Astrophys.*, **130**, 227.

Knapp, G. R., Sandell, G., & Robson, E. I. 1993, *Astrophys. J. (Suppl.)*, **88**, 173.

Mundy, L. G., Wootten, H. A., Wilking, B. A., Blake, G. A., & Sargent, A. I. 1992, *Astrophys. J.*, **385**, 306.

Mundy, L. G., Wootten, H. A., & Wilking, B. A. 1990, *Astrophys. J.*, **352**, 159.

Sandell, G. 1994, private communication.

Sutton, E. C., Blake, G. A., Masson, C. R., & Phillips, T. G. 1985, *Astrophys. J. (Suppl.)*, **58**, 341.

Sutton, E. C., Jaminet, P. A., Danchi, W. C., & Blake, G. A. 1991, *Astrophys. J. (Suppl.)*, **77**, 255.

Turner, B. E. 1989, *Astrophys. J. (Suppl.)*, **70**, 539.

Walker, C. K., Lada, C. J., Young, E. T., & Margulis, M. 1988, *Astrophys. J.*, **332**, 335.

Walker, C. K., Carlstrom, J. E., Bieging, H. H., Lada, C. J., & Young, E. T. 1990, *Astrophys. J.*, **364**, 173.

van Dishoeck, E. F., Blake, G. A., Jansen, D. J., & Groesbeck, T. D. 1994, in preparation.